

**Synthesis, Structures, Spectroscopic
Characterization and Oxidation State
Distributions in Metalloporphyrins**

By

WOORMILEELA SINHA

CHEM07201104008

**National Institute of Science Education and Research,
Bhubaneswar, Odisha**

*A thesis submitted to the
Board of Studies in Chemical Sciences
In partial fulfillment of requirements
for the Degree of*

DOCTOR OF PHILOSOPHY

Of

HOMI BHABHA NATIONAL INSTITUTE

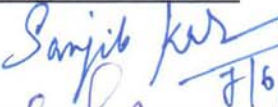
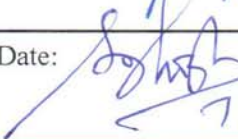
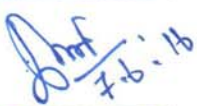
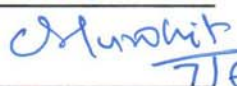


June, 2016

Homi Bhabha National Institute¹

Recommendations of the Viva Voce Committee

As members of the Viva Voce Committee, we certify that we have read the dissertation prepared by **Woormileela Sinha** entitled “**Synthesis, Structures, Spectroscopic Characterization and Oxidation State Distributions in Metalloporphyrins**” and recommend that it may be accepted as fulfilling the thesis requirement for the award of Degree of Doctor of Philosophy.

Chairman - <Prof. Tapobrata Som>	Date:  07/06/16
Guide / Convener - <Dr. Sanjib Kar>	Date:  7/6/2016
Examiner - <Prof. Sundargopal Ghosh, (IIT Madras)>	Date:  7/6/2016
Member 1- <Prof. A. Srinivasan>	Date:  7.6.16
Member 2- <Dr. Chandra Shekhar Purohit>	Date:  7/6/16

Final approval and acceptance of this thesis is contingent upon the candidate's submission of the final copies of the thesis to HBNI.

I/We hereby certify that I/we have read this thesis prepared under my/our direction and recommend that it may be accepted as fulfilling the thesis requirement.

Date: 07.06.2016
Place: NISER
BHUBANESWAR


<Signature>
Guide

¹ This page is to be included only for final submission after successful completion of viva voce.

STATEMENT BY AUTHOR

This dissertation has been submitted in partial fulfillment of requirements for an advanced degree at Homi Bhabha National Institute (HBNI) and is deposited in the Library to be made available to borrowers under rules of the HBNI.

Brief quotations from this dissertation are allowable without special permission, provided that accurate acknowledgement of source is made. Requests for permission for extended quotation from or reproduction of this manuscript in whole or in part may be granted by the Competent Authority of HBNI when in his or her judgment the proposed use of the material is in the interests of scholarship. In all other instances, however, permission must be obtained from the author.

Woormileela Sinha

Woormileela Sinha

DECLARATION

I, hereby declare that the investigation presented in the thesis has been carried out by me. The work is original and has not been submitted earlier as a whole or in part for a degree / diploma at this or any other Institution / University.

Woormileela Sinha

Woormileela Sinha

LIST OF PUBLICATIONS

Journal

1. ***Sinha, W.**; Sommer, M. G.; Deibel, N.; Ehret, F.; Bauer, M.; Sarkar, B.; Kar, S., Experimental and Theoretical Investigations of the Existence of Cu^{II}, Cu^{III}, and Cu^{IV} in Copper Corroloato Complexes. *Angew. Chem. Int. Ed.* **2015**, *54* (46), 13769-13774. (*Hot Paper*)
2. ***Sinha, W.**; Sommer, M. G.; Deibel, N.; Ehret, F.; Sarkar, B.; Kar, S., Silver Corrole Complexes: Unusual Oxidation States and Near-IR-Absorbing Dyes. *Chem. Eur. J.* **2014**, *20* (48), 15920-15932.
3. ***Sinha, W.**; Kar, S., Reactions of Grignard Reagents with Tin-Corrole Complexes: Demetalation Strategy and σ -Methyl/Phenyl Complexes. *Organometallics* **2014**, *33* (22), 6550-6556.
4. ***Sinha, W.**; Kumar, M.; Garai, A.; Purohit, C. S.; Som, T.; Kar, S., Semi-insulating behaviour of self-assembled tin(IV) corrole nanospheres. *Dalton Trans.* **2014**, *43* (33), 12564-73.
5. ***Sinha, W.**; Deibel, N.; Agarwala, H.; Garai, A.; Schweinfurth, D.; Purohit, C. S.; Lahiri, G. K.; Sarkar, B.; Kar, S., Synthesis, Spectral Characterization, Structures, and Oxidation State Distributions in [(corroloato)Fe^{III}(NO)]ⁿ (n= 0,+ 1,- 1) Complexes. *Inorg. Chem.* **2014**, *53* (3), 1417-1429.
6. **Sinha, W.**; Ravotto, L.; Ceroni, P.; Kar, S., NIR-emissive iridium(III) corrole complexes as efficient singlet oxygen sensitizers. *Dalton Trans.* **2015**, *44*, 17767-17773.

*Pertaining to thesis

-
7. **Sinha, W.**; Sommer, M. G.; van der Meer, M.; Plebst, S.; Sarkar, B.; Kar, S., Structural, Electrochemical and Spectroelectrochemical Study on the Geometric and Electronic Structures of [(corrolato)Au^{III}]ⁿ (n = 0, +1, -1) Complexes. *Dalton Trans.* **2016**, *45*, 2914–2923.
 8. **Sinha, W.**; Deibel, N.; Garai, A.; Schweinfurth, D.; Anwar, S.; Purohit, C. S.; Sarkar, B.; Kar, S., In-situ spectroelectrochemistry (EPR, UV–visible) and aggregation behavior of H₂BDCP and Zn(II)BDCP [BDCP={5, 10, 15, 20-tetrakis [3, 4-(1, 4-dioxan) phenyl] porphyrin}²⁻]. *Dyes Pigm.* **2014**, *107*, 29-37.
 9. Garai, A.; Kumar, S.; **Sinha, W.**; Purohit, C. S.; Das, R.; Kar, S., A comparative study of optical nonlinearities of trans-A₂B-corroles in solution and in aggregated state. *RSC Adv.* **2015**, *5* (36), 28643-28651.
 10. Garai, A.; Kumar, M.; **Sinha, W.**; Chatterjee, S.; Purohit, C. S.; Som, T.; Kar, S., Synthesis, electron transports, and charge storage properties of fullerene–zinc porphyrin hybrid nanodiscs. *RSC Adv.* **2014**, *4*, 64119-64127.
 11. Garai, A.; Nandy, P.; **Sinha, W.**; Purohit, C. S.; Kar, S., A New Synthetic Protocol for the Preparation of 5-Cyano-10, 15, 20-tris(alkoxyphenyl)porphyrins. *Polyhedron* **2013**, *56*, 18-23.

Woormileela Sinha

Conferences

1. Indo-European Symposium on Frontiers of Chemistry, November 10-12th, 2011, conducted at School of Chemical Sciences, National Institute of Science Education & Research (NISER), Bhubaneswar.
2. “Synthesis, Spectral Characterization, Structures, and Oxidation State Distributions in [(corrolato)Fe^{III}(NO)]ⁿ (n = 0, +1, -1) Complexes”- in Indo-French Symposium on Functional Metal-Organics: Applications in Materials and Catalysis, February 24-26th, 2014 organized at School of Chemical Sciences, National Institute of Science Education & Research, Bhubaneswar. **(Poster Presentation)**
3. “Silver Corrole Complexes: Model Compounds for Photosynthetic Special-Pairs”- in XXXIII Annual Conference, Indian Council of Chemists, December 15-17th, 2014, conducted at Department of Applied Chemistry, Indian School of Mines, Dhanbad. **(Oral Presentation)**
4. “Fabrication of a Semi-insulating Device and Demetalation Strategy Using Novel Tin(IV) Corroles”- in International Symposium on Modern Trends in Inorganic Chemistry-XVI, December 3-5, 2015, conducted at Department of Chemistry, Jadavpur University, Kolkata. **(Poster Presentation)**
5. “Exploration of Cu^{II}, Cu^{III} and Cu^{IV} in Copper(III) Corroles”- in National Seminar on Science and Technology for Indigenous Development in India, Indian Science Congress Association, December 9-11, 2015, conducted at KIIT University, Bhubaneswar. **(Poster Presentation)**

Woormileela Sinha

Woormileela Sinha

Dedicated to....

Maa, Baba & Dada

ACKNOWLEDGEMENTS

*I am extremely grateful to the **Almighty** for showering immense blessings and guiding me through the twists and turns of life. Life would not have bestowed me a better destiny than this without the grace of my **Lord**.*

*I extend my deepest gratitude and respect to my Supervisor, **Dr. Sanjib Kar**, Reader-F, NISER for his knowledge, patience, kind-heartedness and active support. His optimism, behavior and belief throughout the entire phase of my PhD will be remembered life-long.*

*I am thankful to **Prof. V. Chandrasekhar**, Director, NISER and also **Prof. T. K. Chandrashekar**, Founder Director, NISER for providing the laboratory and instrumental facilities. I would also like to acknowledge **NISER** for providing fellowship.*

*I will take this opportunity to thank my thesis monitoring committee members, **Dr. C. S. Purohit**, **Dr. M. Sarkar**, Chairperson, and also **Prof. A. Srinivasan**, **Dr. A. Ghosh**, **Dr. N. K. Sharma**, **Dr. S. Nembenna**, **Dr. H. S. Biswal**, **Dr. A. Kumar**, NISER for their useful suggestions and support on several occasions.*

*I owe my deepest gratitude to my collaborators, **Prof. G. K. Lahiri**, **Prof. T. Som**, **Prof. B. Sarkar**, **Prof. P. Ceroni** for helping me explore and expand various aspects of my research.*

*I sincerely thank **Mr. Deepak**, **Mr. Sanjaya**, **Mr. Pravakar**, **Mr. Amit** and **Mr. Raj Kumar**, NISER for performing characterization of my samples.*

*I am indebted to **all my teachers** of school, graduation and post-graduation who inculcated knowledge, discipline and encouragement.*

*It gives me immense pleasure to thank all those seniors, friends and juniors who made my stay at NISER really enjoyable and memorable. Special mention must be made of my labmates, **Antara**, **Arindam**, **Yogesh**, **Subbu**, **Dr. Jitendra**, **Rishabh**, **Gaurav**, **Mainak**, **Prerna**, **Bratati**, **Narugopal**, **Payel** & **Sajal**, senior **Mohit** (IOP) and my best friends **Adi**, **Gargi** & **Manali** for their support.*

*I am privileged to stay strongly bonded to my beloved **Baba**, **Maa** and **Dada**, who cared for my education and everything else. Their unconditional love, sacrifices, blessings and inspiration have strengthened me to face all the hurdles in my journey of life. Staying away from family, in Bhubaneswar was possible because of a very dear friend **Dr. Sandip Kr. Nandi** whose encouragement, support and company will be remembered forever.*

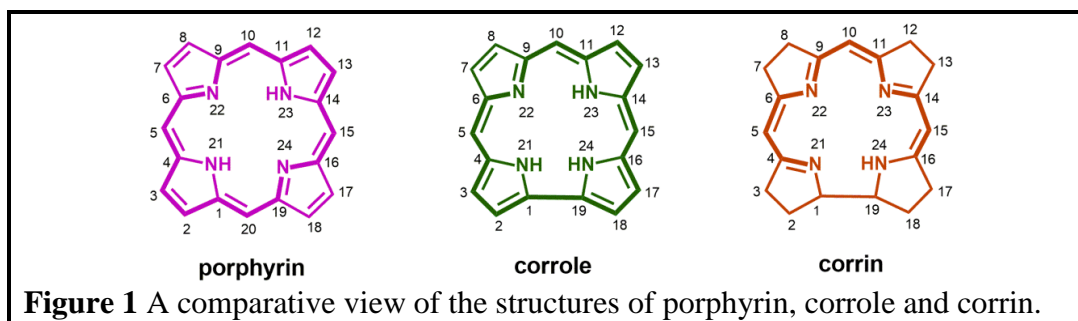
Woormileela Sinha

CONTENTS

	Page No.
Synopsis	xi
List of Tables	xxi
List of Schemes	xxiii
List of Figures	xxv
Glossary of Acronyms	xxxiii
Chapter 1	1
Chapter 2	35
Chapter 3	83
Chapter 4	113
Chapter 5	143
Chapter 6	179
Summary and Future Prospect	210
References	213
Appendix	242

SYNOPSIS

Porphyrins are a unique class of aromatic tetrapyrroles that are capable of performing diverse roles in natural processes such as oxygen carriage, electron transport, etc. Due to its functional versatility, it remains the most abundant and studied “pigment of life”^{1, 2}. Corroles, a classification of contracted porphyrin have recently gained a lot of research interest for its interesting structural and spectroscopic properties³. The name corrole was chosen by Johnson and Price due to its strong structural resemblance with the naturally occurring corrin ring of vitamin B₁₂⁴. Because of the similarity of the corroles also with the 18 π -electron aromatic porphyrins, corroles are better designated as intermediates between corrins and porphyrins (Figure 1)^{2, 5}.



Since the discovery of the corroles, research in this field failed to flourish much when compared to porphyrins, due to lack of efficient and simple synthetic methodologies till 1999. After the reports of several facile synthetic methodologies at the end of the 20th century, advances in the field of corrole chemistry came into limelight^{6, 7}. In recent years, research on corroles have gained a huge impetus and corroles have been already explored as oxidation catalysts (Fe, Mn, Sb), reduction catalysts (Fe, Mn, Cr), group transfer catalysts (Fe, Rh), sensors (Co), as dyes in dye-sensitized solar cells (Sn, Ga), drugs in medicinal research (Ga), etc³.

Despite of the huge efforts of several scientists in this field, many more challenges are yet to be overcome, particularly in exploring some of their superior

electronic, spectroscopic, photophysical properties and their applications in mimicking the natural occurring biological processes and device fabrication.

Scope and Organization of the Present Thesis

In this thesis, attempts have been made to explore various scaffolds of corrole frameworks and their corresponding metal derivatives on the basis of either biological or physical significances. Attempts were made to understand the mechanistic aspects of their reactivity and also electronic, structural, morphological and spectroscopic changes in individual cases. Additionally, application of one of the metallocorroles in device fabrication has been also explored. The present thesis has been organized in six chapters and the contents of each chapter have been summarised as follows:

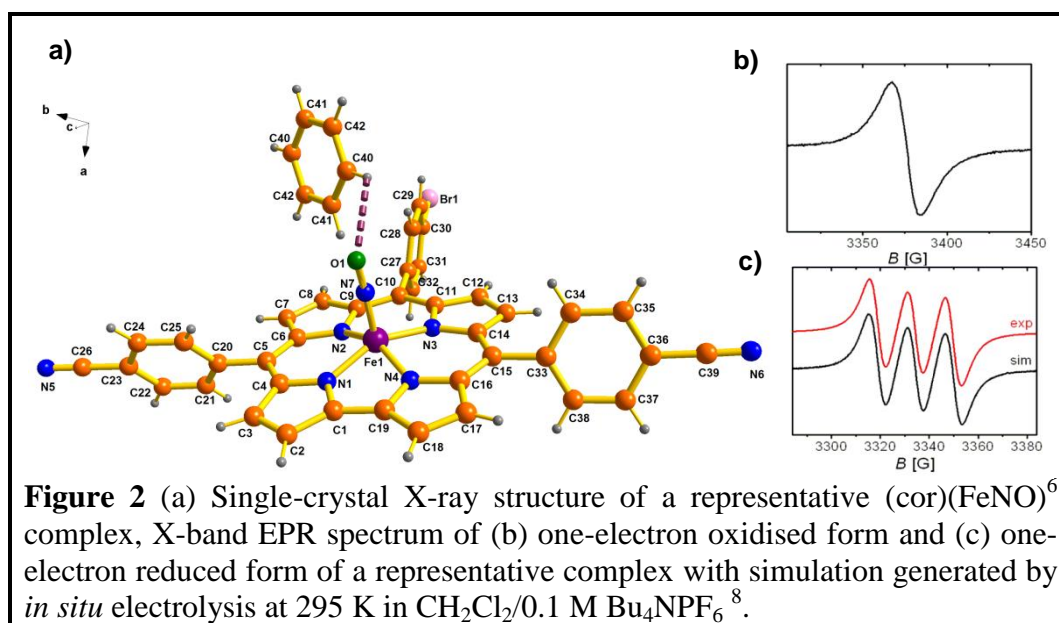
Chapter 1 Introduction

In Chapter 1, biological significance and structure of some of the “pigments of life” with special mention to porphyrins and its structural modifications has been narrated ¹, ². The history and development of the various types of contracted porphyrins are also highlighted. Major discussion in this chapter is centered on the origin, characteristic properties and various synthetic protocols of one of the most studied contracted porphyrins, corroles. A review on the rich coordination chemistry of corroles exploring the various coordination modes in metallocorroles and the importance of spectroelectrochemical investigations for their characterization are included. The mode of usage of several metallocorroles in various applications, such as catalysis, sensors, dye sensitized solar cells and medicine-based researches are also demonstrated. From an exhaustive literature study, several lacunae were identified, and on the basis of that the objectives set are mentioned at the end of this chapter.

Chapter 2 Synthesis, Spectral Characterization, Structures, and Oxidation State Distributions in [(corrolato)Fe^{III}(NO)]ⁿ (n = 0, +1, -1) Complexes

In Chapter 2, we have studied the synthesis and characterization of two novel trans-A₂B corroles and three [(corrolato){FeNO}]⁶ complexes⁸. The ¹H NMR and ¹³C NMR studies established the diamagnetic nature of these complexes in the native state. The structural characterization of two of the [(corrolato){FeNO}]⁶ derivatives has been discussed in this chapter. The distorted square pyramidal geometry around the centrally placed iron atoms, have axially coordinated NO at Fe–N–O bond angles of 175.0(4)° and 171.70(3)° (DFT: 179.94°) and are thus designated as linear nitrosyls (Figure 2a). In order to investigate the characteristic spectroscopic changes in all the accessible redox states, spectroelectrochemical studies were performed. FTIR thin-layer measurements on one of the complexes exhibited a small shift of 38 cm⁻¹ and a considerable shift of 177 cm⁻¹ in the ν_{NO} stretching frequencies on one-electron oxidation and one-electron reduction respectively. The small shift indicated that the oxidation occurred on the corrolato ring while the large shift was a clear indication of the fact that on reduction, {FeNO} unit was directly perturbed. The X-band EPR spectrum at 295 K in CH₂Cl₂/0.1 M Bu₄NPF₆ of both the one-electron oxidized and one-electron reduced species showed an isotropic signal centered at $g = 2.005$ with a peak to peak separation of about 15 G and $g = 2.029$, with a hyperfine coupling to one nitrogen nucleus ($I = 1$) respectively (Figure 2b and 2c). Although earlier literature established that EPR signals predominantly originated from a low spin Fe^{III} center^{9, 10}, however, our observations clearly prove that the predominant location of the spin was on the corrole unit⁸. The DFT results on the one-electron reduced species indicated the occurrence of reduction predominantly at NO unit. Thus, in this chapter, our investigation on the one-electron oxidized species delivers the non-innocent

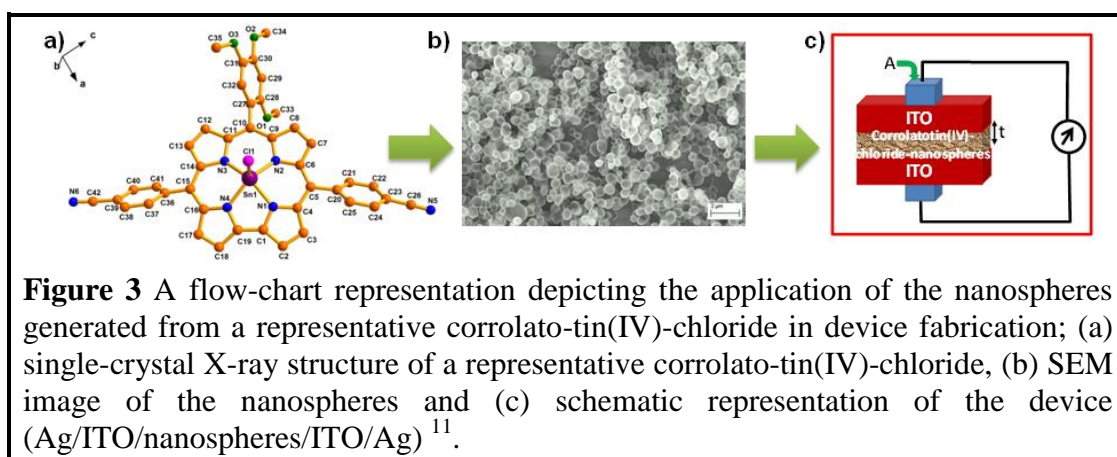
character of the corrole ring and while that on the one-electron reduced species reveals the non-innocent nature of the oldest known non-innocent ligand, NO.



Chapter 3 Semi-Insulating Behaviour of Self-assembled Tin(IV) Corrole Nanospheres

In Chapter 3, we have investigated the synthesis and characterization of three novel tin(IV) corrole complexes¹¹. All the three tin(IV) corroles were found to exhibit strong absorptions corresponding to $\pi \rightarrow \pi^*$ transitions in the range 400-650 nm and also strong emission in the red-regions of the visible spectra at room temperature in dichloromethane solvent. ¹H NMR studies on the corrolato-tin(IV) complexes reconfirmed the diamagnetic nature of the complexes. X-ray crystal analysis of the studied corrolato-tin(IV) complexes indicated distorted square pyramidal geometry around the central tin atoms (Figure 3a). Further revelations from the crystal packing diagrams on the structures of these complexes were the presence of C–H \cdots Cl hydrogen bonding interactions with H \cdots Cl distances in the range of 2.848–3.051 Å and C–H \cdots Cl angles varying from 119.72° to 147.08°. Such type of interaction lead to the formation of infinite one-dimensional polymeric chains in two of the complexes

while in the remaining one, dimers were formed. Self-aggregation properties of these complexes and their morphological characterization by SEM have been discussed in this chapter. SEM images indicated an almost uniform and well-defined distribution of hollow nanospheres of tin(IV) corroles with diameters of *ca.* 676 nm and 661 nm (Figure 3b). Finally application of the generated nanospheres in device fabrication has been also explored in this chapter. A device was fabricated with the composition of Ag/ITO-coated glass/nanospheres/ITO-coated glass/Ag using a layer of the nanospheres on ITO surface (AFM height of ITO films: 200 nm) (Figure 3c). I-V plot of the device indicated its Ohmic characteristic and observed resistance was $\sim 4.8 \times 10^7 \Omega$. Assuming uniform distribution of the nanospheres, resistivity (ρ) of the device was calculated to be $\sim 2.4 \times 10^8 \Omega \text{ cm}$, which falls in the zone of semi-insulating semiconductors. Further CAFM measurements were performed to understand local

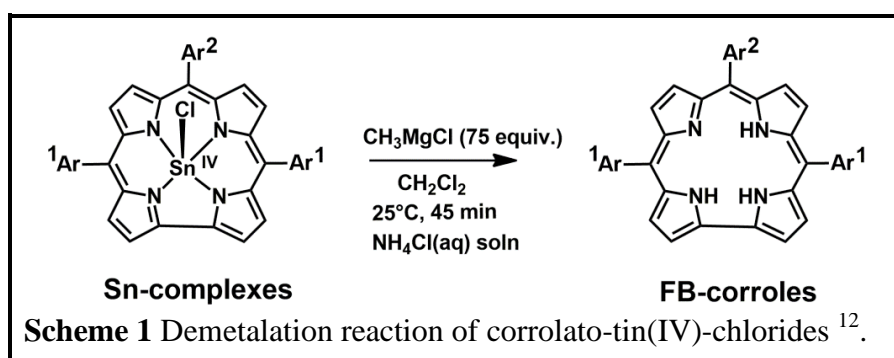


electrical properties and current conduction pathways in the device. At 10 V bias, CAFM current maps showed bright spots with 10–20 pA intensity suggesting that nanospheres (~ 250 nm in diameter) are preferentially electron-conducting pathways in the device.

Chapter 4 Reactions of Grignard Reagents with Tin-Corrole Complexes: Demetalation Strategy and σ -Methyl/Phenyl Complexes

In Chapter 4, a one-step demetalation strategy has been developed for the efficient

conversion of tin(IV) corroles to the corresponding free-base corroles¹². The reagent used for such transformation is a Grignard reagent. It was observed that on reaction with different types of Grignard reagents with the tin(IV) chlorides, different types of products were formed. σ -methyl and σ -phenyl complexes of tin(IV) corrole were obtained when the Grignard reagents used were methyl magnesium bromide and phenyl magnesium bromide respectively. Surprisingly, almost complete destannation was observed when methyl magnesium chloride was used (Scheme 1). The versatility of this demetalation protocol has been tested on a wide variety of substrates and a mechanism has been also proposed. In addition to the optimization of this demetalation protocol, the synthesis and characterization of a series of novel compounds, viz. one A₃ corrole, corrolato-tin(IV)-chloride, three σ -methyl complexes and two σ -phenyl complexes have been discussed in this chapter. Structural characterizations of σ -methyl/ σ -phenyl tin(IV) corroles revealed that the central tin atoms sit in a slightly distorted square pyramidal geometry. ¹H NMR studies of the tin(IV) complexes revealed that the signals corresponding to the σ -bonded phenyl rings and σ -bonded methyl groups appeared in the high field regions of 6.42–3.62 ppm and (-)3.28–(-)3.41 ppm.

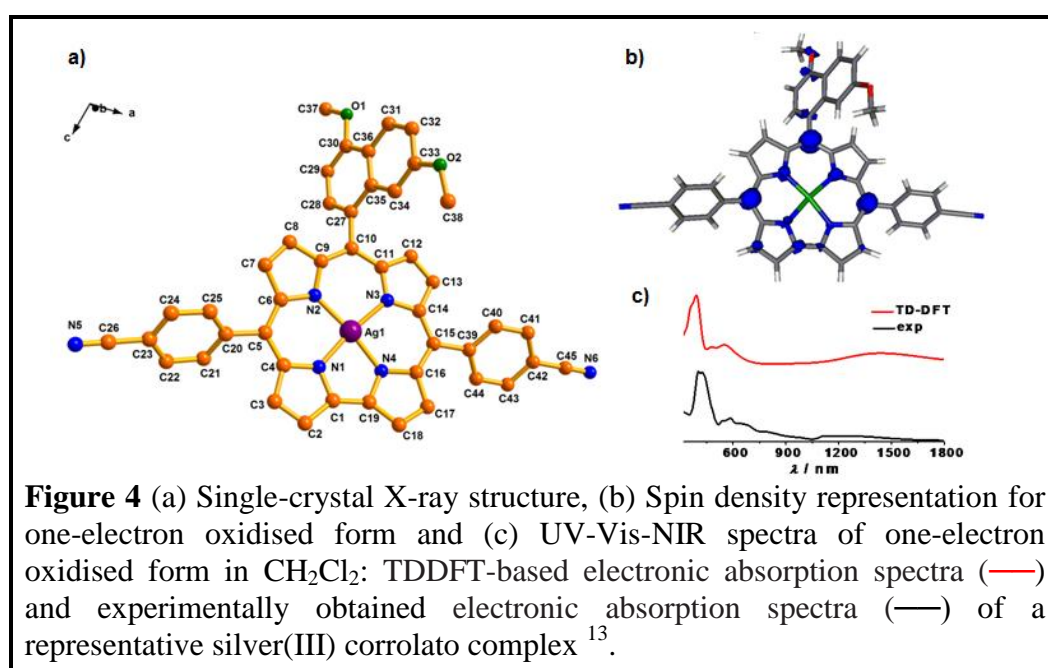


Chapter 5 Silver Corrole Complexes: Unusual Oxidation States and NIR

Absorbing Dyes

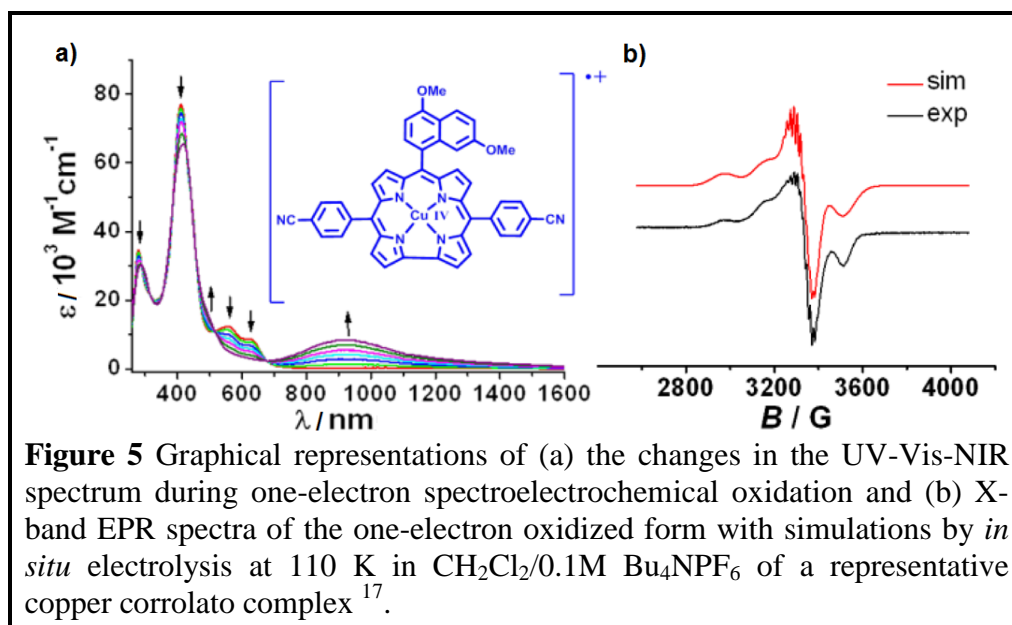
In Chapter 5, we have described the generation of four novel Ag^{III}- complexes of

corroles. A combination of several characterization tools has been adopted including structural, spectroscopic, electrochemical, UV-Vis-NIR/EPR spectroelectrochemical and DFT studies, to understand the geometric and electronic properties of these complexes in different accessible redox states (Figure 4)¹³. The results of such investigations conclusively proves that the one-electron oxidized forms of these complexes have ligand centered spins (Figure 4b), the native states are neutral, stable, diamagnetic Ag^{III} complexes and the one-electron reduced forms have unusual stabilization of the metal centre at +II oxidation state. A very rare phenomenon of broad absorptions in the near IR region has been observed in two of the oxidised complexes (Figure 4c). This spectral change is particularly interesting, since NIR transitions were never observed from mononuclear, *meso*-substituted corrole derivatives previously. On detailed theoretical study, it was identified that such NIR transitions had a mixed ILCT/intra ligand character and was strongly dependent on the substituents on the corrole frameworks. Thus in this chapter, the importance of modulation of the *meso*-substituents on the corrolato rings on perturbing their electronic structure/properties has been also explored.



Chapter 6 Experimental and Theoretical Investigations of the Existence of Cu^{II}, Cu^{III}, and Cu^{IV} in Copper Corrolato Complexes

In Chapter 6, we have highlighted the importance of higher oxidation states of some metals because of their relevance as probable intermediates in several biological and catalytic processes ¹⁴⁻¹⁶. In the quest for accessing the higher oxidation state of copper, we have synthesized and characterized three novel copper corrolato complexes. A series of studies involving electrochemistry, UV-Vis-NIR and EPR spectroelectrochemistry, XANES and DFT measurements were performed in order to invoke unambiguous +II, +III and +IV oxidation states to the three different redox states of the copper centers in these complexes (Figure 5)¹⁷. Thus in this chapter detailed discussion on the first theoretical and spectroscopic characterizations of a Cu^{IV} species has been done. XANES measurement of one of the complexes confirmed the native state of the complex with copper at +III oxidation state. EPR measurements and DFT calculations of the one-electron reduced species of the studied complexes indicated the stabilization of the usual Cu^{II} oxidation state. In two of the oxidized complexes, a rare and very significant appearance of prominent bands in the NIR region, with mixed ILCT and LMCT character, was observed (Figure 5a). For the oxidized forms of these complexes, considerable spin densities at the copper centers as observed from both experimental as well as theoretical results, led to the assignment of +IV oxidation state at the copper centers (Figure 5b). Thus our investigations in this chapter may lead to future exploration of interesting reactivity patterns of higher oxidation states of metals, especially in catalysis.



References

1. Battersby, A. R.; Fookes, C.; Matcham, G.; McDonald, E., *Nature* **1980**, 285, 17-21.
2. Kadish, K. M.; Smith, K. M.; Guilard, R.; Editors, *The Porphyrin Handbook; Volume 2, Heteroporphyrins, Expanded Porphyrins and Related Macrocycles*. Academic Press: 2000.
3. Aviv-Harel, I.; Gross, Z., *Chem. Eur. J.* **2009**, 15, 8382-8394.
4. Johnson, A.; Price, R., *J. Chem. Soc.* **1960**, 1649-1653.
5. Sessler, J. L.; Weghorn, S. J., *Expanded, contracted & isomeric porphyrins*. Elsevier: 1997; Vol. 15.
6. Gross, Z.; Galili, N.; Simkhovich, L.; Saltsman, I.; Botoshansky, M.; Bläser, D.; Boese, R.; Goldberg, I., *Org. Lett.* **1999**, 1, 599-602.
7. Paolesse, R.; Mini, S.; Sagone, F.; Boschi, T.; Jaquinod, L.; J. Nurco, D.; M. Smith, K., *Chem. Commun.* **1999**, 1307-1308.
8. Sinha, W.; Deibel, N.; Agarwala, H.; Garai, A.; Schweinfurth, D.; Purohit, C. S.; Lahiri, G. K.; Sarkar, B.; Kar, S., *Inorg. Chem.* **2014**, 53, 1417-1429.

-
9. Autret, M.; Will, S.; Caemelbecke, E. V.; Lex, J.; Gisselbrecht, J.-P.; Gross, M.; Vogel, E.; Kadish, K. M., *J. Am. Chem. Soc.* **1994**, *116*, 9141-9149.
 10. Singh, P.; Saltsman, I.; Mahammed, A.; Goldberg, I.; Tumanskii, B.; Gross, Z., *J. Porphyrins Phthalocyanines* **2012**, *16*, 663-673.
 11. Sinha, W.; Kumar, M.; Garai, A.; Purohit, C. S.; Som, T.; Kar, S., *Dalton Trans.* **2014**, *43*, 12564-12573.
 12. Sinha, W.; Kar, S., *Organometallics* **2014**, *33*, 6550-6556.
 13. Sinha, W.; Sommer, M. G.; Deibel, N.; Ehret, F.; Sarkar, B.; Kar, S., *Chem. Eur. J.* **2014**, *20*, 15920-15932.
 14. Sheldon, R., *Metal-catalyzed oxidations of organic compounds: mechanistic principles and synthetic methodology including biochemical processes.* Elsevier: 2012.
 15. Wang, G.; Zhou, M.; Goettel, J. T.; Schrobilgen, G. J.; Su, J.; Li, J.; Schlöder, T.; Riedel, S., *Nature* **2014**, *514*, 475-477.
 16. Aboeella, N. W.; Kryatov, S. V.; Gherman, B. F.; Brennessel, W. W.; Young, V. G.; Sarangi, R.; Rybak-Akimova, E. V.; Hodgson, K. O.; Hedman, B.; Solomon, E. I., *J. Am. Chem. Soc.* **2004**, *126*, 16896-16911.
 17. Sinha, W., Sommer, M. G., Deibel, N., Ehret, F., Bauer, M., Sarkar, B., Kar, S., *Angew. Chem., Int. Ed.* **2015**, *54* (46), 13769-13774.

List of Tables

1	Table 1.1	A List of the First Reports on Contracted Porphyrins	10
2	Table 2.1	Crystallographic Data for 1B and 2B	51
3	Table 2.2	Comparison of Structural Parameters and NO Stretching Frequencies of (cor)(FeNO) ⁶ Species having Electronic Configuration of (FeNO) ⁶ Already Available in the Literature with 1B and 2B	60
4	Table 2.3	Electrochemical Data ^a	60
5	Table 2.4	UV-Vis Data of 1Bⁿ , 2Bⁿ and 3Bⁿ [$n = -1, +1, 0$] from Spectroelectrochemistry ^a	64
6	Table 2.5	IR Data of 1Bⁿ , 2Bⁿ and 3Bⁿ [$n = -1, +1, 0$] from Spectroelectrochemistry ^a	67
7	Table 2.6	EPR Data ^a of Paramagnetic States ^b	67
8	Table 2.7	DFT Calculated (UB3LYP/6-31G [*] /SDD) Mulliken Spin Densities for 2Bⁿ ($n = 1+, 1-$)	71
9	Table 2.8	IR Spectral Data (Experimental from Spectroelectrochemistry ^a and DFT ^b) for 2Bⁿ ($n = 1+, 0, 1-$)	71
10	Table 2.9	TD-DFT (B3LYP/6-31G [*] /SDD/CPCM/CH ₂ Cl ₂) Calculated Electronic Transitions for 2Bⁿ ($n = 1+, 0, 1-$)	72
11	Table 3.1	Crystallographic Data for 1B , 2B and 3B	94
12	Table 4.1	Optimization of the Destannation Reaction (1B to 1A)	119
13	Table 4.2	Formation of σ -Bonded Tin(IV)-Corrole Complexes	119
14	Table 4.3	Scope of the Destannation Reaction	120
15	Table 4.4	Crystallographic Data for 1C and 2D	131
16	Table 5.1	Crystallographic Data for 4B	156
17	Table 5.2	UV-Vis and Electrochemical Data	159
18	Table 5.3	EPR Data ^[a] of Paramagnetic States ^[b]	162
19	Table 5.4	DFT (B3LYP/TZVPP-ZORA) Calculated Löwdin Spin Densities on Ag	162
20	Table 5.5	UV-Vis-NIR Data of 1Bⁿ , 2Bⁿ , 3Bⁿ , and 4Bⁿ , [$n = -1, +1, +2, 0$] from Spectroelectrochemistry ^[a]	168

21	Table 6.1	Crystallographic Data for 3	188
22	Table 6.2	UV–Vis and Electrochemical Data	193
23	Table 6.3	EPR Data ^[a] of Paramagnetic States ^[b]	196
24	Table 6.4	DFT (B3LYP/TZVPP-ZORA) Calculated Löwdin Spin Densities on Cu	197
25	Table 6.5	UV-Vis-NIR Data of 1ⁿ , 2ⁿ and 3ⁿ [$n = -1, +1, 0$] from Spectroelectrochemistry ^[a]	201

List of Schemes

1	Scheme 1.1	Porphyrin ring-modifications	7
2	Scheme 1.2	Cyclization of a,c-biladienes to 10-substituted corroles	14
3	Scheme 1.3	Synthesis of corrole by sulphur-extrusion	15
4	Scheme 1.4	Synthesis of corroles from bipyrrolic units by “2+2” condensation	15
5	Scheme 1.5	First direct synthesis of <i>meso</i> -substituted corrole 33	17
6	Scheme 1.6	Efficient synthesis of a representative A ₃ -corrole 34 starting from pyrrole and aldehyde	18
7	Scheme 1.7	Efficient synthesis of a representative A ₂ B-corrole 36 starting from dipyrromethane 35 and aldehyde	18
8	Scheme 1.8	Commonly observed coordination modes in metallocorroles	20
9	Scheme 1.9	Catalytic cycles proposed for the decomposition of peroxynitrite and activation of molecular oxygen by 41 and 43 respectively. The corrole frameworks have been replaced by cartoon representation	26
10	Scheme 2.1	Structures of the A ₃ -corrole 1A , and <i>trans</i> -A ₂ B-corroles 2A , and 3A and the corresponding (A ₃ -cor)Fe ^{III} NO, 1B , and (<i>trans</i> -A ₂ B-cor)Fe ^{III} NO, 2B and 3B	40
11	Scheme 2.2	Representative synthesis of 2B	41
12	Scheme 2.3	Structural parameters of 1B and 2B	54
13	Scheme 3.1	Structures of the A ₃ -corrole 2A , and <i>trans</i> -A ₂ B-corroles 1A and 3A and the corresponding corrolato-tin(IV)- chlorides, 10-(2,4,5-trimethoxyphenyl)-5,15-bis(4- cyanophenyl)corrolato-tin(IV)-chloride, 1B , 5,10,15- tris(4-cyanophenyl)corrolato-tin(IV)-chloride, 2B and 10-(4-bromophenyl)-5,15-bis(4-cyanophenyl)corrolato- tin(IV)-chloride, 3B	86
14	Scheme 3.2	Synthesis of 3B	88
15	Scheme 4.1	Comparative reactivities of tin(IV) corroles with aryl- and alkyl-magnesium bromides/chlorides	116
16	Scheme 4.2	Structures of the FB corroles 1A , 2A , 3A , and 4A and the	117

	corresponding corrolato-tin(IV)-chlorides 1B , 2B , 3B , and 4B . The corresponding σ -phenyl complexes 1C , and 2C and σ -methyl complexes 1D , 2D , and 4D	
17	Scheme 4.3 Proposed mechanism	122
18	Scheme 5.1 Structures of the A ₃ -corrole 1A , and <i>trans</i> -A ₂ B-corroles 2A , 3A and 4A and the corresponding silver(III) complexes 1B , 2B , 3B and 4B	147
19	Scheme 5.2 Synthesis of 4B	148
20	Scheme 6.1 Structures of three novel corrolato-copper(III) complexes 1 , 2 and 3	183

List of Figures

1	Figure 1.1	Structures of biologically significant tetrapyrrolic macrocycles.	4
2	Figure 1.2	Parent structure of porphyrin, porphine, 4 .	5
3	Figure 1.4	Representative contracted porphyrins.	9
4	Figure 1.5	Comparison between structures of porphyrin 1 , corrole 10 and corrin 21 .	11
5	Figure 1.7	Periodic table depicting the elements chelated inside the corrole cavity.	22
6	Figure 1.8	Structures of metallocorroles which behave as oxidation catalysts.	23
7	Figure 1.9	Structures of metallocorroles tested as reduction catalysts.	25
8	Figure 1.10	Structures of metallocorrole catalysts used for cyclopropanation reaction.	26
9	Figure 1.11	Structures of cobalt(III) corroles tested as sensors for CO.	27
10	Figure 1.12	Representative metal complexes as sensitizers in dye-sensitized solar cells.	28
11	Figure 1.13	Effect of metallocorroles on mice with atherosclerosis: (a) types of metallocorroles tested, (b) distribution of sizes of atherosclerotic lesions upon injection, (c) aortic cross-section of a control mouse and (d) aortic cross-section of a mouse treated with 40 . Formation of plaques has been depicted in black colour in (c) and (d).	30
12	Figure 1.14	Distribution of fluorescence in the mice injected with a combination of a gallium(III) corrole 52 and a carrier protein (HerGa) by using fluorescence-based imaging.	31
13	Figure 2.1	ESI-MS spectrum of 10-(4-bromophenyl)-5,15-bis(4-cyanophenyl)corrole, 2A shows the isotopic distribution pattern.	42
14	Figure 2.2	ESI-MS spectra of (a) 10-(2,4,5-trimethoxyphenyl)-5,15-bis(4-cyanophenyl)corrole, 3A , (b) [10-(4-bromophenyl)-5,15-bis(4-cyanophenyl)cor]Fe ^{III} NO, 2B and (c) [10-	43

	(2,4,5-trimethoxyphenyl)-5,15-bis(4-cyanophenyl)cor]Fe ^{III} NO, 3B show the isotopic distribution patterns.	
15	Figure 2.3 FTIR spectra of 1B , 2B and 3B as KBr pellets.	44
16	Figure 2.4 ¹ H NMR spectrum of 2A in CDCl ₃ .	45
17	Figure 2.5 ¹ H NMR spectrum of 3A in CDCl ₃ .	46
18	Figure 2.6 ¹³ C NMR spectrum of 3A in CDCl ₃ .	46
19	Figure 2.7 ¹ H NMR spectrum of 1B in CDCl ₃ .	47
20	Figure 2.8 ¹³ C NMR spectrum of 1B in CDCl ₃ .	47
21	Figure 2.9 ¹ H NMR spectrum of 2B in CDCl ₃ .	49
22	Figure 2.10 ¹³ C NMR spectrum of 2B in CDCl ₃ .	49
23	Figure 2.11 ¹ H NMR spectrum of 3B in DMSO- <i>d</i> ₆ .	50
24	Figure 2.12 ¹³ C NMR spectrum of 3B in DMSO- <i>d</i> ₆ .	50
25	Figure 2.13 Single-crystal X-ray structure of 1B .	53
26	Figure 2.14 Single-crystal X-ray structure of 2B .	53
27	Figure 2.15 X-ray single crystal structure analysis of (5,10,15-Tris(4-bromophenyl)cor) Fe ^{III} NO, 1B , (a) C—H···N interactions, [2.840 Å], (b) C—H···π interactions, [3.258 Å] and (c) C—H···C interactions, [2.849 Å]; C—H···O interactions, [2.716 Å]. The entries in square brackets are the distances.	55
28	Figure 2.16 X-ray single crystal structure analysis of 2B , (a) C—H···N interactions, [2.854 Å], (b) C—H···O interactions, [2.693 Å] and (c) C—H···π interactions, [2.874 Å], The entries in square brackets are the distances.	56
29	Figure 2.17 X-ray single crystal structure analysis of 2B , (a) C—H···C interactions, [2.790 Å] and (b) π-π stacking interactions [3.661 Å]. The entries in square brackets are the distances.	57
30	Figure 2.18 Packing diagrams of [5,10,15-tris(4-bromophenyl)cor] Fe ^{III} NO, 1B , viewed down the <i>c</i> -axis.	58
31	Figure 2.19 Packing diagrams of [10-(4-bromophenyl)-5,15-bis(4-cyanophenyl)cor]Fe ^{III} NO, 2B , viewed down the <i>b</i> -axis with π-π stacking interactions of 3.96 Å.	58
32	Figure 2.20 (a) Cyclic voltammograms of 1B (—) in CH ₂ Cl ₂ (b)	61

		cyclic voltammograms(—) and differential pulse voltammograms (-----) of 2B in CH ₂ Cl ₂ and (c) cyclic voltammograms of 3B (—) in CH ₂ Cl ₂ . The potentials are <i>versus</i> ferrocene/ferrocenium.	
33	Figure 2.21	Changes in the UV-Vis spectrum of 3B (a) during first oxidation and (b) during first reduction. Results from OTTLE spectroelectrochemistry in CH ₂ Cl ₂ /0.1 M Bu ₄ NPF ₆ .	65
34	Figure 2.22	Changes in the IR spectrum of 3B (a) during first oxidation and (b) during first reduction. Results from OTTLE spectroelectrochemistry in CH ₂ Cl ₂ /0.1 M Bu ₄ NPF ₆ .	66
35	Figure 2.23	X-band EPR spectra of (a) (3B) ^{•+} and (b) (3B) ^{•-} with simulation generated by <i>in-situ</i> electrolysis at 295 K in CH ₂ Cl ₂ /0.1 M Bu ₄ NPF ₆ .	69
36	Figure 2.24	Spin density (UB3LYP/6-31G [*] /SDD) representations for (a) 2B ⁺ and (b) 2B ⁻ .	71
37	Figure 3.1	ESI-MS spectra of (a) 10-(2,4,5-Trimethoxyphenyl)-5,15-bis(4-cyanophenyl)corrolato-tin(IV)-chloride, 1B (b) 5,10,15-tris(4-cyanophenyl)corrolato-tin(IV)-chloride, 2B and (c) 10-(4-bromophenyl)-5,15-bis(4-cyanophenyl)corrolato-tin(IV)-chloride, 3B in CH ₃ CN show the isotopic distribution patterns.	89
38	Figure 3.2	Electronic absorption spectra of 1B , (green line), 2B , (blue line) and 3B , (red line) in dichloromethane.	90
39	Figure 3.3	Electronic emission spectra of 1B , (green line), 2B , (red line) and 3B , (blue line) in dichloromethane ($\lambda_{\text{ex}} = 423 \text{ nm}$).	90
40	Figure 3.4	¹ H NMR spectrum of 1B in CDCl ₃ .	91
41	Figure 3.5	¹ H NMR spectrum of 2B in CDCl ₃ .	91
42	Figure 3.6	¹ H NMR spectrum of 3B in CDCl ₃ .	92
43	Figure 3.7	¹³ C NMR spectrum of 3B in CDCl ₃ .	92
44	Figure 3.8	Single-crystal X-ray structure of 1B , (a) top view (b) side view. Hydrogen atoms are omitted for clarity.	95
45	Figure 3.9	Single-crystal X-ray structure of 2B , (a) top view (b) side	96

	view, and (c) π - π stacking interactions. Hydrogen atoms are omitted for clarity.	
46	Figure 3.10 Single-crystal X-ray structure of 3B , (a) top view (b) side view. Hydrogen atoms are omitted for clarity.	97
47	Figure 3.11 Vertical displacement of the peripheral carbon atoms from the N4 corrole planes in (a) 1B (b) 2B and (c) 3B .	98
48	Figure 3.12 Single-crystal X-ray structure analysis of 1B ; C2–H2 \cdots C11 hydrogen bonding interaction [Bonding parameters of C–H \cdots Cl (D^i –H i \cdots A): C2–H2 \cdots C11; H \cdots A: 2.848 Å; D \cdots A: 3.405 Å; \angle D–H \cdots A: 119.72°, symmetry codes: (i) 1– x, – 0.5+y, 0.5–z].	99
49	Figure 3.13 (a) Single-crystal X-ray structure analysis of 2B ; C18–H18 \cdots C11 (D^i –H i \cdots A): hydrogen bonding interaction [Bonding parameters of C18–H18 \cdots C11; H18 \cdots C11: 3.051 Å; C18 \cdots C11: 3.849 Å; \angle C18–H18 \cdots C11: 144.70°, symmetry codes: (i) 1– x, 1– y, 1– z]; (b) Space filling representation of the rectangular channels (dimension = 16 \times 7 Å) in the crystal structure of 2B .	100
50	Figure 3.14 Single-crystal X-ray structure analysis of 3B ; C12–H12 \cdots C11 (D –H \cdots A i) hydrogen bonding interaction [Bonding parameters of C12–H12 \cdots C11; H12 \cdots C11: 2.915 Å; C12 \cdots C11: 3.730 Å; \angle C12–H12 \cdots C11: 147.08°, symmetry codes: (i) –1+ x, y, z], and C7–H7 \cdots N6 (D^i –H i \cdots A) hydrogen bonding interactions [Bonding parameters of C7–H7 \cdots N6; H7 \cdots N6: 2.595 Å; C7 \cdots N6: 3.285 Å; \angle C7–H7 \cdots N6: 131.32°, symmetry codes: (i) 2– x, 1– y, – z].	101
51	Figure 3.15 SEM images of the 1B nanospheres in DCM-Hexane mixture.	103
52	Figure 3.16 Particle size distribution histograms of 1B nanospheres.	103
53	Figure 3.17 SEM images of 3B nanospheres in DCM-Hexane mixture.	103
54	Figure 3.18 Particle size distribution histograms of 3B nanospheres.	104
55	Figure 3.19 EDX element map obtained from the surface of the nanospheres of 1B showing the presence of the entire	104

		constituent elements: C, N, O, Sn and Cl.	
56	Figure 3.20	EDX elemental analysis obtained from the nanospheres of 3B showing the presence of the entire constituent elements: C, N, Cl, Br, and Sn.	105
57	Figure 3.21	(a) Schematic representation of the device (Ag/ITO/ 1B -nanospheres/ITO/Ag), (b) <i>I-V</i> characteristics of the device, (c) AFM image showing the 1B -nanospheres and (d) current mapping of 1B -nanospheres by conductive atomic force microscopy.	106
58	Figure 4.1	ESI-MS spectra of (a) 5,10,15-tris(2,4,5-trimethoxyphenyl)corrole, 4A (b) 5,10,15-tris(2,4,5-trimethoxyphenyl)corrolato-tin(IV)-chloride, 4B and (c) (phenyl){10-(2,4,5-trimethoxyphenyl)-5,15-bis(4-cyanophenyl)corrolato}tin(IV), 1C in CH ₃ OH show the isotopic distribution patterns.	124
59	Figure 4.2	ESI-MS spectra of (a) (Methyl){10-(2,4,5-trimethoxyphenyl)-5,15-bis(4-cyanophenyl)corrolato}tin(IV), 1D (b) (Methyl){5,10,15-tris(4-cyanophenyl)corrolato}tin(IV), 2D and (c) (Methyl){5,10,15-tris(2,4,5-trimethoxyphenyl)corrolato}tin(IV), 4D in CH ₃ OH show the isotopic distribution patterns.	125
60	Figure 4.3	¹ H NMR spectrum of 4A in CDCl ₃ .	126
61	Figure 4.4	¹ H NMR spectrum of 1C in CDCl ₃ .	126
62	Figure 4.5	¹ H NMR spectrum of 2C in CDCl ₃ .	127
63	Figure 4.6	¹ H NMR spectrum of 1D in CDCl ₃ .	127
64	Figure 4.7	¹ H NMR spectrum of 2D in CDCl ₃ .	128
65	Figure 4.8	¹ H NMR spectrum of 4D in CDCl ₃ .	128
66	Figure 4.9	¹ H NMR spectrum of 4B in CDCl ₃ .	129
67	Figure 4.10	Single-crystal X-ray structure of 1C .	130
68	Figure 4.11	Single-crystal X-ray structure of 2D .	132
69	Figure 4.12	Crystal-packing diagram of 1C along crystallographic <i>a</i> -axis.	132
70	Figure 4.13	Crystal-packing diagram of 2D along crystallographic <i>b</i> -axis.	133

71	Figure 5.1	ESI-MS spectra of (a) 5,10,15-tris(4-cyanophenyl)corrolato-silver(III), 1B , (b) 10-(4-bromophenyl)-5,15-bis(4-cyanophenyl)corrolato-silver(III), 2B , (c) 10-(2,4,5-trimethoxyphenyl)-5,15-bis(4-cyanophenyl)corrolato-silver(III), 3B and (d) 10-(4,7-dimethoxynaphthalen-1-yl)-5,15-bis(4-cyanophenyl)corrolato-silver(III), 4B in CH ₃ CN show the isotopic distribution patterns.	150
72	Figure 5.2	¹ H NMR spectrum of 1B in CDCl ₃ .	151
73	Figure 5.3	¹ H NMR spectrum of 2B in CDCl ₃ .	151
74	Figure 5.4	¹ H NMR spectrum of 3B in CDCl ₃ .	152
75	Figure 5.5	¹ H NMR spectrum of 4B in CDCl ₃ .	153
76	Figure 5.6	¹³ C NMR spectrum of 4B in CDCl ₃ .	153
77	Figure 5.7	Single-crystal X-ray structure of 4B .	155
78	Figure 5.8	Pine-tree like arrangement observed in the crystal structure of 4B when observed along the <i>a</i> -axis.	155
79	Figure 5.9	Orientation of silver atoms in single-crystal X-ray structure of 4B viewed along the <i>a</i> -axis.	157
80	Figure 5.10	Cyclic voltammograms (—) and differential pulse voltammograms (-----) of (a) 1B , (b) 2B , (c) 3B and (d) 4B in CH ₂ Cl ₂ . The potentials are <i>versus</i> ferrocene/ferrocenium.	158
81	Figure 5.11	X-band EPR spectra of (a) (1B) ^{•-} with simulation and (b) (1B) ^{•+} generated by <i>in situ</i> electrolysis at 295 K in CH ₂ Cl ₂ /0.1 M Bu ₄ NPF ₆ .	161
82	Figure 5.12	Spin density representations for (a) 4B ⁺ , (b) 4B ^{•-} , (c) 2B ⁺ and (d) 2B ^{•-} . (iso-value 0.005)	164
83	Figure 5.13	Electronic absorption spectra of 1B , (black line), 2B , (red line), 3B , (green line) and 4B , (blue line) in CH ₂ Cl ₂ .	165
84	Figure 5.14	UV-Vis-NIR spectra of (a) 2B , 2B ⁺ , and 2B ^{•-} and (b) 4B , 4B ⁺ , and 4B ^{•-} in CH ₂ Cl ₂ : TDDFT-based electronic absorption spectra (—) and experimentally obtained electronic absorption spectra (—).	167

85	Figure 5.15	Changes in the UV-Vis spectra of (a) 1B , (b) 2B , (c) 3B and (d) 4B during first reduction. Result from OTTLE spectroelectrochemistry in CH ₂ Cl ₂ /0.1 M Bu ₄ NPF ₆ .	169
86	Figure 5.16	Changes in the UV-Vis-NIR spectra of (a) 1B , (b) 2B , (c) 3B and (d) 4B during first oxidation. Result from OTTLE spectroelectrochemistry in CH ₂ Cl ₂ /0.1 M Bu ₄ NPF ₆ .	170
87	Figure 5.17	Changes in the UV-Vis-NIR spectra of (a) 1B , (b) 2B , (c) 3B and (d) 4B during second oxidation. Result from OTTLE spectroelectrochemistry in CH ₂ Cl ₂ /0.1 M Bu ₄ NPF ₆ .	171
88	Figure 6.1	ESI-MS spectra of (a) 5,10,15-tris(4-cyanophenyl)corrolato-copper(III), 1 , (b) 10-(2,4,5-trimethoxyphenyl)-5,15-bis(4-cyanophenyl)corrolato-copper(III), 2 , and (c) 10-(4,7-dimethoxynaphthalen-1-yl)-5,15-bis(4-cyanophenyl)corrolato-copper (III), 3 show the isotopic distribution patterns.	184
89	Figure 6.2	¹ H NMR spectrum of 1 in CD ₂ Cl ₂ .	185
90	Figure 6.3	¹ H NMR spectrum of 2 in CDCl ₃ .	186
91	Figure 6.4	¹ H NMR spectrum of 3 in CDCl ₃ .	186
92	Figure 6.5	(a) Single-crystal X-ray structure of 3 . Hydrogen atoms are omitted for clarity. (b) Side-view of the crystal structure of 3 , representing the saddling (all the hydrogen atoms and the <i>meso</i> -substituents have been removed for clarity).	187
93	Figure 6.6	Crystal-packing diagram of 3 along crystallographic <i>b</i> -axis.	189
94	Figure 6.7	Zig-zag arrangement of the corrolato-copper(III) molecules of 3 with representative portray of interactions. (Selected distances C-H...N 2.852 Å & C-H...π 2.702 Å; Cu...Cu distance 4.994 Å)	190
95	Figure 6.8	Cu K-edge XANES spectrum of complex 2 . The pre-edge area is shown enlarged in the inset.	191
96	Figure 6.9	Cyclic voltammograms (—) and differential pulse voltammograms (-·-·-·-) of (a) 1 , (b) 2 and (c) 3 in CH ₂ Cl ₂ . The potentials are <i>versus</i> ferrocene/ferrocenium.	192

97	Figure 6.10	X-band EPR spectra of (a) (1)^{•+} , (b) (2)^{•+} , (c) (3)^{•+} , (d) (1)^{•-} , (e) (2)^{•-} and (f) (3)^{•-} with simulations by in-situ electrolysis at 110 K in CH ₂ Cl ₂ /0.1 M Bu ₄ NPF ₆ .	194
98	Figure 6.11	Spin density representations for (a) (1)^{•+} , (b) (1)^{•-} , (c) (3)^{•+} and (d) (3)^{•-} (iso-value 0.005). Blue color shows positive, red color negative sign.	197
99	Figure 6.12	Electronic absorption spectra of 1 (red line), 2 (green line) and 3 (blue line) in CH ₂ Cl ₂ .	199
100	Figure 6.13	Changes in the UV-Vis-NIR spectra of (a) 1 , (b) 2 and (c) 3 during first oxidation and (d) 1 , (e) 2 and (f) 3 during first reduction. Results from OTTLE spectroelectrochemistry in CH ₂ Cl ₂ /0.1 M Bu ₄ NPF ₆ .	200
101	Figure 6.14	Formal oxidation state distributions for the various redox states in corrolato-copper complexes (left), and their silver analogues (right) discussed in Chapter 5. Species with majority contribution have been shown in red.	203

Glossary of Acronyms

^1H NMR	Proton Nuclear Magnetic Resonance
DDQ	2,3-Dichloro-5,6-dicyano-1,4-benzoquinone
CH_2Cl_2	Dichloromethane
CHCl_3	Chloroform
^{13}C NMR	Carbon-13 Nuclear Magnetic Resonance
FTIR	Fourier Transform Infrared
EPR	Electron Paramagnetic Resonance
UV-Vis	Ultraviolet–Visible
NO	Nitric oxide
tpfc	5,10,15-tris(pentafluorophenyl)corrole
CO	Carbon monoxide
NIR	Near-Infrared
XANES	X-Ray Absorption Near Edge Structure
DFT	Density Functional Theory
cor	corrole
TD-DFT	Time-Dependent Density Functional Theory
HCl	Hydrogen chloride
TFA	Trifluoroacetic acid
NaNO_2	Sodium nitrite
KBr	Potassium bromide
CDCl_3	Deuterated chloroform
$\text{DMSO-}d_6$	Hexadeuterodimethyl sulfoxide
GOF	Goodness of Fit
CCDC	Cambridge Crystallographic Data Centre
TBAP	Tetrabutylammonium perchlorate
Bu_4NPF_6	Tetrabutylammonium hexafluorophosphate
OTTLE	Optically Transparent Thin Layer
HOMO	Highest Occupied Molecular Orbital
SOMO	Singly Occupied Molecular Orbital
LUMO	Lowest Unoccupied Molecular Orbital
expt.	Experimental

Anal. Calcd	Analytically Calculated
CH ₃ CN	Acetonitrile
SEM	Scanning Electron Microscopy
EDX	Energy Dispersive X-Ray Spectroscopy
ITO	Indium tin oxide
CAFM	Conductive Atomic Force Microscopy
FB	Free-Base
TLC	Thin Layer Chromatography
ESI	Electrospray Ionization
CH ₃ OH	Methanol
KOH	Potassium hydroxide
CaH ₂	Calcium hydride
HPLC	High-Performance Liquid Chromatography
ILCT	Intra-Ligand Charge Transfer
MLCT	Metal to Ligand Charge Transfer
LMCT	Ligand to Metal Charge Transfer
Na ₂ SO ₄	Sodium sulphate
CD ₂ Cl ₂	Dideuteromethylenechloride
XAS	X-Ray Absorption Spectroscopy
Cu(OAc) ₂ .H ₂ O	Copper acetate monohydrate
Ag(OAc)	Silver acetate
FeCl ₂ .4H ₂ O	Iron(II) chloride tetrahydrate

CHAPTER 1

Evolution of Corroles

1.1	Introduction	3
1.2	Nomenclature of Porphyrinoids	5
1.3	Structural Modifications of Porphyrins	6
1.3.1	Contracted Porphyrins	8
1.3.1.1	Subphthalocyanine	8
1.3.1.2	Isocorrole	9
1.3.1.3	Subporphyrins	9
1.3.1.4	Norcorrole	9
1.3.1.5	Corroles	10
1.3.1.5.1	Characteristic Properties	12
1.3.1.5.2	Synthetic Protocols	13
1.3.1.5.3	Metallocorroles	19
(a)	Coordination Modes in Metallocorroles	19
(b)	Periodic Table of Metallocorroles	21
(c)	Spectroelectrochemical Investigations	21
1.3.1.5.4	Applications of Metallocorroles	23
(i)	Oxidation Catalysis	23
(ii)	Reduction Catalysis	24
(iii)	Group Transfer Catalysis	26
(iv)	Metallocorrole Sensors	26
(v)	Dye Sensitized Solar Cells (DSSC)	27
(vi)	Medicinal Applications	29
1.4	Scope and Objectives of the Present Thesis	31
1.4.1	Lacunae	31
1.4.2	Objectives	33

1.1 Introduction

Since the dawn of the civilization, humans have been striving to decipher and mimic the naturally occurring processes. During this long never ending quest, thousands of discoveries have enriched our knowledge of chemistry. Many such researches have revealed that Life on Earth is steered by several tetrapyrrolic macrocyclic entities, universally known as the “pigments of life” (Figure 1.1) ¹. One of the most abundant and most studied, intensely coloured pigments is porphyrins ². The name porphyrin has its origin from the twentieth century Greek word ‘porphura’ which means purple. Metallo derivatives of porphyrins and the related macrocyclic molecules (e.g. chlorin, corrin, etc.) perform many vital and indispensable functions as prosthetic groups in several biological processes. Haemoglobin (Hb) helps in oxygen transport in blood from the lungs throughout the body and the myoglobin (Mb) of muscle tissues mediates oxygen storage ³. Both Hb and Mb have the basic iron protoporphyrin XI unit **1**, known as heme, which reversibly bind to oxygen to form adducts. On photoexcitation of the chlorins **2** in the chlorophylls of green plants, photosynthesis is initiated. The cobalt-corrin complex in vitamin-B₁₂ **3** and its coenzyme aid in several isomerisations and redox reactions in biological systems. Several electron transfer processes in biology mediated by cytochromes, catalyses and peroxidases also have the heme unit in their structures and are commonly called hemoproteins.

Porphyrins are tetrapyrrolic macrocycles in which the four pyrrole rings are connected through methine linkages (Figure 1.2) ². They are considered as Hückel aromatic molecules with 18 π -electron conjugation. The parent structure of porphyrin is known as porphine **4** (Figure 1.2). The positions 5, 10, 15 and 20 are stated as *meso*-positions. The positions (2, 3), (7, 8), (12, 13) and (17, 18) are considered as β -positions according to the general convention of nomenclature for five-membered

heterocycles. The remaining methine-bridged positions (1, 4), (6, 9), (11, 14) and (16, 19) are the α -carbons. The inner core contains two types of nitrogens, two imine nitrogens and two amine nitrogens.

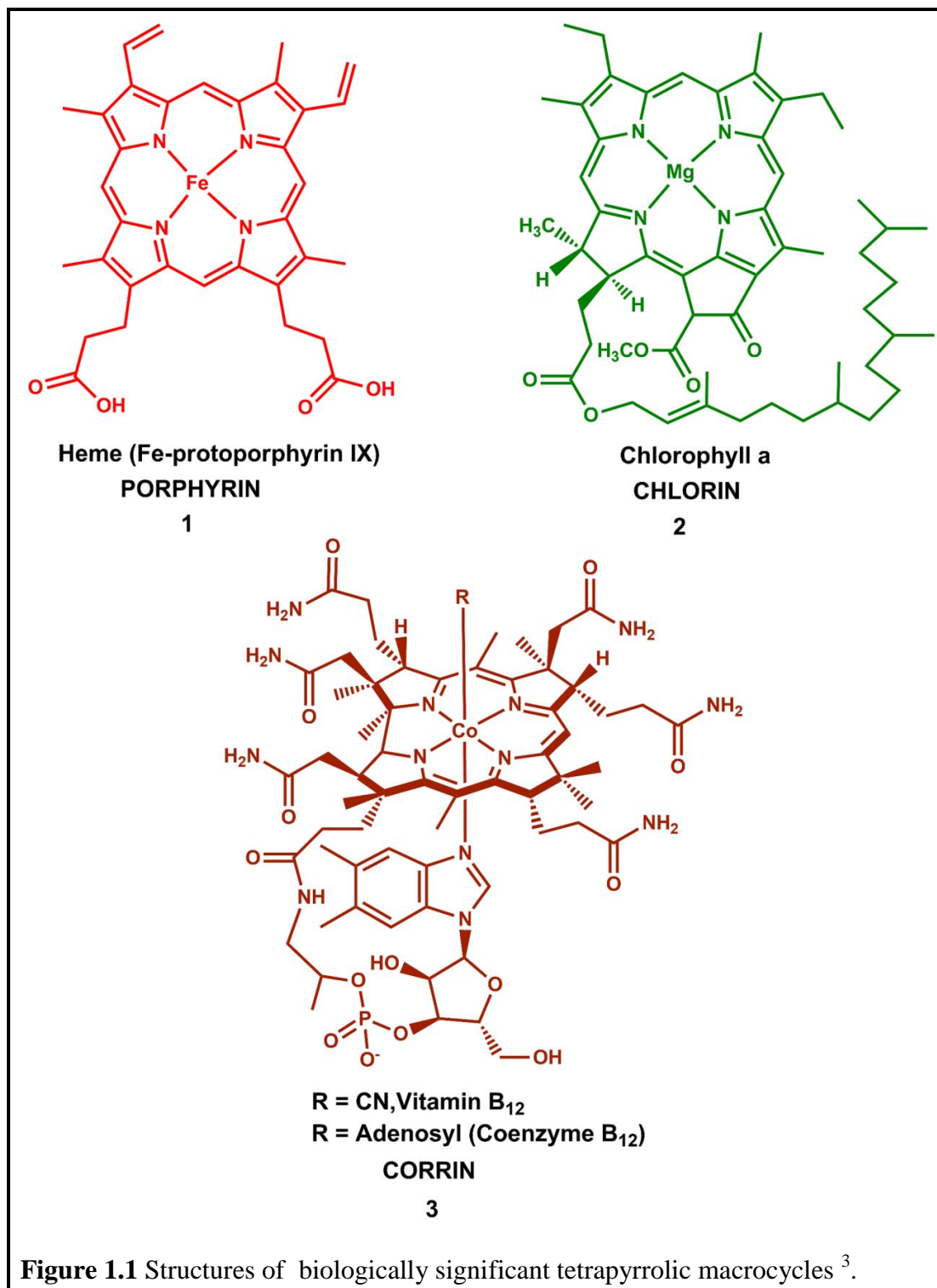
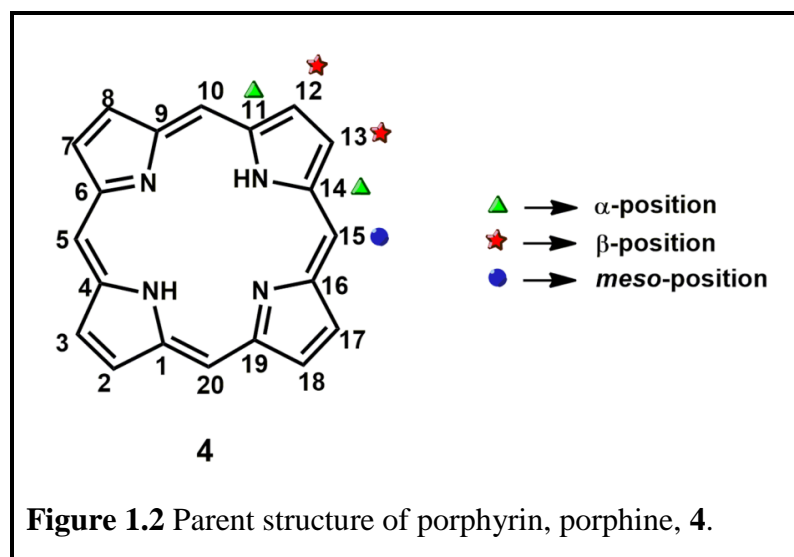


Figure 1.1 Structures of biologically significant tetrapyrrolic macrocycles ³.



Porphyrin and its derivatives are deeply coloured and show strong characteristic absorptions with high values of molar extinction coefficients ($\sim 10^5 \text{ M}^{-1}\text{cm}^{-1}$) in the visible region at around 400 nm known as Soret band alongwith weak bands known as Q-bands in the range of 450-700 nm^{4,5}.

¹H NMR studies on porphyrins indicate the aromatic nature of the ring^{6,7}. Accordingly, ¹H NMR spectrum of free-base porphyrin reveals that the inner protons of the core resonate in the shielded region of δ -2 ppm to -4 ppm. The *meso*-protons appear at very low field in the region of ~ 10 ppm. The β -pyrrolic protons also manifest in the deshielded region of δ 8 ppm to 9 ppm.

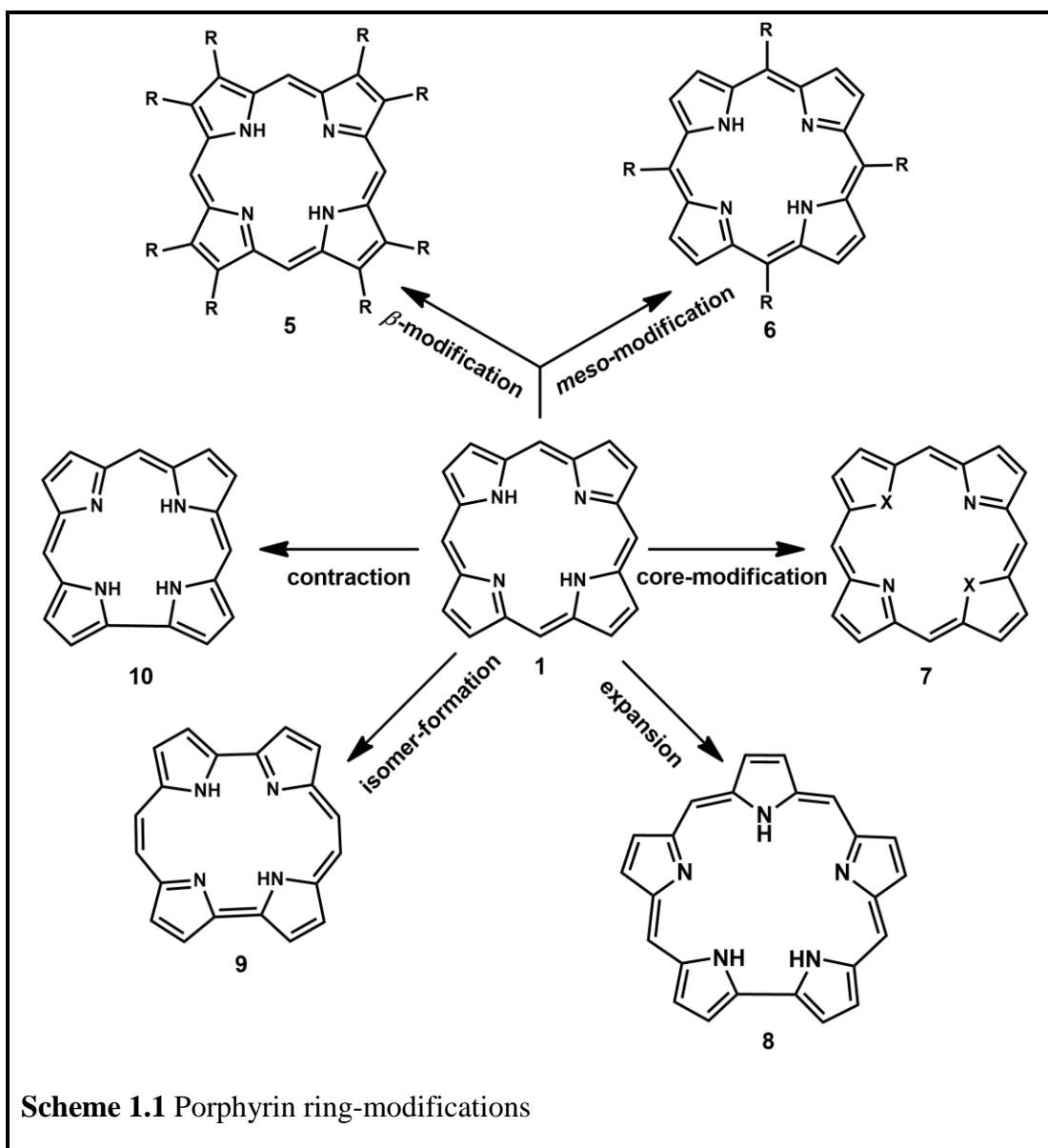
1.2 Nomenclature of Porphyrinoids

During the initial years of discovery, the porphyrinoids were given trivial names on the basis of colour, size or number of heterocyclic rings followed by the suffixes “phyrin” or “rin” from porphyrin⁸. A pentapyrrolic porphyrinoid was named sapphyrin after it got crystallized as blue coloured solid. Similarly many more were named following similar trend, e.g rubyrin (red-coloured), texaphyrin (Texas-sized), pentaphyrin (with five pyrroles), hexaphyrin (with six pyrroles), etc. The systematic

naming of the porphyrin analogues was put forward by Franck and Nonn⁹. According to this nomenclature there are three aspects that should be included while designating a porphyrinoid: a) a general name reflecting the number of pyrrole rings, b) the number of π -electrons participating in the conjugation is specified inside square-brackets and c) the number of bridging carbon atoms between the heterocyclic rings are also mentioned separated by dots within first brackets. For example sapphyrin is represented as [22]pentaphyrin-(1.1.1.1.0).

1.3 Structural Modifications of Porphyrins

Since the importance of these macrocycles came into limelight, intense research has been devoted towards the development of their synthetic derivatives in laboratories, i.e. novel porphyrinoids with several distinct types of modifications of the porphyrin core (Scheme 1.1). This has resulted in various tailoring techniques to modulate the electronic and structural properties of the basic porphyrin framework². Two of the most widely used strategies for the above-mentioned purpose have been β -substitution and *meso*-substitution. The symmetric as well as unsymmetric octaalkyl porphyrins **5**, resembling the naturally occurring protoporphyrin IX are developed through the β -substitution pathway. The *meso*-substituted porphyrins **6**, though not structurally similar to the naturally occurring ones, are used as models for the biological prosthetic groups and also for applications in materials chemistry¹⁰. Core-modification is another approach to modify the reactivity and catalytic properties of porphyrins. Core-modified porphyrins **7** have at least one nitrogen atom of the inner core replaced by another heteroatom, such as oxygen, sulphur, selenium, tellurium or carbon, retaining the aromaticity of four pentacyclic rings connected at the four *meso*-positions². Three of the most important modifications that gradually developed and spread as giant



branches are that of expanded, isomeric and contracted porphyrins. Expanded porphyrins **8** include all those macrocycles comprising of a minimum of 17 internally conjugated atoms from at least three heterocyclic units such as pyrrole, furan or thiophene². The chemistry of expanded derivatives have flourished with the aim to explore the possibility of stabilizing higher coordination numbers of metal ions, especially that of the lanthanides and actinides, to study the change in their aromatic behaviour and also to check their binding affinities towards anionic and neutral species. Isomeric porphyrins **9** are those analogues having the basic $C_{20}H_{14}N_4$

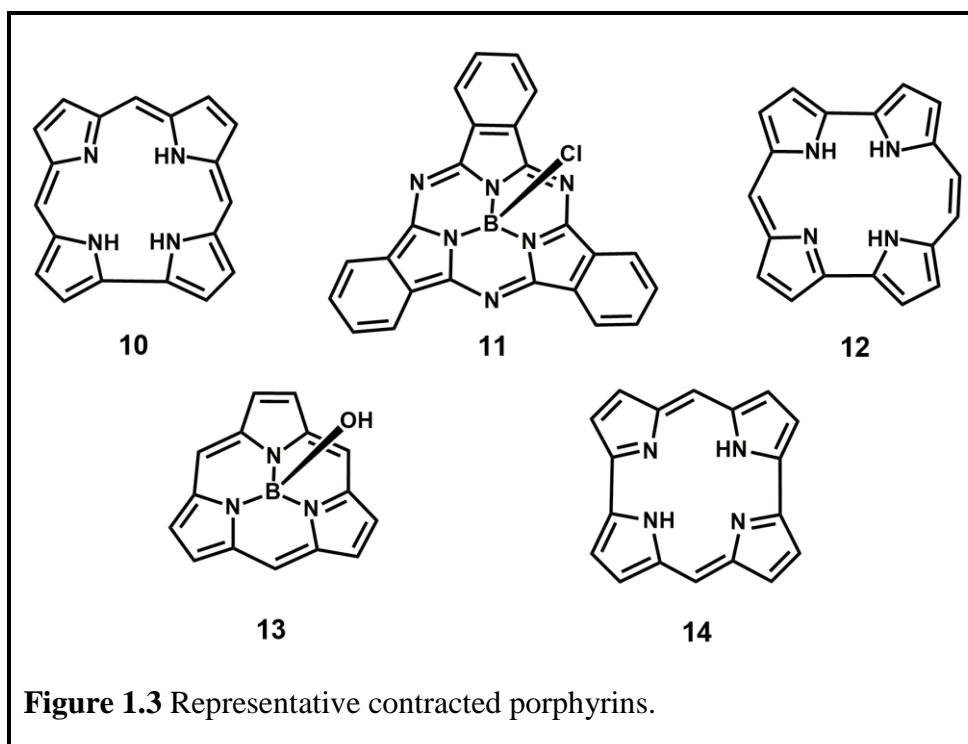
molecular formula and generated by shuffling of the positions of pyrrole rings and *meso*-carbons². Contracted porphyrins **10** count for those macrocycles in which at least three of the pyrrole or pyrrole-like subunits are in conjugation and at least are either one *meso*-carbon or one pyrrole-ring short of the parent porphyrin structure^{2,8}.

1.3.1 Contracted Porphyrins

The advent of contracted porphyrins was possible only after the structural characterization of vitamin B₁₂ revealed the existence of a naturally occurring macrocycle, corrin, without a *meso*-carbon, similar to porphyrin ring¹¹⁻¹³. Soon after the structural elucidation of the corrin ring, tremendous efforts were dedicated towards the development of efficient synthetic methodologies for the biosynthesis of Vitamin B₁₂^{1,14}. Consequently in the year 1960, Johnson and Price prepared a series of metallic derivatives of pentadehydrocorrins, containing eleven double bonds and named them as corroles **10**¹⁵. In 1965, Johnson and Kay reported the synthesis of corrole for the first time and clarified the fact that corroles are tetrahydrocorrins with ten double bonds¹⁶. Since then, several interesting contracted porphyrinoids were developed (Figure 1.3). Some of the well-explored contracted porphyrins have been discussed as follows:

1.3.1.1 Subphthalocyanine

Subphthalocyanine **11** is a contracted 14 π -electron porphyrinoid with a nonplanar cone-shaped structure (Figure 1.3). They have been synthesized only as boron derivatives, e.g. **15** (Table 1.1). The macroskeleton is formed by joining of three isoindole subunits with three aza-linkages^{17,18}.



1.3.1.2 Isocorrole

Isocorrole **12** is a stable isomer of corrole and is represented as [18]corrole-(2.0.1.0). Isocorroles (e.g. **17**) also have a structural similarity with porphycenes (e.g. **16**) (Figure 1.3, Table 1.1) ¹⁹.

1.3.1.3 Subporphyrins

Subporphyrin **13** is an example of a ring-contracted porphyrin with 14 π -electron aromatic core (Figure 1.3). It has a bowl-shaped structure arising from three pyrrolic rings connected by three *meso*-carbon with a boron atom at the centre (Table 1.1) ²⁰.

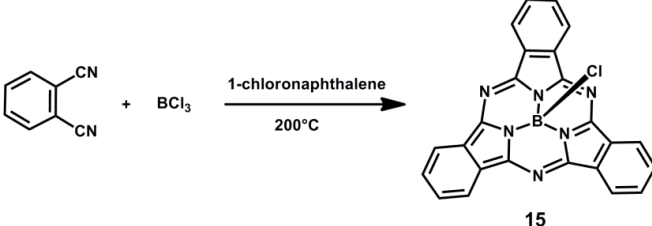
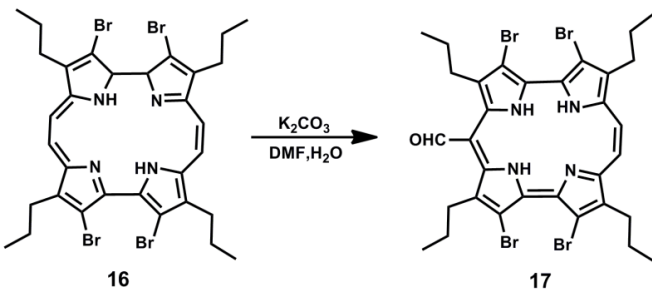
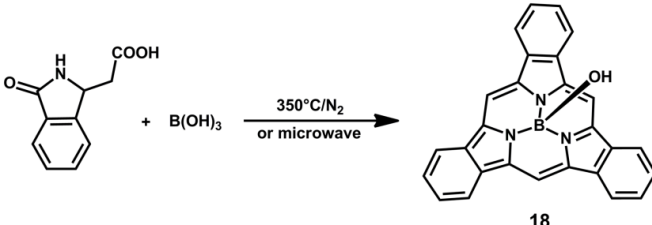
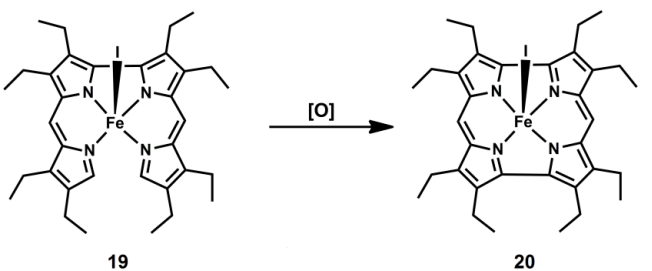
Free-base form of subporphyrin, subpyriporphyrin was reported by replacement of a pyrrole-ring by a pyridine unit ²¹.

1.3.1.4 Norcorrole

Norcorrole **14** is a contracted porphyrinoid with two *meso*-carbons short of a regular porphyrin (Figure 1.3). It is a 16 π -electron conjugated anti-aromatic system as was

confirmed by Kobayashi and Shinokuba and co-workers²². The ring system of the dimerised structure of a decomposition form of **20** obtained from a metalated 2,2'-bidipyrin **19** was found to be bowl-shaped (Table 1.1)²³.

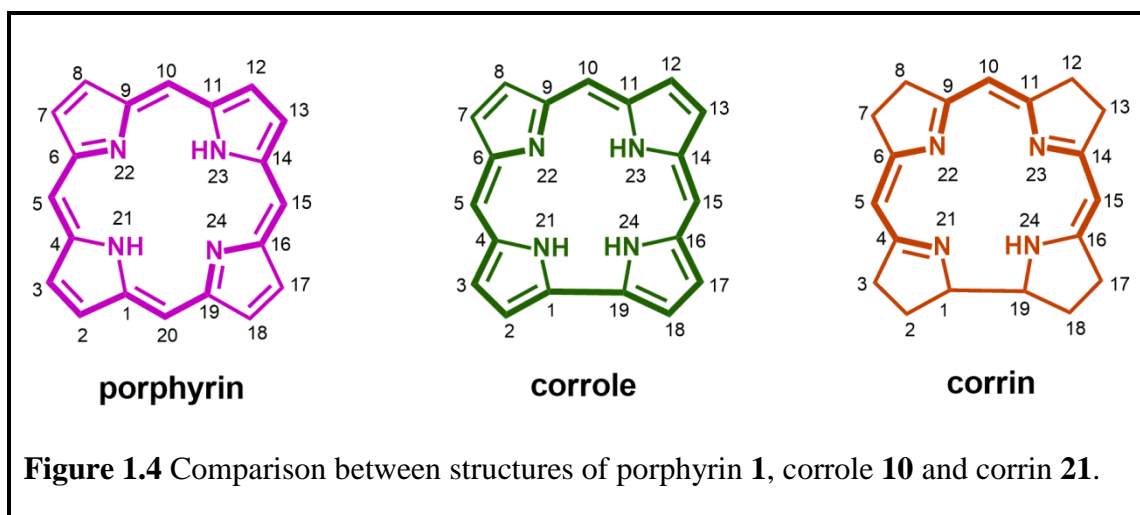
Table 1.1 A List of the First Reports on Contracted Porphyrins

Type of Contracted Porphyrin	Details of First Report	Reaction Scheme
Subphthalocyanine	A. Meller and A. Ossko in 1972 ²⁴	 <p style="text-align: center;">15</p>
Isocorrole	E. Vogel and co-workers in 1990 ²⁵	 <p style="text-align: center;">16</p> <p style="text-align: center;">17</p>
Subporphyrin	A. Osuka and co-workers in 2006 ²⁶	 <p style="text-align: center;">18</p>
Norcorrole	C. Kleeberg and co-workers in 2008 ²³	 <p style="text-align: center;">19</p> <p style="text-align: center;">20</p>

1.3.1.5 Corroles

Corroles contribute as a huge classification of contracted porphyrins. The name

corrole **10** was derived by Johnson and Price due its strong structural resemblance with the naturally relevant corrin ring of vitamin B₁₂¹⁵. Also due to resemblance in some of the properties with 18 π -electron aromatic porphyrins, corroles are also closely related to porphyrins. Thus corroles are better designated as intermediates between corrins and porphyrins (Figure 1.4)^{2, 8}.



The most distinct structural difference between porphyrin and corrole is that one of the *meso*-carbons, C-20 is missing and as a result two of the pyrrole rings are directly linked by a bond between atoms C-1 and C-19. Numbering in case of corroles is performed in a similar fashion as that is done in case of porphyrins. The position 20 is omitted and the inner nitrogen atoms are numbered from N21-N24 for maintaining parity with the porphyrin numbering scheme. More recently, the effect of direct linkage between two pyrrole rings has been ignored in the numbering scheme and the inner nitrogen atoms are numbered as N20-N23. Inside the core are present three amino nitrogens and one imino nitrogen which undergo NH tautomerization very rapidly in the free-base corrole^{27, 28}. Due to this disappearance of the *meso*-carbon, the inner N₄ core gets contracted, enabling the stabilization of metal ions in higher oxidation states.

1.3.1.5.1 Characteristic Properties

Corroles are highly stable **aromatic** tetrapyrrolic macrocycles. The most significant property of corroles is that it has three protons in the inner core unlike porphyrins and corrins (Figure 1.4). Thus they behave as **trianionic** chelating ligands contrary to the monoanionic corrin **21** and dianionic porphyrin **1**. This particular property has enriched the metallocorrole chemistry.

They are also **intensely coloured**. The UV-visible spectra of corroles demonstrate an intense band at around 400 nm and weaker bands in the region of 500-600 nm^{16, 29}. This spectral signature strongly resembles the B and Q bands of porphyrins. The free-base corroles are strongly **fluorescent** and the luminescence is observed in the span of 600-700 nm with a fluorescence lifetime in the nanosecond range²⁹.

Corroles are found to be more **acidic** in nature compared to porphyrins. This is demonstrated by the ease at which the free-base corroles liberate protons to form the monoanionic species in presence of dilute bases¹⁶. On reaction with dilute acids, they form monoprotonated species^{16, 30}. Both the monoanionic and monoprotonated forms of corroles are found to retain aromaticity as indicated by the presence of Soret bands in their electronic absorption patterns.

¹H NMR spectra of corroles exhibit a strong deshielding of the *meso*-protons and the β -protons in case of octaalkyl and *meso*-substituted corroles respectively. This **diatropic** ring current clearly indicates the aromatic nature of the ring. Since the imino protons of the inner core fall in the shielding region of the ring current, they appear upfield with respect to TMS, in the region of -2.00 to -3.00 ppm, as a broad singlet. The broadness has been assigned due to two reasons: non-identical tautomers and highly acidic nature of the corrole core³¹. However three distinct singlets

corresponding to the three different types of –NH protons have been observed at low temperatures (below 226 K) in some of the cases.

The first X-ray characterization of corrole was possible in the year 1971 and was reported by Crowfoot Hodgkin and co-workers³². The structure of 8,12-diethyl-2,3,7,13,17,18-hexamethyl corrole revealed that the macrocycle is **not exactly planar**. This deviation from planarity is directly related to the steric crowding inside the core, resulting from the direct C1–C19 bond. Low temperature X-ray analysis of the free-base corroles provided further information about their structures in the later years³³. In case of 5,10,15-tris(pentafluorophenyl)corrole, the molecular structure clearly indicates that only one of the inner core protons are in the mean corrole plane while the other two are above and below the plane respectively, due to the saddling of the pyrrole rings.

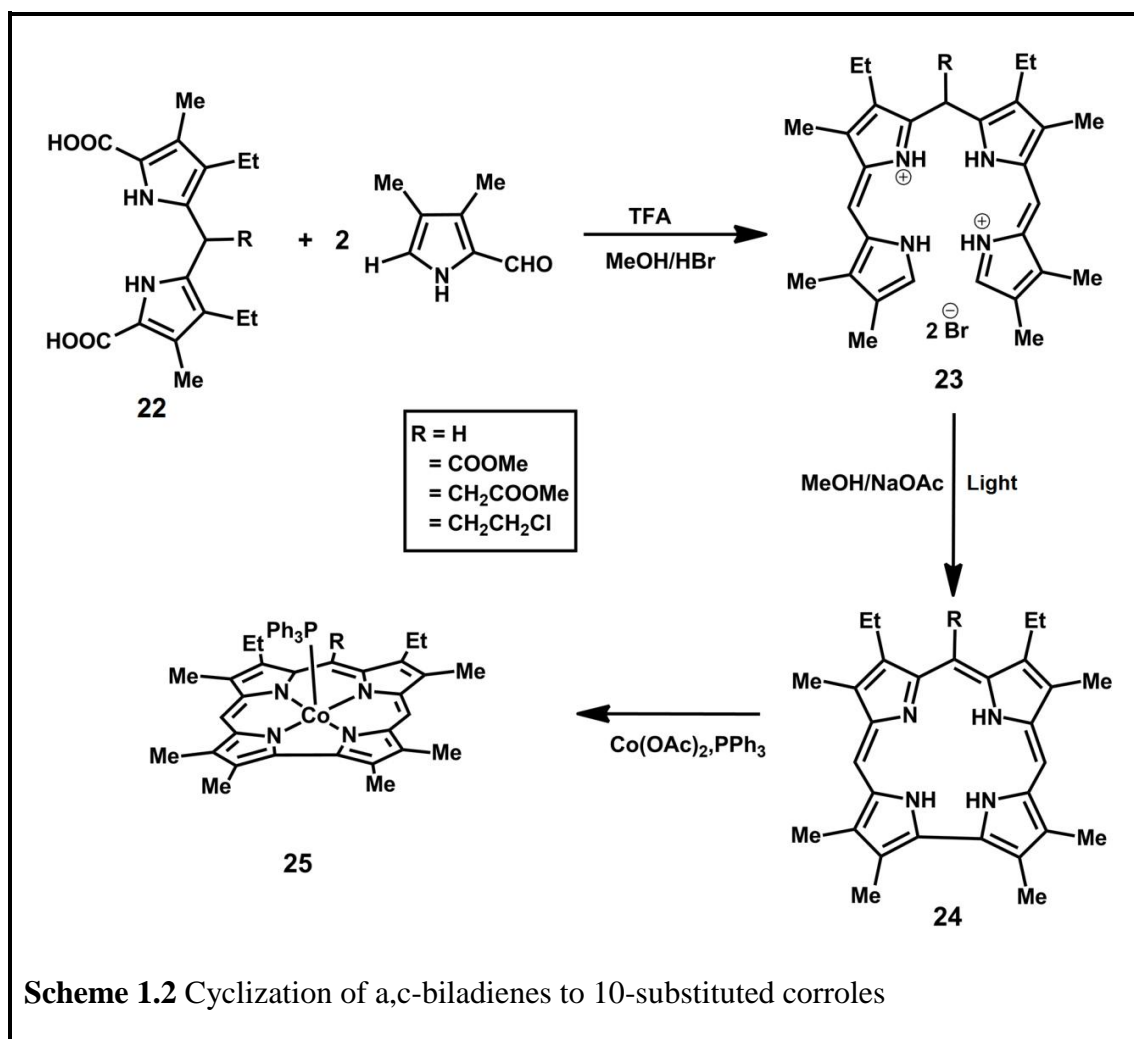
1.3.1.5.2 Synthetic Protocols

The synthetic chemistry of corroles came into limelight only after the report by Johnson and Kay in the year 1965¹⁶. Since then a bunch of varied synthetic strategies have been exploited in order to simplify the routes and amplify the corrole yields. This has resulted in various types of substitutions in the ring, such as β -substitution or *meso*-substitution or both simultaneously.

From a,c-biladienes

The first synthesis of corrole (as a representative example **24**) as reported by Johnson and Kay involved the photochemical cyclization of a,c-biladienes **23** in methanolic solution when treated with ammonium hydroxide or sodium acetate (Scheme 1.2)¹⁶. The yield of these reactions varied from 20-60%. a,c-biladienes are tetrapyrrolic molecules which exist mostly as crystalline dihydrobromide salts and synthesized by

the condensation between two equivalents of 2-formylpyrrole and one equivalent of dipyrromethanedicarboxylic acid **22** in methanol in presence of hydrobromic acid. The free-bases were usually transformed into their cobalt(III) derivatives, **25** in order to sort out NMR broadening issues³⁴.

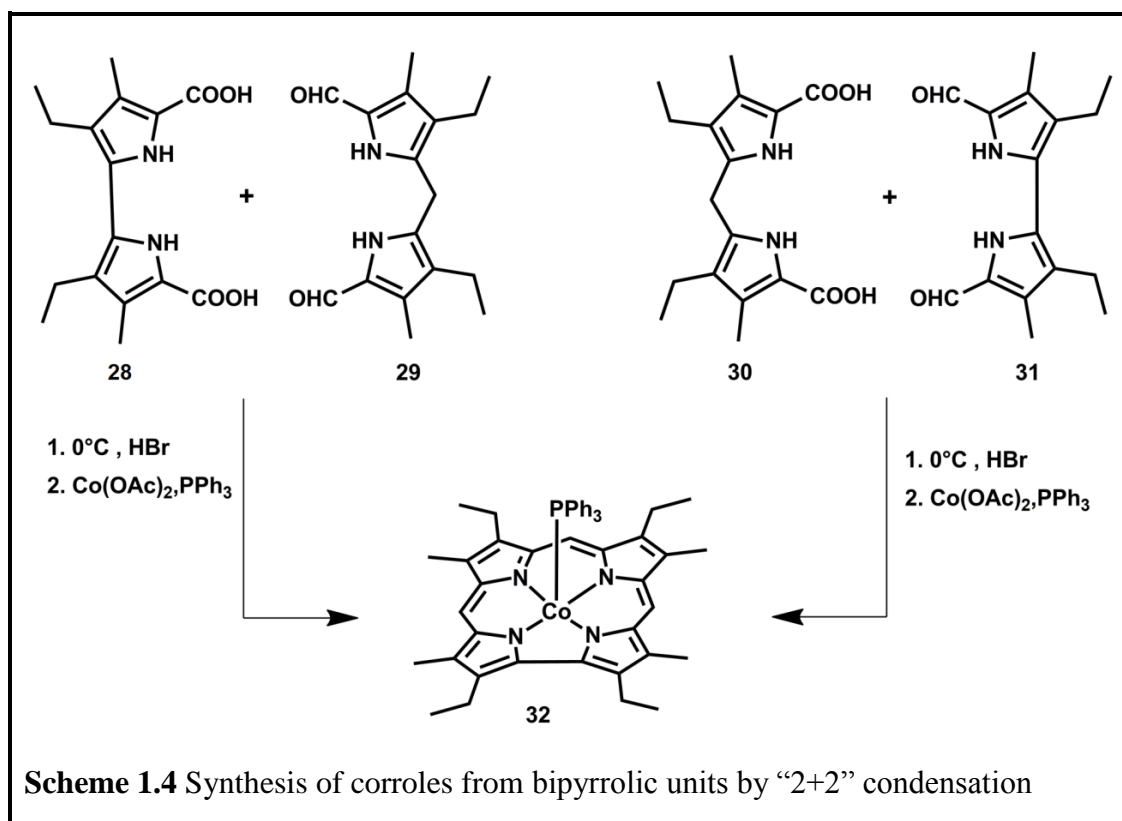
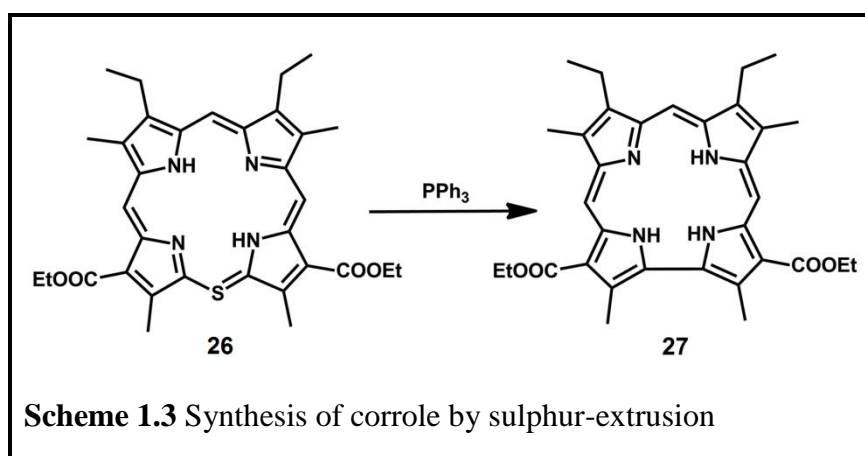


From ring-contraction of macrocycles

Synthesis of corroles by atom-extrusion was performed when a non aromatic intermediate, *meso*-thiaphlorin **26** was either heated in dichlorobenzene (yield=40%) for two hours or treated with triphenylphosphine (yield=60%), leading to the removal of the bridging sulphur atom in the final product **27** (Scheme 1.3)³⁵. Ring contraction of porphyrins to corroles was first reported by Shing Chan and co-workers³⁶.

From bipyrrolic units

The “2+2” approach for the synthesis of corroles was employed by Johnson and co-workers for the first time³⁷. The reaction involved two steps: the condensation of a bipyrrolic unit, either **28** or **31** with a dipyrromethane unit, either **29** or **30** under acidic condition in methanol at 0°C, followed by treatment with cobalt acetate and triphenylphosphine to result in **32** (yield=20%) (Scheme 1.4).



From pyrroles

The basic building block, pyrrole has been utilized in two different approaches to synthesize corroles in a very similar fashion as that was employed for porphyrins. The two approaches are: i) tetramerization of 2-substituted pyrrole and ii) condensation between pyrrole and aldehyde. Although these strategies proved to be very successful for the synthesis of porphyrins, yet in case of corroles there was always the chance of getting the corresponding porphyrins in a competitive yield percentage. Securing corrole as the only product was however achieved in few of the cases by proper selection of the templating metal ions and substitutions in the pyrrole ring.

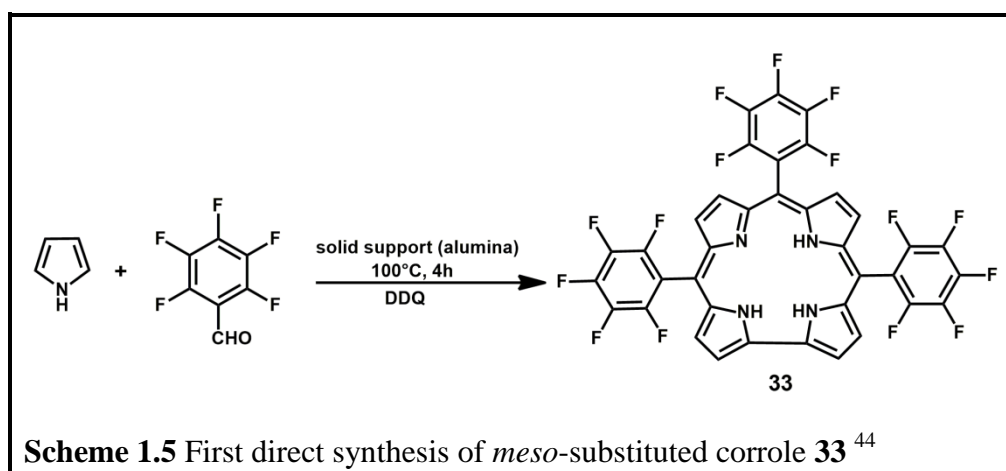
Paolesse *et al.* reported self condensation of substituted pyrroles in the presence of cobalt acetate and PPh_3 to a corrole framework for the first time (Yield=20-25%)³⁸. According to the proposed reaction mechanism, the reaction proceeded via the formation of a dipyrromethane species³⁹.

Similarly, the first report on the one-step self-condensation of 2-formyl pyrroles to *meso*-unsubstituted corroles also proved to be successful⁴⁰. The condensation of pyrroles and aldehydes has been used very commonly for the synthesis of *meso*-substituted porphyrins⁴¹. Various modifications have been already applied for the optimization of this methodology. During the course of time, several unprecedented side-products were also formed by this reaction and were characterized which resulted in the forms such as sapphyrin, expanded porphyrin, inverted porphyrin⁴² and also corrole⁴³.

Thus researchers tried to optimize the yield of corroles by modification of the Rothmund method of porphyrin synthesis. Since 1999, a new era of corroles began, hailed with the reports of very simple synthetic methodologies on *meso*-substituted corroles. In 1999, Gross and co-workers reported the direct synthesis of 5,10,15-

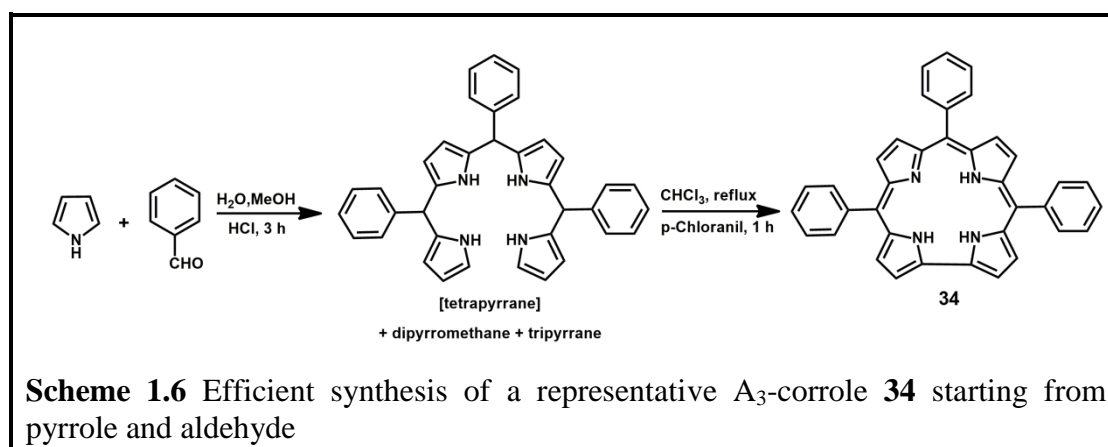
tri(2,3,4,5,6-pentafluorophenyl)corrole **33** by heating equimolar proportions of pyrrole and pentafluorobenzaldehyde in a solid support followed by addition of DDQ and chromatographic separation (Scheme 1.5) ⁴⁴. A maximum yield of 11% was reported by this procedure. In the same year, Paolesse and co-workers devised the one-pot synthesis of 5,10,15-triphenylcorrole **34** by the reaction of pyrrole and benzaldehyde (3:1) in acetic acid under reflux condition for 4 hours ⁴⁵. However the corresponding porphyrin was also formed and both the corrole and porphyrin were formed in equal proportions (yield=6%).

Another solvent-free modified protocol was also reported in which equimolar proportions of pyrrole and aldehyde in CH₂Cl₂ were mixed with alumina and heated under atmospheric conditions for four hours ³³. After chromatographic separation, pure crystals of the desired corrole (9%) were obtained.

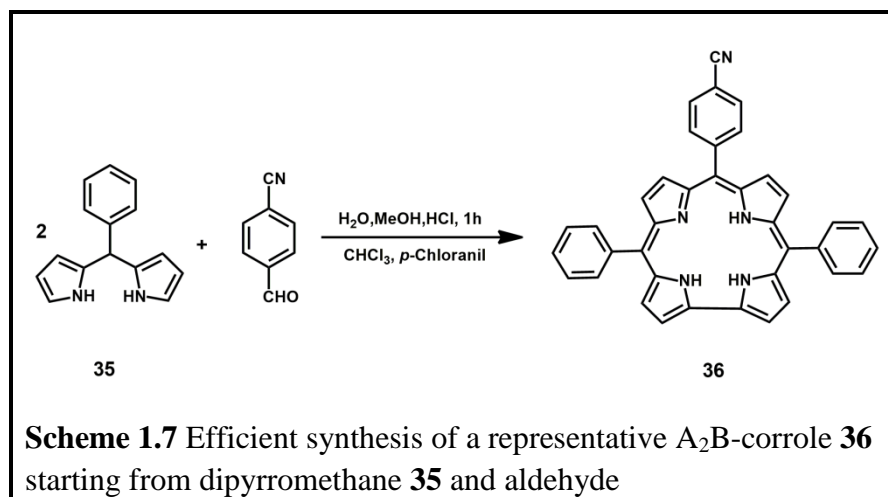


In the year 2006, Gryko and co-workers reported a highly efficient method for the synthesis of a varied range of *meso*-substituted A₃ as well as A₂B corroles, which still remains one of the most widely followed protocols ⁴⁶. According to the report, the one-pot synthesis of *meso*-substituted A₃ corroles, starting with pyrrole and aldehyde involve two different steps. The initial step for this reaction involves the acid-catalyzed electrophilic substitution to produce several types of oligocondensates, such as tetrapyrane/bilane (unconjugated open-chain corrole precursor), dipyrromethane,

tripyrane, etc. In the second step oxidation of the open chain is mediated by oxidising agents. Following the development in the synthesis of dipyrromethanes in water, by Kral and co-workers⁴⁷, the first step of condensation was carried out in water and methanol solution (Scheme 1.6). The maximum yield of a representative corrole **34** was obtained when the tetrapyrane obtained after the acid-mediated condensation of pyrrole and aldehyde in water-methanol (1:1) solvent composition was refluxed with *p*-chloranil in CHCl₃ (Scheme 1.6). Following this methodology the yield of 5,10,15-triphenylcorrole could be increased from 17% to 32% along with the successful synthesis of several other A₃-corroles in good yields.



In line with the above optimizations, Gryko and co-workers also enhanced the yield of *trans*-A₂B corroles (to a maximum of 56%, in case of **36**) considerably especially from unhindered dipyrromethanes with insignificant scrambling (Scheme 1.7).

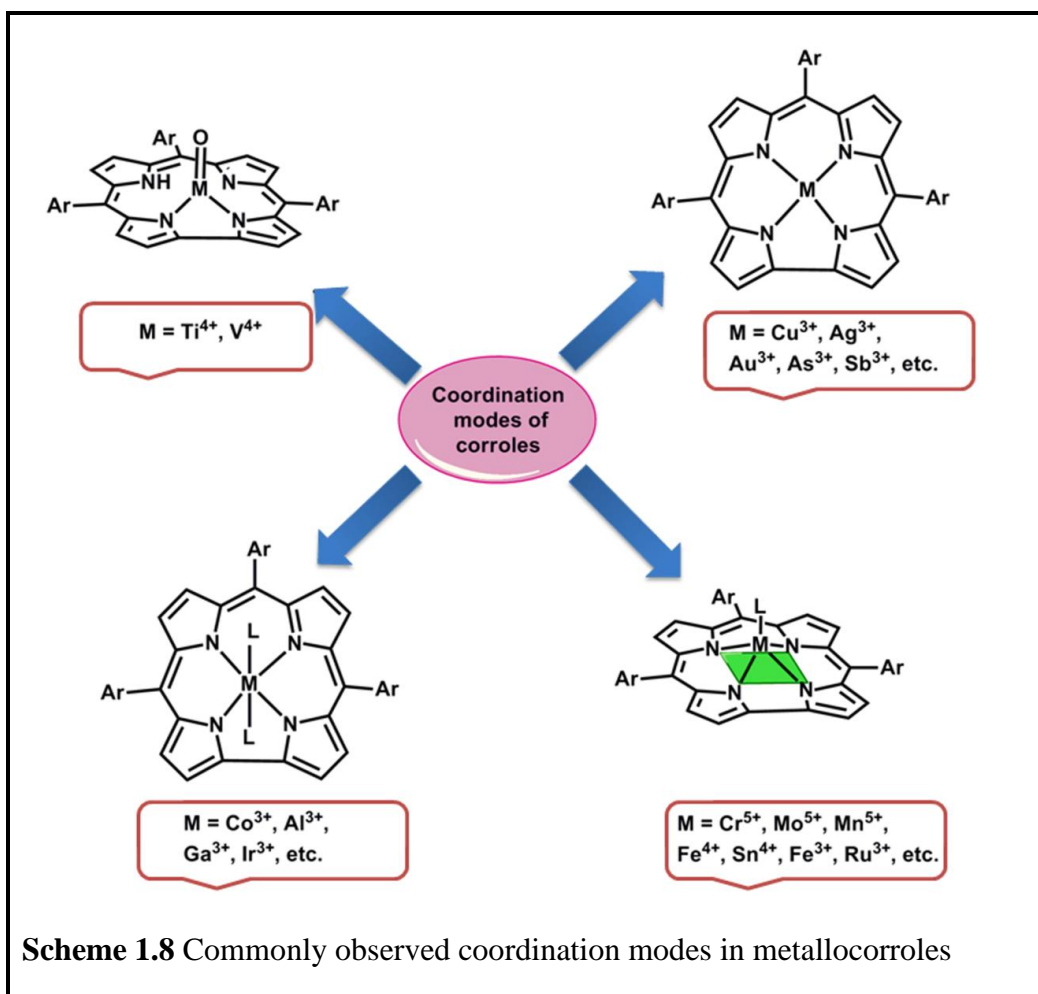


1.3.1.5.3 Metalloporphyrins

Researchers explored the chemistry of metalloporphyrins soon after the discovery of the free-base porphyrins. However, the exploration of the various types of porphyrin complexes with metals throughout the length and breadth of the periodic table especially in the initial years was quite restricted due to the absence of suitable synthetic methodologies for the synthesis of the free-base ligands. The recent developments in the facile synthesis of porphyrins have revolutionized the chemistry of porphyrins and metalloporphyrins. The synthesis of the metallo-derivatives of porphyrins can be broadly classified into two types: i) macrocyclization by using a metal ion as a template and ii) by incorporating a metal of choice into the inner porphyrin cavity². In both the cases, the choice of the metal ion plays a very crucial role. The first methodology has been already discussed to some extent in the previous section 1.3.1.5.2. For the second case, the methods implemented for the insertion of different types of metals vary which will be discussed in details in the following sections.

(a) Coordination Modes in Metalloporphyrins

The most common coordination mode for metal binding by porphyrins is the one in which the chelate adopts a square-pyramidal geometry around the central metal ion (Scheme 1.8)⁴⁸. This penta-coordinated structure gives rise to a domed configuration due to the axial displacement of the central metal atom from the N₄ plane. Such type of geometry is observed in case of complexes with Cr, Mo, Mn, Fe, Co, Rh, Ge, Sn or Pb having neutral as well as anionic axial ligands such as triphenylphosphine, pyridine or halides (F⁻, Cl⁻, Br⁻, I⁻), phenyl, methyl and also exist as oxo, nitride and nitrosyl complexes⁴⁹⁻⁵¹.



Another common coordination mode observed for corroles is the one observed in hexa-coordinated complexes (Scheme 1.8). Such octahedral geometry is observed in the axially coordinated pyridine complexes of cobalt(III), aluminium(III), gallium(III) and iridium(III) complexes⁵²⁻⁵⁵.

The four-coordinated complexes of corroles are observed in the square planar complexes of few transition metals and main group metals such as Cu^{III}, Ag^{III}, Au^{III}, In^{III}, As^{III}, Sb^{III}, Bi^{III}, etc. (Scheme 1.8)⁵⁶⁻⁵⁹. In absence of any coordinating solvents, this geometry is also adopted by corrole complexes of Co^{III}, Mn^{III} and also Ru^{III} where two Ru centers are connected by triple bonds^{16, 60, 61}.

In case of all the above-discussed cases, corroles behave as trianionic and tetradentate ligands (Scheme 1.8). In rare cases, they act as tridentate and dianionic

ligands, such as in oxovanadium(IV) and oxotitanium(IV) complexes of corroles ⁶².

(b) Periodic Table of Metallocorroles

Although the Periodic Table of corroles has not yet been enriched like that of porphyrins, yet considerable research inputs have helped in its growth process to give rise to an architecture as can be seen in Figure 1.5 ⁶³. The versatile applications of the metallocorroles in different branches of science have helped in the evolution and exploration of newer air-sensitive metallocorrole complexes. The early investigations revolved around those elements of the periodic table which were either easily accessible or biologically significant. Till 2012, no reports were observed for the corrole complexes with alkali metals, early transition metals, lanthanides and actinide series. Reports on the third row transition metals and heavier members of the main-group series were also very rare ⁶⁴. Recent developments have helped to overcome the synthetic obstacles and made the accessibility of these air-sensitive complexes possible.

The periodic table of corroles can be broadly classified into a) alkali metal corroles (only lithium corrole has been structurally characterized) ⁶⁵, b) transition metal corroles (starting from Group 4 to Group 11) ², c) early main group corroles (Group 13-15) ⁶⁴ and d) inner transition corroles [lanthanide corroles namely lanthanum, gadolinium and terbium corroles ⁶⁶; actinide corroles namely thorium and uranium corroles ⁶⁶].

(c) Spectroelectrochemical Investigations

Apart from the conventional characterization techniques such as absorption spectroscopy, ¹H NMR and ¹³C NMR spectroscopy, X-ray crystallography, Mass

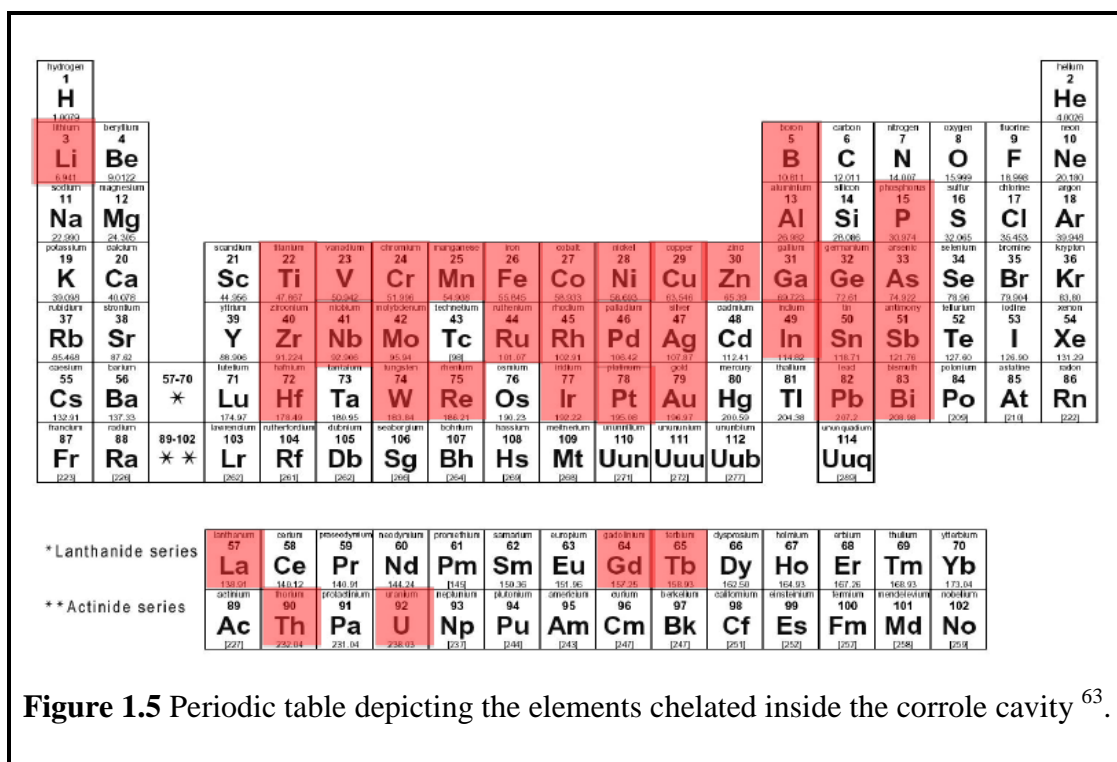


Figure 1.5 Periodic table depicting the elements chelated inside the corrole cavity⁶³.

Spectroscopy, Cyclic Voltammetry, etc., majority of the metallocorroles reported till date has also been investigated by a combination of thin-layer spectroelectrochemical measurements such as UV-Vis, FTIR and EPR spectroscopy. The *in situ* measurements of the electro-oxidised and electro-reduced species of metallocorroles by these spectroelectrochemical tools are useful in deciphering the change in the spectral signature upon oxidation or reduction, the exact location of electron-transfer and also the reversibility of the redox processes². Such conclusive results cannot be drawn solely by electrochemical measurements of the complexes. With the help of this combined spectroelectrochemical technique, complete and rapid electrolysis of the compounds under inert conditions are possible⁶⁷.

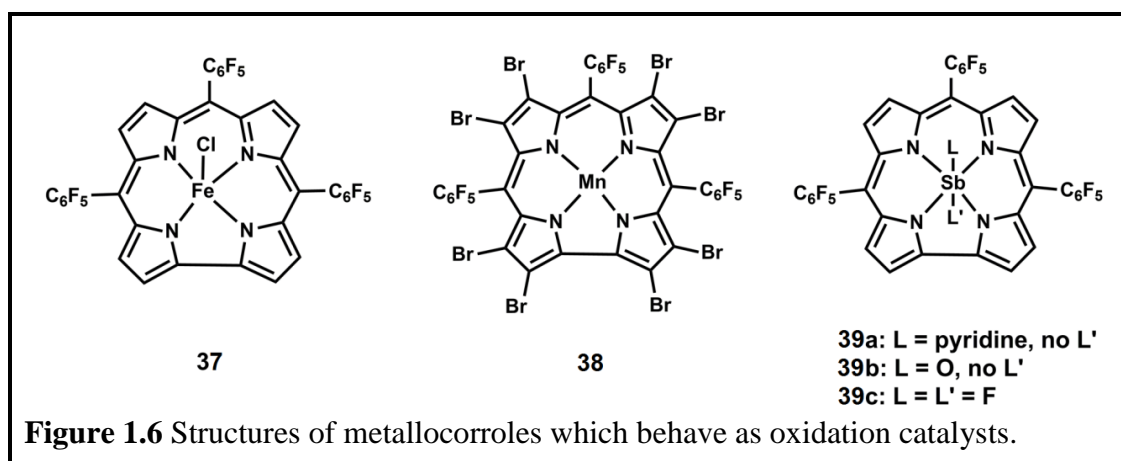
The combination of UV-Vis, FTIR and EPR measurements have been particularly useful in analyzing the non-innocence of the free-base corrole ligand and also in other cases some axial ligands such as NO, oxide, etc. in metallocorrole complexes with redox-active metal centers².

1.3.1.5.4 Applications of Metallocorroles

The renaissance in the field of corrole chemistry, since 1999, had a direct impact on the ongoing research ideas which finally led to the flourishing of various reports on their applications. Some of the representative applications have been discussed in the following section^{48, 68}.

(i) Oxidation Catalysis

The utilization of metallocorroles, and many other related macrocycles as oxidation catalysts has been inspired by the naturally occurring heme containing enzymes (e.g. Cytochrome P450, etc.) which mediate several oxidation reactions³. The usage of metallocorroles in oxidation reactions such as epoxidation and hydroxylation was



reported for the first time in the year 1999⁶⁹. The catalyst employed was an iron(IV) corrole, Fe(tpfc)Cl, **37** (Figure 1.6). Though the catalytic results indicated that the iron(IV) corrole was a good oxidation catalyst, yet it did not prove as a very efficient alternative to the previously studied analogous porphyrin counterpart for the epoxidation of styrene (yield=66%) and hydroxylation reaction of ethylbenzene (yield=6.6%).

Later better catalytic properties were observed by using manganese(III) corrole complexes such as **38** in the oxidation of cyclohexene in respect of yield,

reaction time, stability and turnover frequency (Figure 1.6)^{70, 71}. Later in the year 2006, a report on the antimony corroles, **39a**, **39b**, **39c** revealed high efficiencies as well as selectivities for the aerobic oxidation of thioanisole as photocatalysts (Figure 1.6)⁷².

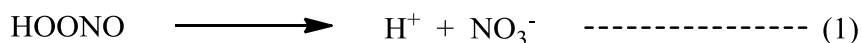
(ii) Reduction Catalysis

Since corroles are capable of stabilizing higher oxidation states of metals, the low-valent metallocorroles are expected to be quite reactive. These reactive metallocorroles have been explored for reducing small molecules (Figure 1.7).

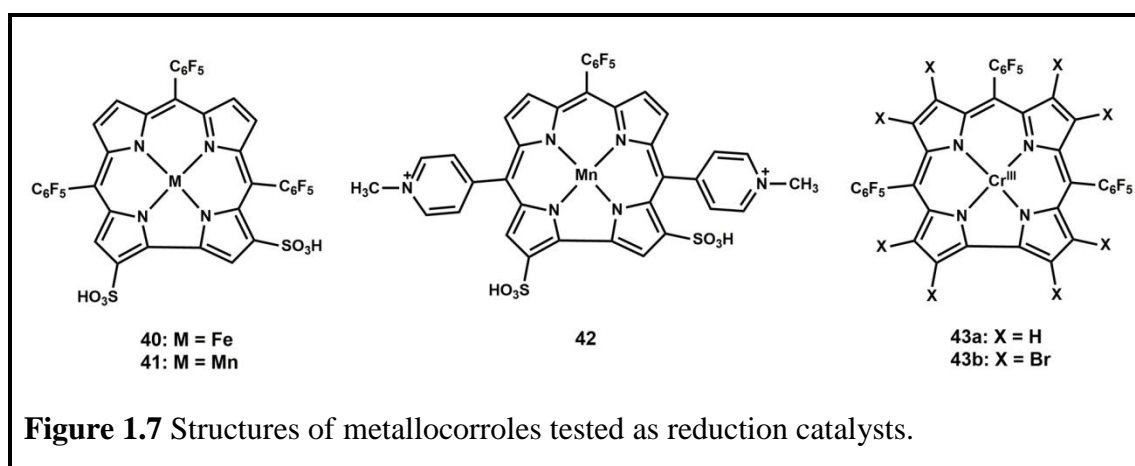
One of the significant catalytic properties demonstrated by metallocorroles lies in the efficient decomposition of reactive oxygen species (ROS) such as H₂O₂ and peroxyntirite^{73, 74}. Inside biological environment, excess of ROS and reactive nitrogen species (RNS) leads to unprecedented oxidation or nitration of biomolecules, leading to a condition commonly known as nitrooxidative stress. This specific stress is related to several diseases and neurodegenerative disorders such as Parkinson's, Alzheimer's, Huntington's diseases, etc⁷⁵. Peroxyntirite produced *in vivo* is particularly a very harmful species (being both ROS and RNS) because of the lack of enzymes to prevent the decomposition of its protonated form (HOONO) to potentially dangerous radicals⁷⁶⁻⁷⁹.



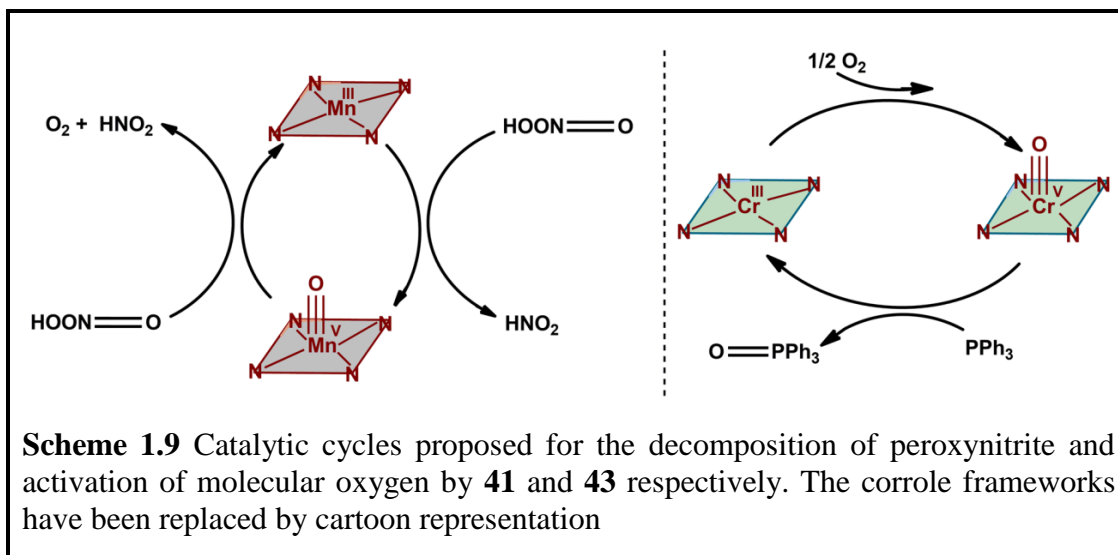
In the quest for developing suitable catalysts for its decomposition to innocent products as demonstrated in the following equations, the reports on the application of Fe^{III} corrole and Mn^{III} corrole for the same, came into existence (Figure 1.7)⁷⁴.



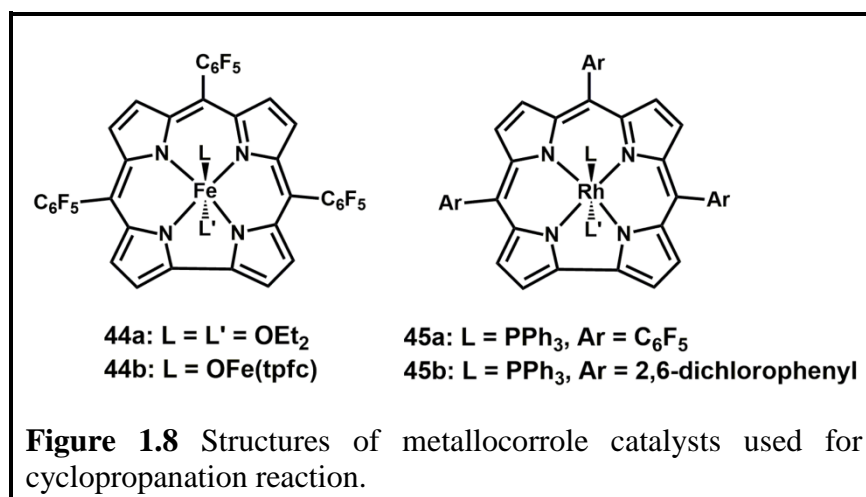
Both the studied metallocorroles, **40** and **41**, were found to be efficient catalysts for the detoxification of peroxyxynitrites. The decomposition pattern of both the catalysts was however found to be different. The iron(III) corrole **40** was found to catalyze the decomposition by isomerisation to nitrates as given in equation (1). After quantification of the products, it was inferred that the manganese(III) corrole followed the disproportionation catalytic pathway to nitrite and oxygen as depicted in the second equation (2) which is particularly interesting (Scheme 1.9). The rate of catalysis by iron(III) corrole was found to be quite higher when compared with its congeners. Water soluble manganese(III) corrole complexes with *p*-pyridinium appended *meso*-substituents, **42** were found to be ten times faster catalysts compared to **41** for the decomposition of peroxyxynitrite⁸⁰.



Chromium corroles were used as efficient catalysts for the oxidation of small organic molecules⁸¹. The Cr^{III} corrole complex **43** on oxidation converts into the oxo-chromium(V) species, which in turn oxidises triphenylphosphine to triphenylphosphine oxide (Scheme 1.9)⁸². In order to enhance the reactivity of the oxo-chromium(V) corrole complex, for epoxidation of norbornene, the β -positions of the pyrrole rings were substituted with -Br atoms in **43**.



(iii) Group Transfer Catalysis

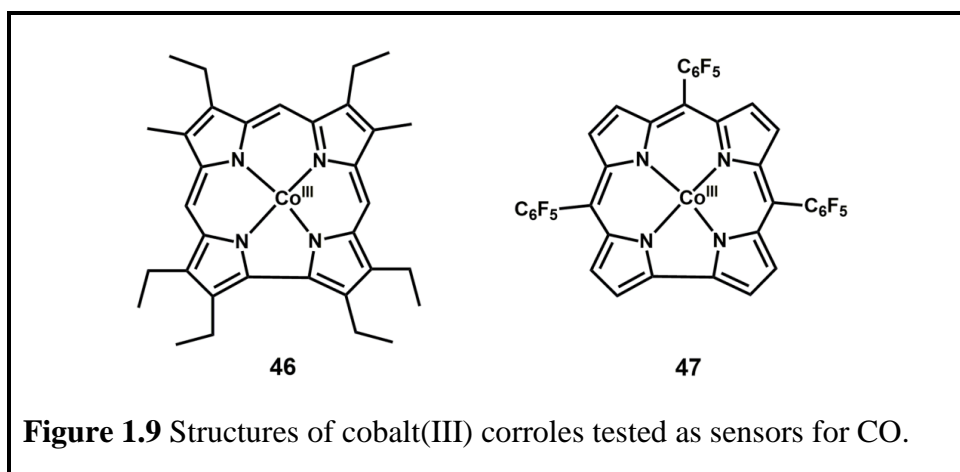


The superiority of metalcorroles compared to their metalloporphyrin counterparts as catalysts, was first demonstrated in the cyclopropanation reaction of olefins⁶⁹. Iron(IV) corroles such as **37**, **44a**, **44b**⁵⁰ and rhodium corrole complexes, **45a** and **45b**^{50, 83, 84} were found to be efficient catalysts for cyclopropanation of styrene (Figure 1.8).

(iv) Metalcorrole Sensors

Metalcorroles as sensors emerged with the detection of the deadly gas carbon monoxide by cobalt(III) corroles after the discovery of CO binding with the

cobalt(III) corroles^{85, 86}. CO detection is very crucial and the CO detection tools serve extremely beneficial for household as well as industrial purposes. Although commercially available detectors are available, still each of them has their own merits and demerits. The reported cobalt(III) corroles were found to bind with CO *versus* O₂ and N₂ in a highly selective and efficient manner⁸⁷. Out of the six cobalt(III) corroles whose adsorption properties were studied, it was observed that increasing electron density on the central cobalt atom was directly proportional to the decreasing Lewis acidity and consequently decreasing affinity towards CO. Thus the cobalt(III)



octaethylcorrole complex **46** with electron-donating substituents at β -positions of the ring, did not absorb CO as precededented (Figure 1.9). The maximum CO affinity was observed for the cobalt(III) corrole complex **47** with the maximum electron-withdrawing nature.

(v) Dye Sensitized Solar Cells (DSSC)

In order to reduce the usage of non-renewable sources for energy requirements, intense research has been dedicated towards the development of dye sensitized solar cells for the conversion of solar energy to chemical energy. Sensitizers play a very important role in harvesting the solar energy in these cells (Figure 1.10). The most popular of all the studied dyes for DSSC are the ruthenium bipyridine derivatives and

various kinds of porphyrinoids^{88, 89}. Ruthenium complexes with efficiencies reaching greater than 11% have been used for this purpose since the last two decades⁹⁰. However due to the cost and environmental viability issues, newer and safer sensitizers have been developed. The applicability of several porphyrinoids have been examined because of their interesting photophysical properties which can be modulated by suitable substitutions at *meso*- as well as β -positions and also by varying the central metal atoms. Since the frontier molecular orbitals of corroles are higher in energy compared to their porphyrin counterparts, so the applications of some corrole derivatives as sensitizers were also explored. A free-base corrole, bis-sulfonated tris(pentafluorophenyl) corrole **48** and its complexes with gallium **49** and tin **50** were chosen for this purpose⁹¹. All these complexes were found to bind with the mesoporous material TiO₂ although their efficiencies differed in the order: **49** ~ **48** >> **50**. The measured cell efficiencies using these sensitizers revealed that suitably substituted corroles have exhibited cell efficiencies upto half of that for a popular ruthenium based sensitizer, N3 **51** and even higher compared to that observed in cells with other tetrapyrrolic counterparts.

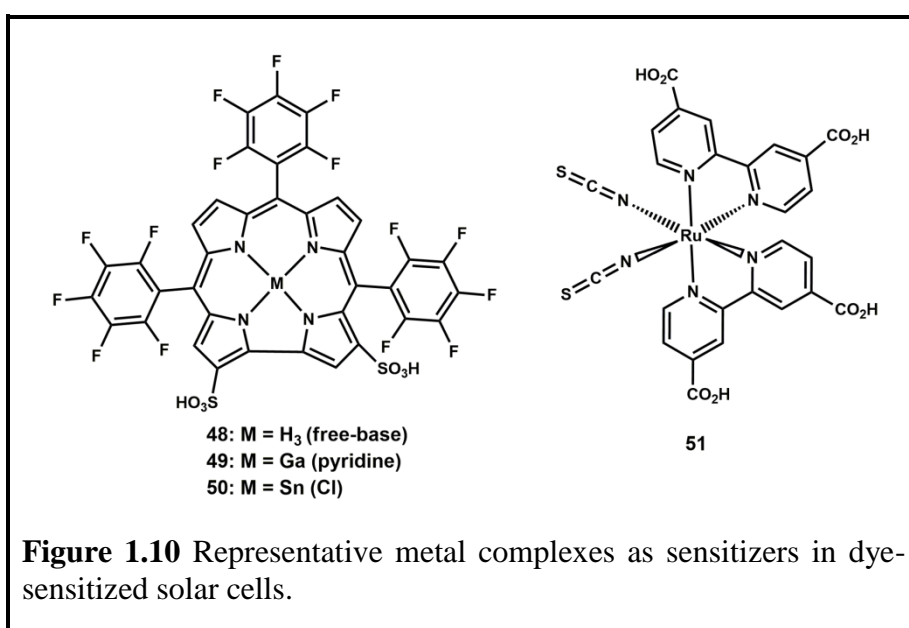


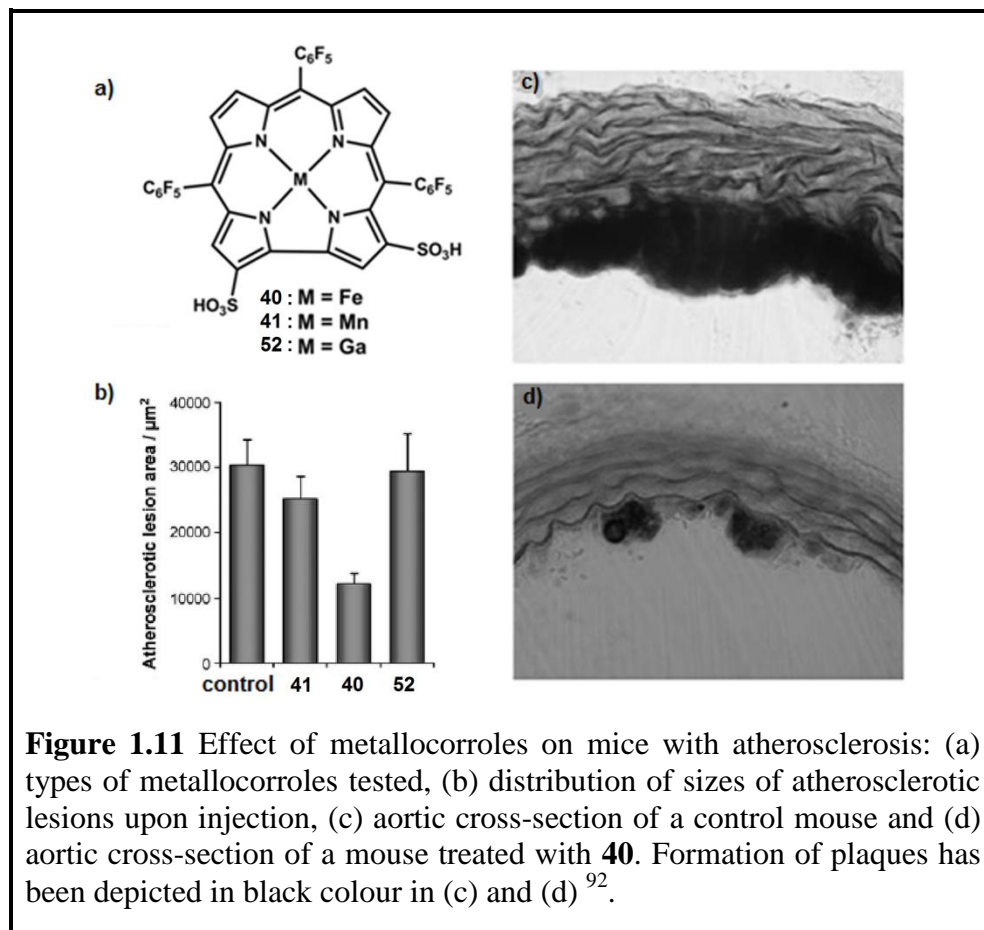
Figure 1.10 Representative metal complexes as sensitizers in dye-sensitized solar cells.

(vi) Medicinal Applications

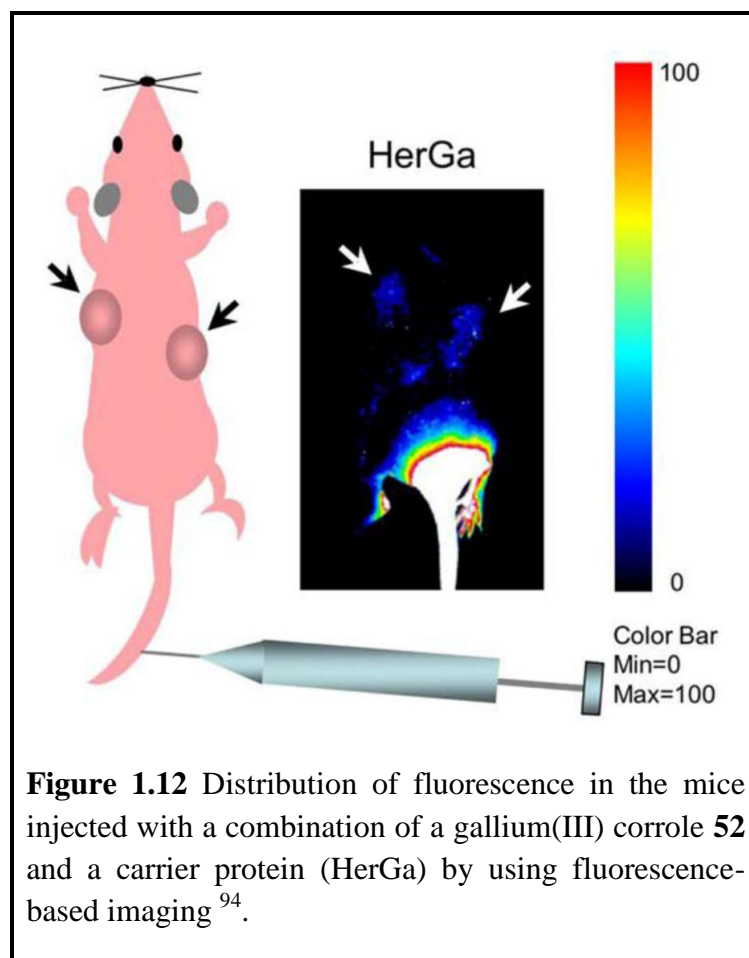
The first implementation of the peroxynitrite decomposition mediated by metallocorroles, to avoid damage to biological systems, was reported for the prevention of atherosclerosis. Atherosclerosis is a vascular disease caused by the accumulation of cholesterol in the form of plaques in the arteries which ultimately causes blockage, resulting in heart attack or stroke if not detected or treated. It has been researched that oxidation of lipoproteins trigger this condition in the body. The ability of the Fe^{III} corrole and Mn^{III} corrole to cause decomposition of peroxynitrite motivated the research towards their effect on the prevention of oxidative damage to low- and high-density lipoproteins (LDL and HDL respectively)⁹². The effectiveness of these two metallocorroles was also examined for the inhibition of oxidation or nitration of small molecules by peroxynitrite. Both the catalysts were found to be quite effective, but superiority of **41** was observed especially for the prevention of nitration reactions by the RNS.

In vivo investigations on common murine model were also performed for the study on the development of atherosclerosis (Figure 1.11). The mice were divided into four groups, depending on the additives of drinking water: without any additive, with **40**, with **41** and with gallium(III) corrole **52**. A very good result was observed in the case of mice treated with **40**. No atherosclerotic lesions were observed in two out of six mice treated with **40**. For the remaining four mice, the lesion area was found to reduce by 60% compared to those in the control group. A small reduction (17% compared to the control group) in the area of the lesion was observed for those treated with **41**. The average lesion area was found to be quite high in the untreated mice without any additives and also in the group treated with **52**. These results surpassed the effect of potential natural anti-oxidants namely red wine and pomegranate juice.

One of the latest contributions of the metallocorroles in pharmaceuticals has been dedicated by a gallium(III) corrole complex **52**. The prominent fluorescence exhibited by **52** has made its application in imaging purpose extremely useful. In vitro results indicated that **55** can be transported by the delivery proteins inside the cells



and can destroy the tumor cells with high specificity ⁹³. These results instigated further in vivo experiments on murine model to confirm these remarkable observations (Figure 1.12) ⁹⁴. Mice with human breast cancer tumors when treated with the gallium complex alongwith the carrier proteins, made the detection of tumors by in vivo fluorescence-based imaging and also the suppression of tumor growth possible without any side-effects (contrary to anti-cancer drugs and photodynamic therapy) (Figure 1.12). The dosage required for this tumor suppression was also found to be minimal when compared to a leading anti-cancer drug, doxorubicin.



1.5 Scope and Objectives of the Present Thesis

In this thesis, attempts have been made to explore various scaffolds of corrole frameworks and their corresponding metal derivatives on the basis of either biological or physical significances. Complete structural as well as spectroscopic characterizations of the newly synthesized molecules have been also elucidated. Attempts were also made to understand the mechanistic aspects of their reactivity and also structural, morphological and spectroscopic changes in individual cases. Application of one of the metallocorroles in device fabrication has been also explored.

1.5.1 Lacunae

1. It is already well established that NO[•] is a gaseous signaling molecule with immense biological significance in regulating several physiological functions⁹⁵⁻⁹⁷.

Research interests have thus developed in elucidating the mechanism of interaction of NO[•] with hemoproteins and their model synthetic counterparts⁹⁸⁻¹⁰². Since the involvement of (macrocycle)FeNO complexes as intermediates in the oxidised state in enzyme catalyzed conversion of nitrite to ammonia is already known¹⁰³, it is extremely important to understand the oxidation state distribution in higher oxidation states of (macrocycle)FeNO systems. Very limited studies are done on such higher oxidation state complexes such as [corrolato(FeNO)⁶], which has resulted in a very narrow source of information on the oxidation state distribution in the electro-oxidised and electro-reduced form of these complexes¹⁰⁴⁻¹⁰⁹.

2. Researchers have been putting immense efforts on understanding the role of aggregates of metalloporphyrins and porphyrins in the light harvesting complexes of chlorophyll and bacteriochlorophyll for the construction of newer and promising bio-inspired devices¹¹⁰⁻¹²⁰. Consequently, among many other metalloporphyrin derivatives, work in the field of tin complexes has gained special importance in the recent years. This has led to a considerable number of reports focussed on the synthesis of tin(IV) porphyrin based aggregates and their various applications¹²¹⁻¹²⁴. Although corroles being more superior to porphyrins particularly on the basis of their photophysical properties, none of the investigations has been done on the generation of tin(IV) corrole aggregates and exploration of their application in device fabrication.

3. While exploring a particular property of a macrocycle such as corrole, it is often necessary to modulate its structure by varying the substitutions at either *meso*- or β - positions. Such structural modifications can be done more comfortably in the metalated corroles compared to their free-base counterparts. In majority of such transformations, the final step demands the removal of the metal. However there is no generalized protocol for the demetalation of metallocorroles. Although few protocols

are available on demetalation of particular metals, such as Cu, Mn and Ag from the corrole cavity, all of them are carried out under strongly acidic conditions¹²⁵⁻¹²⁸.

4. (a) Absorption bands in the NIR region are particularly significant because of their origin from the π -dimer species of the photosynthetic reaction center special-pairs¹²⁹⁻¹³⁴. Synthetic NIR-absorbing dyes have been already explored by using porphyrin and corrole dimers^{29, 135-139}. However, NIR transitions have never been observed from mononuclear, *meso*-substituted corrole derivatives.

(b) Since the most stable and usual oxidation state of silver is +1, reports on Ag^{II} and Ag^{III} complexes are rare¹⁴⁰. The reported high-valent silver-containing compounds have been synthesized under harsh conditions.

(c) Influence of the *meso*-substituents of the corrolato rings on the electronic structures of their metal complexes and in turn on their NIR absorption properties has not been explored.

5. Higher oxidation states of metals have been often postulated to exist in various intermediates of several biological and also in catalytic processes.^{3, 141, 142} Despite the importance of higher oxidation states of copper (viz. +III, +IV), spectroscopic data for these oxidation states remain under-explored, with such information on Cu^{IV} complexes being non-existent.¹⁴³⁻¹⁴⁸

1.4.2 Objectives

1. To synthesize a series of [corrolato(FeNO)⁶] complexes and evaluate them with concomitant structural and spectroscopic characterizations; to explore and establish the exact site of electron transfer in the oxidised as well as reduced forms of those [corrolato(FeNO)⁶] complexes with potentially non-innocent ligands by using combined UV-Vis, IR, and EPR spectroelectrochemical as well as theoretical studies.

2. To synthesize nanoscale aggregates of structurally as well as spectrally characterized novel tin(IV) corrole complexes and to investigate the viability of those aggregates in the fabrication of a semiconductor device.
3. To develop and optimize an efficient and mild one-step methodology for the demetalation of tin(IV) corroles to the corresponding free-base corroles; to further check the reactivities of those tin(IV) chloride complexes of corroles with various Grignard reagents and also characterize the products by both structural as well as by different spectroscopic techniques.
4. To synthesize and characterize a series of novel silver(III) corrole complexes; to detect NIR absorptions from the mononuclear forms of these complexes if any; to study the accessibility of Ag^{II}, Ag^{III} and Ag^{IV} in corrolato-silver(III) complexes; to understand the influence of the *meso*-substituents on the NIR absorption properties of silver(III) corroles with the help of combined electrochemical, UV-Vis-NIR/EPR spectroelectrochemical and DFT approach.
5. To prepare and characterize a series of novel copper(III) corrole complexes by various spectroscopic and electrochemical techniques including UV-Vis-NIR/EPR spectroelectrochemistry. To utilize XANES measurements, and DFT calculations for exploring the existence of three distinct redox states in these molecules for which oxidation states +II, +III and +IV can be invoked for the copper centers.

CHAPTER 2

Synthesis, Spectral Characterization, Structures, and Oxidation State Distributions in [(corrolato)Fe^{III}(NO)]ⁿ (n = 0, +1, -1) Complexes

2.1	Introduction	37
2.2	Results and Discussion	40
2.2.1	Synthesis	40
2.2.2	Spectral Characterization	42
2.2.2.1	Mass Spectroscopy	42
2.2.2.2	Infra-Red Spectroscopy	44
2.2.2.3	NMR Spectroscopy	45
2.2.2.4	X-Ray Crystallography	48
2.2.2.5	Electrochemistry	59
2.2.3	UV-Vis, IR and EPR Spectroelectrochemistry	62
2.3	Conclusions	73
2.4	Experimental Section	74
2.4.1	Materials	74
2.4.2	Physical Measurements	74
2.4.3	Crystal Structure Determination	75
2.4.4	Computational Details	76
2.4.5	Synthesis of 4-(Di(1H-pyrrol-2-yl)methyl)benzotrile, 1	76
2.4.6	Synthesis of 5,10,15-Tris(4-bromophenyl)corrole, 1A	77
2.4.7	Synthesis of 10-(4-Bromophenyl)-5,15-bis(4-cyanophenyl)corrole, 2A	78
2.4.8	Synthesis of 10-(2,4,5-Trimethoxyphenyl)-5,15-bis(4-cyanophenyl)corrole, 3A	78
2.4.9	Synthesis of [5,10,15-Tris(4-bromophenyl)cor]Fe ^{III} NO, 1B	79
2.4.10	Synthesis of [10-(4-Bromophenyl)-5,15-bis(4-cyanophenyl)cor]Fe ^{III} NO, 2B	80
2.4.11	Synthesis of [10-(2,4,5-Trimethoxyphenyl)-5,15-bis(4-cyanophenyl)cor] Fe ^{III} NO, 3B	81

2.1 Introduction

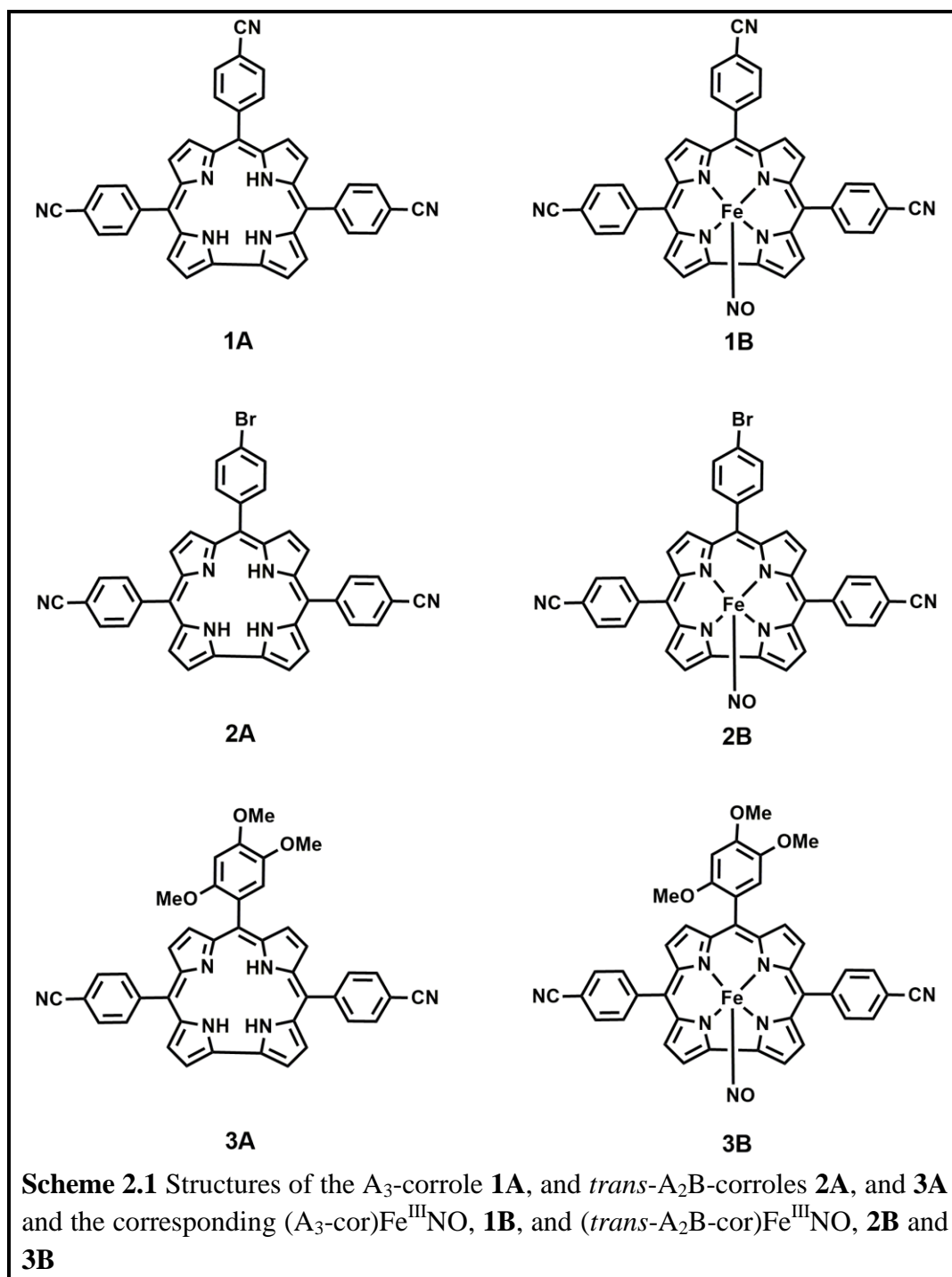
The free radical, NO^\bullet acts as a messenger molecule in biological systems by activating the ferrous heme of the guanylate cyclase (sGC)^{95, 96}. Implications of this signaling behavior have been widely studied by many researchers in chemistry, biology and medicine. NO^\bullet , widely known as reactive nitrogen species (RNS), is also essential for homeostasis of cellular organism⁹⁷. Understanding the mechanism of redox signaling is of great importance from the perspectives of physiological functions. Inside cellular organisms, NO^\bullet targets a variety of metalloproteins including hemoglobin and cytochrome c oxidase (CcOx). However the binding of NO^\bullet with metalloproteins is case sensitive. The binding can be either reversible or irreversible. Methemoglobin, where iron is in the +3 oxidation state, binds NO^\bullet in a reversible fashion, whereas oxy-hemoglobin with iron in the +2 oxidation state, binds NO^\bullet in an irreversible fashion⁹⁸⁻¹⁰². The signaling mechanism of NO^\bullet is directly dependent on the reversible binding of NO^\bullet . Thus, it is evident that the mechanism of binding of NO^\bullet with hemoproteins is of considerable importance from a biological and chemical point of view. This has led to the development of an intense research interest in elucidating the mechanism of the interaction of NO^\bullet with hemoproteins and their model compounds⁹⁸⁻¹⁰². It is also known that certain enzymes use (macrocycle)FeNO complexes in the oxidized state as transient intermediates for the conversion of nitrite to ammonia¹⁰³. All these observations necessarily point towards the extreme importance of understanding the oxidation state distribution in higher oxidation states of (macrocycle)FeNO systems.

Corrole, being a special one among the macrocyclic systems as has been already justified in Chapter 1, may be a perfect choice to study the same. In this regard, it should be kept in mind that corrole ring is just one *meso*-carbon shorter than

related porphyrin macrocycle^{2, 8, 33, 50, 81, 82, 149-171}. Compared to porphyrin which has two imino hydrogens, corrole contains three imino hydrogens. Therefore, it can act as a trianionic ligand. Because of the smaller cavity size and more anionic nature of corrole, it tends to stabilize metals in higher oxidation states^{2, 8, 33, 50, 81, 82, 149-171}. In majority of the cases, in the native state, the oxidation state of metal is one unit higher in metallocorrole than its metalloporphyrin analogue. Thus it has been proven to be easier and more realistic to study the higher oxidation states of metal in corrole based macrocycle^{2, 8, 33, 50, 84, 85, 154-177}. It was also found that in various catalytic reactions, like carbene-transfer and nitrene-transfer reactions, iron corrole has been proven to be more superior than its iron porphyrin analogue^{73, 156, 165, 172-184}. Owing to very limited availability of information, [(corolato)(FeNO)⁶] complexes¹⁰⁴⁻¹⁰⁹ could be a perfect choice to study the oxidation state distribution and to get deeper insight into the peculiar reactivities of iron corrole complexes. A detailed literature survey reveals that there are very few reports on the *in situ* generated oxidized and reduced species of [(cor)(FeNO)⁶] moieties^{104, 109}. cor stands for corolato and the (FeNO)⁶ nomenclature is based on the Enemark and Feltham notation¹⁸⁵, where the exponent term six is obtained by using the summation of five iron d-electrons and one unpaired electron from NO.

This chapter describes the synthesis of one A₃-corrole and two novel *trans*-A₂B-corroles, 5,10,15-tris(4-bromophenyl)corrole, **1A**, 10-(4-bromophenyl)-5,15-bis(4-cyanophenyl)corrole, **2A**, and 10-(2,4,5-trimethoxyphenyl)-5,15-bis(4-cyanophenyl)corrole, **3A** (Scheme 2.1) and the corresponding one [(A₃-cor)(FeNO)⁶] and two novel [(*trans*-A₂B-cor)(FeNO)⁶] derivatives namely [(5,10,15-tris(4-bromophenyl)cor)(FeNO)⁶], **1B**, [(10-(4-bromophenyl)-5,15-bis(4-cyanophenyl)cor)(FeNO)⁶], **2B**, and [(10-(2,4,5-trimethoxyphenyl)-5,15-bis(4-

cyanophenyl)cor)(FeNO)⁶], **3B**. Compared to A₃-corroles, *trans*-A₂B corroles would be more versatile scaffolds and would be a better modulator of the steric and electronic factors for synthesizing a diverse range of metal complexes. A series of electron-withdrawing (like -CN) and -releasing (like -OMe) groups have been chosen as substituents in the corrole frameworks keeping in view that these modifications might influence the energies of the molecular orbitals of the respective complexes, thus affecting the spectral features. Moreover, cyanide has been adopted as a substituent in these corroles because of its tendency to get readily converted into a series of other organic functional groups. Thus these complexes can be considered as potential building blocks for construction of various other metallocorrole-based architectures. Although the syntheses of free base A₃-corrole, **1A** and [(A₃-cor)(FeNO)⁶], **1B** have been already reported in the literature¹⁰⁷, the crystal structure and UV-Vis, IR, and EPR-spectroelectrochemical investigations of **1B** have not been reported so far. This chapter further relates to the synthesis of two new *trans*-A₂B-corroles, **2A** and **3A** and their corresponding [(cor)(FeNO)⁶] derivatives. In addition to the synthesis and spectral characterization of **1A**, **1B**, **2A**, **2B**, **3A** and **3B**, the crystal structures of **1B** and **2B** and electrochemistry, UV-Vis, IR, and EPR-spectroelectrochemical investigations of **1B**, **2B** and **3B** are also discussed here. To garner further support of the experimentally obtained results, density functional theory (DFT) and time dependent-DFT (TD-DFT) calculations have been also carried out.



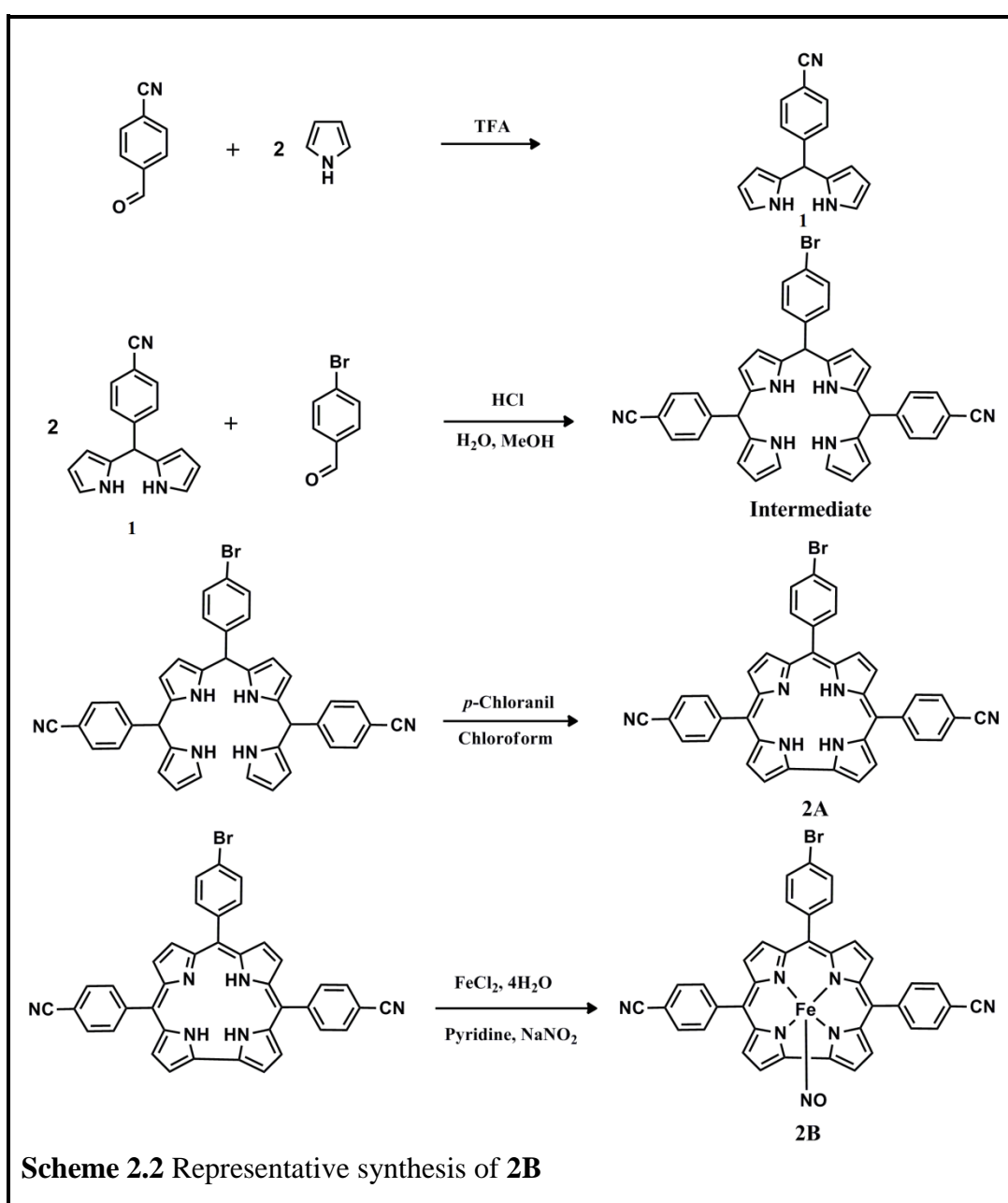
2.2 Results and Discussion

2.2.1 Synthesis

Symmetric A₃-corrole, **1A** was already reported in the literature^{46, 186}; however, two *trans*-A₂B-corroles, **2A** and **3A** were prepared for the first time. Reaction of the 4-(Di(1H-pyrrol-2-yl)methyl)benzotrile, **1** and pyrrole, which were dissolved in 1:2

mixture of methanol and water in the presence of HCl, and the subsequent oxidation by *p*-chloranil (Scheme 2.2; representative synthesis of **2B**), resulted in the formation of the corrole derivatives.

The [(cor)(FeNO)⁶] derivatives were synthesized by following a reported procedure¹⁰⁴⁻¹⁰⁹. A mixture of the desired corrole and ferrous chloride tetrahydrate was refluxed in a solution of pyridine/methanol (1:2) under a dinitrogen atmosphere. Upon addition of a saturated aqueous NaNO₂ solution, the corresponding derivatives

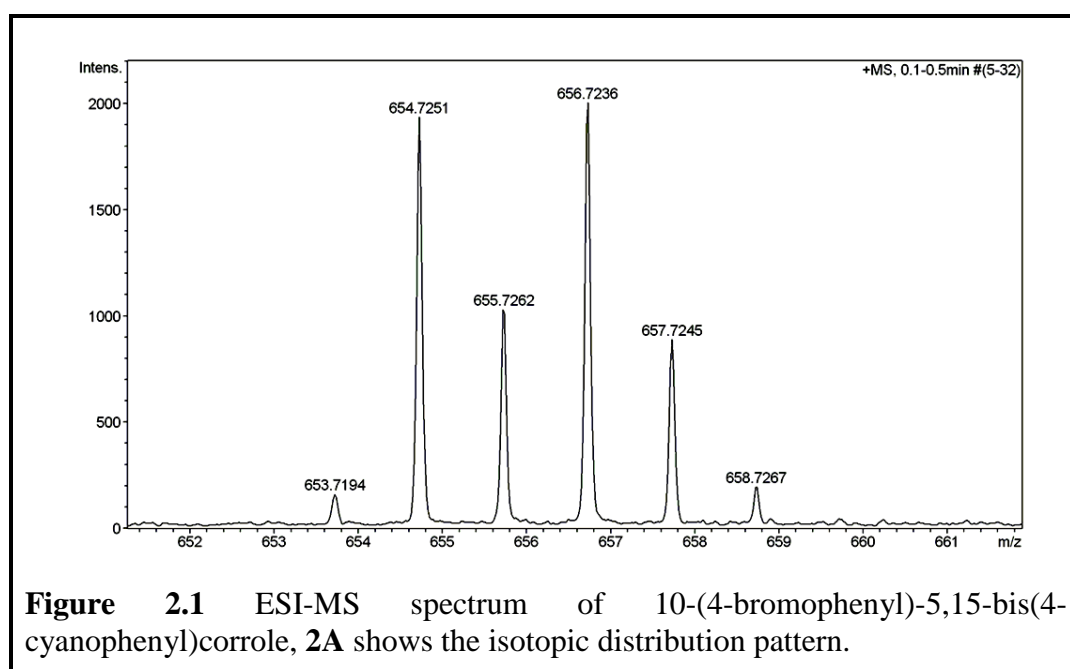


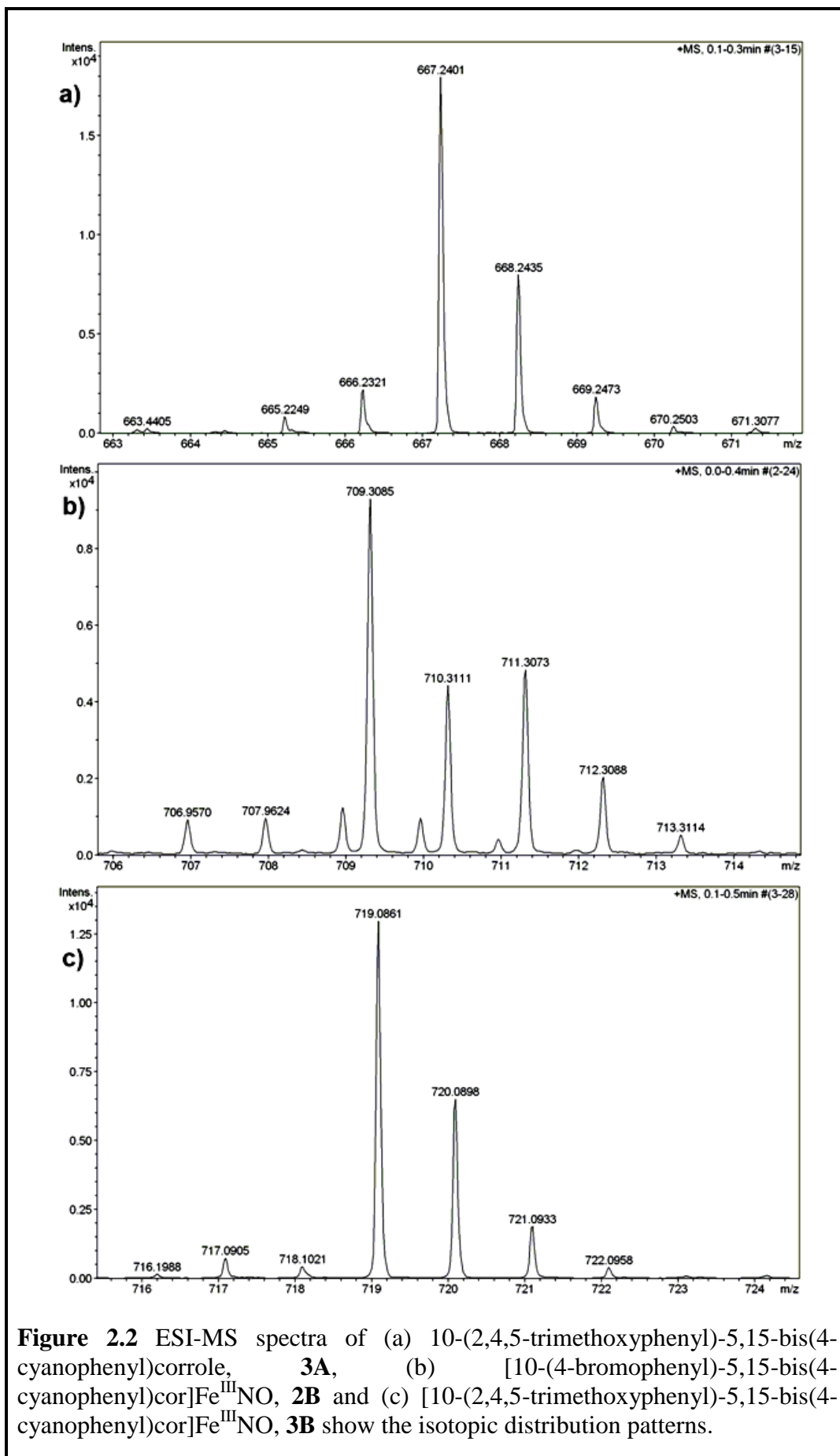
1B, **2B**, and **3B** were formed. Purity and identity of the free base corroles and the corresponding $[(\text{cor})(\text{FeNO})^6]$ derivatives have been demonstrated by their satisfactory elemental analyses, IR spectroscopy data, and by the electrospray mass spectra.

2.2.2 Spectral Characterization

2.2.2.1 Mass Spectroscopy

The electrospray mass spectra of the newly synthesized free base corroles in acetonitrile, **2A** and **3A** exhibit characteristic peaks at $m/z = 656.724$ corresponding to $[\mathbf{2A+H}]^+$ (calculated molecular mass: 655.544) and $m/z = 667.21$ corresponding to $[\mathbf{3A+H}]^+$ (calculated molecular mass: 666.230) respectively (Figures 2.1 and 2.2a). The mass spectroscopic data for **1A** was found to be at par with that reported previously^{46, 186}. The electrospray mass spectrum of **1B** in chloroform matched well with the earlier reported data¹⁰⁷. The electrospray mass spectrum of **2B** in acetonitrile (Figure 2.2b) shows peaks centered at $m/z = 709.308$ corresponding to $[\mathbf{M}^+-\text{NO}]$ (calculated molecular mass: 708.365). The electrospray mass spectrum of **3B** in





acetonitrile (Figure 2.2c) shows peaks centered at $m/z = 719.09$ corresponding to $[M^+ - NO]$ (calculated molecular mass: 719.14).

2.2.2.2 Infra-Red Spectroscopy

All the reported nitrosyl derivatives, **1B**, **2B** and **3B**, were subjected to FTIR spectral analysis in the form of KBr pellets. Distinct NO vibrations were observed at 1773, 1774 and 1772 cm^{-1} for **1B**, **2B** and **3B** respectively (Figure 2.3).

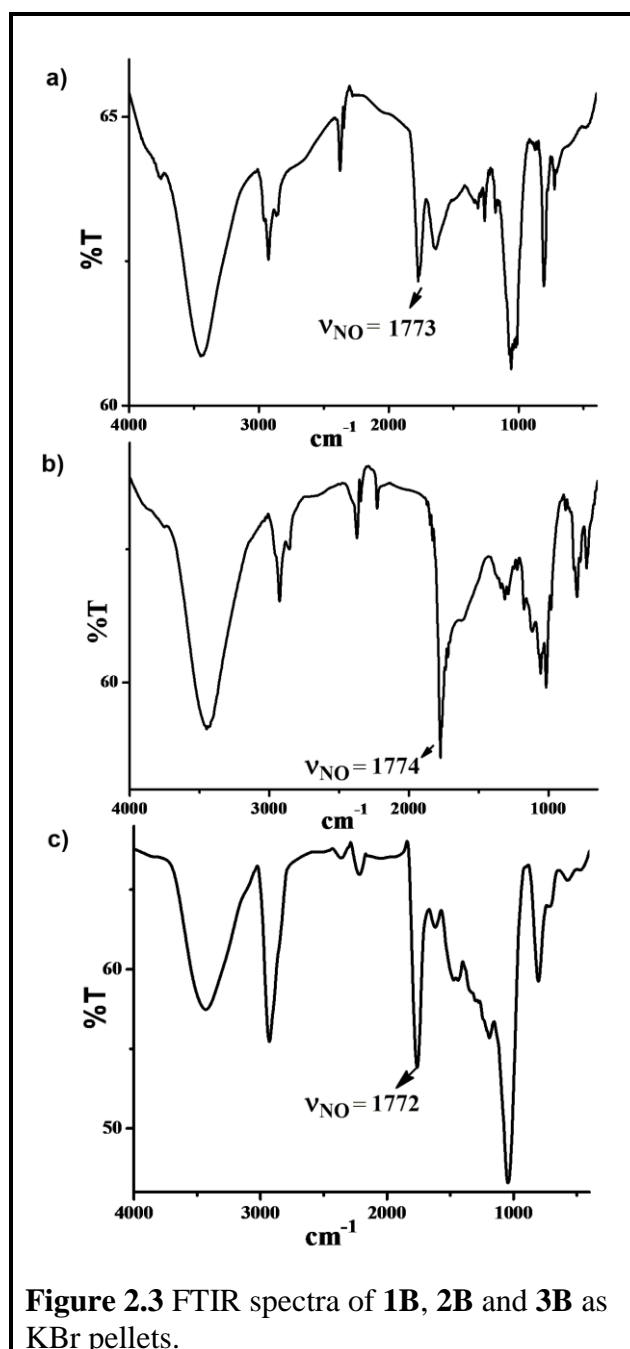
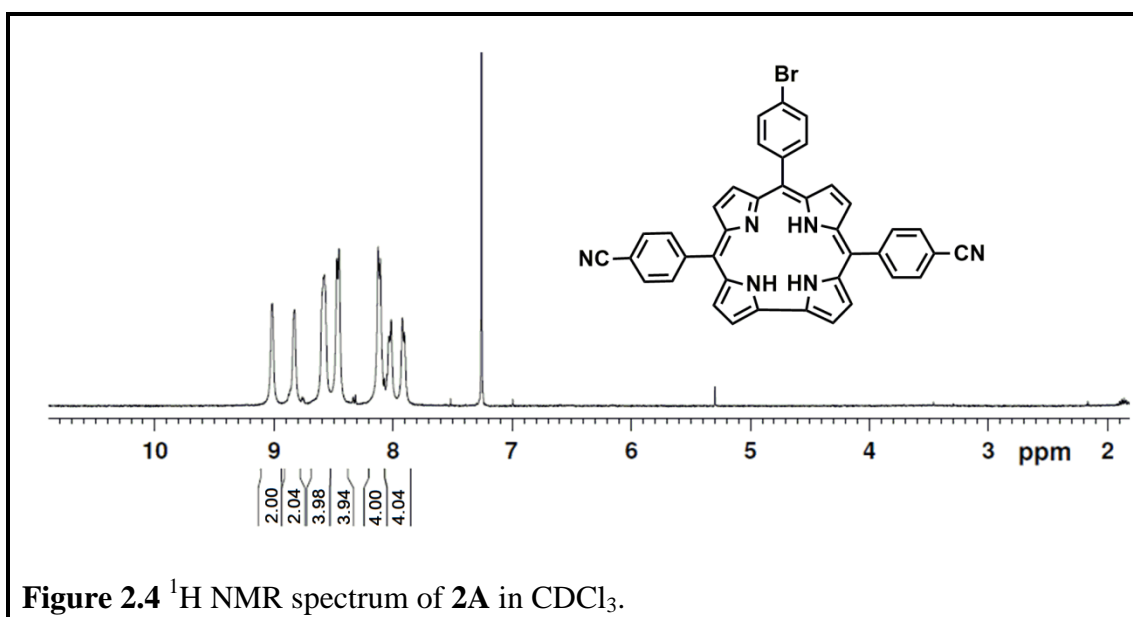
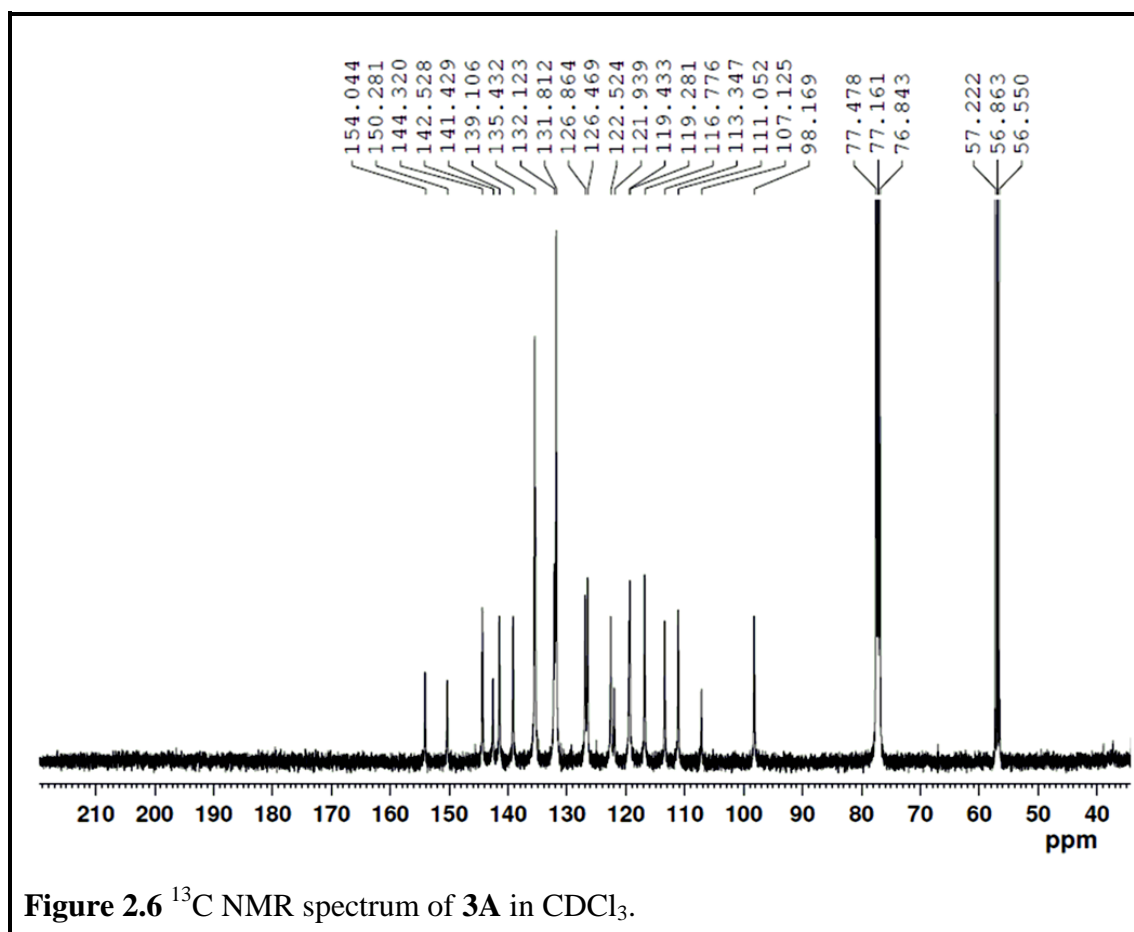
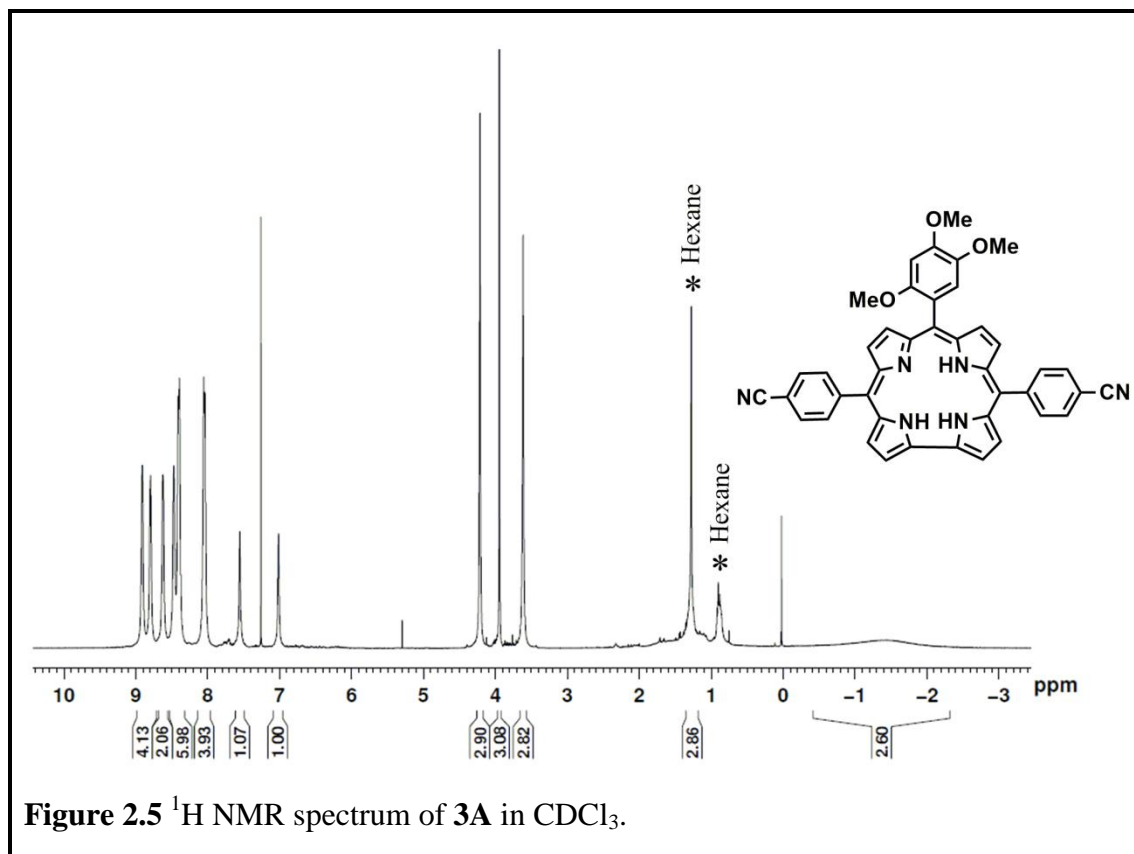


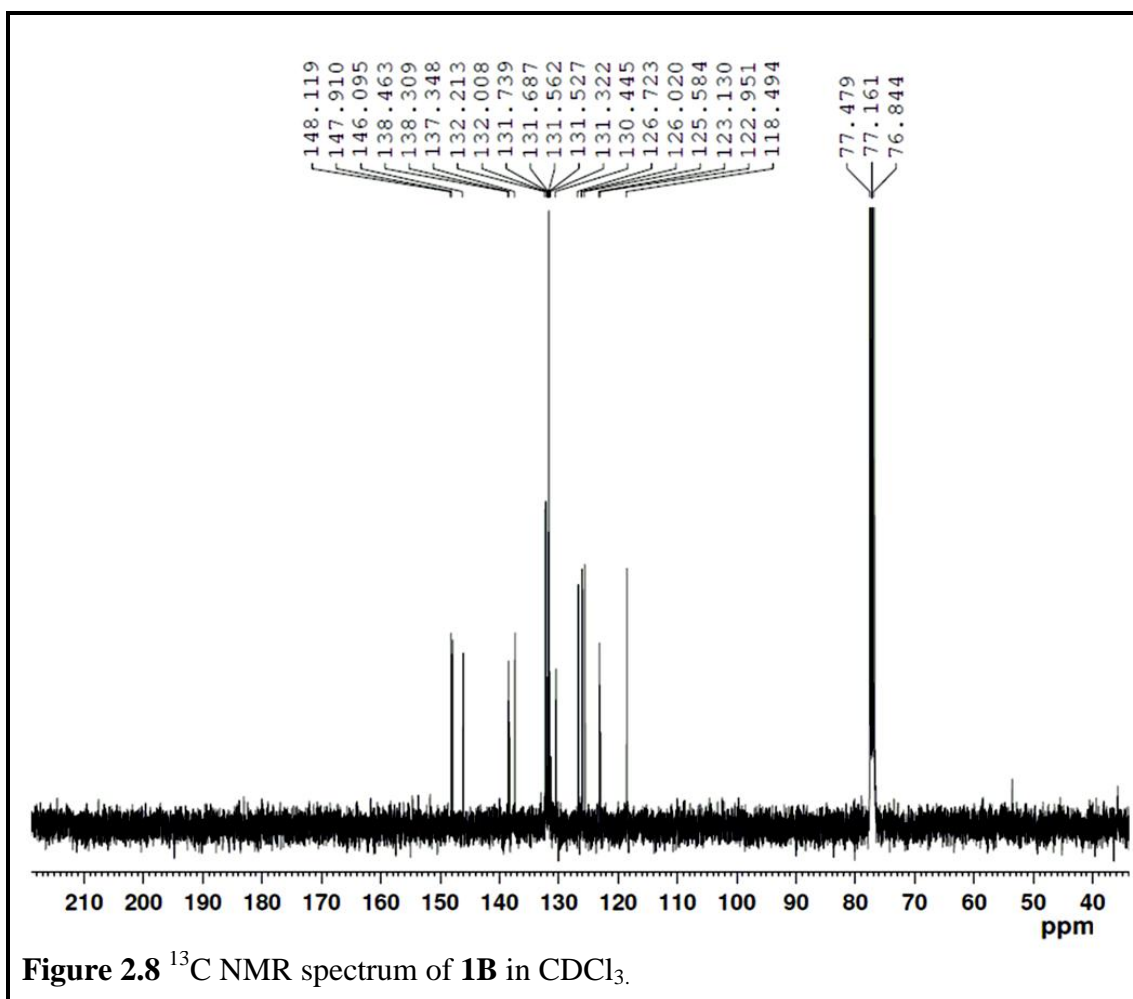
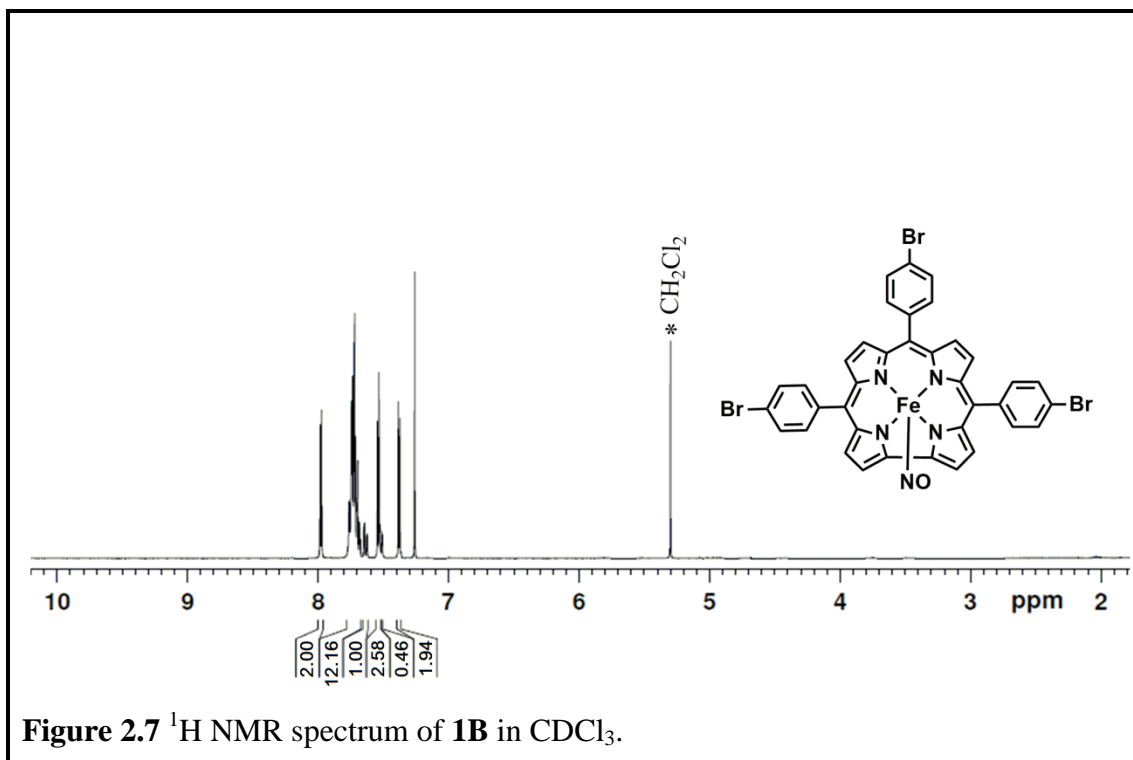
Figure 2.3 FTIR spectra of **1B**, **2B** and **3B** as KBr pellets.

2.2.2.3 NMR Spectroscopy

The proton resonances for **1A** match very well with the earlier reported chemical shift values ¹⁸⁶. In case of **2A**, peaks corresponding to twenty aromatic protons are observed in the region of δ , 9.06–7.92 ppm (Figure 2.4). The free base corrole **3A** was easily identified by eighteen partially overlapping aromatic protons in the region of δ , 8.91–7.02 ppm and three singlets appear in the region of δ , 4.22–3.62 ppm corresponding to the three types of nine methoxy protons (Figure 2.5). ¹³C NMR experiment for **3A** depicts the presence of twenty-three signals only (Figure 2.6). The ¹H NMR spectrum of **1B** exhibits sharp peaks in accordance with twenty partially overlapping aromatic protons in the region δ , 8.0–7.3 ppm (Figure 2.7). Out of these signals three doublets ($\delta = 7.98, 7.38, 7.53$ ppm) are easily distinguishable with characteristic coupling constants $J = \sim 5.0$ Hz. On the basis of earlier observations ³¹, these doublets can be assigned to β -pyrrolic hydrogen atoms. Another doublet is



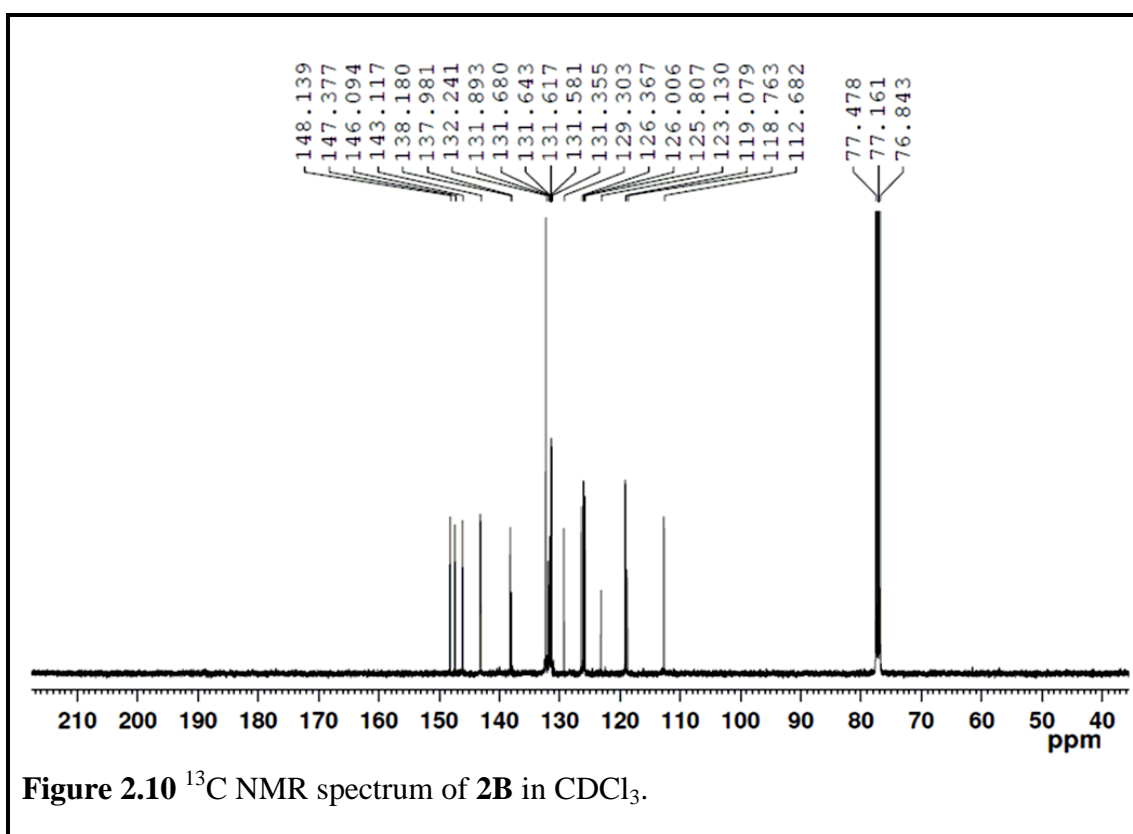
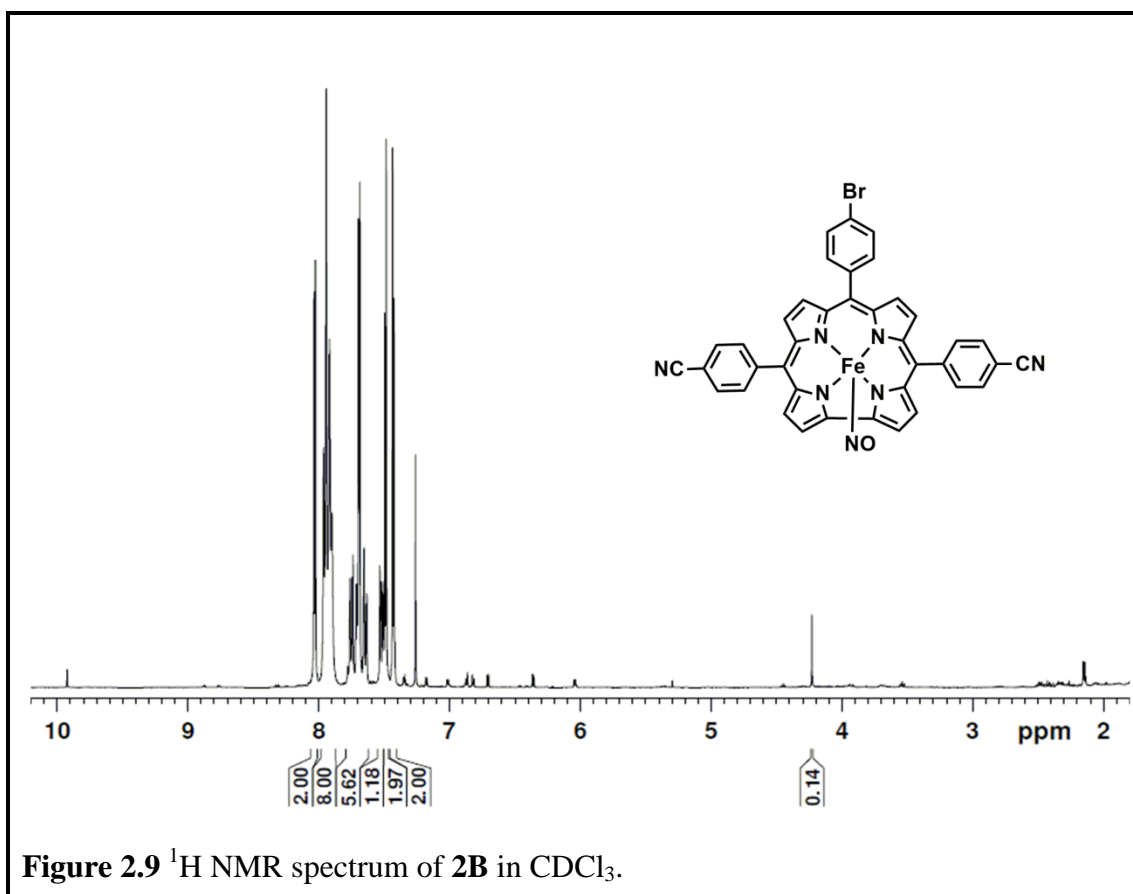




overlapped with the aryl ring protons. The aryl ring protons are observed at 7.76-7.50 ppm region. ^{13}C NMR spectrum shows the presence of the expected twenty signals (Figure 2.8). The ^1H NMR spectrum of **2B** exhibits the expected number of twenty partially overlapping aromatic protons in the region $\delta = 8.04$ -7.4 ppm (Figure 2.9). Out of these signals two doublets ($\delta = 8.04, 7.44$ ppm) are easily distinguishable with characteristic coupling constants $J = \sim 5.0$ Hz. These doublets are assigned as β -pyrrolic hydrogen atoms. Two more doublets are overlapped with the aryl ring protons. The aryl ring protons are observed at 7.96-7.48 ppm region. ^{13}C NMR spectrum (Figure 2.10) shows the presence of the expected twenty-one signals. The ^1H NMR spectrum of **3B** shows sharp resonances corresponding to eighteen partially overlapping aromatic protons in the region $\delta, 8.18$ -6.9 ppm (Figure 2.11). Nine methoxy protons appear in the region of 3.95-3.55 ppm. ^{13}C NMR spectrum (Figure 2.12) shows the presence of expected thirty-eight signals due to complete asymmetric nature of the molecule. Out of those thirty-eight signals three methoxy group signals ($\delta = 56.38, 56.00$ and 55.51 ppm) can be easily distinguished by their characteristic chemical shifts. All the signals in the $[(\text{cor})(\text{FeNO})^6]$ derivatives show upfield shift compared to free base corroles. The ^1H and ^{13}C NMR data thus unequivocally establish the diamagnetic nature of the iron complexes **1B-3B**.

2.2.2.4 X-Ray Crystallography

The crystal structures of **1B** and **2B** are shown in Figure 2.13 and Figure 2.14 respectively. The crystal system is triclinic for **1B** and monoclinic for **2B**. The unit cell of **1B** contains two molecules and that of **2B** contains eight molecules. Important crystallographic parameters are presented in Table 2.1. The DFT calculated bond



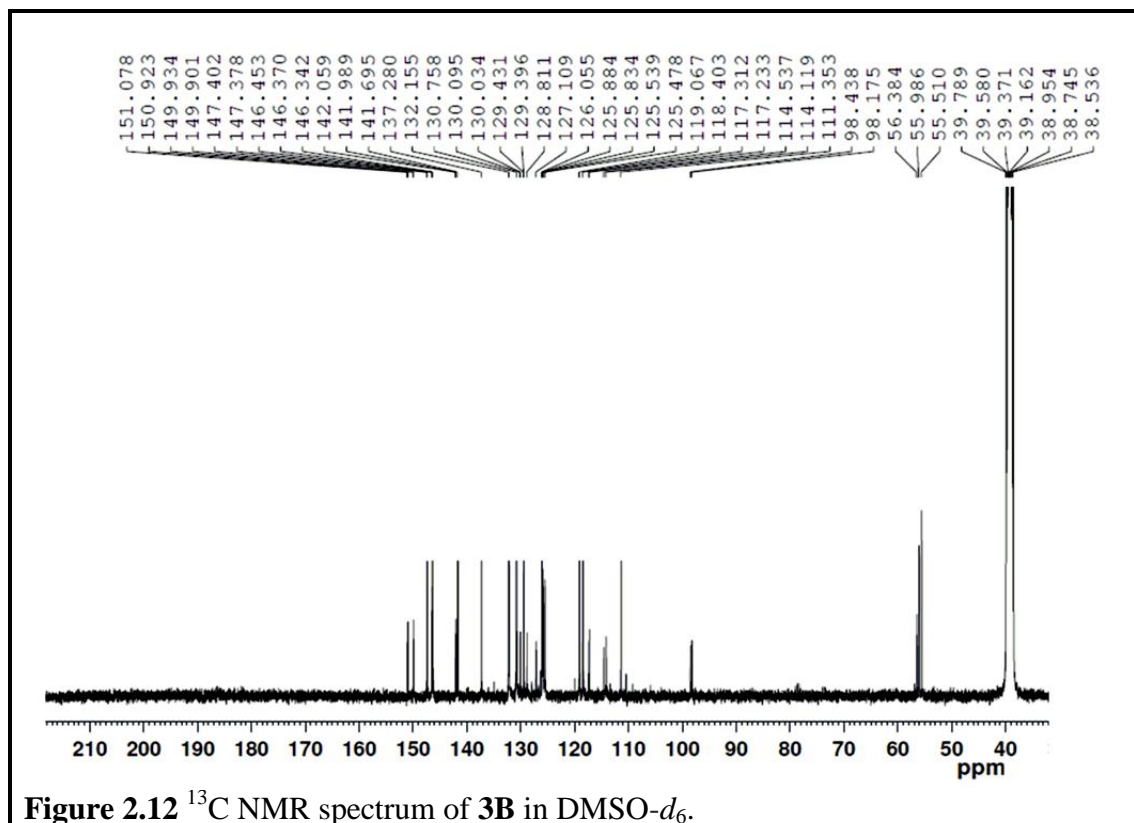
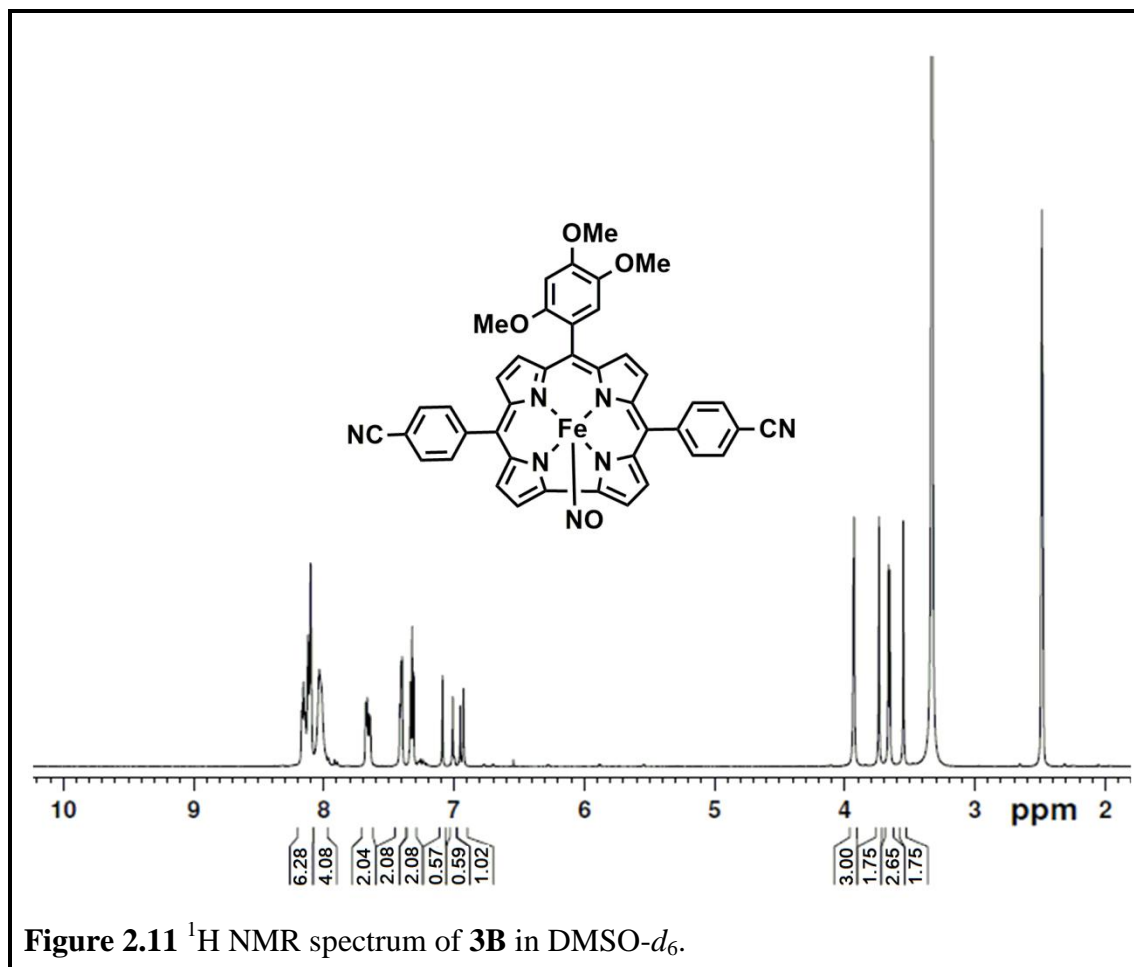


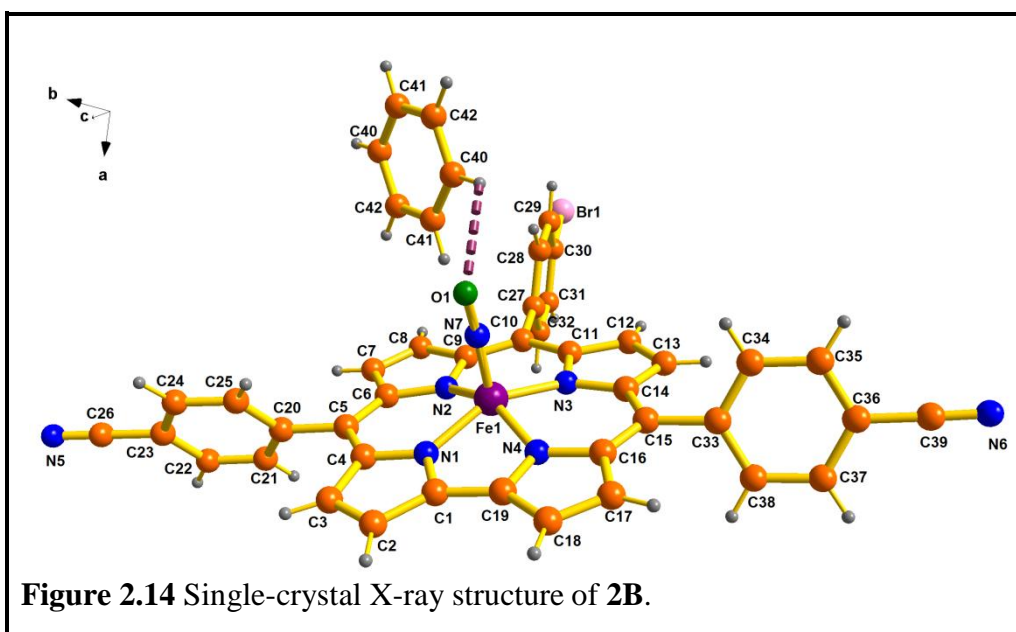
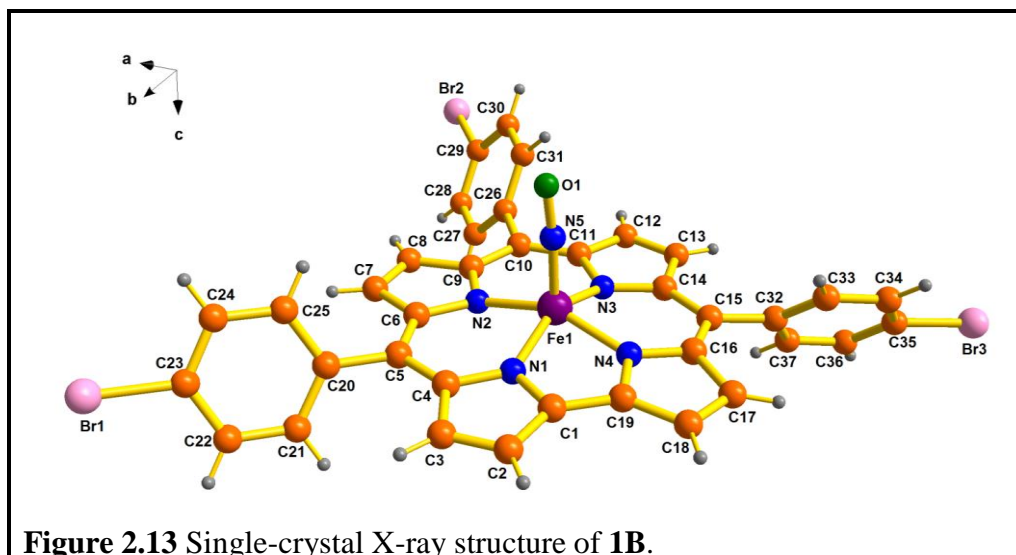
Table 2.1 Crystallographic Data for **1B** and **2B**

Compound Name	1B	2B
Molecular formula	C ₃₇ H ₂₀ Br ₃ FeN ₅ O,CH ₂ Cl ₂	C ₃₉ H ₂₀ BrFeN ₇ O,C ₆ H ₆
Formula weight	931.09	816.49
Radiation	MoK α	MoK α
Crystal symmetry	Triclinic	Monoclinic
Space group	<i>P</i> - 1	<i>C</i> 1 2 / <i>c</i> 1
<i>a</i> (Å)	10.5391(6)	34.2226(6)
<i>b</i> (Å)	12.3467(7)	8.6007(10)
<i>c</i> (Å)	14.4850(8)	25.0044(4)
α (deg)	69.869(4)	90
β (deg)	85.551(4)	96.839(2)
γ (deg)	79.549(4)	90
<i>V</i> (Å ³)	1740.09(17)	7307.39(19)
<i>Z</i>	2	8
μ (mm ⁻¹)	4.072	1.554
<i>T</i> (K)	293(2)	296(2)
<i>D</i> _{calcd} (g cm ⁻³)	1.777	1.484
2 θ range (deg)	4.84 to 61.22	4.88 to 57.48
<i>e</i> data (<i>R</i> _{int})	10579 (0.0586)	9435 (0.0493)
<i>R</i> 1 (<i>I</i> > 2 σ (<i>I</i>))	0.0658	0.0564
<i>wR</i> 2	0.1680	0.1291
GOF	1.045	1.032
Largest diff. peak and hole (e Å ⁻³)	3.488 and -1.495	2.617 and -1.634
CCDC No.	959930	959931

distances and angles match fairly well with the experimental values for **2B** (Table A2.1, see Appendix). In **1B**, iron is penta-coordinated and surrounded by five nitrogen atoms. The geometry around the iron is distorted square pyramidal. The Fe–N distances are 1.9059(4), 1.929(4), 1.921(4), and 1.898(4) Å respectively and are typical for low-spin iron(III). The N–Fe–N bond angles are 87.44(17)°, 93.18(18)°,

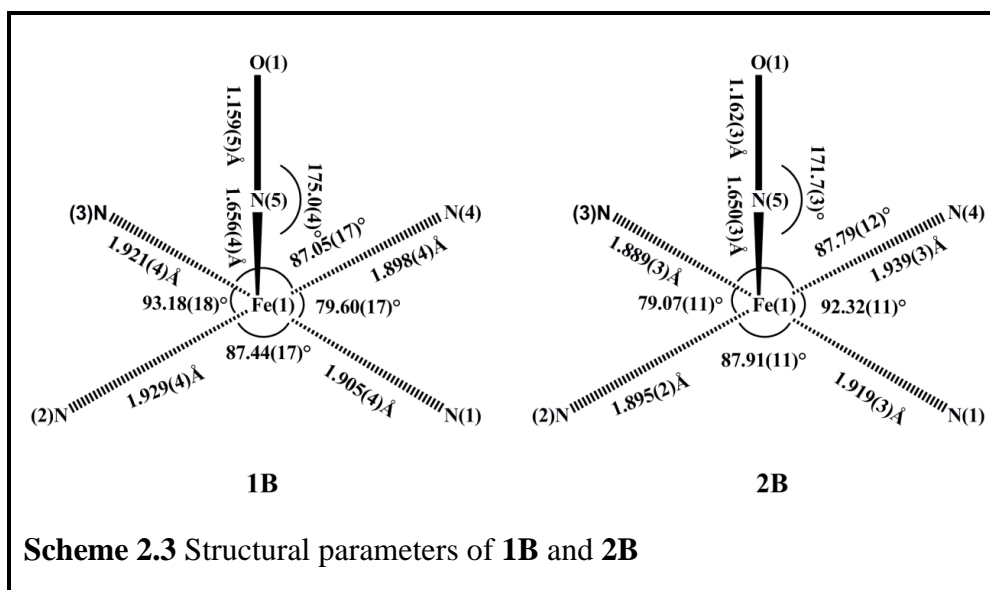
87.05(17)°, and 79.60(17)°. The Fe—N—O bond angle, 175.0(4)° justifies calling it as a linear nitrosyl. The Fe—N (NO) bond distance, 1.656(4) Å points towards a significant Fe^{III} → NO back bonding. The NO bond length, 1.159(5) Å depicts its elongated character (Scheme 2.3 and Table 2.2). The iron atom is elevated from the peripheral 19-atom corrole carbon ring by 0.512(9) Å to give rise to a domed conformation. This leads to a consequent deviation of the pyrrole ring nitrogen atoms from the 19-atom corrole carbon ring by distances ranging from 0.018-0.140 Å. The *meso*-substituted phenyl rings are tilted with respect to the mean corrole plane (considered as the 19-atom corrole carbon ring) by dihedral angles ranging from 58.05-61.68°. In **2B**, iron is penta-coordinated and surrounded by five nitrogen atoms. The geometry around the iron is distorted square pyramidal. Distance of iron(III) from mean corrole plane is 0.516 (5) Å. The Fe—N distances are 1.919(3) (DFT: 1.927 Å), 1.895(2) (DFT: 1.902 Å), 1.889(3) (DFT: 1.901 Å), and 1.939(3) (DFT: 1.932 Å) Å (Table A2.1, see Appendix) and are typical for low-spin iron(III). The N—Fe—N bond angles are 87.91(11)° (DFT: 87.72°), 79.06(12)° (DFT: 79.45°), 87.82(12)° (DFT: 87.59°), and 92.32(11)° (DFT: 93.10°). The Fe—N—O bond angle, 171.70(3)° (DFT: 179.94°) justifies calling it as a linear nitrosyl. The Fe—N(NO) bond distance, 1.650(3) Å (DFT: 1.597 Å) points towards a significant Fe^{III}→NO back bonding. The N—O bond length, 1.162(3) Å (DFT: 1.162 Å) (Table A2.1, see Appendix) depicts its elongated character.

Because of the square-pyramidal geometry around the central metal atom, the nitrogen atoms of the pyrrole rings in the macrocycle **2B** are alternately tilted up and down the mean corrole plane by a range of 0.0367-0.0873 Å. This prominent saddling

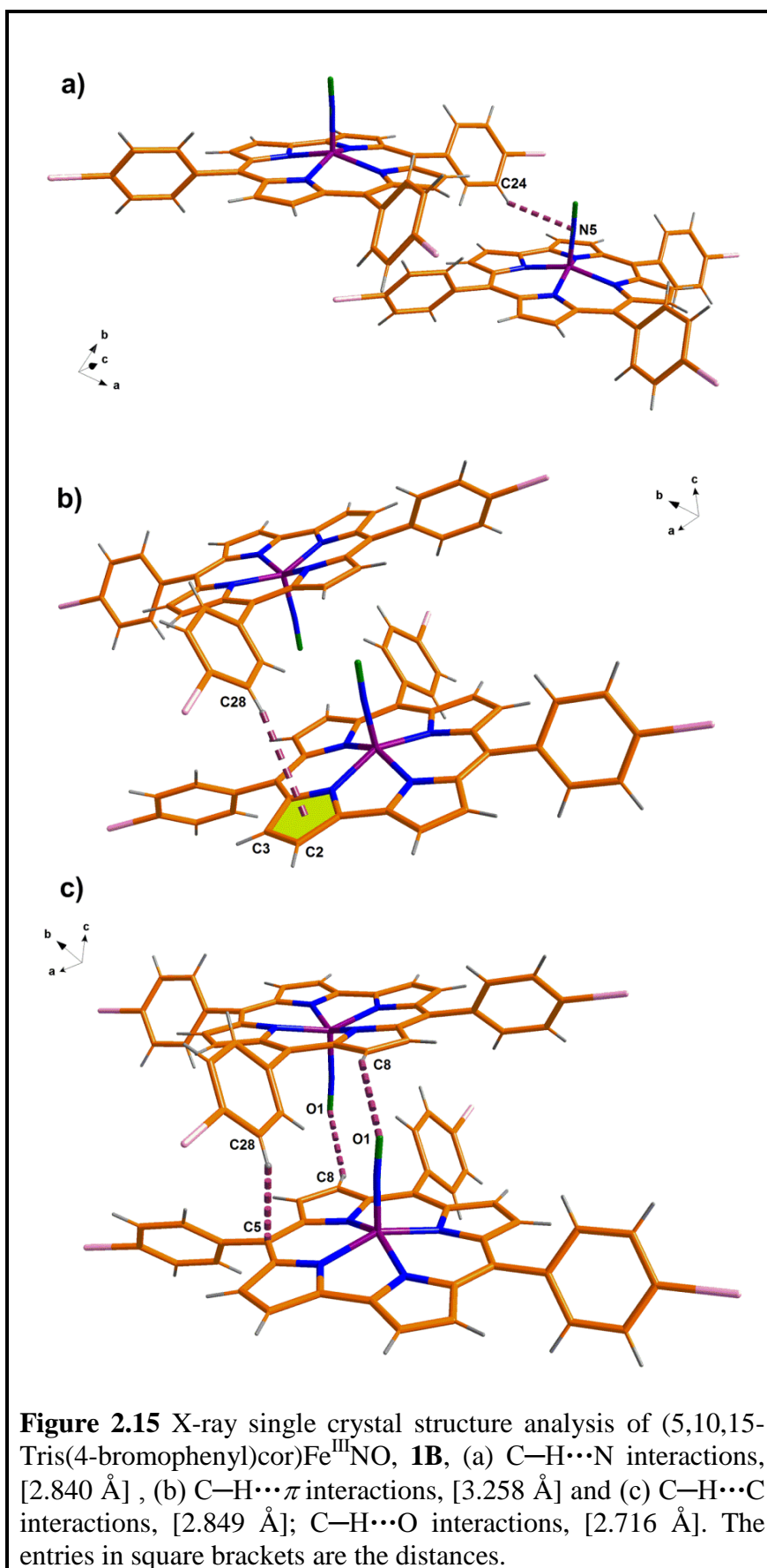


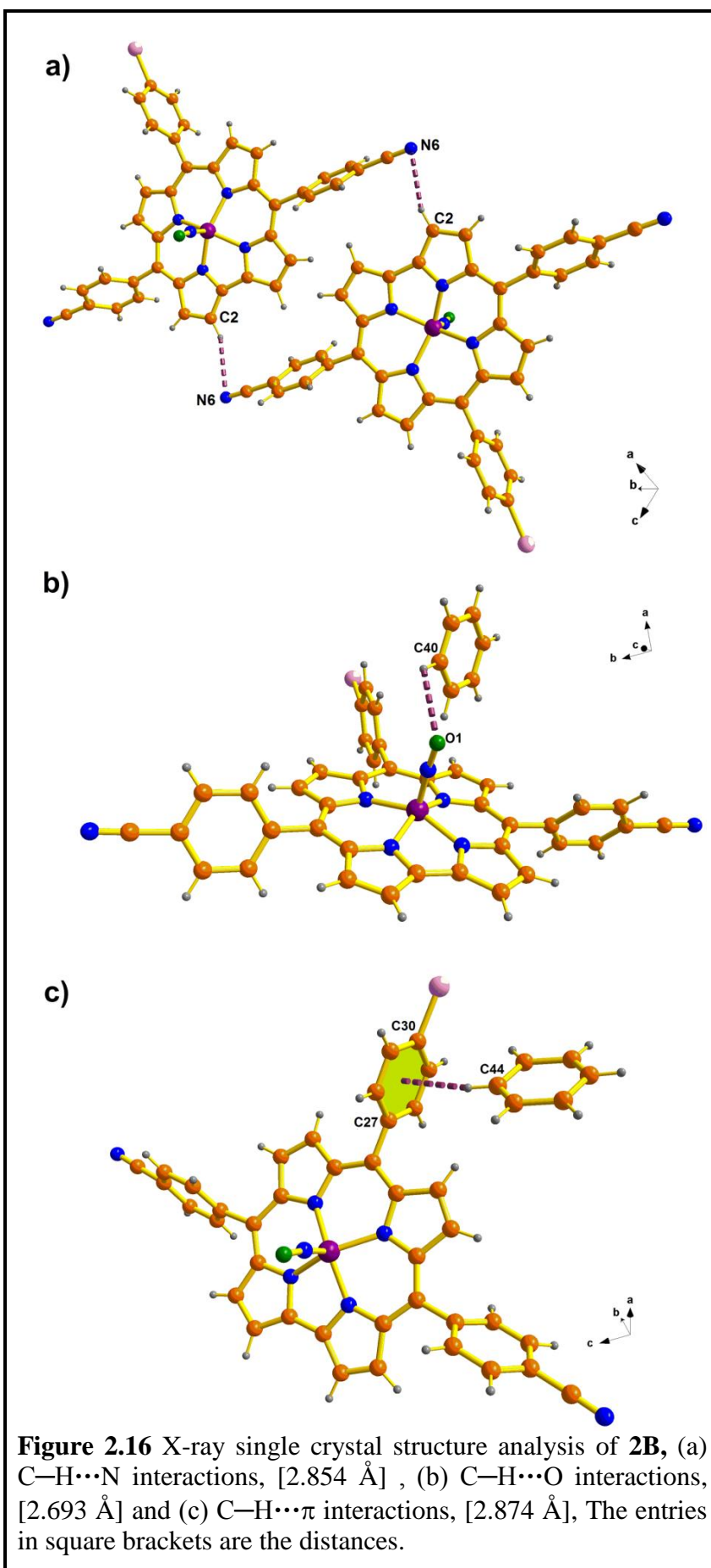
effect in the corrole ring of **2B** is also consistent with the alternate deviation of the dihedral angles between the pyrrole rings with the mean corrole plane, which lie between 1.906-4.925°. The substituted phenyl rings at the *meso*-positions of the corrole rings are placed at angles varying from 65.04- 80.54° with respect to the mean corrole plane.

The comparison of all these structural parameters involving **1B** and **2B** with those of the [(cor)(FeNO)⁶] derivatives reported by others¹⁰⁴⁻¹⁰⁹ earlier clearly justifies the aforesaid discussions. In the packing diagram of both **1B** and **2B** between

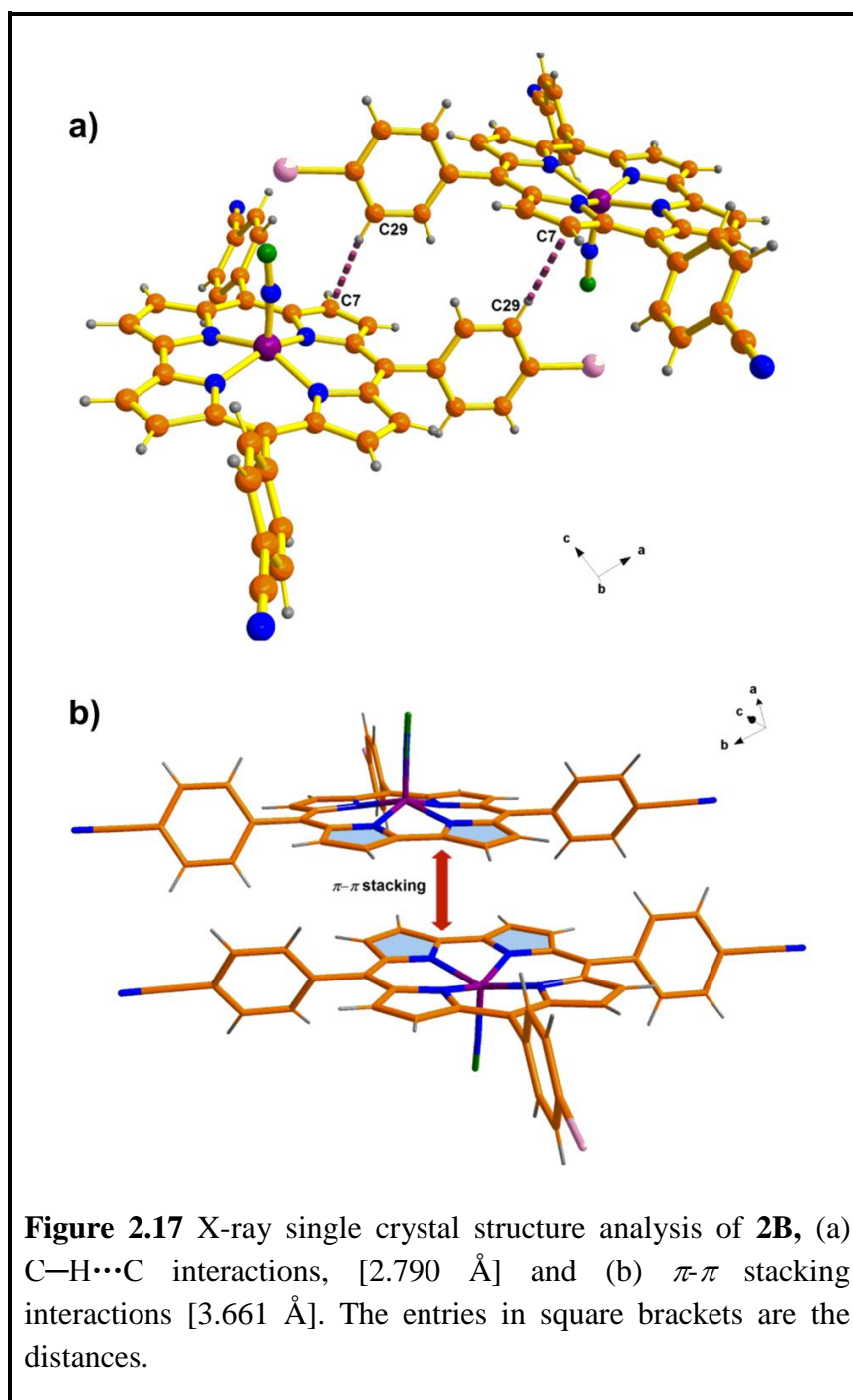


two neighboring molecules, NO groups are facing in opposite directions and the planes of the rings are approximately parallel. For **1B** the interplanar distance between two corrole planes is ~ 3.53 Å. The distance between two iron atoms is $7.0949(11)$ Å. For **2B**, the interplanar distance between two corrole planes is ~ 4.63 Å. The distance between two iron atoms is $8.60(7)$ Å. The crystal structure analyses of both the compounds **1B** (Figure 2.15) and **2B** (Figures 2.16 and 2.17) show several C—H \cdots N interactions, C—H \cdots C interactions, C—H \cdots O interactions, and C—H \cdots π interactions. **1B** molecules are stacked together and form layer-like arrangements throughout the crystal lattice (Figure 2.18). Similarly **2B** molecules are stacked together and form cylindrical tube-like arrangements throughout the crystal lattice. These tubes are filled with benzene molecules. Inside the tube, benzene molecules are interconnected through π - π stacking interaction (Figure 2.19). The closest atom distance between two neighboring [(cor)(FeNO) 6] molecules responsible for π - π stacking interactions is ~ 3.18 Å for **1B** and ~ 3.32 Å for **2B**. This clearly indicates that there is a reasonably strong adjacent parallel plane π - π stacking interaction between the [(cor)(FeNO) 6]





molecules. The shortest intermolecular distance between two [(cor)(FeNO)⁶] molecules responsible for C–H···O interactions, C–H···C interactions, C–H···N interactions, and C–H··· π interactions are close to ~ 2.716 Å, ~ 2.849 Å, ~ 3.01 Å and 3.258 Å respectively for **1B** and ~ 2.693 Å, ~ 2.790 Å, ~ 2.854 Å and 2.874 Å



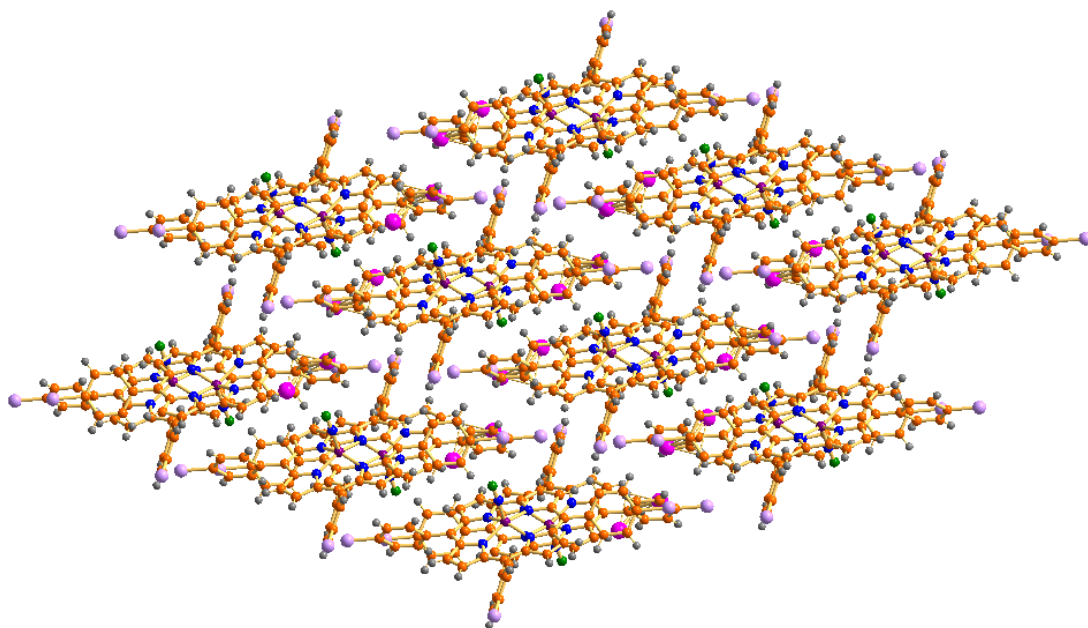


Figure 2.18 Packing diagrams of [5,10,15-tris(4-bromophenyl)cor]Fe^{III}NO, **1B**, viewed down the *c*-axis.

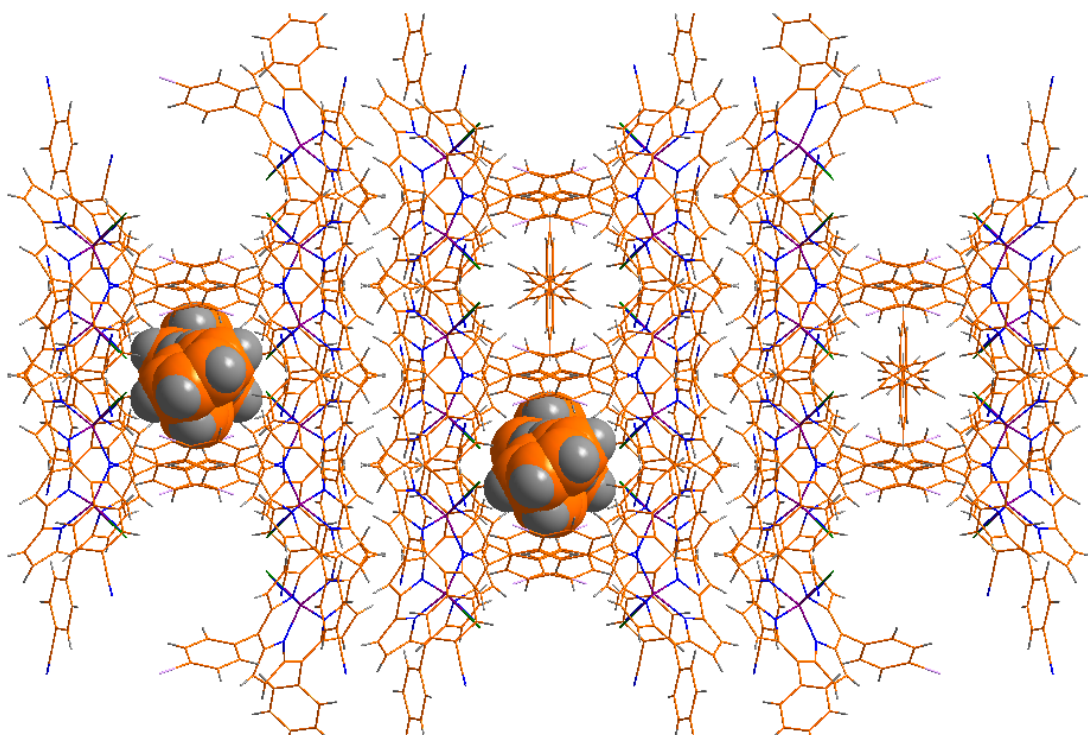


Figure 2.19 Packing diagrams of [10-(4-bromophenyl)-5,15-bis(4-cyanophenyl)cor]Fe^{III}NO, **2B**, viewed down the *b*-axis with π - π stacking interactions of 3.96 Å.

respectively for **2B**. This is quite clearly indicative of the fact that fairly strong intermolecular C—H $\cdots\pi$ interactions, C—H \cdots O, C—H \cdots N and C—H \cdots C interactions are also present between adjacent [(cor)(FeNO) 6] molecules. It has been assumed that the solid state structures are stable due to intermolecular parallel-displaced π - π stacking interactions, C—H $\cdots\pi$ interactions, C—H \cdots O, C—H \cdots N and C—H \cdots C interactions¹⁸⁷⁻¹⁹².

2.2.2.5 Electrochemistry

The redox properties of the **1B**, **2B** and **3B** were investigated in CH₂Cl₂/0.1 M TBAP by using cyclic voltammetric techniques and differential pulse voltammetric techniques (Figure 2.20 and Table 2.3). The oxidation processes at the positive side of Ag-AgCl reference electrode were recorded by using a platinum working electrode; a glassy-carbon working electrode was used for recording the reduction processes. All the three iron complexes **1B**, **2B**, and **3B** exhibited one reversible oxidative couple E_{298}^0, V (ΔE_p , mV): +0.54 (70) (**1B**), +0.58 (70) (**2B**), and +0.56(70) (**3B**) versus ferrocene/ferrocenium. They also showed one reversible reductive couple E_{298}^0, V (ΔE_p , mV): -0.67(70) (**1B**), -0.61(70) (**2B**), and -0.63(70) (**3B**) versus ferrocene/ferrocenium. The effect of the substituents in the corrolato ring on the redox potentials of the metal complexes is marginal. UV-Vis, IR, and EPR spectroelectrochemical investigations were done on both the oxidative couple and reductive couple to gain insights into the electronic structures of the various states.

Table 2.2 Comparison of Structural Parameters and NO Stretching Frequencies of (cor)(FeNO)⁶ Species having Electronic Configuration of (FeNO)⁶ Already Available in the Literature with **1B** and **2B**

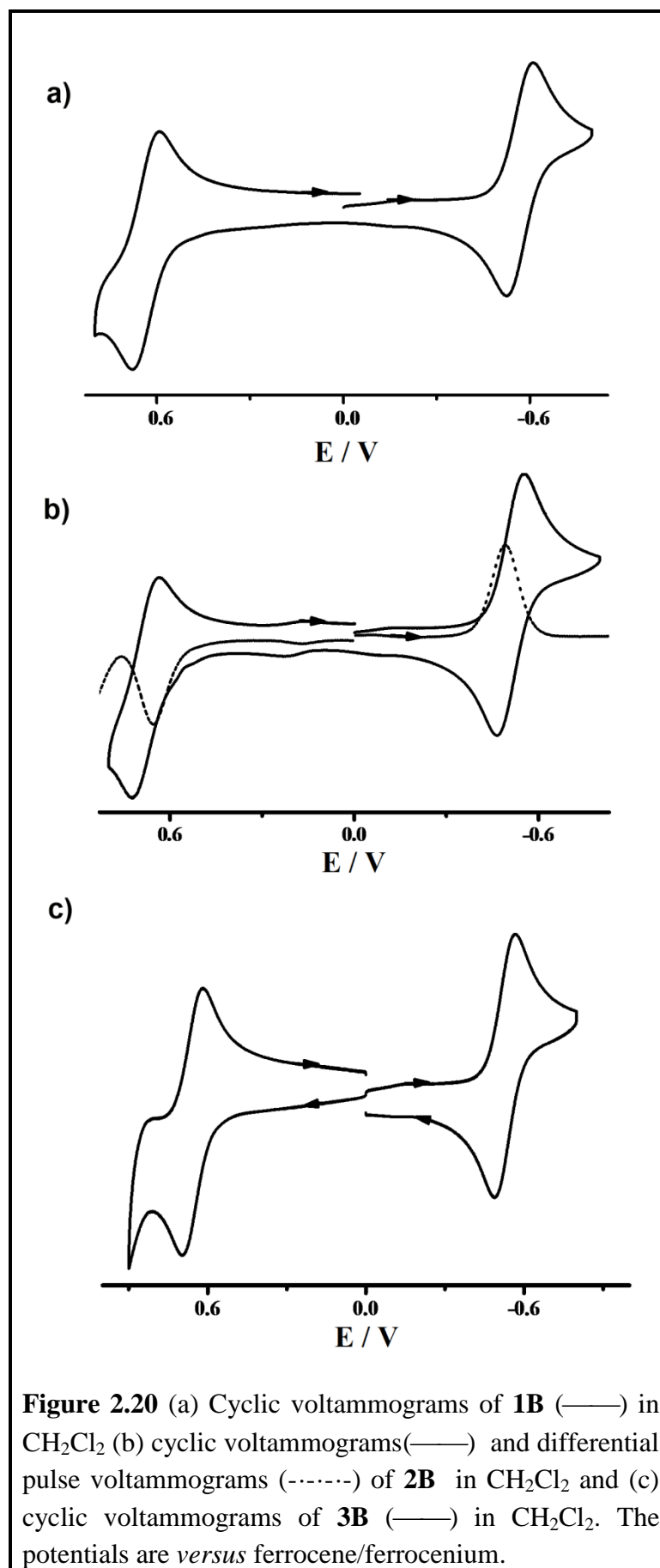
Compound ^a	Fe—NO Bond Distance (Å)	N—O Bond Distance (Å)	Fe—N—O Bond Angle (°)	NO Stretching Freq. (cm ⁻¹)	Ref.
(OEC)Fe(NO)	1.631(3)	1.171(4)	176.9(3)	1767	7(a)
(TMOPC)Fe(NO)	1.702(4)	1.076(4)	172.0(4)	1767	7(d)
(TTC)Fe(NO)	1.645(2)	1.162(2)	177.1(2)	1761	7(d)
(TDCC)Fe(NO)	1.641(4)	1.169(5)	172.3(4)	1783	7(f)
(TF ₅ PC)Fe(NO)	1.639(4), ^b 1.648(4)	1.166(4), 1.171(4)	177.3(4), 178.0(4)	1801	7(f)
(TNPC)Fe(NO)	1.675(14), ^b 1.648(11)	1.144(15), 1.154(13)	172.8(10), 173.3(9)	1778	7(d), 7(b)
1B	1.656(4)	1.159(5)	175.0(4)	1773	this work
2B	1.650(3)	1.162(3)	171.7(3)	1774	this work

^aOEC = octaethylcorrole, TMOPC = tris(*p*-methoxyphenyl)corrole, TTC = tris(*p*-methylphenyl)corrole, TDCC = tris(*o*-dichlorophenyl)corrole, TF₅PC = 5,10,15-Tris(pentafluorophenyl)corrole, TNPC = 5,10,15-Tris(4-nitrophenyl)corrole. ^bTwo crystallographically independent molecule exist in the asymmetric unit.

Table 2.3 Electrochemical Data^a

Compound	Electrochemical Data	
	Oxidation E^0 , V (ΔE_p , mV)	Reduction E^0 , V (ΔE_p , mV)
1B	0.54 (70)	-0.67(70)
2B	0.58 (70)	-0.61(70)
3B	0.56(70)	-0.63(70)

^aIn dichloromethane. The potentials are *versus* ferrocene/ferrocenium.



2.2.3 UV-Vis, IR and EPR Spectroelectrochemistry

Electronic spectral measurements for the compounds in CH_2Cl_2 were also performed. All the three complexes **1B**, **2B**, and **3B** exhibit Soret bands in the range of 385-395 nm. Another weak band in the range of 485-540 nm is observed in the visible region¹⁰⁴⁻¹⁰⁹. The molar absorption coefficient of the Soret bands is in the range of $(5.6-9.6) \times 10^4 \text{ M}^{-1}\text{cm}^{-1}$, and the molar absorption coefficient of the bands in the visible region is in the range of $(5.0-26.0) \times 10^3 \text{ M}^{-1}\text{cm}^{-1}$. Spectroelectrochemical measurements (UV-Vis, FTIR, and EPR) of all the nitrosyl derivatives were carried out in dichloromethane solvent at room temperature. These measurements were carried out to find the characteristic spectroscopic changes involved in all the accessible redox states of the complexes and to establish the site of electron transfer in the nitrosyl derivatives. Furthermore, these measurements were also helpful in elucidating the reversibility of the redox processes. UV-Vis, IR, and EPR spectroelectrochemical studies of all the three nitrosyl derivatives show similar pattern (Figures 2.21, 2.22 and 2.23). Hence one representative example (complex **3B**) will be discussed here. For rest of the complexes, data are presented in a tabular form (Tables 2.4, 2.5 and 2.6). Complex **3B** shows its Soret and Q bands at 391, 532, and 631 nm respectively (Figure 2.21).

On oxidation of **3B** to **3B**⁺ in dichloromethane/0.1 M BuN_4PF_6 using an OTTLE cell¹⁹³, the Soret band at 391 nm loses intensity, and two new bands appear at 365 nm and 397 nm (Figure 2.21a and Table 2.4). The initial Q bands lose its intensity, and new bands appear at 500 nm and 635 nm. The shift of the Soret and Q bands to lower energies is consistent with earlier literature reports^{104, 109}. Literature reports suggest that this kind of shifting of Soret and Q bands to lower energies are due to the formation of corrole radical cation or the formation of iron(IV) corrole¹⁰⁴,

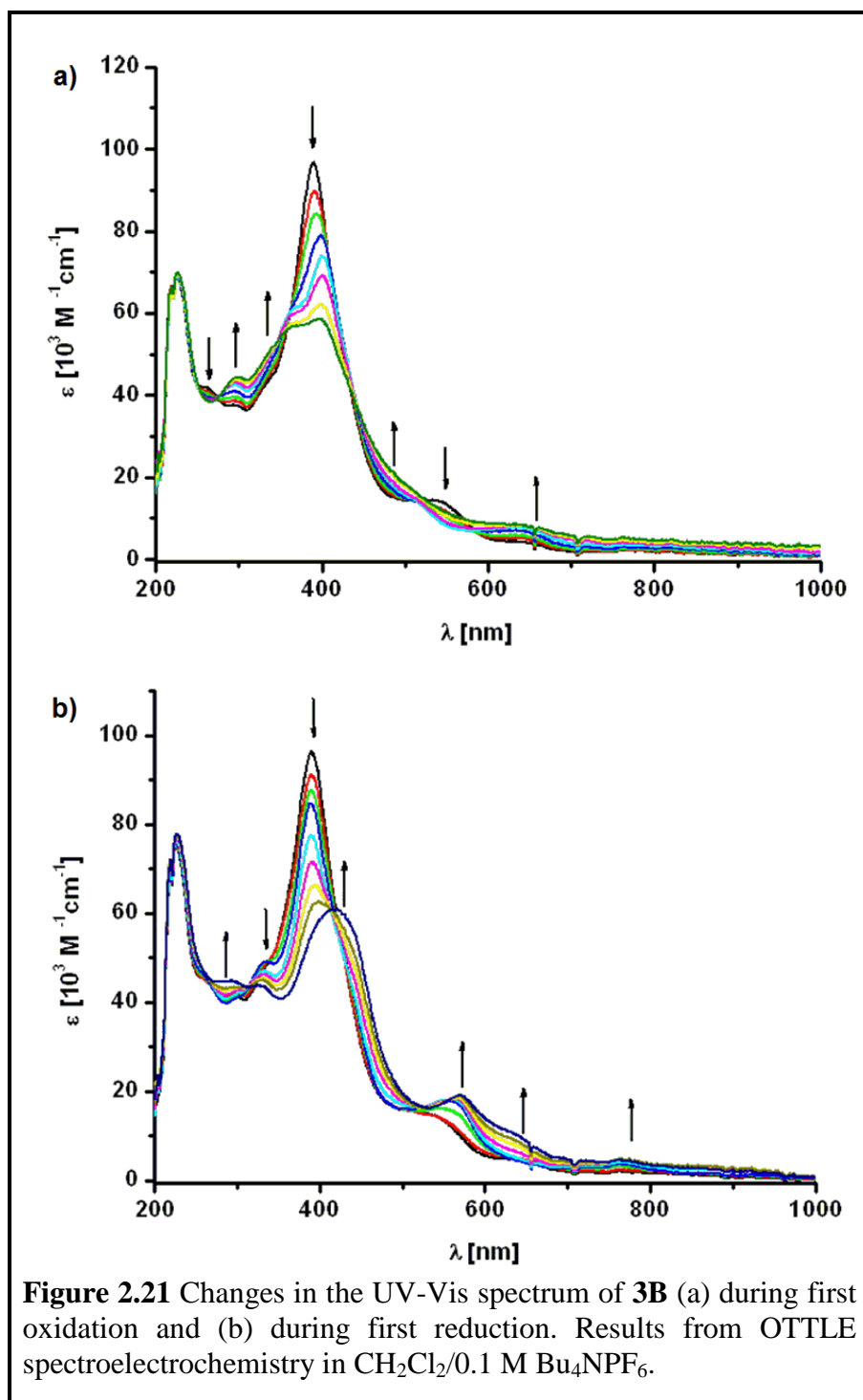
¹⁰⁹. On returning back to the initial potential, the native spectrum of **3B** was regained in band position and intensity to 100 %, thus confirming the reversibility of the oxidation process. The FTIR thin-layer spectroelectrochemical measurement of one electron oxidized species, **3B**^{•+} in dichloromethane/0.1 M BuN₄PF₆ was also performed (Figure 2.22a and Table 2.5). The shift of the ν_{NO} stretching frequency on one-electron oxidation occurs from 1782 cm⁻¹ to 1820 cm⁻¹ which corresponds to 38 cm⁻¹. This small shift is an indication of the (FeNO)⁶ unit remaining largely unaffected by the oxidation step, and the oxidation taking place on the corrolato ring. In order to get a direct proof of the location of the unpaired spin in the paramagnetic **3B**^{•+} form, EPR spectroscopy was performed on the electro-generated **3B**^{•+} in solution. The X-band EPR spectrum of **3B**^{•+} at 295 K in CH₂Cl₂/0.1 M Bu₄NPF₆ displays an isotropic signal centered at $g = 2.005$ with a peak to peak separation of about 15 G (Figure 2.23a and Table 2.6). The observation of the signal in fluid solution at 295 K, the closeness of the g -value to the free electron value of 2.0023, and the narrow line-width of only 15 G is a clear indication of the spin being predominantly localized on an organic ligand. The EPR result, taken together with the relatively small shift of the NO stretching frequency on moving from **3B** to **3B**^{•+} as observed in IR spectroelectrochemistry convincingly proves the generation of a corrole based radical upon one-electron oxidation of **3B**. The one electron oxidized form is thus best described as [(cor)²⁺(FeNO)⁶]^{•+}. It should be noted here that the EPR spectrum of the one-electron oxidized forms of related (cor)FeNO complexes measured at 120 K have been described in terms of a low spin iron(III) signal ^{104, 109}. For the present case, we have convincing data to prove the observation of a corrole radical signal by EPR spectroscopy. Since the literature reports also claim oxidation of the cor unit (from UV-Vis and IR spectroscopic experiments), it remains unclear as

to how the final EPR spectrum observed for the oxidized species originates from a low spin iron(III) center. In the starting complexes $[(\text{cor})^{3-}(\text{Fe}(\text{NO}))^6]$, the $(\text{FeNO})^6$ units are clearly diamagnetic. An oxidation of the corrole unit will generate a species $[(\text{cor})^{2-}(\text{Fe}(\text{NO}))^6]^{*+}$ which should logically possess a corrole centered spin. The only way to obtain a low spin iron(III)-type EPR signal for the $[(\text{cor})^{2-}(\text{Fe}(\text{NO}))^6]$ form would be for the NO centered spin and the $(\text{cor})^{2-}$ spin to couple antiferromagnetically, leaving a lone spin on iron(III). Considering the highly covalent nature of the Fe—NO bond, such a spin situation as stated above is unlikely. There are reports on the generation of porphyrin centered radicals on the oxidation of similar nitrosyl containing metal complexes of porphyrin¹⁹⁴.

Table 2.4 UV-Vis Data of **1Bⁿ**, **2Bⁿ** and **3Bⁿ** [*n* = -1, +1, 0] from Spectroelectrochemistry^a

Complex	λ_{max} [nm] (ϵ [$10^3 \text{ M}^{-1} \text{ cm}^{-1}$])
1B⁰	225 (70.3); 272 sh; 396 (85.0); 514 sh; 627 (4.5)
1B⁺	225 (70.3); 283 sh; 361 (58.0); 416 (57.4); 510 sh; 641 (8.0); 882 (3.8)
1B⁻	225 (69.8); 282 sh; 333 (41.9); 404 (64.6); 565 (16.6); 629 sh; 761 (4.9)
2B⁰	225 (40.1); 262 (24.7); 332 sh; 390 (56.2); 533 (8.5)
2B⁺	226 (40.1); 265 sh; 339 sh; 360 sh; 399 (38.0); 497 sh; 637 (3.7)
2B⁻	224 (42.1); 261 sh; 330 (24.1); 399 sh; 422 (40.7); 570 (12.0); 633 (7.0); 765 (2.1)
3B⁰	226 (69.0); 260 sh; 296 sh; 333 sh; 391 (96.8); 532 (14.5); 631 (4.6)
3B⁺	227 (70.1); 297 (44.2); 365 sh; 397 (58.6); 500 sh; 635 (8.4)
3B⁻	227 (78.0); 293 (44.9); 325 (43.9); 417 (60.9); 571 (19.1); 633 sh; 761 (4.7)

^aMeasurements in $\text{CH}_2\text{Cl}_2/0.1 \text{ M Bu}_4\text{NPF}_6$ (OTTLE spectroelectrochemistry).



On reduction of **3B** to **3B⁻** in dichloromethane/0.1 M BuN_4PF_6 using an optically transparent thin layer electrochemical (OTTLE) cell, the Soret band at 391 nm loses its intensity and is shifted to 417 nm (Figure 2.21b). The initial Q bands show a reduced intensity, and three new bands appear at 571, 633 and 761 nm. The shift of the Soret and Q bands to lower energies is also supported by earlier literature reports

¹⁰⁴, ¹⁰⁹. The FTIR thin-layer spectroelectrochemical measurement of one electron reduced species, $3\mathbf{B}^{\cdot-}$ in dichloromethane/0.1 M BuN₄PF₆ was also performed (Figure 2.22b). The shift of the ν_{NO} stretching frequencies occurs from 1782 cm⁻¹ to 1605 cm⁻¹, which corresponds to 177 cm⁻¹.

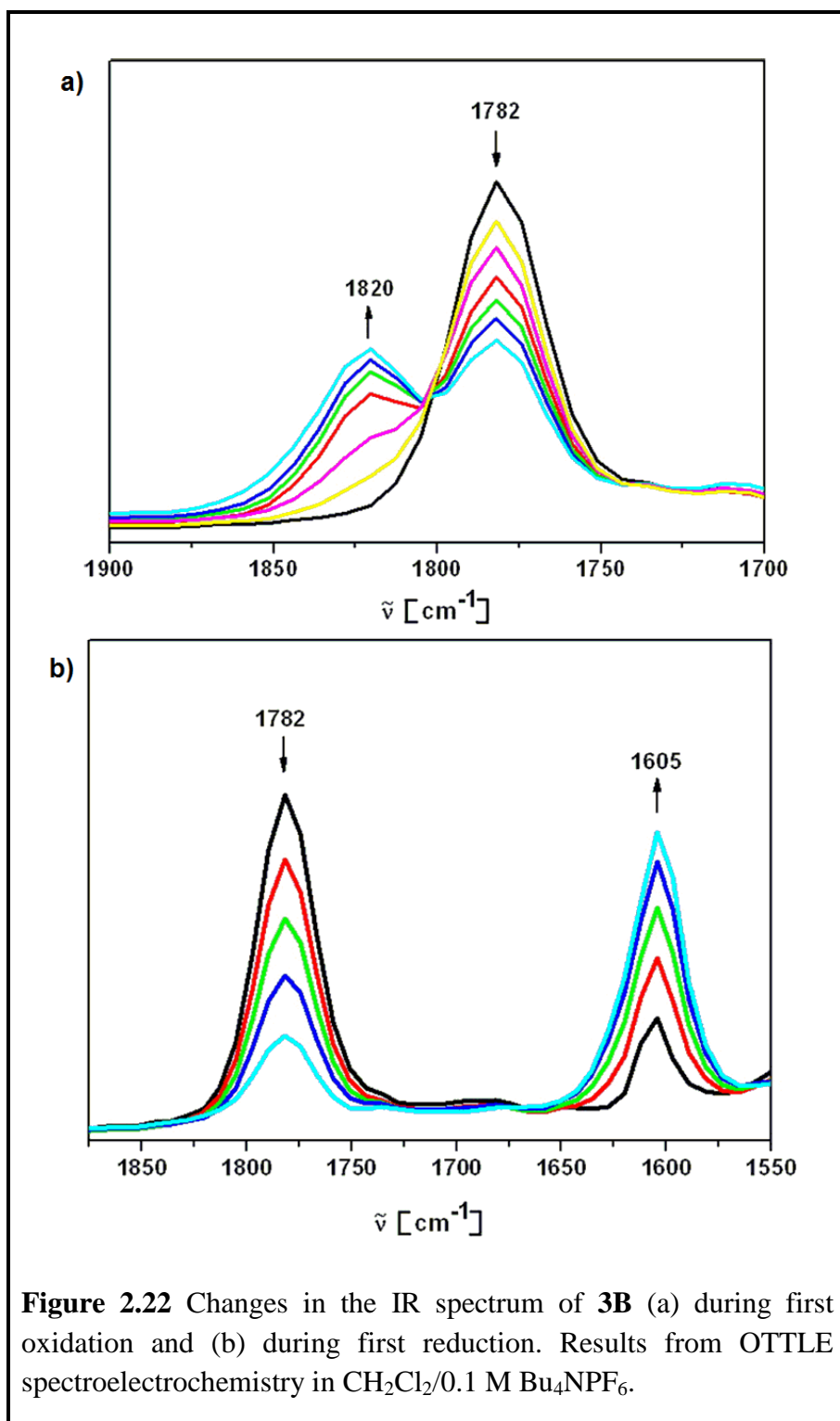


Figure 2.22 Changes in the IR spectrum of $3\mathbf{B}$ (a) during first oxidation and (b) during first reduction. Results from OTTLE spectroelectrochemistry in CH₂Cl₂/0.1 M Bu₄NPF₆.

As compared to the native state, the NO band is shifted to lower wavenumbers on reduction. On oxidation this band shifts to higher wavenumbers (see below). This opposite trend is a result of the different charges induced on the complex on reduction

Table 2.5 IR Data of $1B^n$, $2B^n$ and $3B^n$ [$n = -1, +1, 0$] from Spectroelectrochemistry^a

Complex	IR Data ^a $\nu_{N=O}$ (cm ⁻¹)
$1B^0$	1779
$1B^+$	1820
$1B^-$	1606
$2B^0$	1785
$2B^+$	1825
$2B^-$	1604
$3B^0$	1782
$3B^+$	1820
$3B^-$	1605

^aMeasurements in CH₂Cl₂/0.1 M Bu₄NPF₆ (OTTLE spectroelectrochemistry).

Table 2.6 EPR Data^a of Paramagnetic States^b

Complex	EPR Data ^a (g)
$1B^0$	
$1B^+$	2.002
$1B^-$	2.029; A(¹⁴ N) = 15.4 G
$2B^0$	
$2B^+$	2.003
$2B^-$	2.029 ; A(¹⁴ N) = 15.5 G
$3B^0$	
$3B^+$	2.005
$3B^-$	2.029; A(¹⁴ N) = 15.4 G

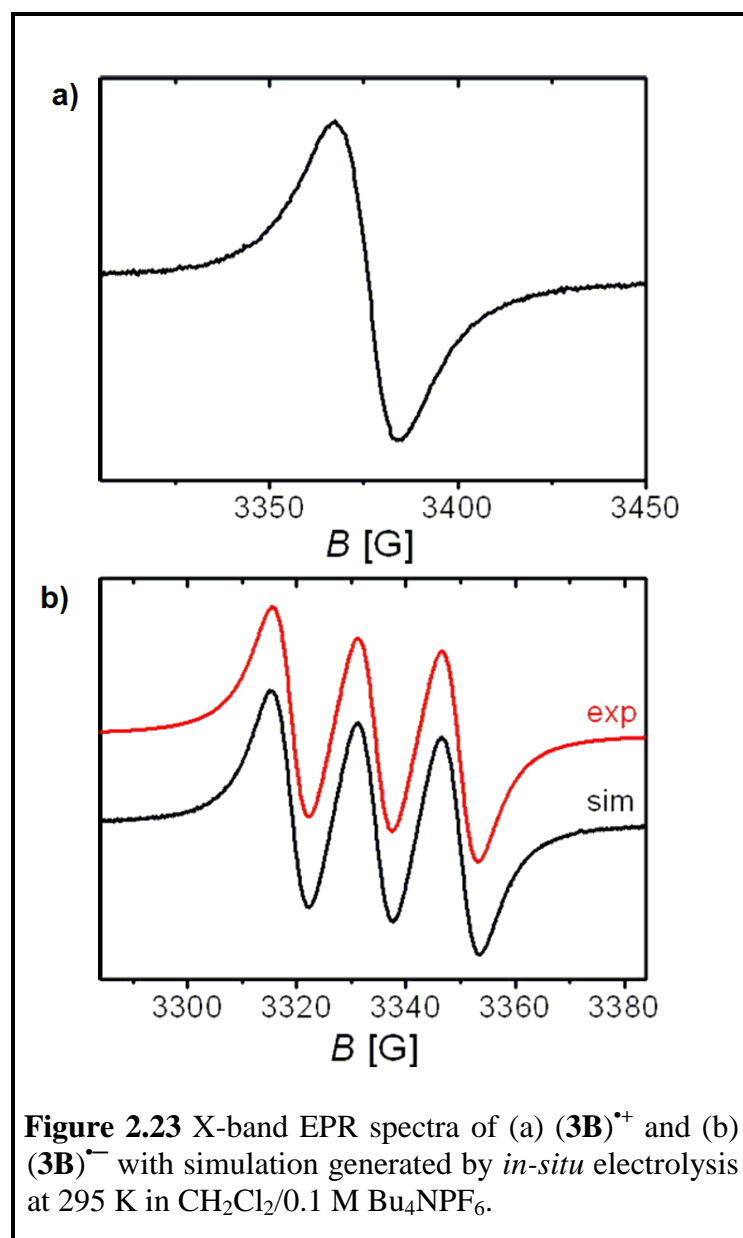
^ag values measured at 295 K. ^bFrom EPR spectroelectrochemistry in CH₂Cl₂/0.1 M Bu₄NPF₆.

and oxidation. The 177 cm^{-1} shift of the NO band to lower energies on reduction as compared to the native state is a direct indication that the (FeNO) unit is predominantly affected by this electron uptake. The IR results thus point to the formation of a complex $[(\text{cor})^3\text{-(FeNO)}^7]^{*-}$ on one electron reduction which contains a bent (FeNO)⁷ unit. EPR spectroscopy of the one-electron reduced form further strengthens this assignment.

The *in situ* generated one-electron reduced species $\mathbf{3B}^{*-}$ in $\text{CH}_2\text{Cl}_2/0.1\text{ M Bu}_4\text{NPF}_6$ at 295 K shows an isotropic signal centered at $g = 2.029$ in its X-band EPR spectrum. Furthermore, hyperfine coupling to one nitrogen nucleus ($I = 1$) is observed. The spectrum could be simulated with a $a(\text{N})$ value of 15.4 G. This signal is thus a direct proof of the spin being predominantly located in the (FeNO) part and hence the EPR spectrum of $\mathbf{3B}^{*-}$ corroborates its assignment as $[(\text{cor})^3\text{-(FeNO)}^7]^{*-}$ as has been stated above. Previous literature reports have drawn similar conclusions regarding the nature of the one-electron reduced form of such compounds^{104, 109}.

The above observations have been supported by detailed theoretical investigations. The energy obtained on open shell singlet optimization is lower than that for a triplet configuration or closed shell singlet state of $\mathbf{2B}$ which supports the anti-ferromagnetic coupling between the unpaired spins on iron(III) (d^5 -low spin, t_{2g}^5) and NO^\bullet . The 99% contribution of cor to the HOMO of $\mathbf{2B}$ (Table A2.2 and Figure A2.3, see Appendix) indicates that oxidation occurs from the corrole moiety which is further supported by the 95% and 96% contributions of cor to the α -SOMO and β -LUMO of $\mathbf{2B}^+$ respectively (Table A2.3 and Figure A2.4, see Appendix). This is also reflected in the increase in Fe-N(cor) bond lengths and shortening of C-N(cor) bond distances on moving from $\mathbf{2B}$ to $\mathbf{2B}^+$ as seen from their DFT optimized structures (Table A2.1, Figure A2.1, see Appendix). A further support arises from the spin

density distribution in $2\mathbf{B}^+$ (Fe: 1.969, NO: -1.020 , cor: 0.044; Table 2.7, Figure 2.24a) where an appreciable spin of 0.044 arises on the corrole moiety unlike the absence of spin on it in $2\mathbf{B}$. The fact that oxidation does not occur from NO is established by a negligible change in the $\nu(\text{N-O})$ frequency ($\Delta\nu \approx 40 \text{ cm}^{-1}$) on moving from $2\mathbf{B}$ (1785 cm^{-1} (exp.) and 1778 cm^{-1} (DFT)) to $2\mathbf{B}^+$ (1825 cm^{-1} (exp.) and 1822 cm^{-1} (DFT)) (Table 2.7, Figure A2.2, see Appendix). The 40%, 23% and 38% contributions of Fe, NO and cor to the HOMO of $2\mathbf{B}$ (Table A2.2, see Appendix) respectively collectively predict the possibility of reduction on any of the three



moieties although the α -SOMO and β -HOMO of $\mathbf{2B}^-$ having 76% and 96% contributions from cor respectively (Table A2.4 and Figure A2.5, see Appendix) predict the reduction taking place at the corrole moiety. The spin density distribution in $\mathbf{2B}^-$ of Fe: 2.192, NO: -1.202 and cor: 0.012 shows appreciable amount of spin residing on the Fe and NO (Table 2.7, Figure 2.24b). Moreover the appreciable lengthening of the N–O bond from 1.162 Å in $\mathbf{2B}$ to 1.196 Å in $\mathbf{2B}^-$ (Table A2.1, see Appendix) predicts that the reduction occurs at the NO. This is further supported by the $\sim 180\text{ cm}^{-1}$ decrease in the $\nu(\text{N-O})$ frequency on moving from $\mathbf{2B}$ (1785 cm^{-1} (exp.) and 1778 cm^{-1} (DFT)) to $\mathbf{2B}^-$ (1604 cm^{-1} (exp.) and 1613 cm^{-1} (DFT)) (Table 2.8, Figure A2.2, see Appendix). These DFT results showing the occurrence of reduction predominantly at NO are further proven by the experimentally obtained triplet EPR showing the hyperfine splitting due to the $I=1$ nuclear spin on ^{14}N which interacts with the spin of the unpaired electron on the NO. The experimentally obtained UV–Vis transitions of native species $\mathbf{2B}$, one electron oxidized species $\mathbf{2B}^+$, and one electron reduced species $\mathbf{2B}^-$ are in good agreement with the computed values (Table 2.9). For instance, $\mathbf{2B}$ displays intense ligand-to-ligand charge transfer (LLCT) transitions in the UV region ($\text{cor}(\pi) \rightarrow \text{cor}(\pi^*)$) at 225 nm and 262 nm (Table 2.9). The visible region transitions at 390 nm and 533 nm arise due to ligand-to-metal charge transfer (LMCT) transition ($\text{cor}(\pi) \rightarrow \text{Fe}(\text{d}\pi)$) (Table 2.9). The one-electron oxidized species $\mathbf{2B}^+$ exhibits LLCT transitions ($\text{cor}(\pi) \rightarrow \text{cor}(\pi^*)$) at 399 nm and 637 nm (Table 2.9). The one-electron reduced species $\mathbf{2B}^-$ shows metal-to-ligand charge transfer (MLCT) transition ($\text{Fe}(\text{d}\pi) \rightarrow \text{cor}(\pi^*)$) in the UV region at 330 nm (Table 2.9). In the visible region it displays LLCT bands at 422 nm ($\text{NO}(\pi)/\text{cor}(\pi) \rightarrow \text{cor}(\pi^*)$), 422 nm, 570 nm, 633 nm and 765 nm ($\text{cor}(\pi) \rightarrow \text{cor}(\pi^*)$) (Table 2.9).

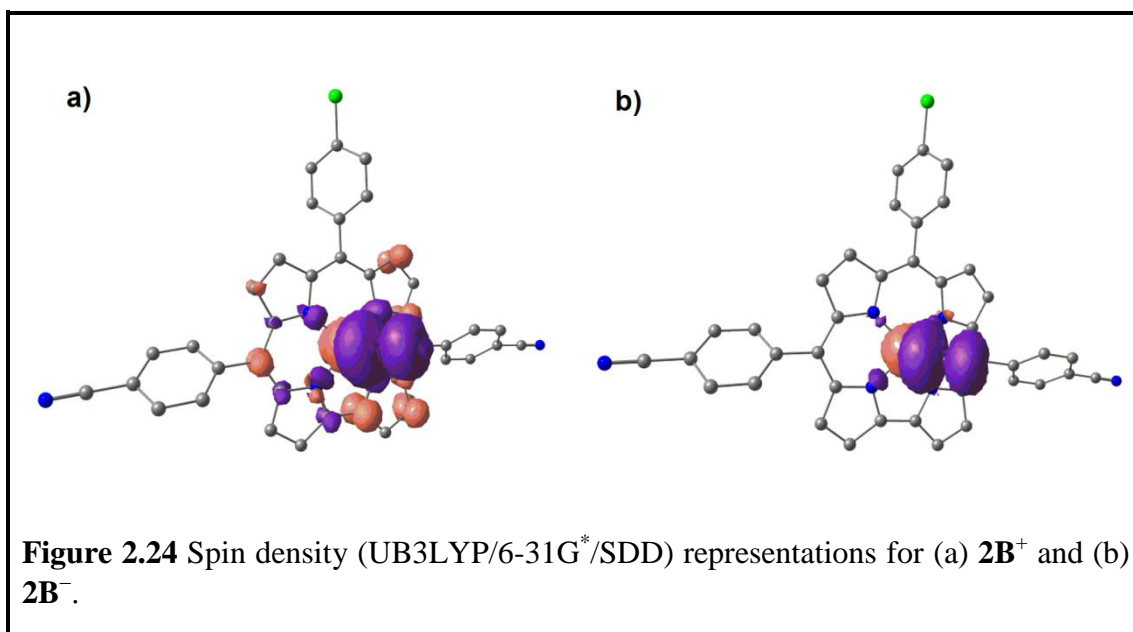


Table 2.7 DFT Calculated (UB3LYP/6-31G*/SDD) Mulliken Spin Densities for $2\mathbf{B}^n$ ($n = 1+, 1-$)

Complex	Fe	NO	cor
$2\mathbf{B}^+$ ($S=1/2$)	1.969	-1.020	0.044
$2\mathbf{B}^-$ ($S=1/2$)	2.192	-1.202	0.012

Table 2.8 IR Spectral Data (Experimental from Spectroelectrochemistry^a and DFT^b) for $2\mathbf{B}^n$ ($n = 1+, 0, 1-$)

Complex	$\nu_{(\text{N-O})}$ (cm^{-1}) (exp) ^a	$\nu_{(\text{N-O})}$ (cm^{-1}) (DFT) ^b
$2\mathbf{B}^0$	1785	1778
$2\mathbf{B}^+$	1825	1822
$2\mathbf{B}^-$	1604	1613

^aMeasurements in $\text{CH}_2\text{Cl}_2/0.1 \text{ M Bu}_4\text{NPF}_6$ (OTTLE spectroelectrochemistry).

^bB3LYP/6-31G*/SDD/CPCM/ CH_2Cl_2 .

Table 2.9 TD-DFT (B3LYP/6-31G^{*}/SDD/CPCM/CH₂Cl₂) Calculated Electronic Transitions for **2Bⁿ** ($n = 1+, 0, 1-$)

	E/eV	λ/nm (expt.) ($\epsilon/M^{-1}cm^{-1}$)	λ/nm (DFT) (f)	Transitions	Character
2B ($S=0$)	5.5055	225(40100)	225(0.1098)	HOMO-7→LUMO+5 (0.48)	cor(π)→cor(π^*)
	4.7106	262(24700)	263(0.0422)	HOMO-2→LUMO+6 (0.49)	cor(π)→cor(π^*)
	3.0014	390(56200)	413(0.4615)	HOMO-5→LUMO (0.50)	cor(π)→Fe(d π)
	2.4125	533(8500)	514(0.0012)	HOMO-14→LUMO (0.38)	cor(π)→Fe(d π)
2B⁺ ($S=1/2$)	2.8725	399(38000)	432(0.0084)	HOMO-3(α)→LUMO+2(α) (0.46)	cor(π)→cor(π^*)
	1.9501	637(3700)	636(0.0121)	HOMO-12(α)→LUMO(α) (0.27)	cor(π)→cor(π^*) cor(π)→cor(π^*)
				HOMO(β)→LUMO+1(β) (0.18)	
2B⁻ ($S=1/2$)	3.8637	330(24100)	321(0.0539)	HOMO-8(α)→LUMO+1(α) (0.45)	Fe(d π)→cor(π^*)
	2.8912	422(40700)	429(0.0229)	HOMO-2(β)→LUMO+13(β) (0.48)	NO(π)/cor(π)→cor(π^*)
	2.1770	570(12000)	569(0.0168)	HOMO-1(β)→LUMO(β) (0.44)	cor(π)→cor(π^*) cor(π)→cor(π^*)
				HOMO-1(β)→LUMO+1(β) (0.42)	
	1.9751	633(7000)	628(0.0646)	HOMO(β)→LUMO+3(β) (0.51)	cor(π)→cor(π^*)
	1.5899	765(2100)	780(0.0022)	HOMO-1(β)→LUMO(β) (0.62)	cor(π)→cor(π^*) cor(π)→cor(π^*)
			HOMO-1(α)→LUMO(α) (0.60)		

2.3 Conclusions

We have presented the synthesis of two new corrole ligands in this chapter. These new, and a literature reported corrole have been used to generate a series of [(cor)(FeNO)⁶] derivatives. Purity and identity of the free base corroles and the corresponding [(cor)(FeNO)⁶] derivatives have been demonstrated by various spectroscopic techniques and elemental analysis. The ¹H NMR spectra of the [(cor)(FeNO)⁶] derivatives show sharp resonances, which indicate their diamagnetic characteristics and the noninnocence nature of the corrole macrocycles. The Fe—N—O bond angle is 175.0(4)° for **1B**, and 171.7(3)° for **2B**. This indicates that these are linear nitrosyls of the (FeNO)⁶ form. In the packing diagram, **2B** molecules are stacked together and form cylindrical tubes-like arrangements throughout the crystal lattice. These tubes are filled with benzene molecules, arranged as benzene clusters. All the three [(cor)(FeNO)⁶] derivatives **1B**, **2B**, and **3B** exhibited one reversible oxidative couple and one reversible reductive couple *versus* ferrocene/ferrocenium. UV-Vis, IR and EPR spectroelectrochemical measurements of one electron oxidized species, supports the formation of [(cor)^{2+-(Fe(NO))⁶]⁺⁺. From earlier observations it was established that EPR signals predominantly originate from a low spin iron(III) center. However, our observations clearly prove the predominant location of the spin on the corrole unit. A rationale has also been provided for this. Thus, the EPR data point towards a new/alternative assignment of corrolato-iron-nitrosyl radical cation. UV-Vis, IR and EPR spectroelectrochemical studies of the reduced form **3B^{•-}** indicate that the unpaired electron in that species resides predominantly on the (FeNO) unit. The above observations have been supported by DFT and TD-DFT calculations. Thus, while the investigation of the one-electron oxidized species delivers the noninnocent character of the corrole ring, the knowledge of the electron}

structure of the one-electron reduced species delivers information about the non-innocent nature of NO, the oldest known non-innocent ligand. Our results here reveal that spectroelectrochemistry is a very useful technique for investigating metal complexes containing several potentially non-innocent ligands. This combined approach can be used to establish the electronic structures of such metal complexes in their various redox states. Information obtained from such studies is often useful while investigating the relevance of such complexes in redox catalysis.

2.4 Experimental Section

2.4.1 Materials

The precursors pyrrole, *p*-chloranil, 2,4,5-trimethoxybenzaldehyde and TBAP were purchased from Aldrich, USA. 4-cyano benzaldehyde, 4-bromo benzaldehyde, and FeCl₂·4H₂O were purchased from Merck, India. Other chemicals were of reagent grade. Hexane and CH₂Cl₂ were distilled from KOH and CaH₂ respectively. For spectroscopy and electrochemical studies HPLC grade solvents were used. Symmetric A₃-corrole, **1A** was obtained by following a literature reported procedure^{46, 186}, however, two *trans*-A₂B-corroles, **2A** and **3A** have been prepared for the first time.

2.4.2 Physical Measurements

UV–Vis spectral studies were performed on a Perkin–Elmer LAMBDA-750 spectrophotometer. The elemental analyses were carried out with a Perkin–Elmer 240C elemental analyzer. FTIR spectra were recorded on a Perkin–Elmer spectrophotometer with samples prepared as KBr pellets. The NMR measurements were carried out using a Bruker AVANCE 400 NMR spectrometer. Tetramethylsilane (TMS) was the internal standard. Electrospray mass spectra were recorded on a

Bruker Micro TOF—QII mass spectrometer. Cyclic voltammetry measurements were carried out using a CH Instruments model CHI1120A electrochemistry system. A glassy carbon working electrode, a platinum wire as an auxiliary electrode and an Ag-AgCl reference electrode were used in a three-electrode configuration. Tetrabutyl ammonium perchlorate (TBAP) was the supporting electrolyte (0.1M) and the concentration of the solution was 10^{-3} M with respect to the complex. The half wave potential E_{298}^0 was set equal to $0.5(E_{pa} + E_{pc})$, where E_{pa} and E_{pc} are anodic and cathodic cyclic voltammetric peak potentials, respectively. The scan rate used was 100 mV s^{-1} . EPR spectra in the X band were recorded with a Bruker System EMX. Simulations of EPR spectra were done using the Simfonia program. UV-Vis-NIR absorption spectra were recorded on an Avantes spectrometer system: Ava Light-DH-BAL (light source), AvaSpec-ULS2048 (UV-Vis-detector) and AvaSpec-NIR256-2.5TEC (NIR-detector). Spectroelectrochemical measurements were carried out using an optically transparent thin layer electrochemical (OTTLE) cell¹⁹³.

2.4.3 Crystal Structure Determination

Single crystals of **1B** were grown by slow diffusion of a solution of the **1B** in dichloromethane into methanol, followed by slow evaporation under atmospheric conditions and those for **2B** were grown by slow diffusion of a solution of the (cor)(FeNO)⁶ in dichloromethane into benzene, followed by slow evaporation under atmospheric conditions. The crystal data of **1B** and **2B** were collected on a Bruker Kappa APEX II CCD diffractometer at 293 K. Selected data collection parameters and other crystallographic results are summarized in Table 2.1. All data were corrected for Lorentz polarization and absorption effects. The program package SHELXTL¹⁹⁵ was used for structure solution and full matrix least squares refinement

on F^2 . Hydrogen atoms were included in the refinement using the riding model. Contributions of H atoms for the water molecules were included but were not fixed. Disordered solvent molecules were taken out using SQUEEZE¹⁹⁶ command in PLATON. CCDC-959930 and CCDC-959931 contain the supplementary crystallographic data for **1B** and **2B**.

2.4.4 Computational Details

Full geometry optimizations were carried out using the density functional theory method at the (U)B3LYP level for **2B**⁺ and **2B**⁻ and (R)B3LYP for **2B**¹⁹⁷. All elements except iron were assigned the 6-31G(d) basis set. The SDD basis set with effective core potential was employed for the iron atom^{198, 199}. Harmonic frequency calculations were performed on the optimized geometries, representing a minimum on the potential energy surface. All harmonic frequencies have been corrected by a scaling factor of 0.975 except $\nu(\text{N-O})$ which was scaled by a factor of 0.92. All calculations were performed with the Gaussian09 program package²⁰⁰. Vertical electronic excitations based on B3LYP optimized geometries were computed for **2B**⁺, **2B** and **2B**⁻ using the time-dependent density functional theory (TD-DFT) formalism²⁰¹⁻²⁰³ in dichloromethane using the conductor-like polarizable continuum model (CPCM)²⁰⁴⁻²⁰⁶. *Chemissian*²⁰⁷ was used to calculate the fractional contributions of various groups to each molecular orbital. All the calculated structures were visualized with *ChemCraft*²⁰⁸.

2.4.5 Synthesis of 4-(Di(1H-pyrrol-2-yl)methyl)benzotrile, **1**

4-(Di(1H-pyrrol-2-yl)methyl)benzotrile, **1** was prepared by slight modification of the direct synthesis method reported by Lee et al., involving the pyrrole-aldehyde

condensation in the presence of a large excess of pyrrole²⁰⁹. Pyrrole served a dual role of reactant and being the solvent in the reaction mixture. In a 100ml two-necked round-bottomed flask, 2 g of 4-cyano benzaldehyde (0.015 mmol) was dissolved in 21 mL of pyrrole (0.300 mmol) and after adding 233 μ L (0.003 mmol) of TFA, was stirred for 20 min at room temperature. The brown coloured crude product was obtained after dilution with CH_2Cl_2 , washing with dilute NaOH solution and concentration of the organic layer. Excess pyrrole was removed by rotary evaporation. The crude product was then purified by column chromatography through a bed of silica-gel (100-200 mesh), using the solvent mixture 85% hexane and 15% ethylacetate as eluent.

The compound 4-(di(1H-pyrrol-2-yl)methyl)benzotrile was characterized by various spectral techniques, such as CHN analysis, UV-Vis, ^1H NMR, ^{13}C NMR, and electrospray mass spectrum. These analyses matched well with the earlier reported values²⁰⁹.

2.4.6 Synthesis of 5,10,15-Tris(4-bromophenyl)corrole, 1A

1A was prepared according to available procedures of corrole synthesis⁴⁶. A total of 0.925 g of 4-bromo benzaldehyde (5 mmol) and 697 μ L of pyrrole (10 mmol) were dissolved in 200 mL of methanol and subsequently 200 mL of water was added. Then 4.25 mL of HCl_{aq} (36%) was added and the reaction was stirred for 3 h. The mixture was extracted with CHCl_3 , and the organic layer was washed twice with water, dried by anhydrous Na_2SO_4 , filtered and diluted to 300 mL with CHCl_3 . A total of 1.23 g of *p*-chloranil (5 mmol) was added, and the mixture was refluxed for 1 h. The solvent was removed by rotary evaporation and the green coloured crude product was purified by column chromatography through silica gel (100-200 mesh) bed and using 20% DCM and 80% hexane as eluent. The compound **1A** was characterized by various

spectral techniques, such as CHN analysis, UV-Vis, ^1H NMR, ^{13}C NMR, and electrospray mass spectrum which also confirmed the purity and identity of **1A**. These analyses matched well with the earlier reported values¹⁸⁶.

2.4.7 Synthesis of 10-(4-Bromophenyl)-5,15-bis(4-cyanophenyl)corrole, **2A**

2A was prepared by following a general procedure of corrole synthesis⁴⁶. A total of 0.247 g of 5-(4-cyanophenyl)dipyrromethane (1 mmol) and 0.092 g of 4-Bromobenzaldehyde (0.5 mmol) were dissolved in 50 mL of MeOH. The reaction was kept for stirring for 1 h. the mixture was extracted with CHCl_3 , the organic layer was washed twice with H_2O , dried by anhydrous Na_2SO_4 , filtered, and diluted to 250 mL with CHCl_3 . Then, 0.369 g (1.5 mmol) of *p*-chloranil was added, and the mixture was refluxed for 1 h. The solvent was removed by rotary evaporation and the green coloured crude product was purified by column chromatography through silica gel (100-200 mesh) column and using 80% DCM and 20% hexane as eluent. Yield: 45% (150 mg). Anal. Calcd (found) for $\text{C}_{39}\text{H}_{23}\text{BrN}_6$ (**2A**): C, 71.45 (71.53); H, 3.54 (3.46); N, 12.82 (12.75). $\lambda_{\text{max}}/\text{nm}$ ($\epsilon/\text{M}^{-1}\text{cm}^{-1}$) in dichloromethane: 425 (100488), 582 (16544), 623 (11766) , 648 (9409). ^1H NMR (400 MHz, CDCl_3) δ 9.063 (broad singlet, 2H), 8.854(broad singlet, 2H), 8.611-8.486 (broad multiplet, 8H), 8.130-8.036 (broad multiplet, 6H), 7.922 (broad singlet, 2H). The electrospray mass spectrum in acetonitrile showed peaks centered at $m/z = 656.724$ correspond to $[\mathbf{2A}+\mathbf{H}]^+$ (calculated molecular mass: 655.544).

2.4.8 Synthesis of 10-(2,4,5-Trimethoxyphenyl)-5,15-bis(4-cyanophenyl)corrole, **3A**

3A was prepared by following a general procedure of corrole synthesis⁴⁶. A total of 0.247 g of 5-(4-cyanophenyl)dipyrromethane (1 mmol) and 0.098 g of 2,4,5-

trimethoxy benzaldehyde (0.5 mmol) were dissolved in 50 mL of MeOH. The reaction was kept for stirring for 1 h. the mixture was extracted with CHCl₃, the organic layer was washed twice with H₂O, dried by anhydrous Na₂SO₄, filtered, and diluted to 250 mL with CHCl₃. Then, 0.369 g (1.5 mmol) of *p*-chloranil was added, and the mixture was refluxed for 1 h. The solvent was removed by rotary evaporation and the green coloured crude product was purified by column chromatography through silica gel (100-200 mesh) column and using 80% DCM and 20% hexane as eluent. Yield: 42% (140 mg). Anal. Calcd (found) for C₄₂H₃₀N₆O₃ (**3A**): C, 75.66 (75.53); H, 4.54 (4.46); N, 12.60 (12.75). λ_{\max}/nm ($\epsilon/\text{M}^{-1}\text{cm}^{-1}$) in dichloromethane: 426 (90,875), 582 (17,250), 627 (13,000), 646 (11,250). ¹H NMR (400 MHz, CDCl₃) δ 8.91 (s, 2H), 8.79 (s, 2H), 8.62 (s, 2H), 8.47 (s, 2H), 8.40 (d, *J* = 6.4 Hz, 4H), 8.05 (d, *J* = 6.7 Hz, 4H), 7.55 (s, 1H), 7.02 (s, 1H), 4.22 (s, 3H), 3.95 (s, 3H), 3.62 (s, 3H), $-(1.37 - 1.43)$ (broad multiplet, 3H). ¹³C NMR (101 MHz, CDCl₃) δ 154.04, 150.28, 144.32, 142.53, 141.43, 139.11, 135.43, 132.12, 131.81, 126.86, 126.47, 122.52, 121.94, 119.43, 119.28, 116.78, 113.35, 111.05, 107.12, 98.17, 57.22, 56.86, 56.55. The electrospray mass spectrum in acetonitrile showed peaks centered at *m/z* = 667.21 corresponding to [**3A+H**]⁺ (calculated molecular mass: 666.23). **3A** displayed strong fluorescence at 678 nm.

2.4.9 Synthesis of [5,10,15-Tris(4-bromophenyl)cor]Fe^{III}NO, **1B**

A mixture of 0.025 g of 5,10,15-tris(4-bromophenyl)corrole (0.03 mmol) and 0.060 g of ferrous chloride tetrahydrate FeCl₂·4H₂O (0.3 mmol) was refluxed in a solution of 15 mL of pyridine/methanol (1:2) for 1½ h under dinitrogen. 1.0 mL aliquot of saturated aqueous NaNO₂ was then added to the hot solution and the system was refluxed for an additional 30 min. The solution was then allowed to cool to room

temperature and the solvent mixture was removed by rotary evaporation. The solid product was finally dissolved in dichloromethane and purified by column chromatography using silica gel (100-200 mesh). The solvent-mixture used for elution of **1B** was 20% DCM and 80% hexane. The final form of the compound was obtained as orange-red crystalline materials. Anal. Calcd (found) for $C_{37}H_{20}Br_3FeN_5O$ (**1B**): C, 52.52 (52.48); H, 2.38 (2.54); N, 8.28 (8.35). λ_{\max}/nm ($\epsilon/M^{-1}\text{cm}^{-1}$) in dichloromethane: 394(84800), 535(9400). $\nu_{\text{N=O}} = 1773 \text{ cm}^{-1}$. $^1\text{H NMR}$ (400 MHz, CDCl_3) δ 7.98 (d, $J = 4.6 \text{ Hz}$, 2H), 7.76 – 7.62 (m, 13H), 7.54 – 7.50 (m, 3H), 7.38 (d, $J = 4.8 \text{ Hz}$, 2H). $^{13}\text{C NMR}$ (101 MHz, CDCl_3) δ 148.12, 147.91, 146.09, 138.46, 138.31, 137.35, 132.21, 132.01, 131.74, 131.69, 131.56, 131.53, 131.32, 130.44, 126.72, 126.02, 125.58, 123.13, 122.95, 118.49. The electrospray mass spectrum in acetonitrile matched well with the earlier reported data ¹⁰⁷.

2.4.10 Synthesis of [10-(4-Bromophenyl)-5,15-bis(4-cyanophenyl)cor]Fe^{III}NO, **2B**

A mixture of 0.050 g of 10-(4-bromophenyl)-5,15-bis(4-cyanophenyl)corrole (0.076 mmol) and 0.152 g of ferrous chloride tetrahydrate $\text{FeCl}_2 \cdot 4\text{H}_2\text{O}$ (0.76 mmol) was refluxed in a solution of 15 mL of pyridine/methanol (1:2) for 1½ h under dinitrogen. 1.0 mL aliquot of saturated aqueous NaNO_2 was then added to the hot solution and the system was refluxed for an additional 30 min. The solution was then allowed to cool to room temperature and the solvent mixture was removed by rotary evaporation. The solid product was finally dissolved in dichloromethane and purified by column chromatography using silica gel (100-200 mesh). The solvent-mixture used for elution of **2B** was 60% DCM and 40% hexane. The final form of the compound was obtained as orange-red crystalline materials. Yield: 55% (31 mg). Anal. Calcd (found) for $C_{39}H_{20}BrFeN_7O$ (**2B**): C, 63.44 (63.48); H, 2.73 (2.84); N, 13.28 (13.40). λ_{\max}/nm

($\epsilon/M^{-1}cm^{-1}$) in dichloromethane: 390(56200), 539 (5000). $\nu_{N=O} = 1774\text{ cm}^{-1}$. 1H NMR (400 MHz, $CDCl_3$) δ 8.04 (d, $J = 4.6$ Hz, 2H), 7.96-7.90 (m, 8H), 7.76-7.63 (m, 5H), 7.53-7.48 (m, 3H), 7.44-7.43(d, $J = 5.0$ Hz, 2H). ^{13}C NMR (101 MHz, $CDCl_3$) δ 148.14, 147.38, 146.09, 143.12, 138.18, 137.98, 132.24, 131.89, 131.68, 131.64, 131.62, 131.58, 131.35, 129.30, 126.37, 126.00, 125.81, 123.13, 119.08, 118.76, 112.68. The electrospray mass spectrum in acetonitrile showed peaks centered at $m/z = 709.308$ corresponding to $[M^+-NO]$ (calculated molecular mass: 708.365).

2.4.11 Synthesis of [10-(2,4,5-Trimethoxyphenyl)-5,15-bis(4-cyanophenyl)cor]

$Fe^{III}NO$, **3B**

A mixture of 0.050 mg of 10-(2,4,5-trimethoxyphenyl)-5,15-bis(4-cyanophenyl)corrole (0.075 mmol) and 0.149 g of ferrous chloride tetrahydrate $FeCl_2 \cdot 4H_2O$ (0.75 mmol) was refluxed in a solution of 15 mL of pyridine/methanol (1:2) for 1½ h under dinitrogen. 1.0 mL aliquot of saturated aqueous $NaNO_2$ was then added to the hot solution and the system was refluxed for an additional 30 min. The solution was then allowed to cool to room temperature and the solvent mixture was removed by rotary evaporation. The solid product was finally dissolved in dichloromethane and purified by column chromatography using silica gel (100-200 mesh). The solvent used for elution of **3B** was 100% DCM. The final form of the compound was obtained as orange-red crystalline materials. Yield: 51% (29 mg). Anal. Calcd (found) for $C_{42}H_{27}FeN_7O_4$ (**3B**): C, 67.30 (67.48); H, 3.63 (3.74); N, 13.08 (12.95). λ_{max}/nm ($\epsilon/M^{-1}cm^{-1}$) in dichloromethane: 388 (96200), 485 (25800). $\nu_{N=O} = 1772\text{ cm}^{-1}$. 1H NMR (400 MHz, $DMSO-d_6$) δ 8.17-8.03 (m, 10H), 7.68-7.64 (dd, $J = 9.6, 4.5$ Hz, 2H), 7.42-7.40 (dd, $J = 4.6, 3.2$ Hz, 2H), 7.33-7.31 (t, $J = 5.3$ Hz, 2H), 7.09-6.93 (m, 2H), 3.93 (d, $J = 2.9$ Hz, 3H), 3.74 (s, 2H), 3.66 (d, $J = 4.8$ Hz,

2H), 3.55 (s, 2H). ^{13}C NMR (101 MHz, DMSO- d_6) δ 151.08, 150.92, 149.93, 149.90, 147.40, 147.38, 146.45, 146.37, 146.34, 142.06, 141.99, 141.69, 137.28, 132.15, 130.76, 130.09, 130.03, 129.43, 129.39, 128.81, 127.11, 126.05, 125.88, 125.83, 125.54, 125.48, 119.07, 118.40, 117.31, 117.23, 114.54, 114.12, 111.35, 98.44, 98.17, 56.38, 56.00, 55.51. The electrospray mass spectrum in acetonitrile showed peaks centered at $m/z = 719.09$ corresponding to $[\text{M}^+-\text{NO}]$ (calculated molecular mass: 719.14).

CHAPTER 3

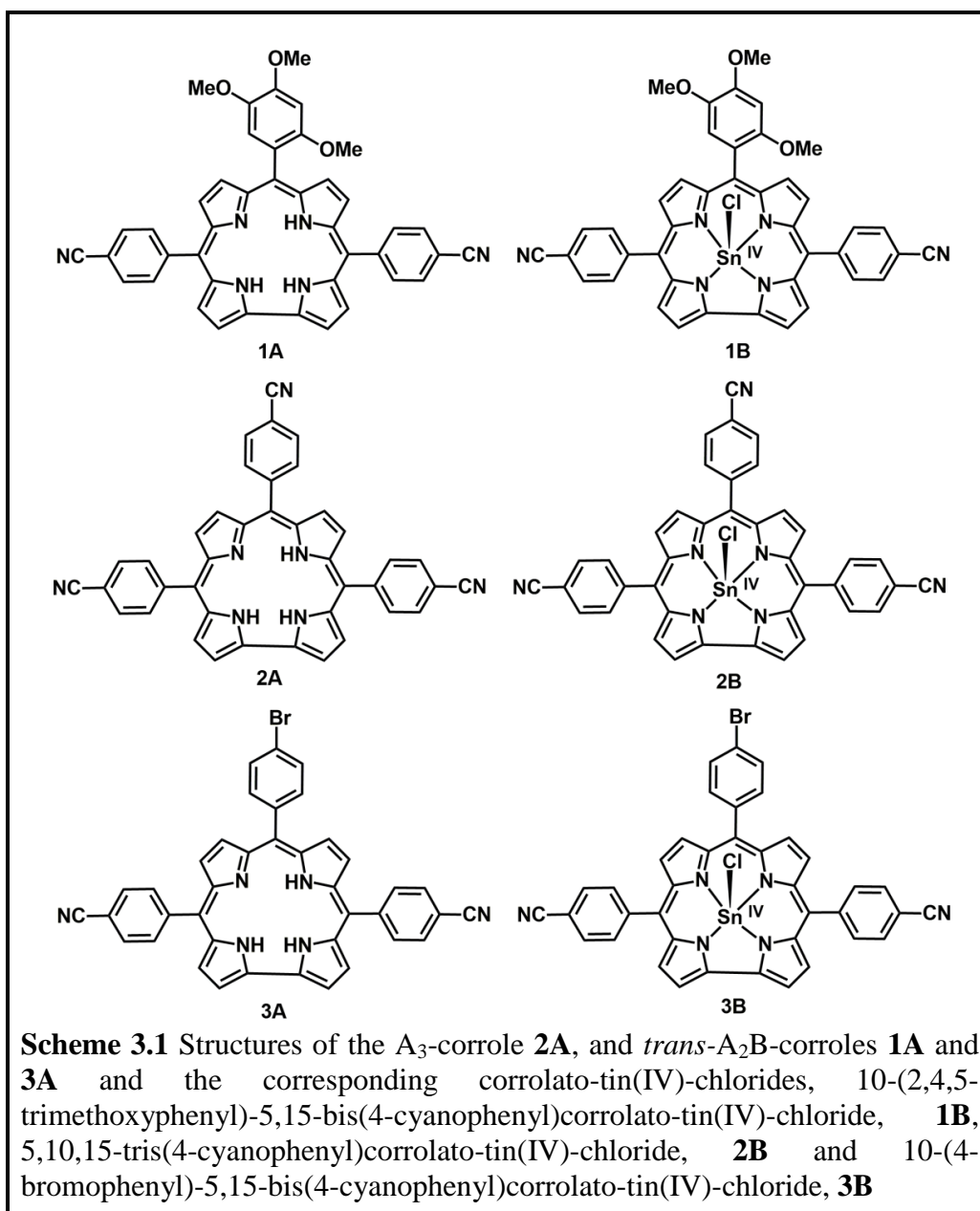
Semi-Insulating Behaviour of Self-Assembled Tin(IV) Corrole Nanospheres

3.1	Introduction	85
3.2	Results and Discussion	87
3.2.1	Synthesis	87
3.2.2	Spectral Characterization	88
3.2.2.1	Mass Spectroscopy	88
3.2.2.2	UV-Vis and Emission Spectroscopy	88
3.2.2.3	NMR Spectroscopy	88
3.2.2.4	X-Ray Crystallography	93
3.2.3	Self Aggregates of Tin(IV) Corroles	101
3.2.4	<i>I-V</i> Characteristics and CAFM Measurements	102
3.3	Conclusions	107
3.4	Experimental Section	108
3.4.1	Materials	108
3.4.2	Physical Measurements	109
3.4.3	Crystal Structure Determination	109
3.4.4	Synthesis of 10-(2,4,5-Trimethoxyphenyl)-5,15-bis(4-cyanophenyl)corrolato-tin(IV)-chloride, 1B	110
3.4.5	Synthesis of 5,10,15-tris(4-cyanophenyl)corrolato-tin(IV)-chloride, 2B	111
3.4.6	Synthesis of 10-(4-Bromophenyl)-5,15-bis(4-cyanophenyl)corrolato-tin(IV)-chloride, 3B	112

3.1 Introduction

Green plants use chlorophyll (magnesium porphyrin) aggregates for light harvesting purposes in nature^{117, 118}. Inspired by this natural phenomenon, a large number of researchers are actively involved in trying to mimic the light harvesting complexes found in green plants and purple bacteria^{110-116, 119, 120}. The ultimate aim of studying the model systems of light-harvesting complexes is to gain a deeper insight into the aggregated porphyrin/metalloporphyrin structures and their unique functions mediated by the excitonic interactions between the adjacent magnesium porphyrin units in the highly ordered aggregates, and to use this knowledge for the construction of newer and efficient classes of bio-inspired devices. Thus the generation of porphyrin/metalloporphyrin nanostructures (e.g., nano sphere, nano tubes, etc.) and their efficient uses for various device fabrications are of utmost importance for the development of modern electronic devices²¹⁰⁻²¹³. In this chapter, a series of novel tin(IV) corrole complexes has been synthesized (Scheme 3.1). The identity of these tin complexes has been established by various spectral techniques. The crystal structures of 10-(2,4,5-trimethoxyphenyl)-5,15-bis(4-cyanophenyl)corrolato-tin(IV)-chloride, **1B**, 5,10,15-tris(4-cyanophenyl)corrolato-tin(IV)-chloride, **2B** and 10-(4-bromophenyl)-5,15-bis(4-cyanophenyl)corrolato-tin(IV)-chloride, **3B** are also reported here. The introduction of a series of electron-releasing (like -OMe) and -withdrawing (like -CN) groups in the corrole frameworks will not only influence the energies of the molecular orbitals of the respective metal complexes but also will make them as useful precursors for the construction of various other metallo-corrole based supramolecular architectures. Corrole,^{2, 82, 85, 149-151, 153, 158, 162-166, 170, 214-221} a contracted porphyrin analogue, is recently gaining a lot of interest in research because of their potential superiority in terms of photophysical properties compared to their

analogous porphyrin derivatives^{8, 29, 48, 54, 64, 68, 139, 156, 159, 160, 167, 222-238}. Among the various metallo-porphyrins, research in field of tin complexes has also gained impetus in the recent years. These tin complexes may find suitable use for designing of various optoelectronic based materials. Although they are expected to be a more potent candidate than analogous tin(IV) porphyrin complexes²³⁹⁻²⁴⁹, surprisingly tin(IV) corrole based systems are rarely reported in literature^{31, 50, 91, 138, 250-255}. Self assembled supramolecular tin(IV) corrole frameworks, in the form of nanospheres



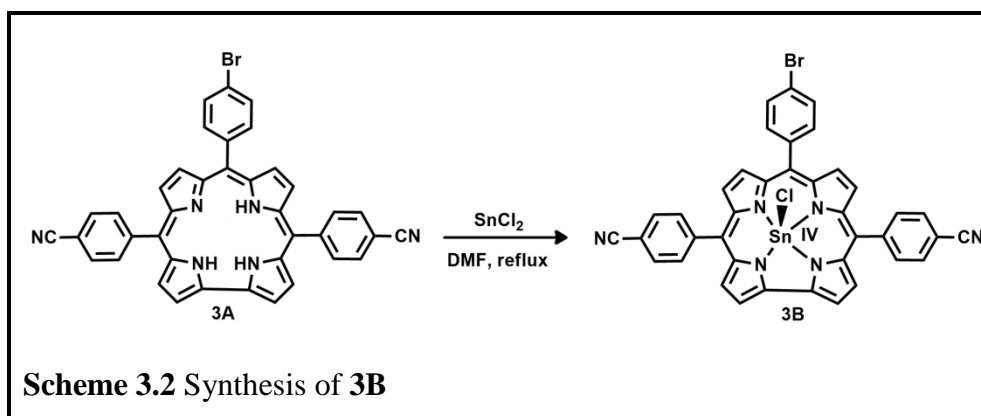
have been synthesized by using noncovalent intermolecular hydrogen bonding interactions in the case of **1B** and **3B** and then one of them has been explored in the field of device fabrication. Although a sizeable number of literature reports cover the generation of tin(IV) porphyrin based aggregates and their various applications¹²¹⁻¹²⁴, however, no reports are yet available that describe the synthesis and application of tin(IV) corrole based aggregates.

Thus the present chapter revolves around the synthesis, structural and spectral characterization of three novel tin(IV) corrole complexes, generation of their aggregates in the form of nanospheres and application of those nanospheres in the fabrication of semi-insulating semiconductor device. Semi-insulating semiconductors have found extensive applications in high speed microelectronic devices, isolation between devices, and also as sensing materials, like radiation sensor²⁵⁶. These semi-insulators are also frequently used in high-electron-mobility transistors (HEMT) which serve as the back bone of today's cell phone devices²⁵⁷.

3.2 Results and Discussion

3.2.1 Synthesis

The free base corroles⁵¹ were prepared according to the general procedure of corrole synthesis⁴⁶. For an example, 2,4,5-trimethoxy benzaldehyde and 5-(4-cyanophenyl)dipyrromethane were dissolved in methanol and subsequent oxidation by *p*-chloranil resulted in the formation of corrole, **1A**⁵¹. The corrolato-tin(IV)-chlorides were synthesized by following a reported synthetic protocol^{31, 50, 91, 138, 250-255}. In a standard protocol a mixture of corrole and the tin chloride were refluxed in a solution of DMF and resulted in the formation of corrolato-tin(IV)-chlorides in good yields (Scheme 3.2). The purity and identity of the corrolato-tin(IV)-chlorides, **1B**,



2B, and **3B** are demonstrated by their satisfactory elemental analyses and by the electrospray mass spectra.

3.2.2 Spectral Characterization

3.2.2.1 Mass Spectroscopy

The electrospray mass spectrum of **1B** in acetonitrile depicts peaks centered at $m/z = 818.07$ corresponding to $[\mathbf{1B}]^+$ (818.08 calcd for $C_{42}H_{27}ClN_6O_3Sn$). Mass spectrum of 5,10,15-tris(4-cyanophenyl)-corrolato-tin(IV)-chloride, **2B** in acetonitrile exhibits characteristic peaks centered at $m/z = 753.034$ corresponding to $[\mathbf{2B}]^+$ (753.049 calcd for $C_{40}H_{20}ClN_7Sn$). In case of **3B**, peaks centered at $m/z = 771.001$ corresponding to $[\mathbf{3B}-Cl]^+$ (770.995 calcd for $C_{39}H_{20}BrN_6Sn$) are observed (Figure 3.1).

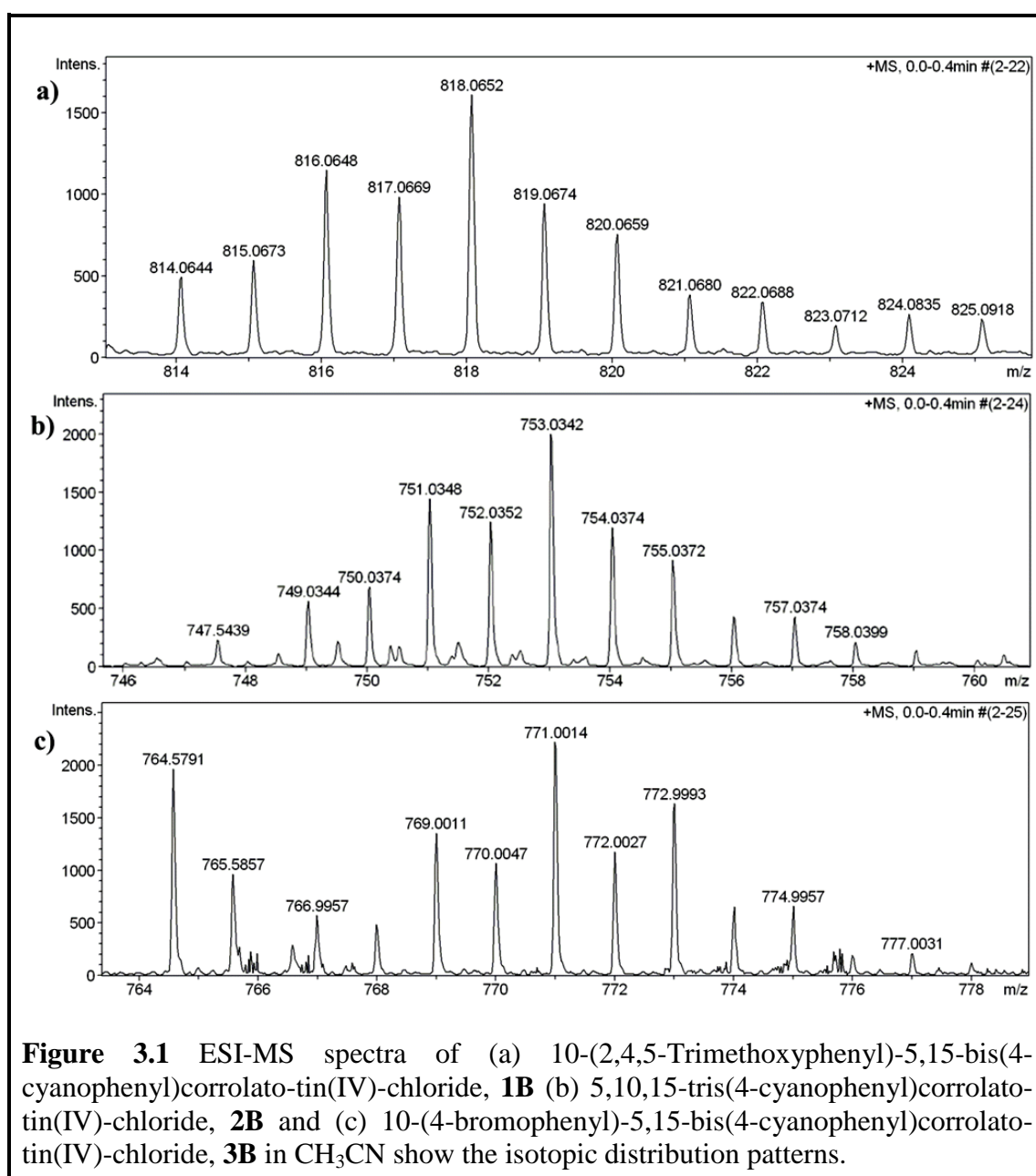
3.2.2.2 UV-Vis and Emission Spectroscopy

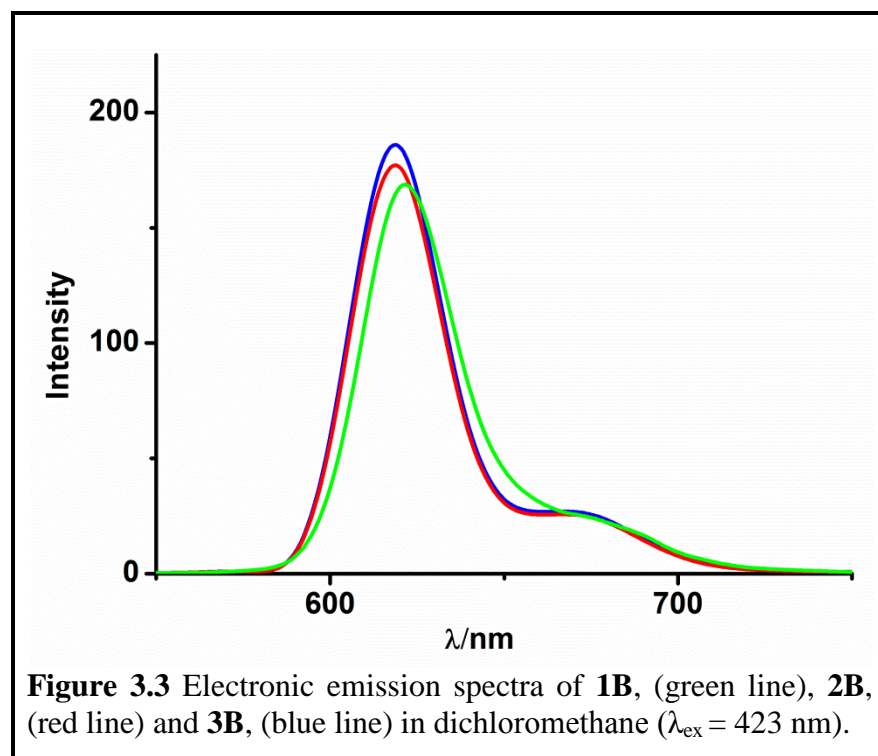
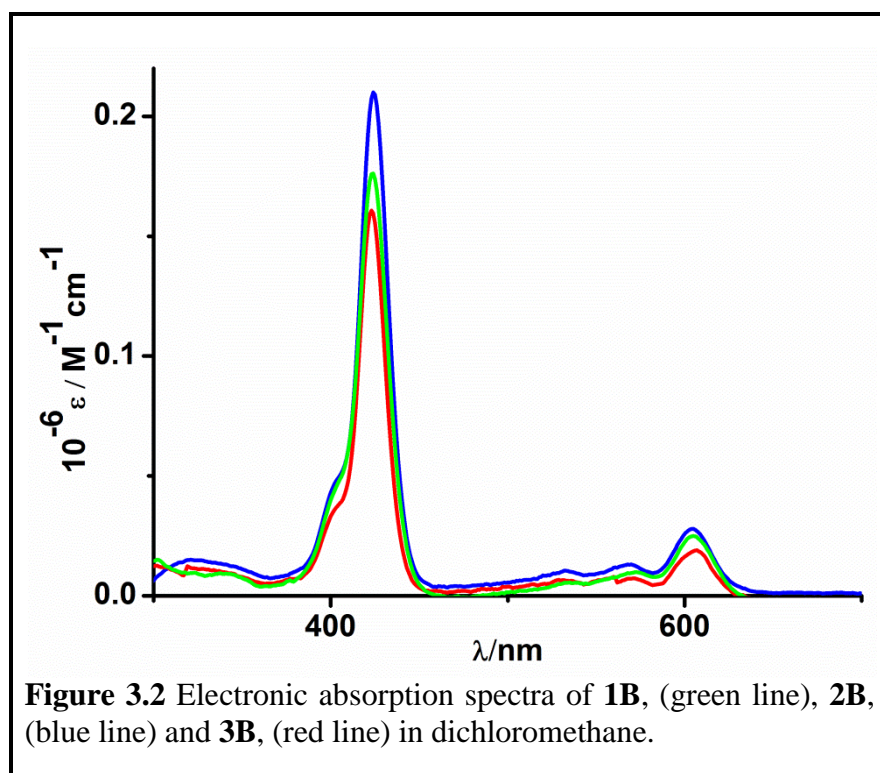
All the three tin(IV) corroles **1B**, **2B**, and **3B** exhibited $\pi \rightarrow \pi^*$ transitions in the ranges 400-650 nm (Figure 3.2). All the three tin(IV) corroles exhibit strong fluorescence in the red-regions of the visible spectra at room temperature in dichloromethane solvent (Figure 3.3)²³¹.

3.2.2.3 NMR Spectroscopy

The 1H NMR spectrum of **1B** exhibits peaks in accordance with eighteen partially

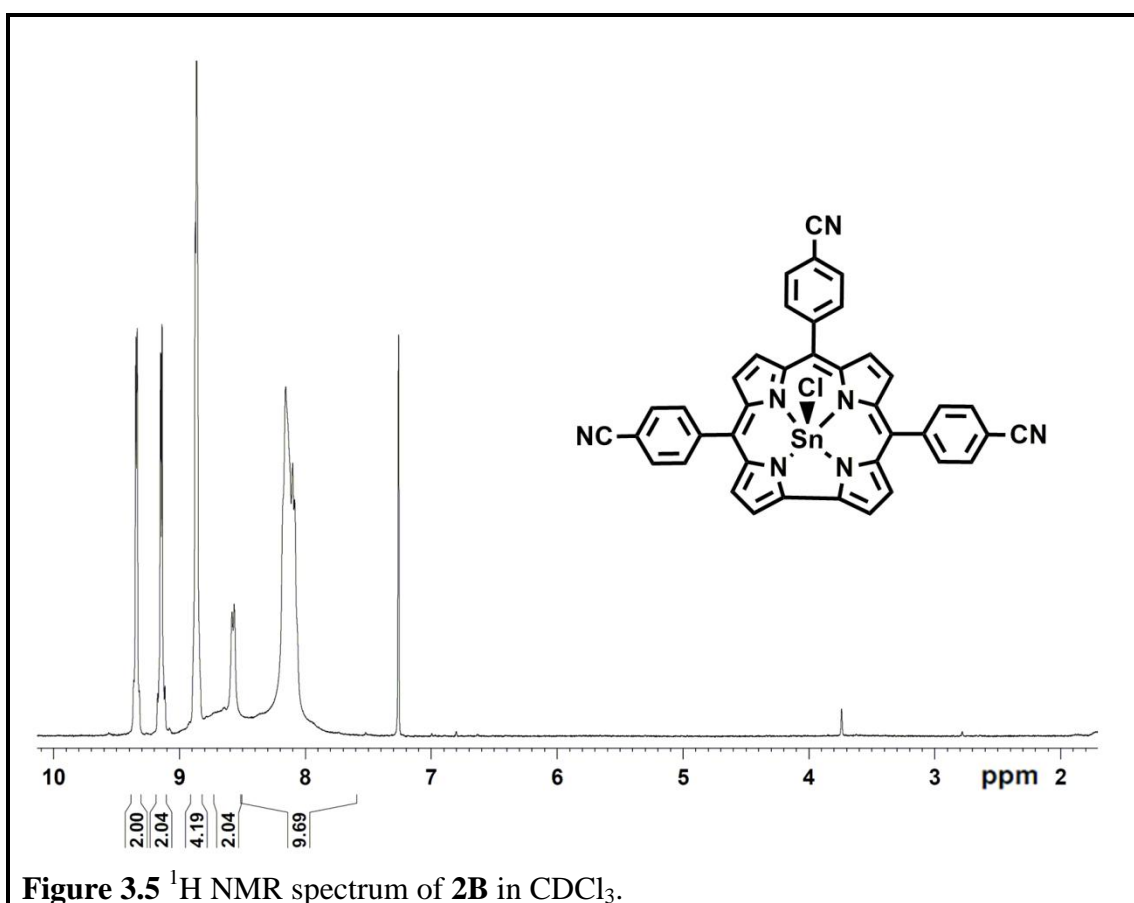
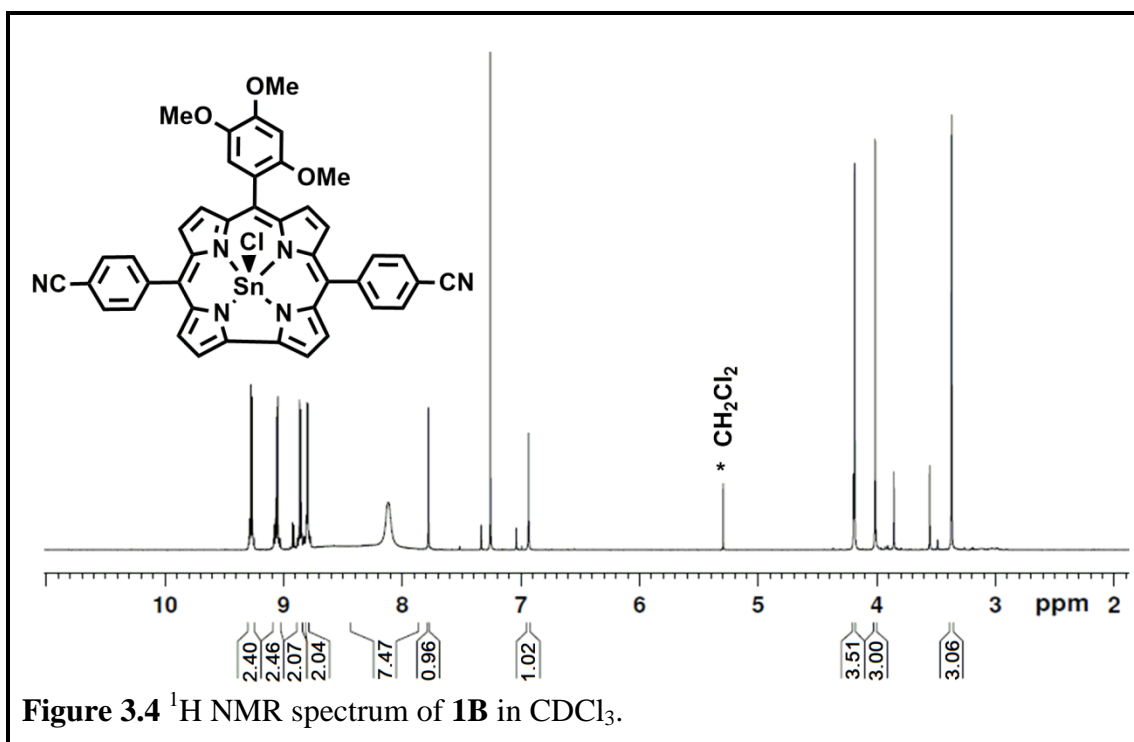
overlapping aromatic protons in the region, $\delta = 9.28$ - 6.94 ppm (Figure 3.4). Four multiplets at $\delta = 9.28$ - 9.25 , 9.09 - 9.03 , 8.87 - 8.85 , and 8.81 - 8.79 ppm are easily distinguishable and are assigned as β -pyrrolic hydrogen atoms. The aryl ring protons are observed at 8.12 - 6.94 ppm region. Out of these signals two singlets are easily distinguishable at 7.78 , and 6.94 ppm. These singlets are assigned as aromatic hydrogens from 2,4,5-trimethoxyphenyl group. The three methoxy group protons are observed at 4.19 , 4.01 , and 3.37 ppm. The ^1H NMR spectrum of **2B** also exhibits

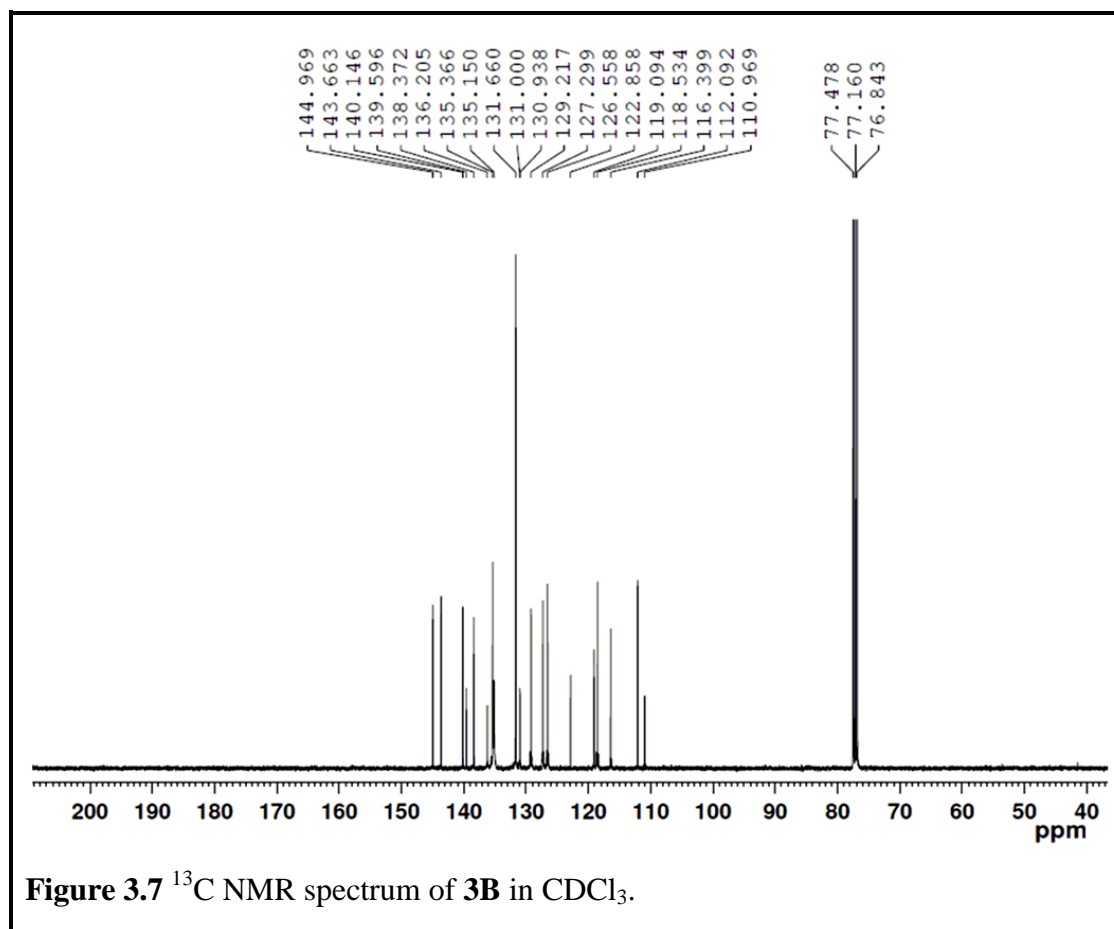
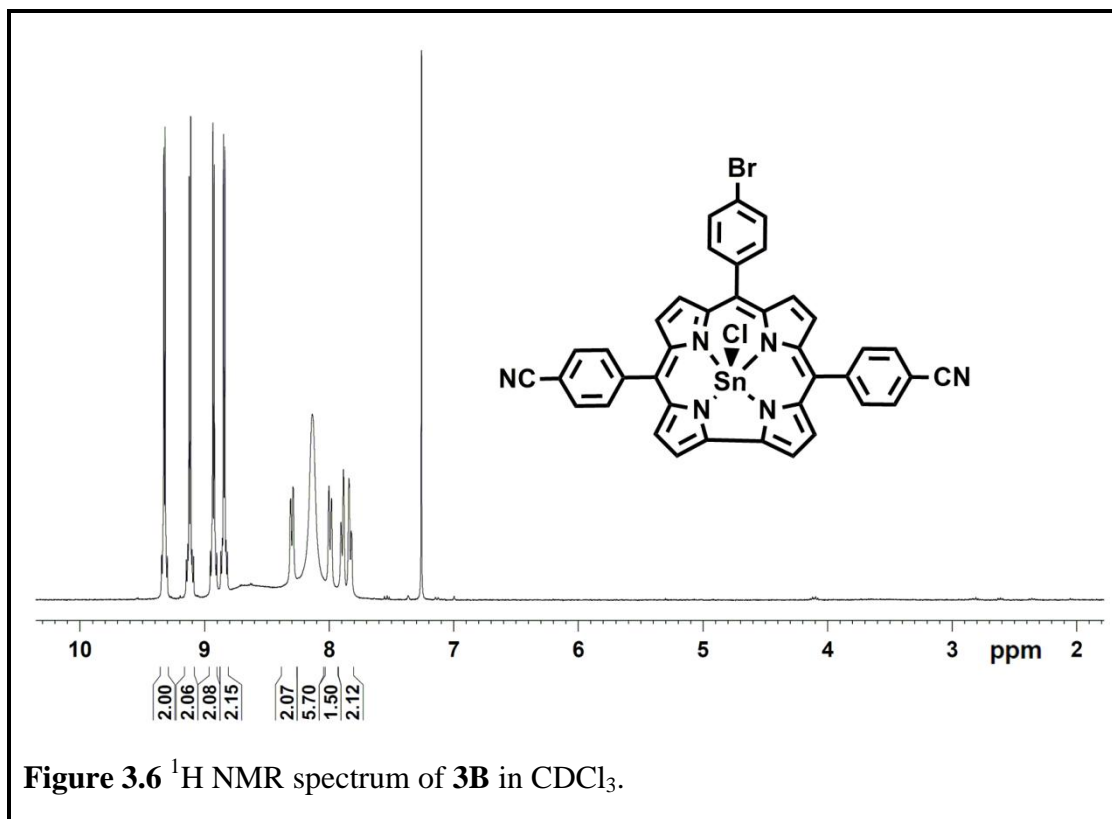




peaks for twenty partially overlapping aromatic protons in the region, $\delta = 9.36\text{-}7.84$ ppm (Figure 3.5). The ^1H NMR spectrum of **3B** exhibits peaks corresponding to

twenty partially overlapping aromatic protons in the region, $\delta = 9.33$ - 7.82





ppm (Figure 3.6). All the signals in the corrolato-tin(IV)-chlorides derivatives show downfield shift compared to free base corroles. Thus, the ^1H NMR data unequivocally establish the diamagnetic nature of the tin complexes **1B-3B**. ^{13}C NMR spectrum of **3B** shows twenty peaks in the region of 144.97-110.97 ppm (Figure 3.7).

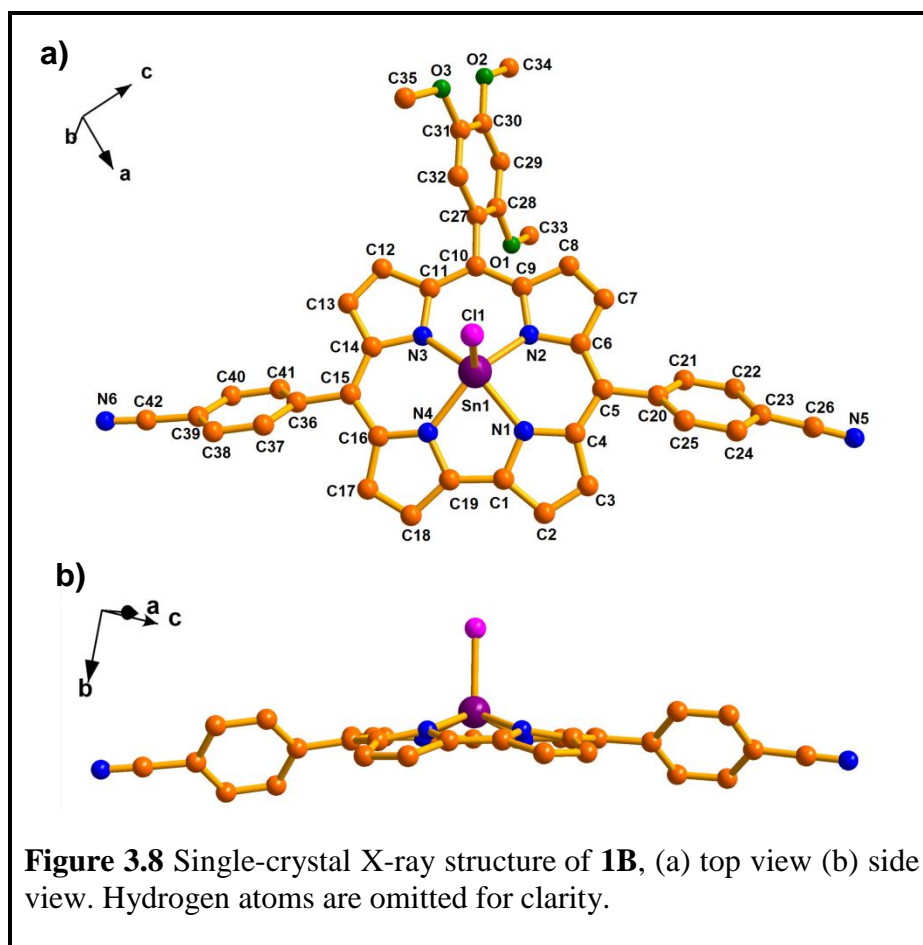
3.2.2.4 X-Ray Crystallography

The crystal structures of **1B**, **2B**, and **3B** are shown in Figures 3.8, 3.9 and 3.10 respectively. The crystal systems are monoclinic, triclinic, and triclinic and the unit cells have four, two, and two corrolato-tin(IV)-chloride molecules for **1B**, **2B**, and **3B** respectively. Important crystallographic parameters for all the three complexes are presented in Table 3.1. Bond distances and angles are comparable with the previously reported other corrolato-tin(IV) molecules^{31, 50, 91, 138, 250-255}. Tin atoms in all the three complexes **1B**, **2B** and **3B** are penta-coordinated and the geometry around the tin atom is distorted square-pyramidal in all the studied complexes. Vertical displacement of the peripheral carbon atoms from the N4 corrole planes signifies the distortion level in all the three corrole complexes (Figure 3.11)²⁵⁸. The tin atom does not perfectly fit inside the corrole cavity of none of the three complexes; instead it is deviated from the N4 corrole planes by distances of 0.6130(3) Å, 0.6516(4) Å and 0.6290(4) Å in **1B**, **2B** and **3B** respectively giving rise to domed conformations in all the three cases. This leads to a consequent deviation of the pyrrole ring nitrogen atoms from the 19-atom corrole carbon ring by distances ranging from 0.0233-0.3601 Å in **1B**. The *meso*-substituted phenyl rings are tilted with respect to the 19-atom corrole carbon plane by dihedral angles ranging from 48.728-65.135°. In the packing diagram of the corrolato-tin(IV)-chloride molecules (**1B**), the cyanide groups of two adjacent corrolato-tin(IV)-chloride molecules are facing towards the same direction,

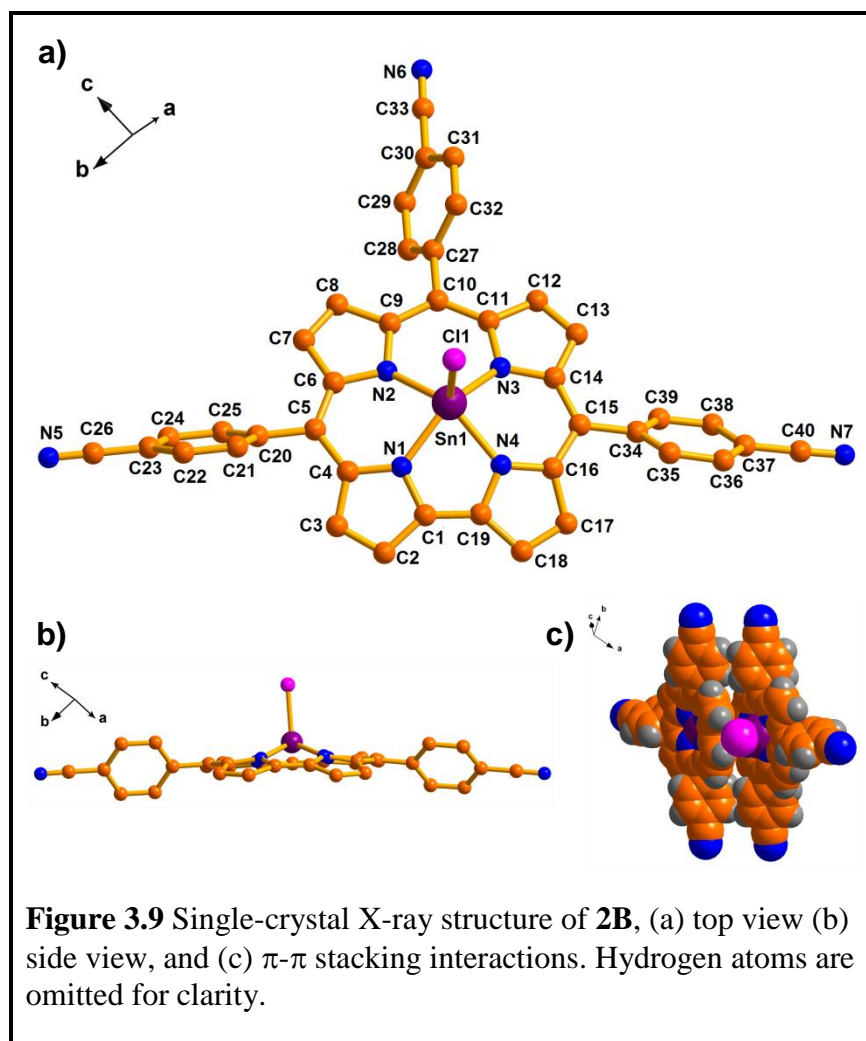
however methoxy groups of two adjacent corroles are facing in the opposite direction to each other. The distance between two neighboring tin(IV) atoms is 8.12 Å.

Table 3.1 Crystallographic Data for **1B**, **2B** and **3B**

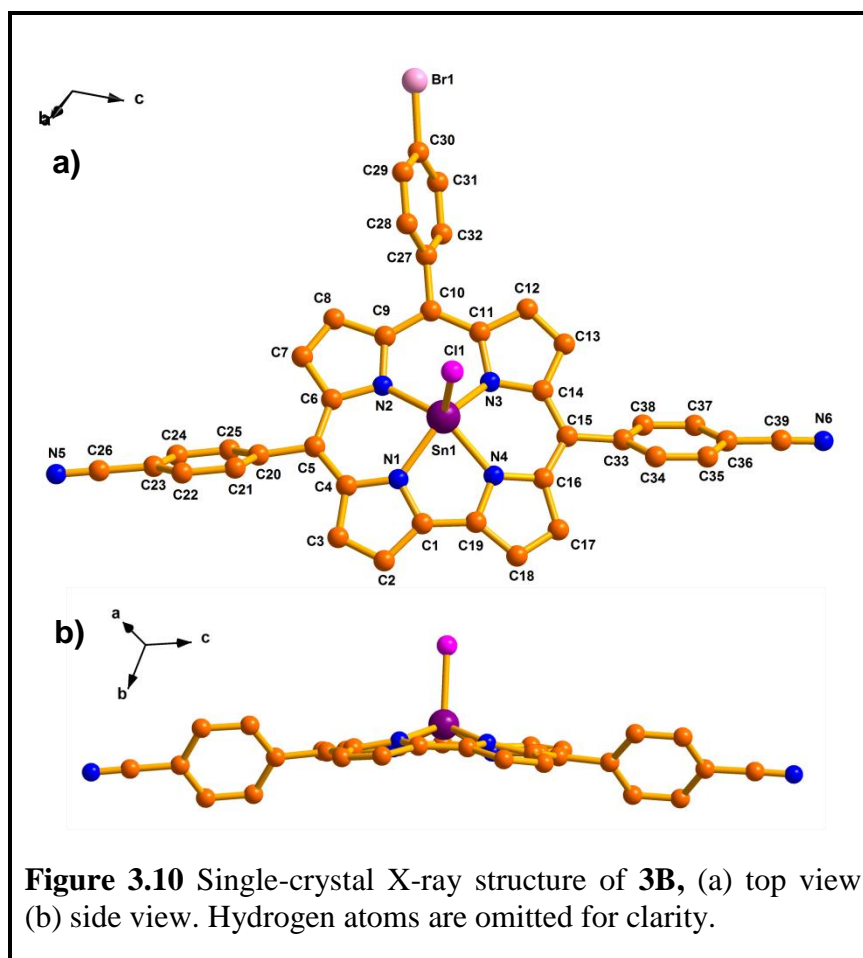
Compound Name	1B	2B	3B
Molecular formula	C ₄₂ H ₂₇ ClN ₆ O ₃ Sn	C ₄₀ H ₂₀ ClN ₇ Sn	C ₃₉ H ₂₀ BrClN ₆ Sn
Formula weight	817.84	752.77	806.66
Radiation	MoK α	MoK α	MoK α
Crystal symmetry	Monoclinic	Triclinic	Triclinic
Space group	<i>P</i> 21/ <i>c</i>	<i>P</i> -1	<i>P</i> -1
<i>a</i> (Å)	17.999(12)	12.020(5)	8.258(5)
<i>b</i> (Å)	12.597 (9)	13.221(5)	15.261(5)
<i>c</i> (Å)	16.249(10)	15.690(5)	16.642(5)
α (deg)	90	93.566(5)	111.107(5)
β (deg)	97.845(3)	109.752(5)	103.712(5)
γ (deg)	90	106.513(5)	98.450(5)
<i>V</i> (Å ³)	3649.8(4)	2215.0(14)	1837.3(14)
<i>Z</i>	4	2	2
μ (mm ⁻¹)	0.822	0.668	1.890
<i>T</i> (K)	293(2)	293(2)	293(2)
<i>D</i> _{calcd} (g cm ⁻³)	1.488	1.129	1.458
2 θ range (deg)	4.52 to 60.3	3.45 to 29.63	1.48 to 30.55
<i>e</i> data (<i>R</i> _{int})	10701 (0.0897)	12221 (0.0384)	11113 (0.0275)
<i>R</i> 1 (<i>I</i> > 2 σ (<i>I</i>))	0.0513	0.0456	0.0403
<i>wR</i> 2	0.1435	0.1243	0.1287
GOF	1.041	1.096	1.009
Largest diff. peak and hole (e Å ⁻³)	1.112 and -0.785	1.471 and -1.909	2.415 and -1.680
CCDC No.	988125	988126	988127



Careful observation of the packing diagram of **1B** reveals that it is actually an assembly of one dimensional (1D) polymeric chains composed of corrolato-tin(IV)-chloride molecules interconnected by intermolecular C–H···Cl hydrogen bonding interaction (Figure 3.12). The C–H···Cl hydrogen bonding interaction²⁵⁹⁻²⁶¹ [Bonding parameters of C–H···Cl; H···Cl: 2.848 Å; C···Cl: 3.405 Å; ∠C–H···Cl: 119.72°] is the driving force for this kind of supramolecular 1D chain formation and this interaction is rather genuine in nature as is shown by its bonding parameters in the bracket. However these one-dimensional (1D) polymeric chains in **1B** are not interconnected instead they are independent of each other. π - π stacking interactions (the shortest distance between two carbon atoms of the interacting rings was 3.98 Å) exist between the C36–C37–C38–C39–C40–C41 (phenyl ring) and



C20–C2–C22–C23–C24–C25 (phenyl ring) in the packing diagram. C–H \cdots π interactions also exist in the structure, e.g. between C24–H24 and C36–C37–C38–C39–C40–C41 (phenyl ring), C37–H37 and N2–C6–C7–C8–C9 (pyrrole ring). Due to the distorted square-pyramidal geometry around the central metal atom, the pyrrole ring nitrogen atoms deviate from the 19-atom corrole carbon ring by distances of 0.1239–0.4317 Å in case of **2B** also. The *meso*-substituted phenyl rings make dihedral angles ranging from 47.204–65.049° with the corrole plane. Analysis of the packing diagram of **2B** reveals that two neighbouring corrolato-tin(IV)-chloride molecules are interconnected by intermolecular C–H \cdots Cl hydrogen bonding interactions and form a dimer (Figure 3.13a). The C–H \cdots Cl hydrogen bonding interaction [Bonding parameters of C18–H18 \cdots C11; H18 \cdots C11: 3.051 Å; C18 \cdots C11: 3.849 Å;



$\angle\text{C18-H18}\cdots\text{C11}$: 144.70°] dictates this kind of dimer formation. The distance between two tin(IV) ion in the dimer is 6.985 \AA . However these dimers are not interconnected instead they are arranged independently in a particular fashion throughout the crystal lattice. Along the crystallographic *b*-axis, they form rectangular channel (dimension = $16 \times 7 \text{ \AA}$) like arrangements (Figure 3.13b). π - π stacking interactions (the shortest distance between two carbon atoms of the interacting rings was 3.38 \AA) exist between the C34–C35–C36–C37–C38–C39 (phenyl ring) and the all four pyrrole rings of corrole in the packing diagram. In addition to that, π - π stacking interactions also exist between the N3–C11–C12–C13–C14 (pyrrole ring) and N4–C16–C17–C18–C19 (pyrrole ring). Pyrrole ring nitrogen atoms undergo deviation by distances ranging from (-0.3179) - $(+0.0619) \text{ \AA}$ with respect to the corrole plane in **3B**. Dihedral angles between the *meso*-substituted phenyl rings and

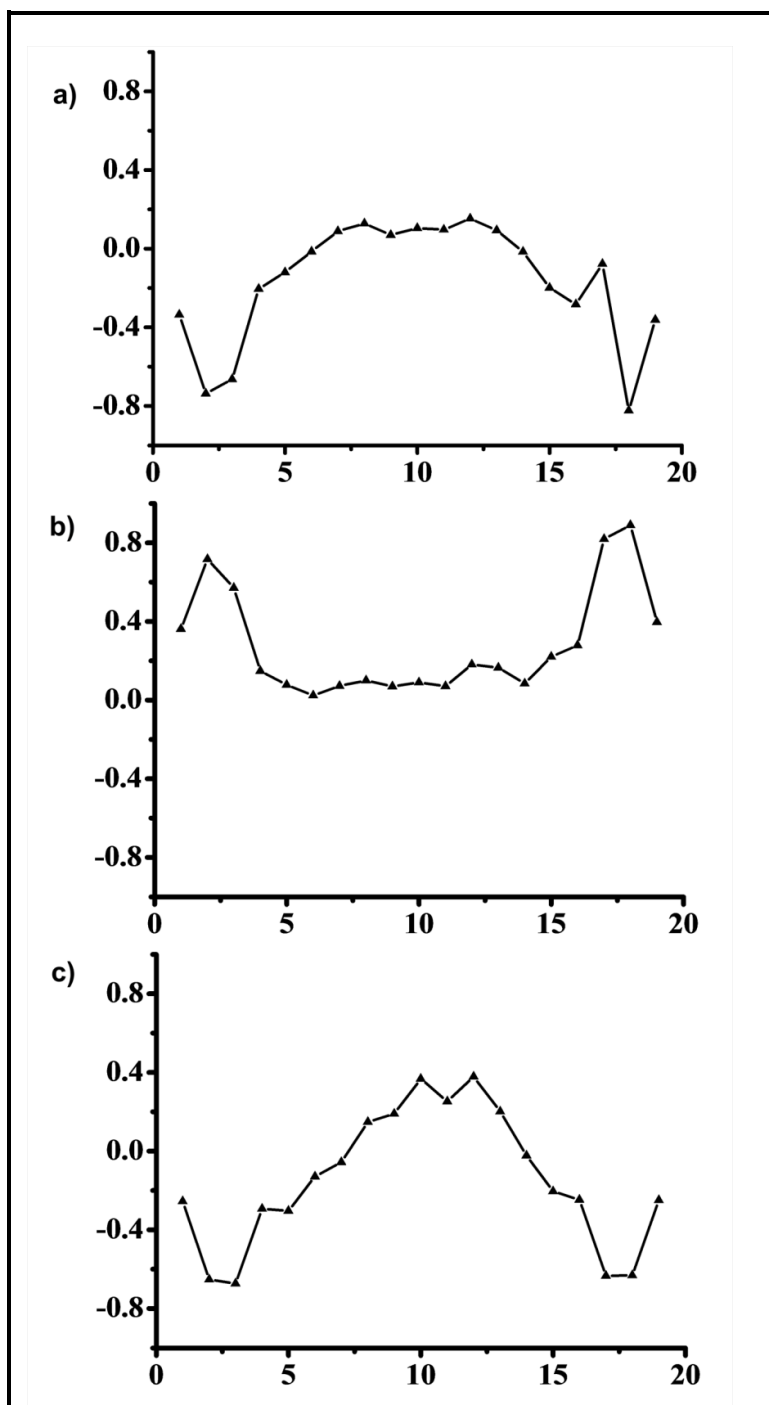
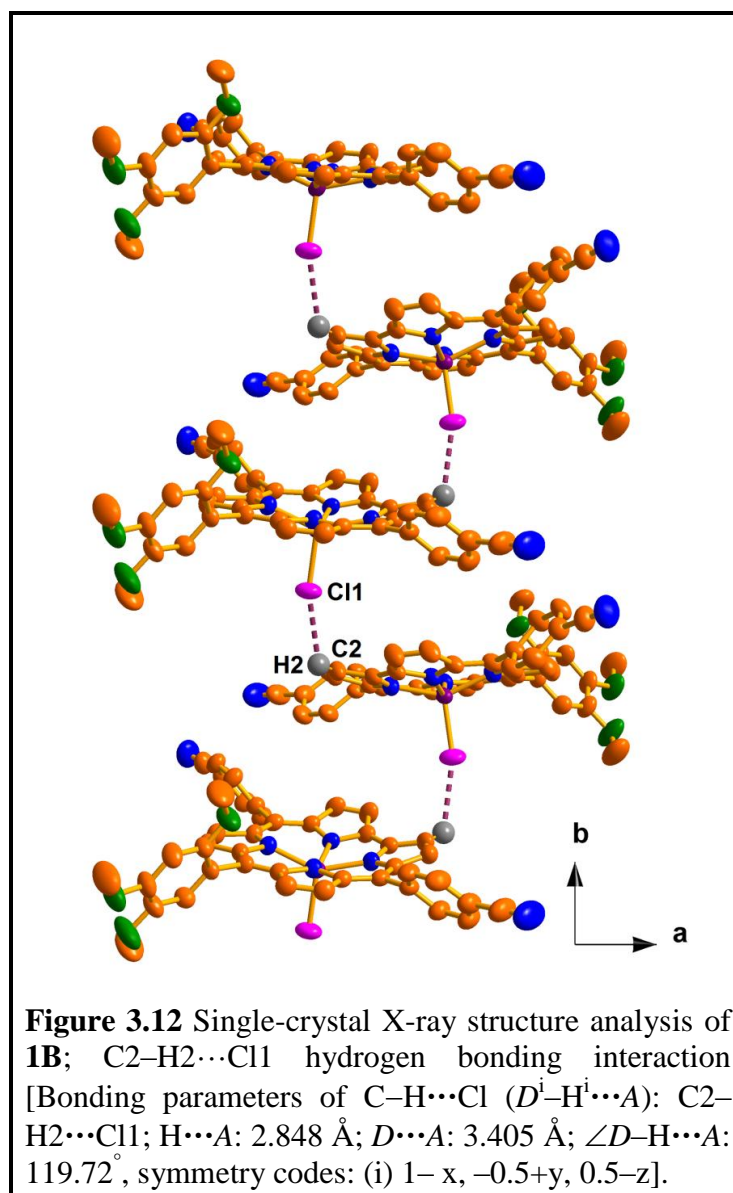
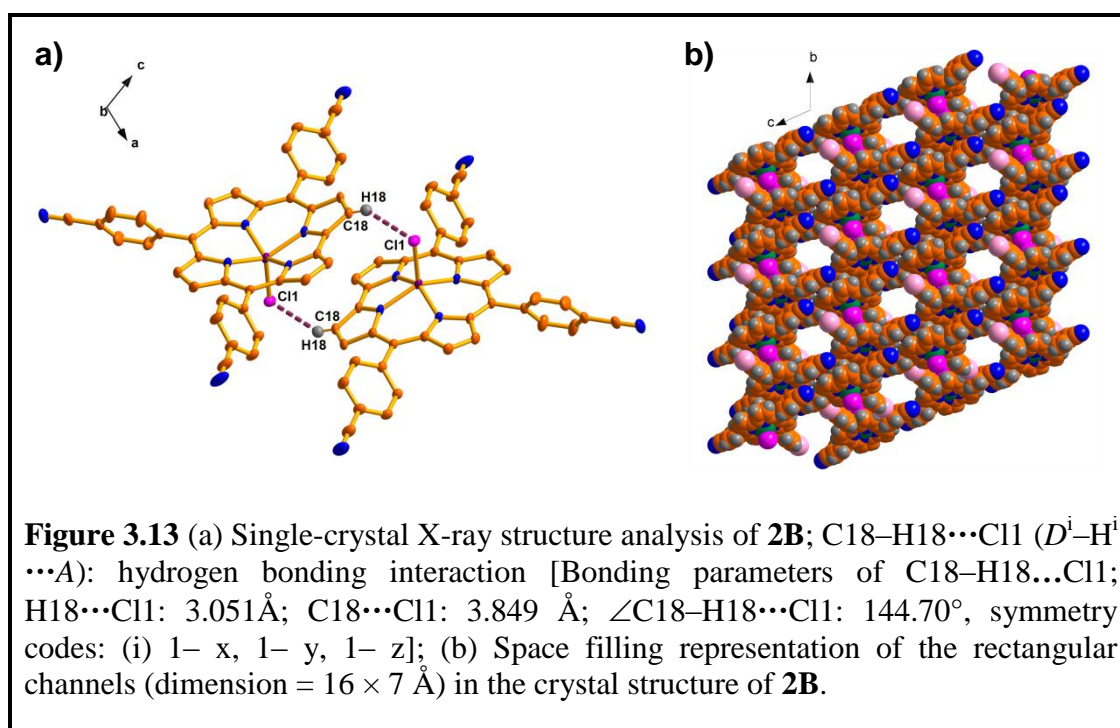


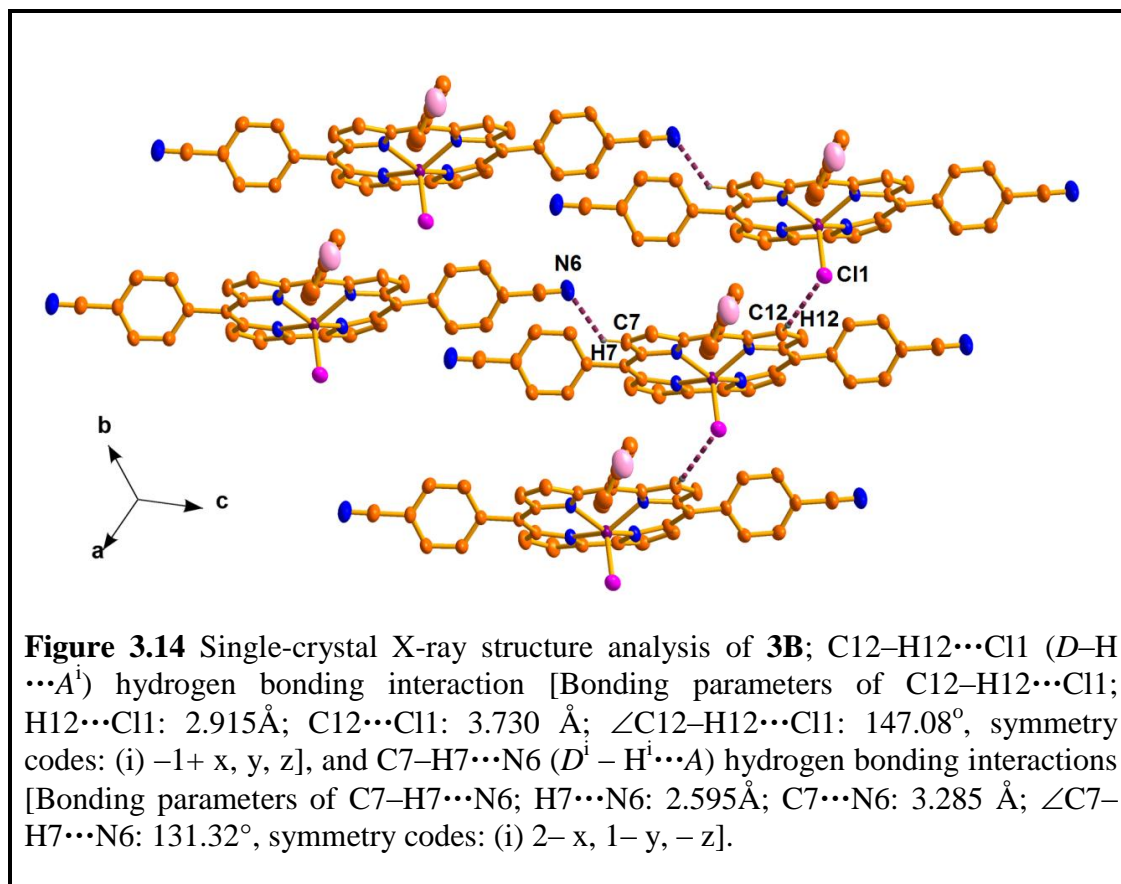
Figure 3.11 Vertical displacement of the peripheral carbon atoms from the N4 corrole planes in (a) **1B** (b) **2B** and (c) **3B**.



the corrole plane range from 48.727–61.52°. In the packing diagram of the corrolato-tin(IV)-chloride molecules (**3B**), cyanide and bromide groups of two adjacent corrolato-tin(IV)-chloride molecules are facing towards the same direction. The distance between two neighbouring tin(IV) ion is 8.258(5) Å. The packing diagram of **3B** indicates that it is actually an assembly of one dimensional (1D) linear polymeric chains composed of corrolato-tin(IV)-chloride molecules, interconnected by intermolecular C–H···Cl hydrogen bonding interaction. This kind of supramolecular 1D linear chain formation is mainly aided by the C–H···Cl hydrogen bonding interactions [Bonding parameters of C–H···Cl; H···Cl: 2.915 Å; C···Cl: 3.730 Å; $\angle C$ –

$\text{H}\cdots\text{Cl}$: 147.08°] (Figure 3.14). Two of these linear 1D polymeric chains in **3B** are interconnected by $\text{C}-\text{H}\cdots\text{N}$ hydrogen bonding interactions [Bonding parameters of $\text{C}-\text{H}\cdots\text{N}$; $\text{H}\cdots\text{N}$: 2.595 \AA ; $\text{C}\cdots\text{N}$: 3.285 \AA ; $\angle\text{C}-\text{H}\cdots\text{N}$: 131.32°] and forms a duplex structure. Thus the tin corroles, as described herein, can assemble on intermolecular level through $\text{C}-\text{H}\cdots\text{Cl}$ hydrogen bonding interactions. $\text{H}\cdots\text{Cl}$ distances are 2.848 \AA , 3.051 \AA , and 2.915 \AA for **1B**, **2B**, and **3B** respectively. In addition, $\angle\text{C}-\text{H}\cdots\text{Cl}$ angles are 119.72° , 144.70° , and 147.08° for **1B**, **2B**, and **3B** respectively. Although these distances are very close to the van der Waals cut-off distance (3.0 \AA) for $\text{H}\cdots\text{Cl}$ hydrogen bonding, however, a plenty of literature reports suggest that these interactions should be considered as genuine $\text{C}-\text{H}\cdots\text{Cl}$ hydrogen bonding interactions²⁵⁹⁻²⁶². Fine tuning of these intermolecular hydrogen bonding interactions leads to different kind of architectures; linear chains, and molecular sieves. For the three of the





above mentioned 1D supramolecular network, it was observed that one forms dimers and in other two form 1D infinite polymer chains.

3.2.3 Self Aggregates of Tin(IV) Corroles

The nano-aggregates of tin corroles were developed in dichloromethane and petroleum ether solvent mixture and, after drop casting, were dried in open air, on a silicon wafer. The generated aggregates were then examined by using SEM and AFM techniques. The SEM images of the aggregates are shown in Figures 3.15 and 3.17. In the case of complexes **1B** and **3B**, well defined and nicely organized three-dimensional hollow nanospheres with diameter of *ca.* 676 nm (Figures 3.15 and 3.16) and 661 nm (Figures 3.17 and 3.18) were obtained. However in the case of complex **2B**, no such three-dimensional well organized objects were obtained. These observations can be explained with the help of Srinivasarao's model²⁶³. According to

this model, any molecular material, when dissolved in a solvent or solvent mixture denser than water and dried in open air, gives rise to two-dimensional air bubbles for those molecules where negligible intermolecular interactions exist and three-dimensional networks for those molecules where there is a significant intermolecular interaction. In the present study, as the density of the DCM is higher than that of water and because of the presence of significant intermolecular interaction in the complexes **1B**, and **3B**, three-dimensional well organized objects were formed in **1B** and **3B** only. With reference to this, it should be mentioned here, that from X-ray crystal structure analysis it has been observed that intermolecular interactions resulted in the formation of 1D infinite polymer chains in **1B** and **3B** only but not in the case of **2B**. The justification behind the formation of three-dimensional objects with specific morphology can be understood with the help of solute-solvent interaction during the solvation processes which affects the thermodynamic and kinetic factors for the generation of aggregates²⁶⁴⁻²⁶⁶. EDX analysis of the individual nanospheres obtained from **1B** molecules clearly confirm their composition and it indicates that spheres are actually composed of **1B** molecules only (Figure 3.19).

All the elements of **1B** are present in these spheres and their weight percentages are also very close to their actual weight percentages in the **1B** molecules. EDX analysis of the individual nanospheres obtained from **3B** molecules also generates same information like **1B** molecules (Figure 3.20)

3.2.4 *I-V* Characteristics and CAFM Measurements

A device was fabricated with the following composition: Ag/ITO-coated glass/**1B**-nanospheres/ITO-coated glass/Ag (Figure 3.21a). Figure 3.21b shows *I-V* characteristics of the device. From the *I-V* characteristics, it appears that the current

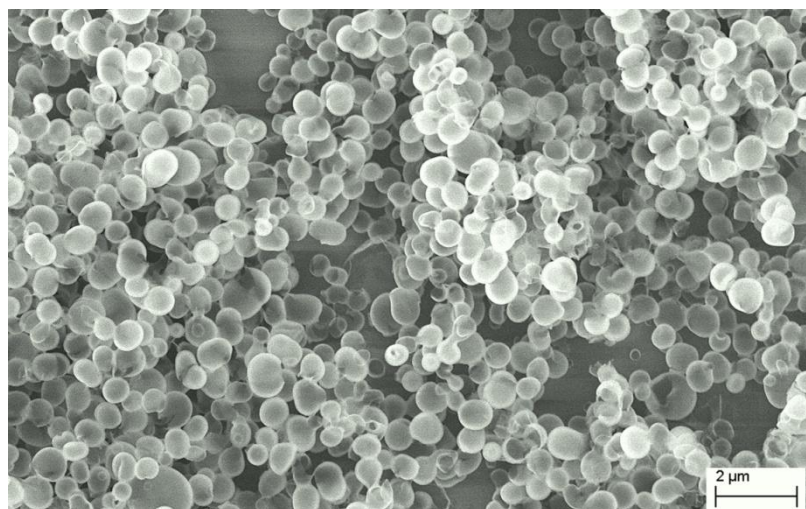


Figure 3.15 SEM images of **1B** nanospheres in DCM-Hexane mixture.

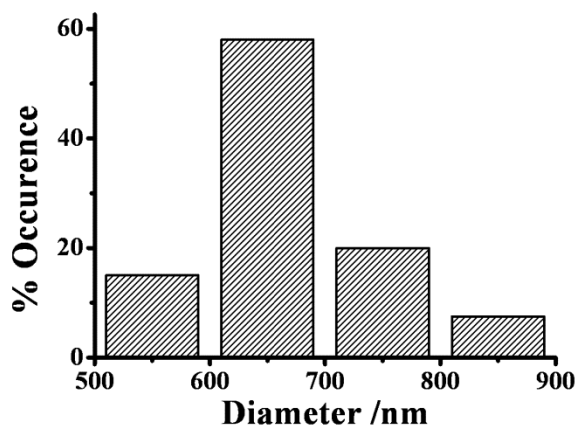


Figure 3.16 Particle size distribution histograms of **1B** nanospheres.

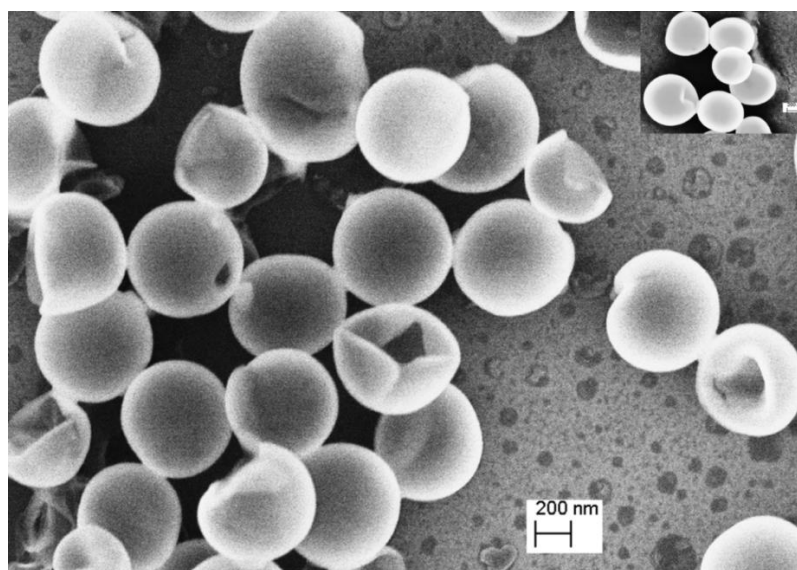
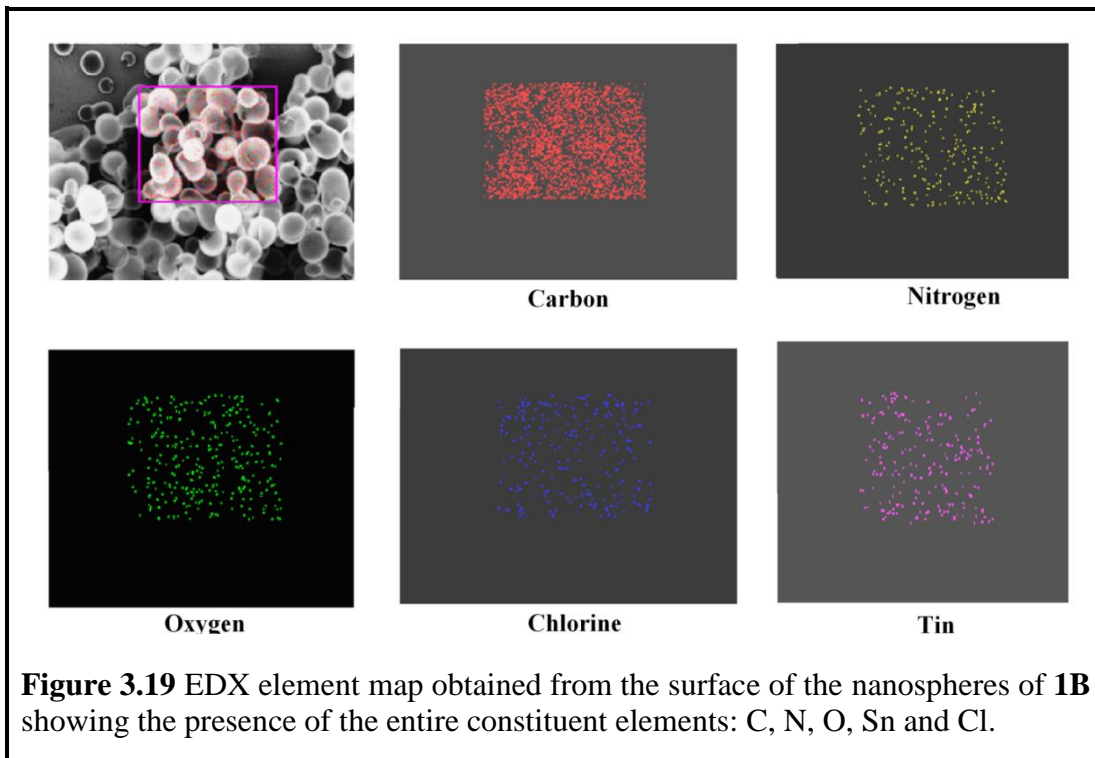
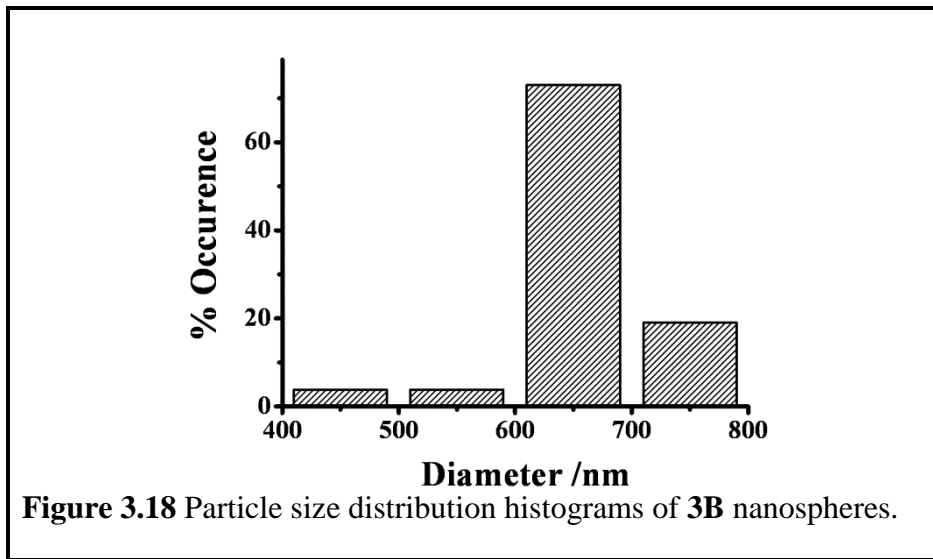


Figure 3.17 SEM images of **3B** nanospheres in DCM-Hexane mixture.



increases linearly with increasing voltage, indicating the Ohmic characteristic of the device. It also appears that the potential barrier at the interface between the ITO/**1B**-nanospheres is very low. The resistance of the nanostructured film, generated from **1B**-nanospheres, has been obtained from the reciprocal of the slope of the I - V plot. The observed resistance was found to be $\sim 4.8 \times 10^7 \Omega$. From the I - V plots, it appears that the Ohmic characteristic of the device is maintained up to +10 V. This

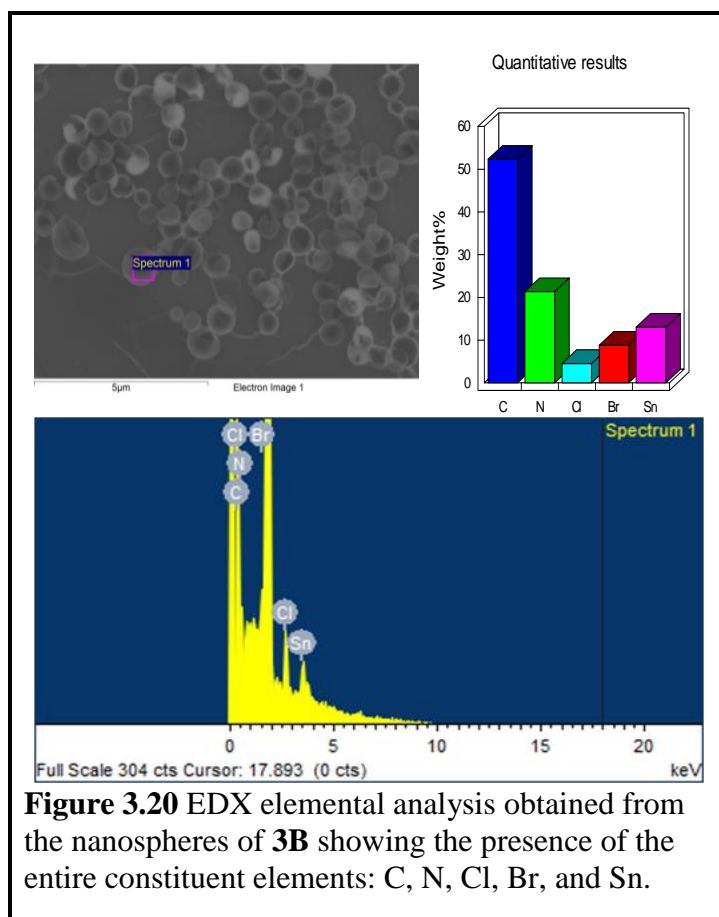
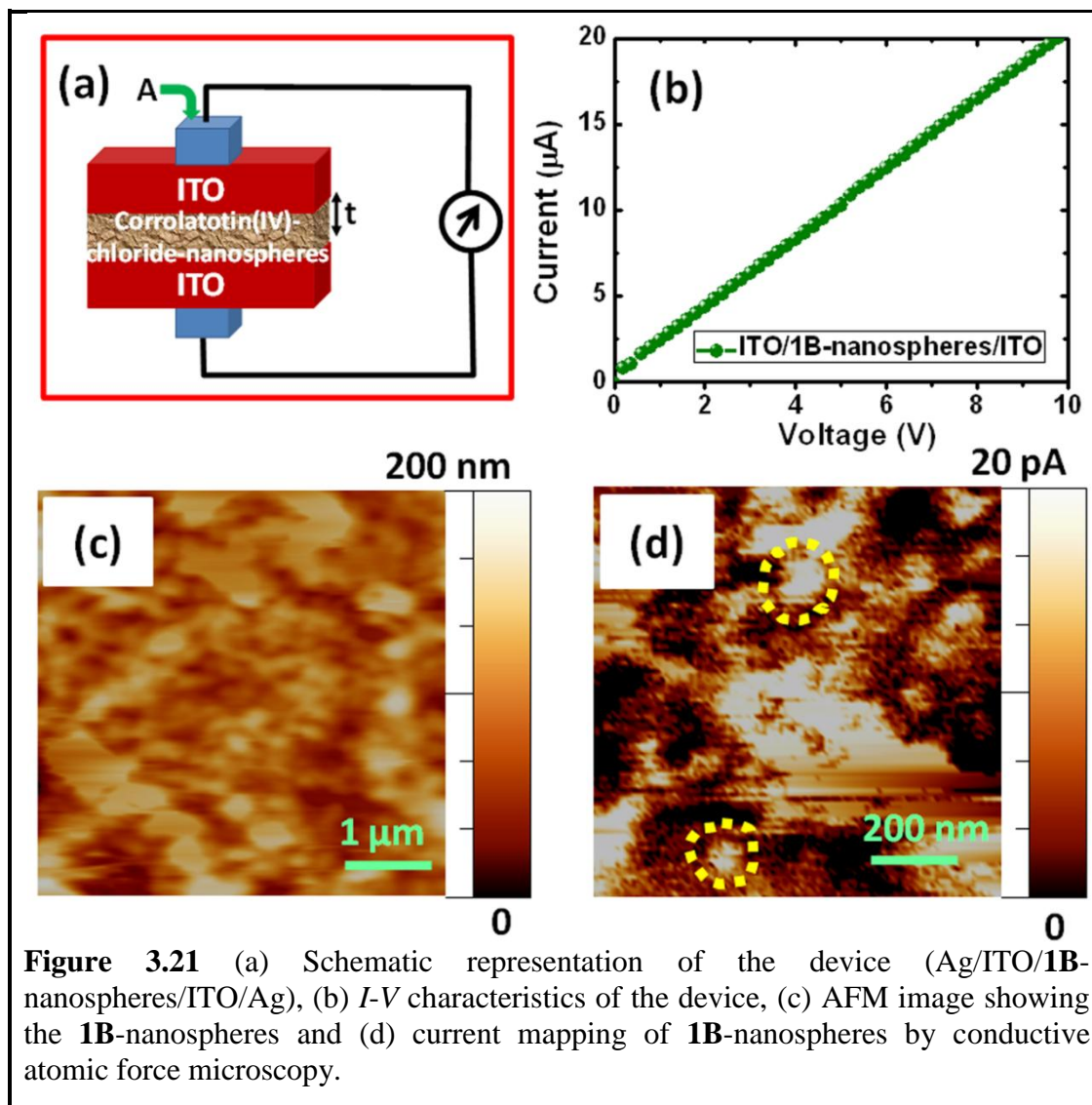


Figure 3.20 EDX elemental analysis obtained from the nanospheres of **3B** showing the presence of the entire constituent elements: C, N, Cl, Br, and Sn.

observation is a significant improvement from the earlier values as reported by Schwab *et al.*²⁶⁷. They used the self-assembled nanorods obtained from *meso*-tetrakis(4-sulfonatophenyl)porphine for the first time and observed that in the dark it acts like an insulator in the voltage range of -0.5 to $+0.5$ V, with a resistance of $2.4 \times 10^8 \Omega$. This resistance value is very close to our observed resistance value. The resistivity (ρ) of the nanostructured film was obtained by using the equation²⁶⁸: $\rho = RA/t$, where R is the resistance, A is the effective area of the electrode, and t is the thickness of the nanostructured film (Figure 3.21a). The effective thickness of the nanostructured film was confirmed from the AFM height profile, it turned out to be ~ 200 nm (Figure 3.21c) and thus, perfectly suits for device application. By making an assumption that the thickness of the nanostructured film is uniform over the ITO surface, the resistivity (ρ) of the device was calculated to be $\sim 2.4 \times 10^8 \Omega \cdot \text{cm}$ and was

found to fall in the zone of semi-insulating materials. These semi-insulators have found extensive applications in developing high-electron-mobility transistors. To understand the current conduction pathways in the device and also the local electrical properties, conductive atomic force microscopy (CAFM) measurements of the **1B**-



nanospheres/ITO configuration were performed by using a Pt coated Si tip (radius \sim 30 nm). Stable images were obtained upon continuous scans on different regions of the device and confirm that the molecules are uniformly and strongly bound to the ITO surface. CAFM current maps at 10 V bias show bright spots with 10-20 pA intensity (Figure 3.21d) which indicate that nano-spheres are preferentially electron-

conducting pathways in the device. It is evident from the CAFM measurements that these active domains are spherical in shape with an average size of ~250 nm in diameter (shown by the yellow circle in Figure 3.21d). The semi-insulating behaviour of the nanospheres can be easily understood from the qualitative model described by Schwab *et al.* All the measurements were carried out in dark (i.e., no photo excitation was present during the experiment). We can consider the aggregated tin(IV) corrole based nanospheres as assemblies/groups of Sn(IV) corrole molecules. The spatially localized HOMOs of the tin(IV) corrole molecules²⁶⁹ are the conduction pathways in the device. Because the electron coupling is less in filled HOMOs, therefore, electron transfer occurs mainly through hopping mechanism. Electron transport through filled HOMOs is not at all facile and requires accessing of higher energy levels as discussed in earlier reports^{267, 269}.

3.3 Conclusions

We have presented here the synthesis of three novel tin(IV) corrole derivatives. The purity and identity of these tin(IV) corrole derivatives have been demonstrated by various spectroscopic techniques and elemental analysis. The ¹H NMR spectra of the tin(IV) corrole derivatives show sharp resonances, which indicate their diamagnetic characteristics. Careful observation of the packing diagrams of **1B** and **3B** reveals assemblies of one dimensional (1D) polymeric chains composed of corrolato-tin(IV)-chloride throughout the crystal lattice. The C–H···Cl hydrogen bonding interaction is the driving force for this kind of supra-molecular 1D chain formation. However in case of **2B**, packing diagram indicates that neighbouring corrolato-tin(IV)-chloride molecules are interconnected by intermolecular C–H···Cl hydrogen bonding interactions to form dimers. In the cases of complexes **1B** and **3B**, well defined and

nicely organized three-dimensional hollow nanospheres with diameter of *ca.* 676 nm (**1B**) and 661 nm (**3B**) were obtained (SEM images on silicon wafers). However in the case of complex **2B**, no such three-dimensional well organized objects were obtained. A device was fabricated with the following compositions: Ag/ITO-coated glass/**1B**-nanospheres/ITO-coated glass/Ag. The resistance of the nanostructured film, generated from **1B**-nanospheres, has been obtained from the slope of the *I-V* plot. The observed resistance was found to be $\sim 4.8 \times 10^7 \Omega$, which falls in the range of semi-insulating materials. CAFM current maps at 10 V bias showed bright spots with 10-20 pA intensity confirming the fact that nanospheres are preferentially electron-conducting pathways in the device. The spatially localized HOMOs of the tin(IV) corrole molecules have been speculated to be the conduction pathways in the device. From the obtained resistivity profile, the nanostructured film can be better called as a semi-insulator. These semi-insulating tin(IV) corroles can be useful for the construction of high-electron-mobility transistors (HEMT).

3.4 Experimental Section

3.4.1 Materials

The precursors pyrrole, *p*-chloranil, and 2,4,5-trimethoxybenzaldehyde were purchased from Aldrich, USA. 4-cyano benzaldehyde, 4-bromo benzaldehyde and tin(II) chloride were purchased from Merck, India. Other chemicals were of reagent grade. Hexane and CH₂Cl₂ were distilled from KOH and CaH₂ respectively. For spectroscopy and electrochemical studies HPLC grade solvents were used. The free base corroles 10-(2,4,5-trimethoxyphenyl)-5,15-bis(4-cyanophenyl)corrole, **1A**⁵¹, 5,10,15-tris(4-cyanophenyl)corrole, **2A**⁴⁶, and 10-(4-bromophenyl)-5,15-bis(4-cyanophenyl)corrole, **3A**⁵¹ were prepared according to published procedures.

3.4.2 Physical Measurements

UV–Vis spectral studies were performed on a Perkin–Elmer LAMBDA-750 spectrophotometer. Emission spectral studies were performed on a Perkin Elmer, LS 55 spectrophotometer using optical cell of 1 cm path length. The elemental analyses were carried out with a Perkin–Elmer 240C elemental analyzer. The NMR measurements were carried out using a Bruker AVANCE 400 NMR spectrometer. Chemical shifts are expressed in parts per million (ppm) relative to residual chloroform ($\delta = 7.26$). Electrospray mass spectra were recorded on a Bruker Micro TOF-QII mass spectrometer. SEM images of the nanoparticles were captured by using a field emission gun scanning electron microscope (FEGSEM) system (Zeiss, Germany make, Supra 55). For fabrication of tin(IV) corrole based devices, ITO-coated glass was used as the substrate. The electrical transport property of Ag/ITO-coated glass/**1B**-nanospheres/ITO-coated glass/Ag was measured by studying *I-V* characteristics using a source meter (Keithley, 2410) based measurement setup. All measurements were carried out on several sets of samples to ensure the repeatability and reproducibility. Conducting atomic force microscopy (cAFM) was used to measure the local electric properties of the samples. cAFM was carried out by *ex situ* atomic force microscopy (AFM) (Asylum Research, MFP3D) in the contact mode with a Pt coated Si cantilever (from NT-MDT) having a radius of curvature of ~ 35 nm. For each sample, several images were taken from different regions to check the uniformity and to estimate the average conducting area.

3.4.3 Crystal Structure Determination

Single crystals of 10-(2,4,5-Trimethoxyphenyl)-5,15-bis(4-cyanophenyl)corrolato-tin(IV)-chloride, **1B**, 5,10,15-tris(4-cyanophenyl)corrolato-tin(IV)-chloride, **2B** and

10-(4-bromophenyl)-5,15-bis(4-cyanophenyl)corrolato-tin(IV)-chloride, **3B** were grown by slow diffusion of solutions of the **1B**, **2B** and **3B** in dichloromethane into hexane, followed by slow evaporation under atmospheric conditions. The crystal data of **1B**, **2B** and **3B** were collected on a Bruker Kappa APEX II CCD diffractometer at 293 K. Selected data collection parameters and other crystallographic results are summarized in Table 3.1. All data were corrected for Lorentz polarization and absorption effects. The program package SHELXTL¹⁹⁵ was used for structure solution and full matrix least squares refinement on F^2 . Hydrogen atoms were included in the refinement using the riding model. Disordered solvent molecules were taken out using SQUEEZE command in PLATON^{196, 270}. CCDC 988125, CCDC 988126, and CCDC 988127 contain the supplementary crystallographic data for **1B**, **2B**, and **3B** respectively.

3.4.4 Synthesis of 10-(2,4,5-Trimethoxyphenyl)-5,15-bis(4cyanophenyl)corrolato-tin(IV)-chloride, **1B**

1B was prepared by slight modifications of the available procedure of corrolato-tin(IV)-chloride synthesis^{31, 50, 95, 143, 255-260}. 100 mg (0.15 mmol) of the free base corrole, **1A** was dissolved in 20 mL of DMF. Then 285 mg (1.50 mmol) of tin(II) chloride was added to the reaction vessel under reflux condition and the stirring was continued till 1 h. Formation of the product was confirmed by TLC examination. The solvent was removed completely by rotary evaporation. The crude product was then purified by column chromatography using silica gel (100-200 mesh) with dichloromethane as eluent. After recrystallization from dichloromethane and hexane, 81 mg (100 μ mol) of pure crystalline compound was collected (66%). Anal. Calcd (found) for $C_{42}H_{27}ClN_6O_3Sn$ (**1B**): C, 61.68 (61.52); H, 3.33 (3.49); N, 10.28 (10.13).

λ_{\max}/nm ($\epsilon/\text{M}^{-1}\text{cm}^{-1}$) in dichloromethane: 423 (176330), 532 (5477), 572 (9850), 605 (24910) (Figure 3.2). ^1H NMR (400 MHz, CDCl_3) δ 9.28-9.25 (m, 2H), 9.09- 9.03 (m, 2H), 8.87-8.85(m, 2H), 8.81-8.79(m, 2H), 8.12 (broad s, 8H), 7.78 (s, 1H), 6.94 (s, 1H), 4.19 (s, 3H), 4.01 (s, 3H), 3.37 (s, 3H). **1B** displayed strong fluorescence at 618.5 nm and 673 nm in dichloromethane (Figure 3.3). The electrospray mass spectrum of **1B** in acetonitrile showed peaks centered at $m/z = 818.07$ corresponding to $[\mathbf{1B}]^+$ (818.08 calcd for $\text{C}_{42}\text{H}_{27}\text{ClN}_6\text{O}_3\text{Sn}$).

3.4.5 Synthesis of 5,10,15-tris(4-cyanophenyl)-corrolato-tin(IV)-chloride, **2B**

2B was synthesized by a procedure similar to **1B**, starting with 100 mg (0.166 mmol) of the free base corrole, **2A** and 315.5 mg (1.66 mmol) of tin(II) chloride. The crude product was purified by column chromatography using silica gel (100-200 mesh) with 20% MeCN and 80% dichloromethane as eluent. After purification, the compound was kept for recrystallization to afford crystals of **2B** (81 mg, 110 μmol , 67%). Anal. Calcd (found) for $\text{C}_{40}\text{H}_{20}\text{ClN}_7\text{Sn}$ (**2B**):C, 63.82 (63.69); H, 2.68 (2.78); N, 13.02 (12.91). λ_{\max}/nm ($\epsilon/\text{M}^{-1}\text{cm}^{-1}$) in dichloromethane: 424 (210000), 532 (10556), 569 (13037), 604 (27927) (Figure 3.2). ^1H NMR (400 MHz, CDCl_3) δ 9.36-9.31 (m, 2H), 9.16- 9.12 (m, 2H), 8.88-8.84 (m, 4H), 8.57 (d, $J = 7.5$ Hz, 2H), 8.35-7.84 (m, 10H). **2B** displayed strong fluorescence at 619 nm and 672.5 nm in dichloromethane (Figure 3.3). The electrospray mass spectrum of 5,10,15-tris(4-cyanophenyl)-corrolato-tin(IV)-chloride, **2B** in acetonitrile showed peaks centered at $m/z = 753.034$ corresponding to $[\mathbf{2B}]^+$ (753.049 calcd for $\text{C}_{40}\text{H}_{20}\text{ClN}_7\text{Sn}$).

3.4.6 Synthesis of 10-(4-Bromophenyl)-5,15-bis(4-cyanophenyl)-corrolato-tin(IV)-chloride, **3B**

3B was synthesized by a procedure similar to **1B**, starting with 100 mg (0.153 mmol) of the free base corrole, **3A** and 290.1 mg (1.53 mmol) of tin(II) chloride. The crude product was then purified by column chromatography using silica gel (100-200 mesh) with 20% MeCN and 80% dichloromethane as eluent. After purification, the compound was kept for recrystallization to afford crystals of **3B** (85 mg, 110 μ mol, 69%). Anal. Calcd (found) for $C_{39}H_{20}BrClN_6Sn$ (**3B**): C, 58.07 (58.52); H, 2.50 (2.60); N, 10.42 (10.79). λ_{max}/nm ($\epsilon/M^{-1}cm^{-1}$) in dichloromethane: 423 (160700), 529 (6680), 570 (7251), 606 (18995) (Figure 3.2). 1H NMR (400 MHz, $CDCl_3$) δ 9.33-9.29 (m, 2H), 9.14- 9.08 (m, 2H), 8.95-8.90 (m, 2H), 8.86-8.81 (m, 2H), 8.30-7.82 (m, 12H). ^{13}C NMR(101 MHz, $CDCl_3$) δ 111.0, 112.1, 116.4, 118.5, 119.1, 122.9, 126.6, 127.3, 129.2, 130.9, 131.0, 131.7, 135.2, 135.4, 136.2, 138.4, 139.6, 140.2, 143.7, 145.0. **3B** displayed strong fluorescence at 618.8 nm and 671 nm in dichloromethane (Figure 3.3). The electrospray mass spectrum of 10-(4-bromophenyl)-5,15-bis(4-cyanophenyl)-corrolato-tin(IV)-chloride, **3B** in acetonitrile showed peaks centered at $m/z = 771.001$ corresponding to $[3B-Cl]^+$ (770.995 calcd for $C_{39}H_{20}BrN_6Sn$).

CHAPTER 4

Reactions of Grignard Reagents with Tin-Corrole Complexes: Demetalation Strategy and σ -Methyl/Phenyl Complexes

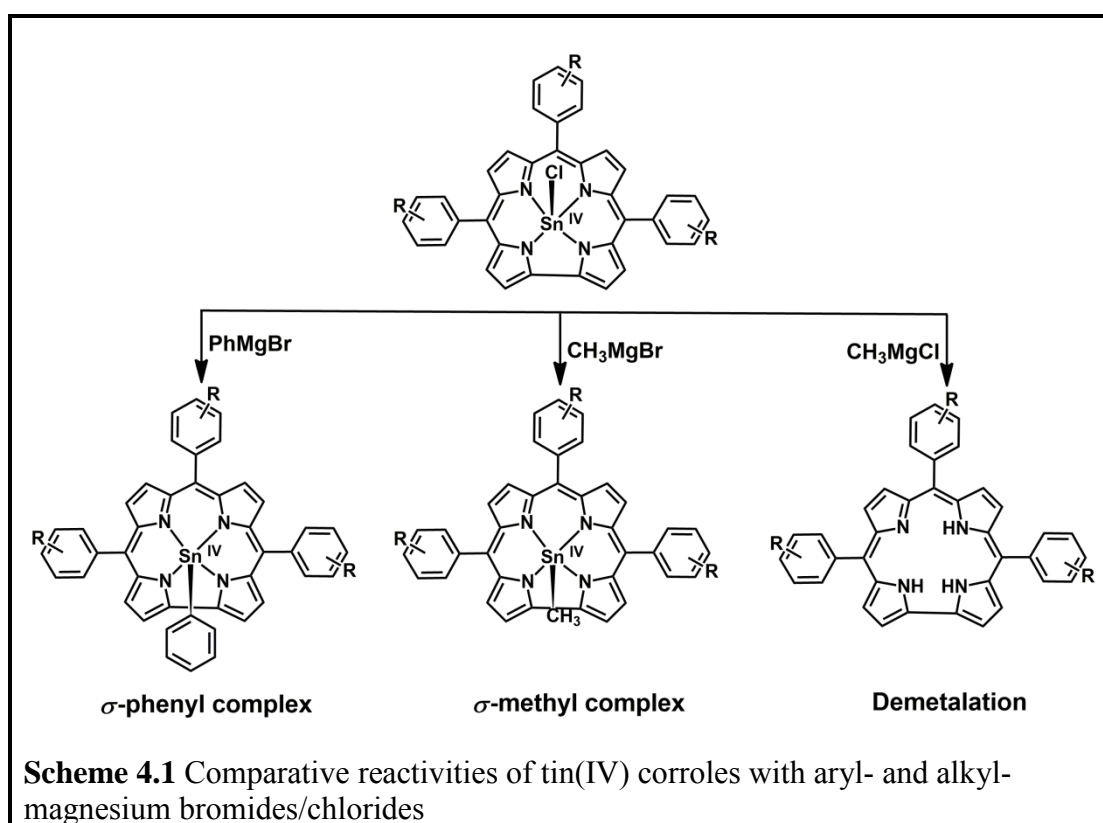
4.1	Introduction	115
4.2	Results and Discussion	118
4.2.1	Exploring Destannation Strategy	118
4.2.2	Proposed Reaction Mechanism	121
4.2.3	Mass Spectroscopy	123
4.2.4	NMR Spectroscopy	124
4.2.5	X-Ray Crystallography	129
4.3	Conclusions	132
4.4	Experimental Section	134
4.4.1	Materials	134
4.4.2	Physical Measurements	134
4.4.3	Crystal Structure Determination	135
4.4.4	Synthesis of 5,10,15-Tris(2,4,5-trimethoxyphenyl)corrole, 4A	135
4.4.5	Synthesis of 5,10,15-Tris(2,4,5-trimethoxyphenyl)corrolato-tin(IV)-chloride, 4B	136
4.4.6	Synthesis of (Phenyl){10-(2,4,5-trimethoxyphenyl)-5,15-bis(4-cyanophenyl)corrolato}tin(IV), 1C	137
4.4.7	Synthesis of (Phenyl){5,10,15-tris(4-cyanophenyl)corrolato}tin(IV), 2C	138
4.4.8	Synthesis of (Methyl){10-(2,4,5-trimethoxyphenyl)-5,15-bis(4-cyanophenyl)corrolato}tin(IV), 1D	139
4.4.9	Synthesis of (Methyl){5,10,15-tris(4-cyanophenyl)corrolato}tin(IV), 2D	140
4.4.10	Synthesis of (Methyl){5,10,15-tris(2,4,5-trimethoxyphenyl)corrolato}tin(IV), 4D	140
4.5	Demetalation	141

4.1 Introduction

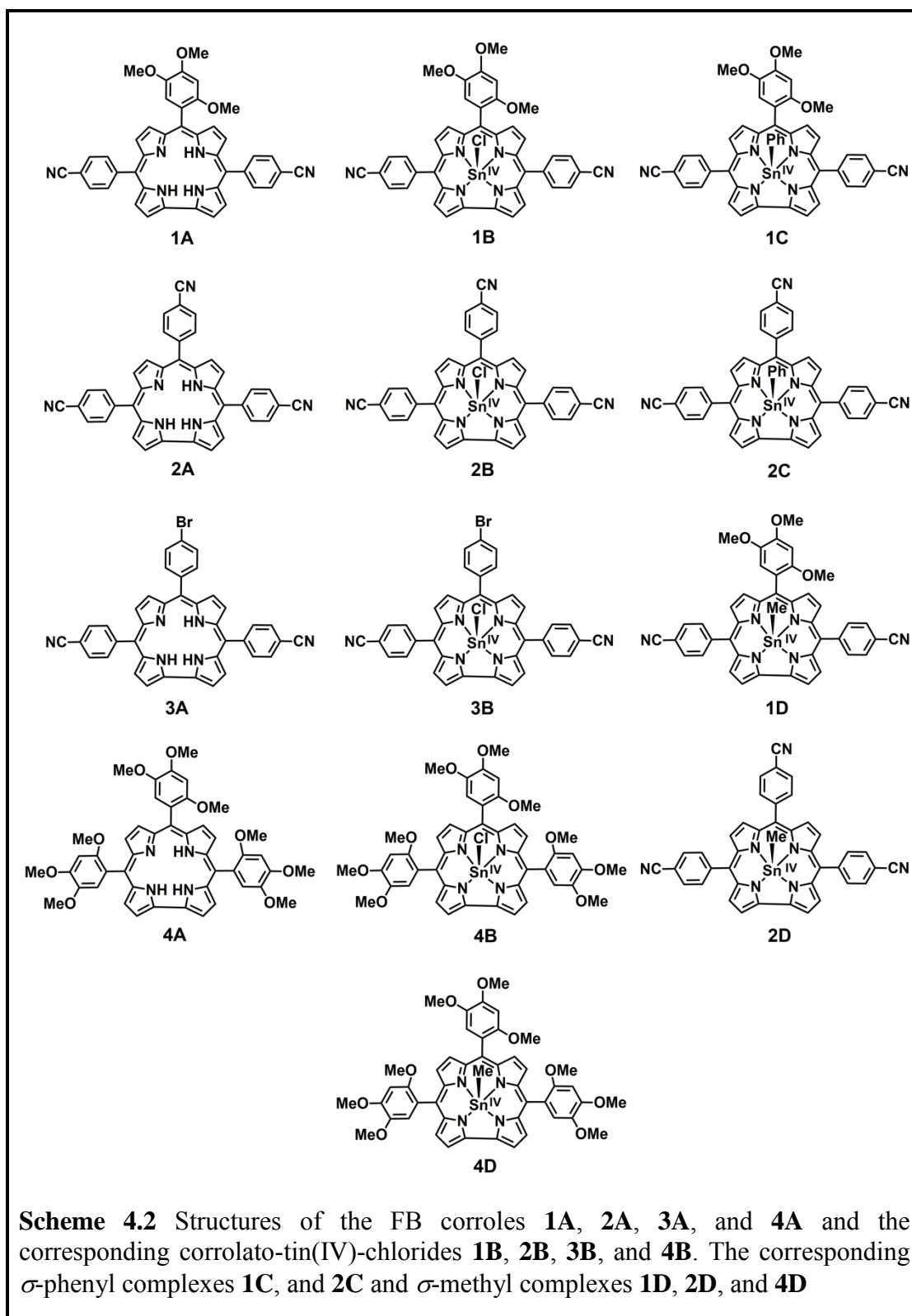
Corrole, a contracted porphyrin analogue, is recently in the forefront of porphyrinoid research because of its versatile application in several realms of chemistry, material science and biology; for example in catalytic reactions, as photosensitizers, sensors, light harvesting materials, and also for therapeutic purposes etc^{2, 65, 66, 71, 80, 137, 217, 218, 230, 235, 250, 271-298}. Because of the lack of suitable synthetic methodologies, corrole chemistry failed to flourish for several decades; however after the discoveries of efficient synthetic methodologies, a renewed interest has developed in the recent years^{2, 65, 66, 71, 80, 137, 217, 218, 230, 235, 250, 271-298}. To understand the unique structure function relationship in corroles, it is of utmost importance to functionalize the corrole macrocycle at the *meso*- and β -positions. It has been already proven that it is easier to functionalize metallocorroles compared to their free-base counterparts. Thus, a suitable methodology to demetalate corroles will definitely help to solve many a riddles in the research and development of corrole chemistry. Unfortunately, there is no generalized protocol available for the demetalation of corrole complexes. To date, very limited information for demetalation and removal of only a few selected metals, like Cu-, Ag- and Mn- from corrole cavities is available¹²⁵⁻¹²⁸.

Tin(IV) porphyrins, bearing highly charged main group metal center, are extensively studied because of their wide application in catalysis, medicine and in nanoscience^{239-241, 243-245, 247, 248}. It has been also observed that tin-porphyrinoids are quite robust in nature and thus a series of postmetalation organic transformations can be easily carried out. Analogically, it can be assumed that tin(IV) corroles, although very less investigated so far, can also serve as a potent candidate with extensive unexplored applications^{50, 138, 167, 250, 252, 255}. Most importantly, the tin(IV) corroles have a diamagnetic ground state, although the photoexcited triplet states are also

reported in the literature, and thus can be easily monitored by NMR spectroscopy^{50, 138, 167, 250, 252, 255}. Substituents, like –CN and –OMe have been chosen in phenyl rings at the periphery of the macrocycle, keeping in mind that they might be used as potential building blocks for the construction of various other corrole-based architectures. Indubitably, a series of organic transformations can be performed in more facile and convenient way in the tin(IV) corroles compared to their free base analogues. However, there is no demetalation protocol available for tin(IV) corroles.



In this chapter, we have observed that corrolato-tin(IV)-chlorides, upon reaction with various Grignard reagents form different products. σ -Phenyl complexes were obtained from corrolato-tin(IV)-chlorides upon treatment with phenylmagnesium bromide. Similarly, σ -methyl complexes resulted from the corresponding corrolato-tin(IV)-chlorides upon reaction with methylmagnesium bromide. Unexpectedly, demetalation was observed exclusively when the



corrolato-tin(IV)-chlorides were subjected to treatment with methylmagnesium chloride (Scheme 4.1). In addition to the development of a new demetalation protocol, the synthesis of one novel A_3 -corrole, namely, 5,10,15-tris(2,4,5-

trimethoxyphenyl)corrole, **4A** and also one novel corrolato-tin(IV)-chloride complex, namely, 5,10,15-tris(2,4,5-trimethoxyphenyl)corrolato-tin(IV)-chloride **4B**, are also described in this chapter (Scheme 4.1). In that connection, two novel σ -phenyl complexes and three novel σ -methyl complexes have also been synthesized, namely (phenyl){10-(2,4,5-trimethoxyphenyl)-5,15-bis(4-cyanophenyl)corrolato}tin(IV), **1C**, (phenyl){5,10,15-tris(4-cyanophenyl)corrolato}tin(IV), **2C**, (methyl){10-(2,4,5-trimethoxyphenyl)-5,15-bis(4-cyanophenyl)corrolato}tin(IV), **1D**, (methyl){5,10,15-tris(4-cyanophenyl)corrolato}tin(IV), **2D**, and (methyl){5,10,15-tris(2,4,5-trimethoxyphenyl)corrolato}tin(IV), **4D** (Scheme 4.2). All the above-mentioned complexes have been thoroughly characterized by various spectroscopic techniques including single crystal X-ray structural analysis of the representative complexes. To establish the demetalation strategy, three of the corrolato tin(IV) chlorides discussed in Chapter 3, viz. **1B**, **2B** and **3B** have been also utilized.

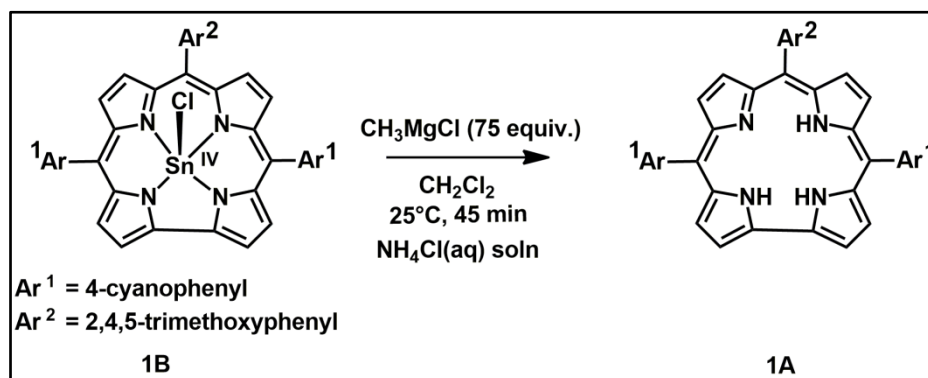
4.2 Results and Discussion

4.2.1 Exploring Destannation Strategy

Corrolato tin(IV)chlorides, when treated with a series of different Grignard reagents, yielded an unusual type of products in addition to the routine σ -bonded organometallic compounds. The Grignard reagents used were phenylmagnesium bromide, methylmagnesium bromide and methylmagnesium chloride. It was indeed a serendipity that corrolato-tin(IV)-chlorides, upon treatment with methylmagnesium chloride, at room temperature in dichloromethane solvent and in stirring condition for 45 min, at an inert atmosphere resulted in the formation of corresponding free-base (FB) corroles (Table 4.1). It was also observed that the obtained yields for this new reaction are also quite high. In the quest for understanding the scope of this new

reaction, a series of different reaction conditions have been screened. The most interesting part of this reaction is that this demetalation reaction is highly specific to

Table 4.1 Optimization of the Destannation Reaction (**1B** to **1A**)



Equiv. of CH ₃ MgCl	Yield (%) of 1A
25	20
50	60
75	90
100	70

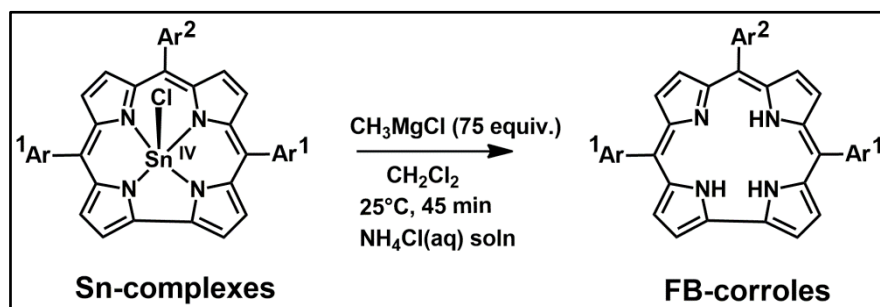
Table 4.2 Formation of σ -Bonded Tin(IV)-Corrole Complexes

	RMgX	Reactant	Product	Yield (%)
1	C ₆ H ₅ MgBr	1B	1C	80
2	C ₆ H ₅ MgBr	2B	2C	85
3	CH ₃ MgBr	1B	1D	85
4	CH ₃ MgBr	2B	2D	87
5	CH ₃ MgBr	4B	4D	80

Grignard reagent used. For three of the above-mentioned Grignard reagents, it was observed that, in the first two cases, the usual σ -methyl and σ -phenyl complexes were obtained (Table 4.2). However in the third case, by using the methylmagnesium

chloride, the product was completely unexpected and we have obtained the free base corroles in good yields. This destannation reaction was applicable to a large varieties of corrolato-tin(IV)-chlorides and the resultant free base corroles were always

Table 4.3 Scope of the Destannation Reaction



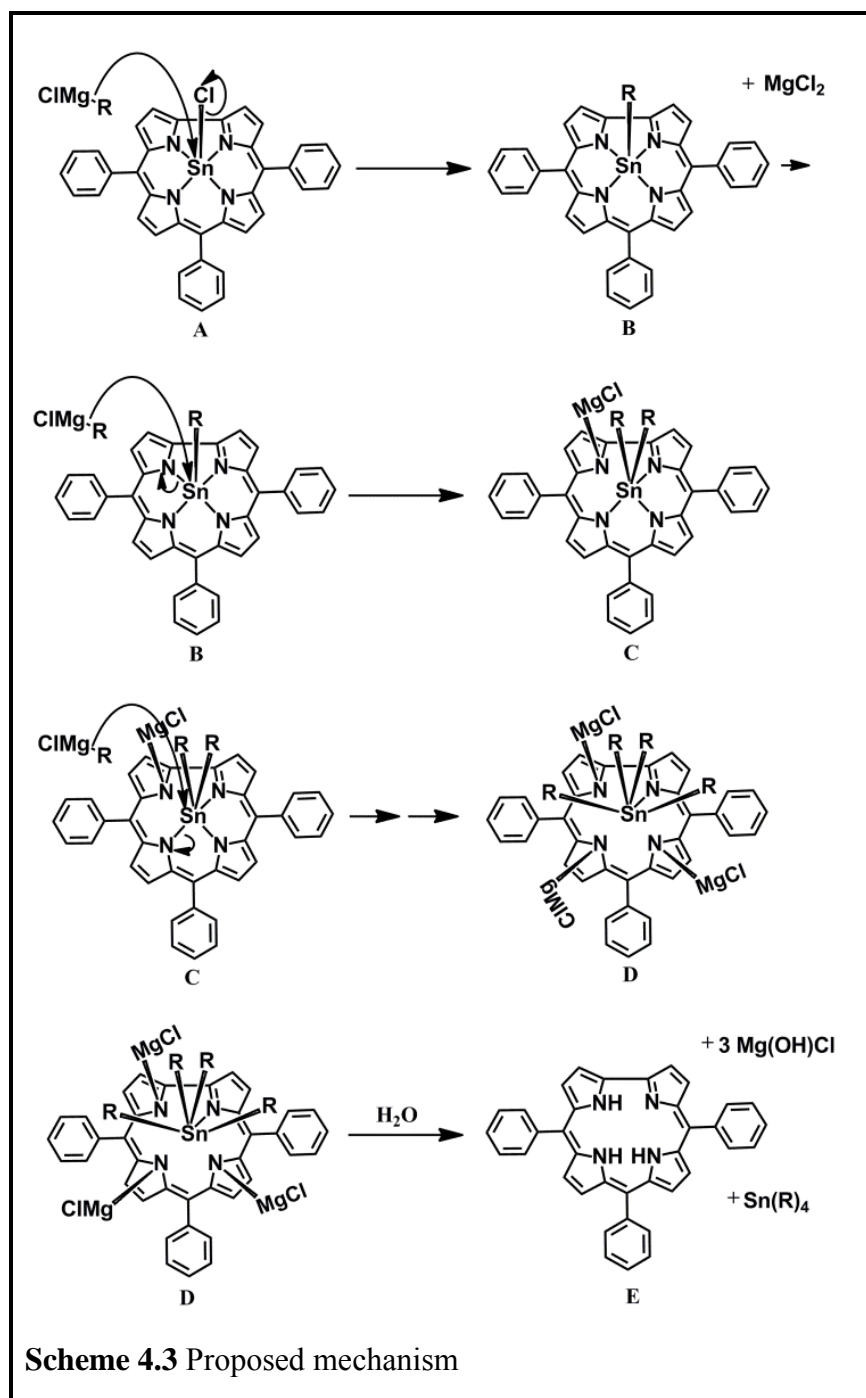
	Sn-complexes → FB-corroles	Yield (%)
1	1B → 1A	90
2	2B → 2A	56
3	3B → 3A	53
4	4B → 4A	50

obtained in considerable yields. A visual color change from deep reddish green to green coloration gives a firsthand idea of the completeness of the reaction. The destannation reactions can be easily monitored by TLC, UV-vis, ^1H NMR or by ESI-MS techniques. However, it is interesting to note that, contrary to that observed by Paolesse *et al.* no isocorrole species were detected in the present case ²⁹⁹. Optimization of the destannation reaction was performed taking **1B** as the representative (Table 4.1). The initial approach was limited to the addition of 25 equivalents of the Grignard reagent. At this point, conversion of corrolato-tin(IV)-chlorides to FB corrole was not fully achieved; thus, we suspected that the conversion of FB corrole might increase with the addition of more equivalents of the Grignard reagent. To our delight, increasing the number of equivalents of Grignard reagent

resulted almost full conversion of the corrolato-tin(IV)-chlorides to FB corroles. After identifying the appropriate reaction conditions, we have attempted to explore the limitations and scope of the demetalation reaction. The reaction is indeed very successful for it gave the desired products in good yields for a wide range of substrates (Table 4.3). Corrolato-tin(IV)-chlorides with both the electron-rich and electron-poor *meso*-aryl substituents turned out to be very effective substrates and demetalation was observed in all the cases studied. Corrolato-tin(IV)-chlorides bearing halogen substituents such as bromide on their *meso*-aryl groups, also underwent the demetalation reaction nicely, giving considerable yield of the free base corrole (Table 4.3). As expected the reaction also tolerated potentially reactive substituents such as cyanide.

4.2.2 Proposed Reaction Mechanism

A mechanism has also been proposed for the demetalation reactions (Scheme 4.3). The mechanism has been proposed based on the earlier reports of demetalation reactions for nickel porphyrins by Grignard reagents as reported by Osuka *et. al*³⁰⁰. The first step of the reaction proceeds via nucleophilic attack of the methylmagnesium chloride on the central tin(IV) ion of corrolato-tin(IV)-chloride (**A**) and gives rise to the σ -methyl tin(IV) corrole derivative (**B**) and generates MgCl₂ as a side product. It can be concluded that in the other two Grignard reagents, like, phenylmagnesium bromide and methylmagnesium bromide, the reaction stops exclusively in the first step and thus affords the σ -methyl/ σ -phenyl tin(IV) corrole derivatives exclusively. Although the first step of this reaction mechanism holds good for two of the above-mentioned Grignard reagents, however it does not hold good for the third Grignard

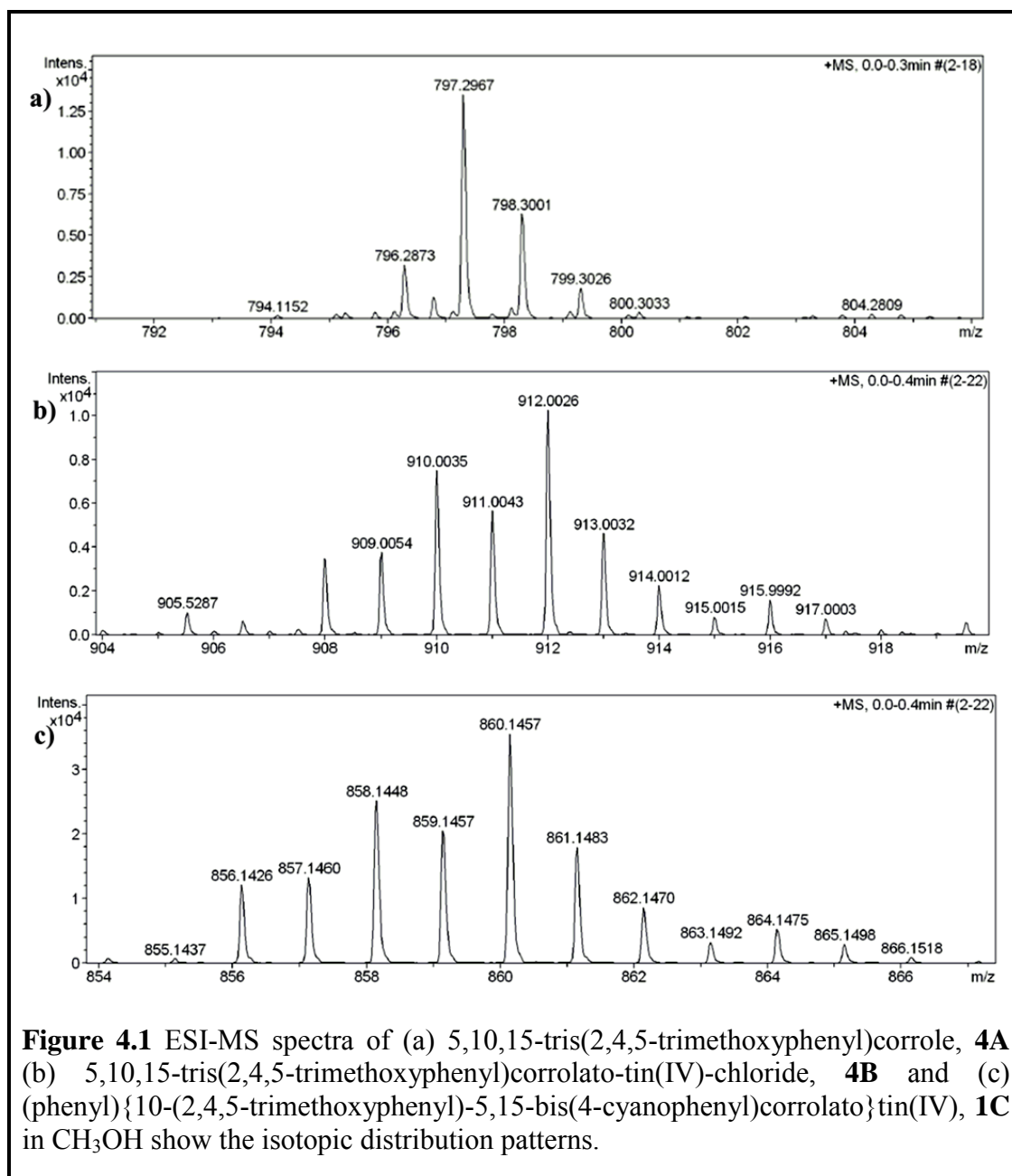


reagent, i.e. methylmagnesium chloride. It is also well-known that RMgBr and RMgI are less-basic and hence less-reactive than RMgCl . In case of methylmagnesium chloride, we believe that the reaction does not stop at the first step. In the consecutive steps, the σ -methyl tin(IV) corrole derivatives are further attacked by methylmagnesium chloride. It consequently leads to the generation of a new dimethyl tin(IV) corrole and simultaneously a tin–nitrogen bond is cleaved and the MgBr gets

attached with one inner ring nitrogen atom. In that way, up to four units of methyl groups can get attached with the tin(IV) ion and three units of MgBr are also expected to get attached with three inner ring nitrogen atoms. Finally in presence of water, all the Mg–N bonds and Sn–N bonds are broken to provide free base corroles, tetramethyltin, and Mg(OH)Cl.

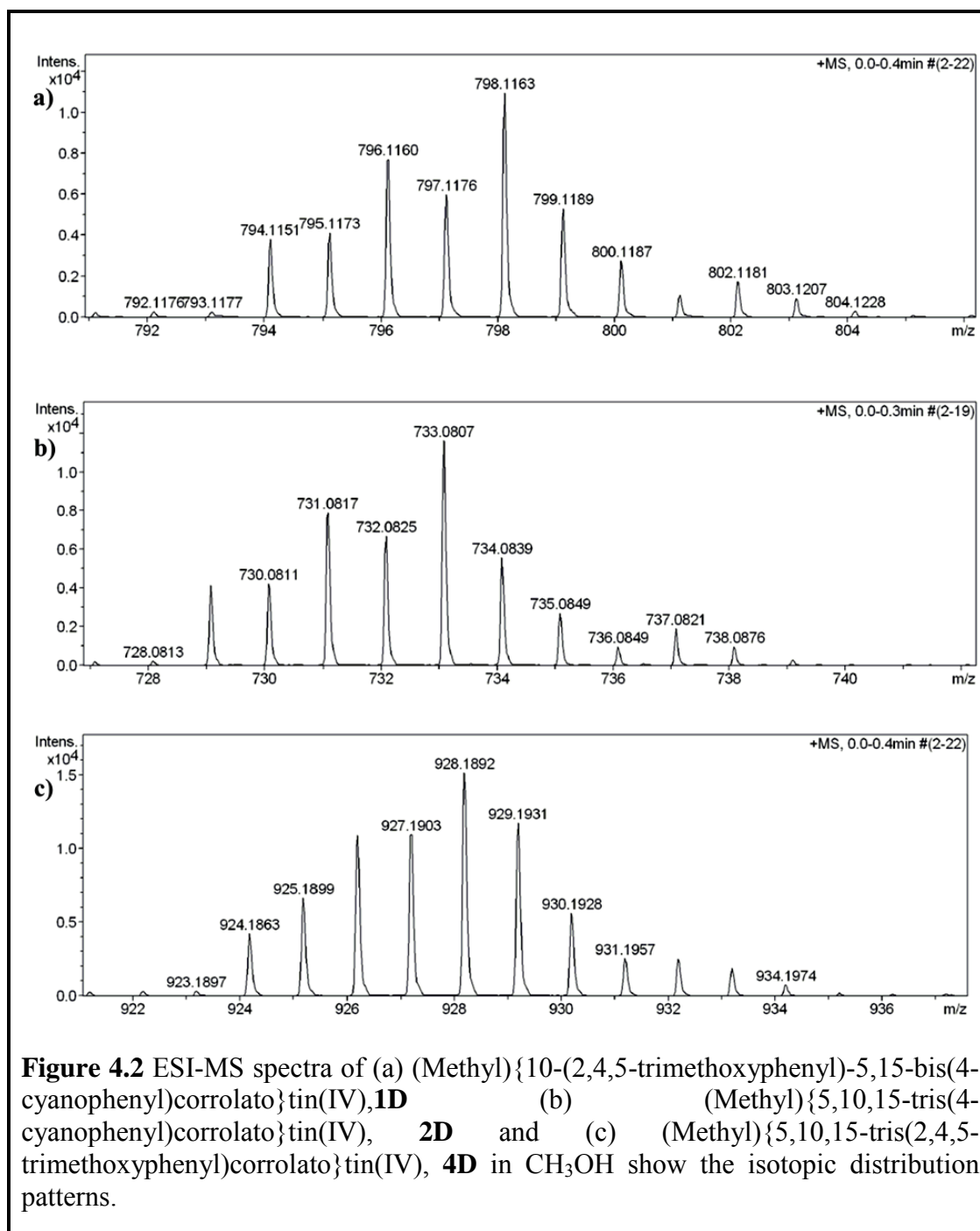
4.2.3 Mass Spectroscopy

The electrospray mass spectrum of the corrole, **4A**, reported in this chapter, shows peaks centered at $m/z = 797.297$ corresponding to $[\mathbf{4A+H}]^+$ (796.310 calcd for $C_{46}H_{44}N_4O_9$) (Figure 4.1a). The corresponding tin(IV) corrole complex, **4B** was characterized by the mass peak centered at $m/z = 912.003$ corresponding to $[\mathbf{4B-Cl}]^+$ (913.189 calcd for peak centered at $m/z = 912.003$ corresponding to $[\mathbf{4B-Cl}]^+$ (913.189 calcd for $C_{46}H_{41}N_4O_9Sn$) (Figure 4.1b). σ -phenyl tin(IV) corrole, **1C** was found to exhibit peaks centered at $m/z = 860.146$ corresponding to $[\mathbf{1C}]^+$ (860.156 calcd for $C_{48}H_{32}N_6O_3Sn$) (Figure 4.1c). The electrospray mass spectrum of the σ -methyl tin(IV) corrole complexes, **1D**, **2D** and **4D** exhibit peaks at m/z values of 798.116, 733.081 and 928.189 corresponding to $[\mathbf{1D}]^+$ (798.14 calcd for $C_{43}H_{30}N_6O_3Sn$) (Figure 4.2a), $[\mathbf{2D}]^+$ (733.104 calcd for $C_{41}H_{23}N_7Sn$) (Figure 4.2b) and $[\mathbf{4D}]^+$ (928.213 calcd for $C_{47}H_{44}N_4O_9Sn$) (Figure 4.2c) respectively.

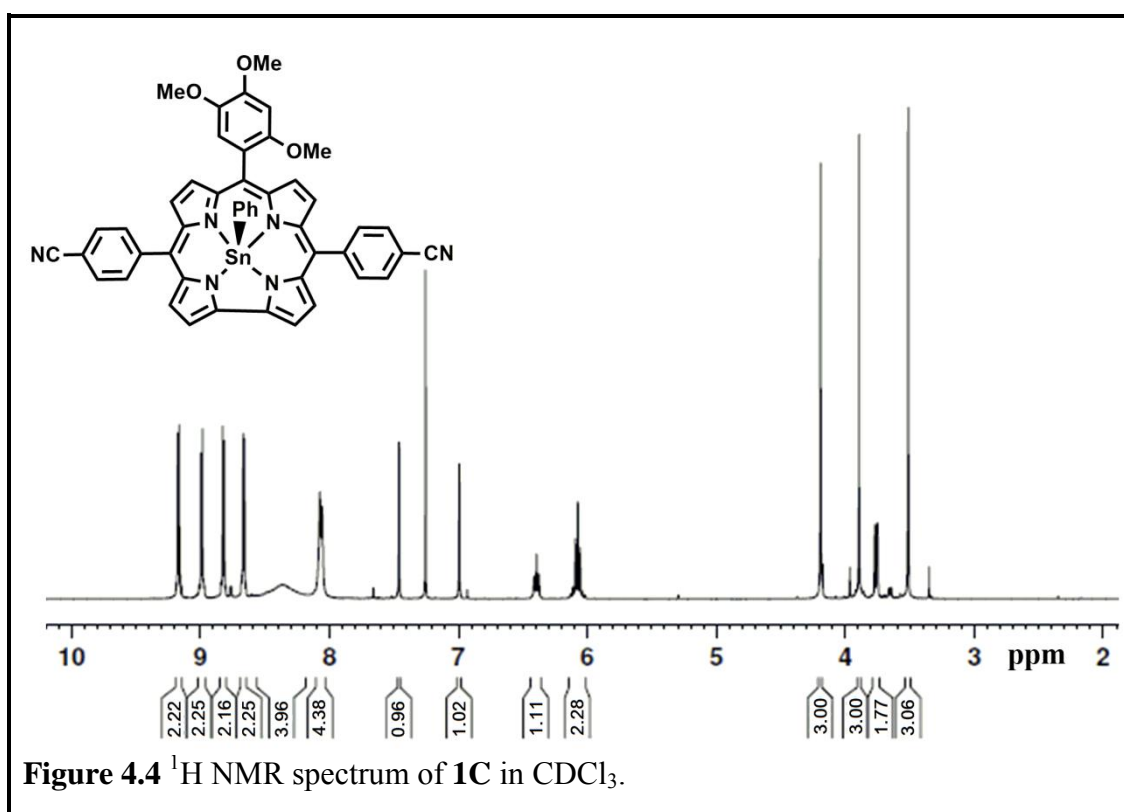
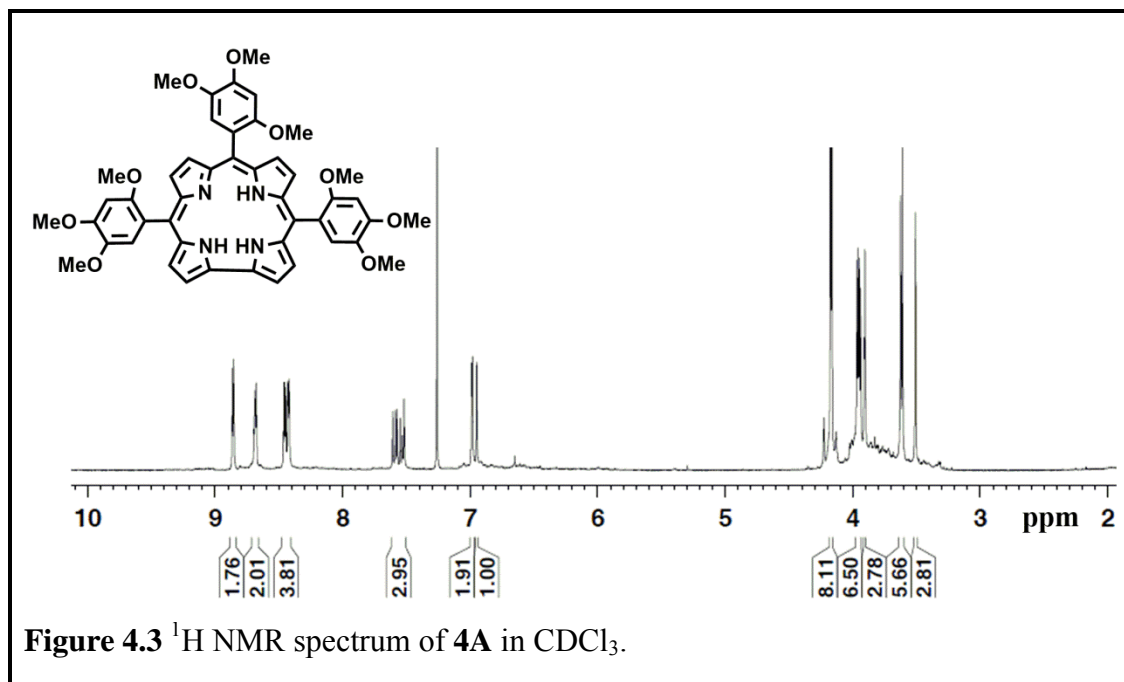


4.2.4 NMR Spectroscopy

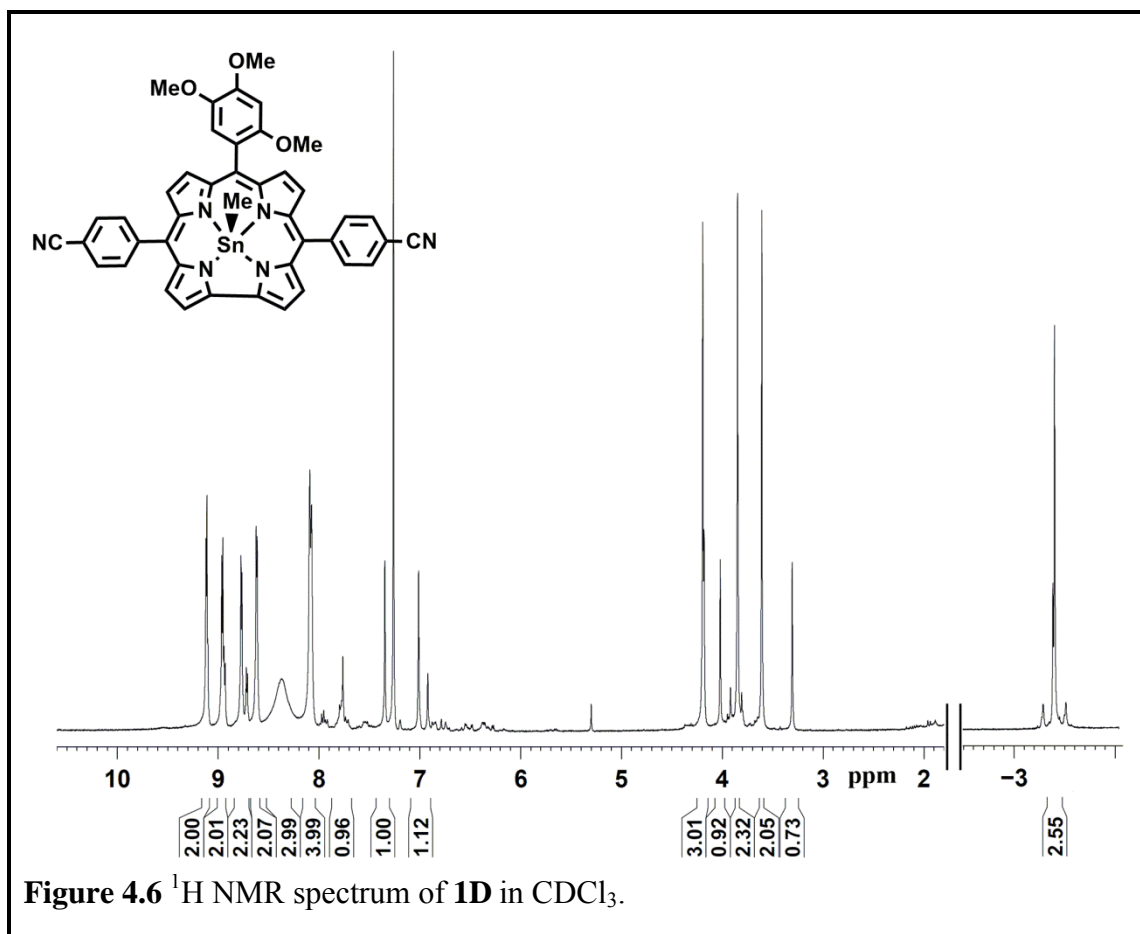
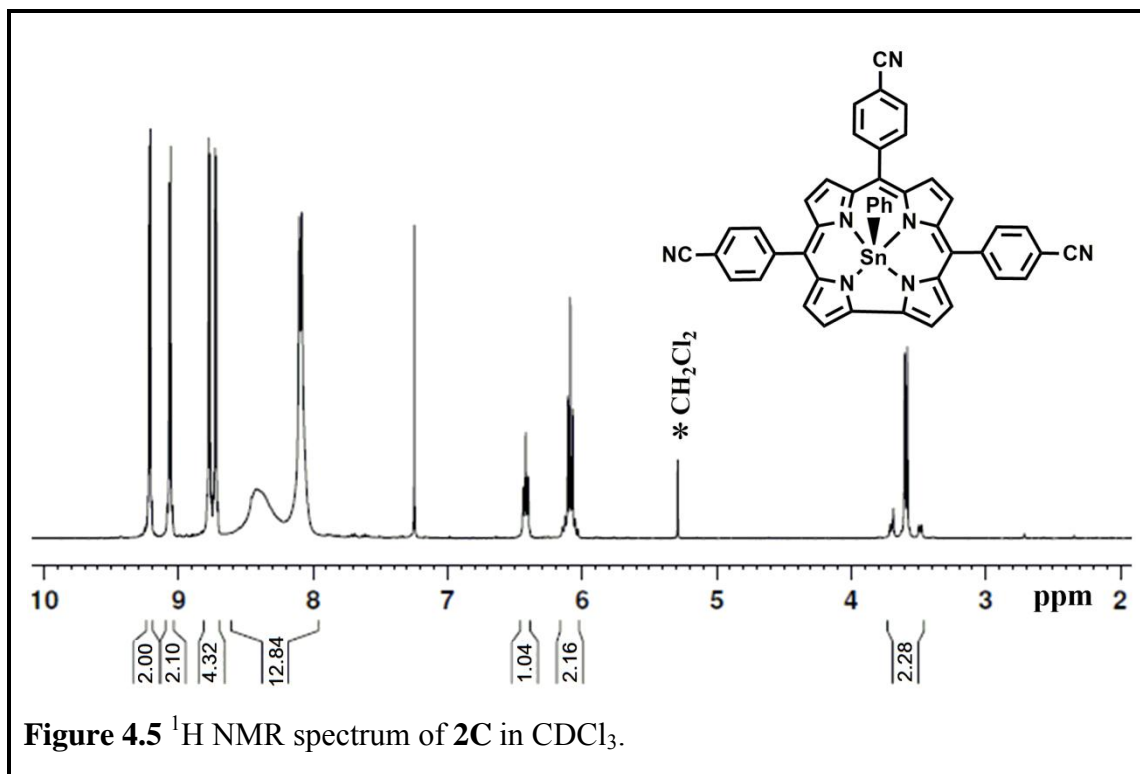
The free base corrole, **4A** gives characteristic proton resonances in the region of 8.86-6.95 ppm for 14 aromatic protons and at 4.17-3.51 ppm for 27 methoxy protons (Figure 4.3). The ¹H NMR spectra of **1C** (Figure 4.4) and **2C** (Figure 4.5) exhibit peaks corresponding to σ-bonded phenyl rings in the high field regions at 6.39, 6.08,

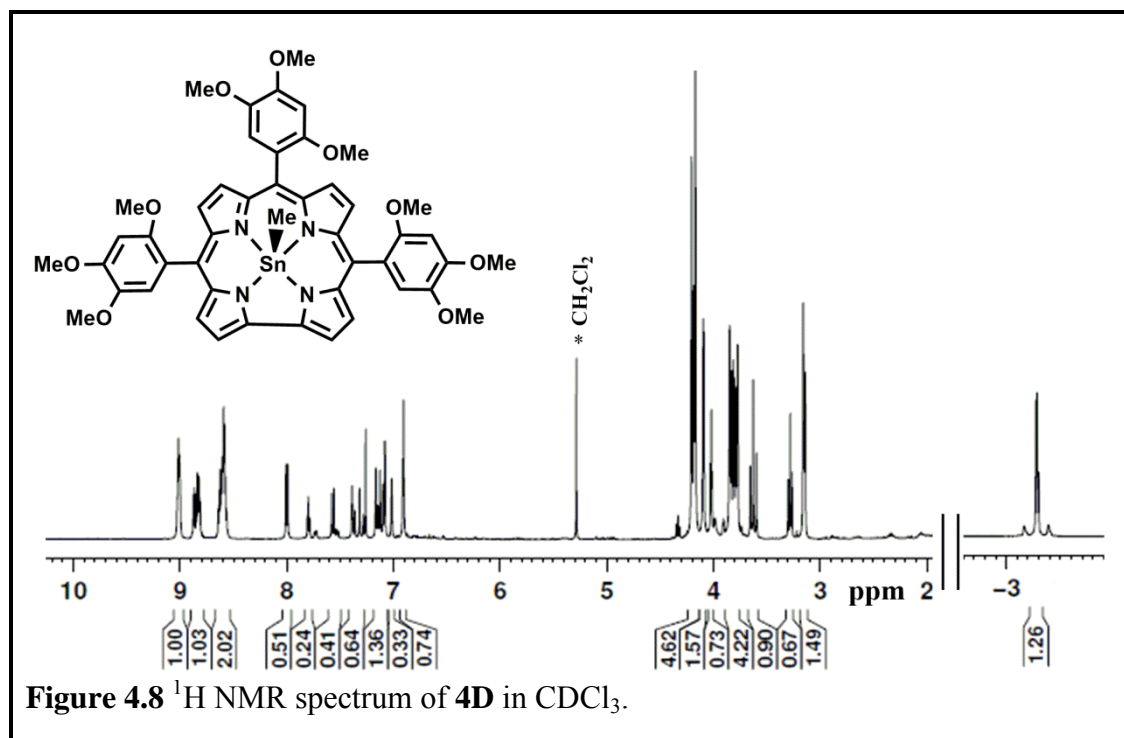
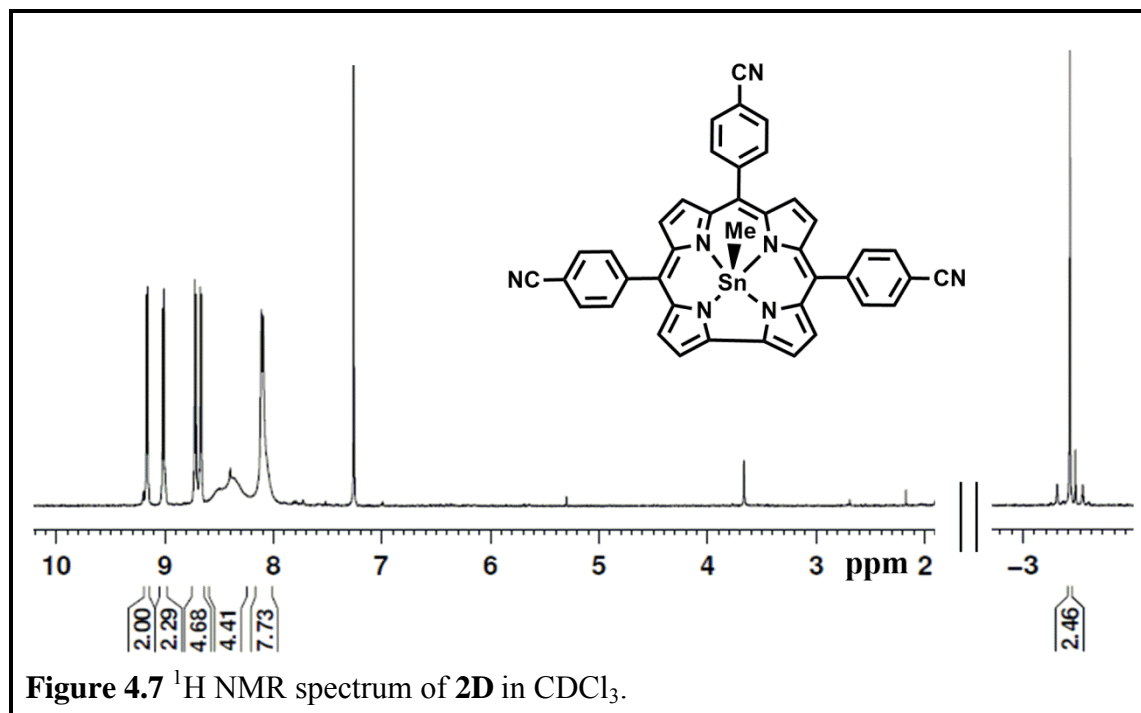


and 3.76 ppm for **1C** and 6.42, 6.16, and 3.62 ppm for **2C**. The ¹H NMR spectra of **1D** (Figure 4.6), **2D** (Figure 4.7) and **4D** (Figure 4.8) exhibit peaks corresponding to σ-bonded methyl groups in the high field regions at −3.39 ppm for **1D**, −3.41 ppm for **2D** and −3.28 ppm for **4D**. The diagnostic ¹¹⁷Sn, ¹¹⁹Sn, and ¹³C couplings were present

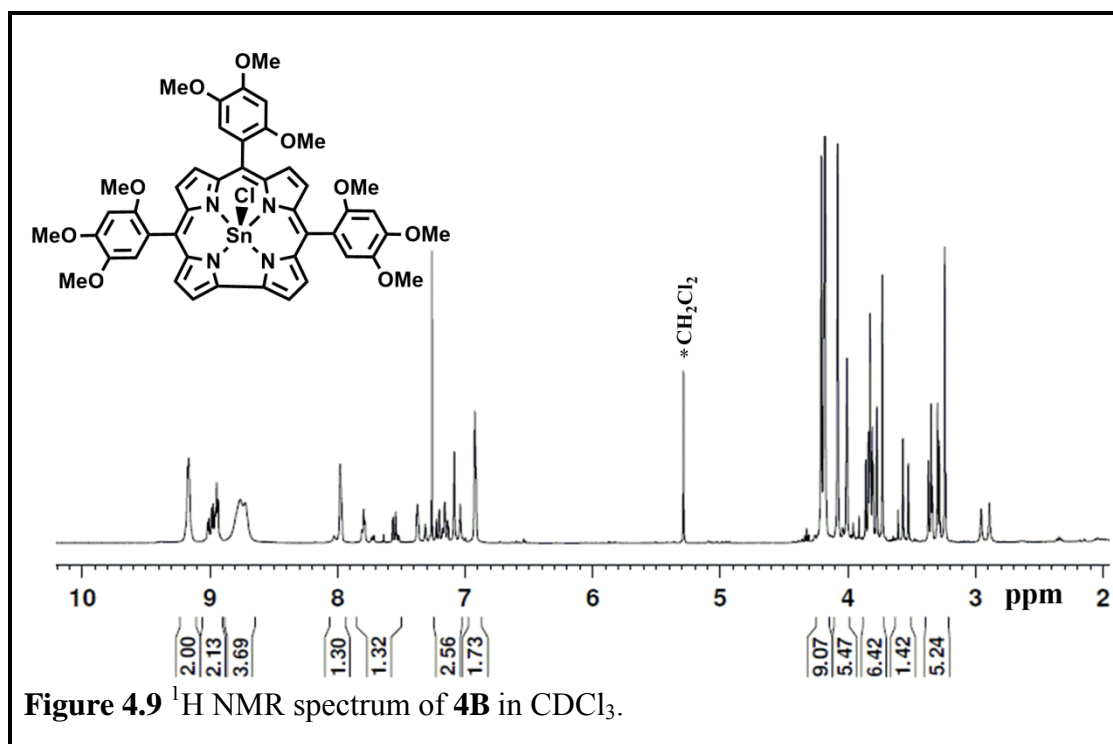


in the signals of axial methyl protons³⁰¹. A slight downfield shift has been observed in all the synthesized corrolato-tin(IV) derivatives compared to their free base analogues. The ^1H NMR spectra of some of the crowded molecules such as the





corrolato-tin(IV)-chloride, **4B** (Figure 4.9) and its σ -methyl complex, **4D** (Figure 4.8) seem to be a bit complex at the methoxy region probably due to the hindered rotation of the 2,4,5-trimethoxyphenyl groups.



4.2.5 X-Ray Crystallography

The crystal structures of **1C** and **2D** are shown in Figure 4.10 and Figure 4.11 respectively. The crystal systems are triclinic and the unit cells have eight and two **1C** and **2D** molecules respectively. Important crystallographic parameters for these two complexes are presented in Table 4.4. Bond distances and angles of **1C** and **2D** are in line with the previously reported other corrolato-tin(IV) molecules^{50, 138, 167, 250, 252, 255}. Tin atoms in both **1C** and **2D** are pentacoordinated and the geometry of the tin is distorted square-pyramidal, as expected. Tin atom deviates from the mean N4 corrole planes by distances 0.7562(8) Å (in case of **1C**) and 0.7712(7) Å (in case of **2D**) and give rise to domed conformations. Pyrrole ring nitrogen atoms deviates from the mean corrole plane (19-carbon atom) by distances ranging from 0.0587-0.4746 Å in **1C** and 0.0945-0.4052 Å in case of **2D**. Paolesse et al. has observed that for a representative free base corrole, 3-formyl-5,10,15-triphenylcorrole, the mean deviation of the 23 corrole atoms from their mean corrole plane (considering 23 atom corrole plane as

mean corrole plane) is 0.152 Å. However, in the present cases, we have observed a mean deviation of ~ 0.12 Å²⁸⁸. Thus it can be concluded that although there is significant distortion present in both the complexes (**1C** and **2D**), but that distortion is marginal compared to their free base analogues. The dihedral angles between the planes of *meso*-substituted phenyl rings and the 19-atom corrole carbon plane are 50.013-84.446° for **1C**, and for 50.309-60.33° for **2D**. The Sn–N bond distances of **1C** are 2.073(10) Å (for N(1)–Sn(1)), 2.059(9) Å (for N(2)–Sn(1)), 2.061(9) Å (for N(3)–Sn(1)) and 2.093(9) Å (for N(4)–Sn(1)) respectively. The above-mentioned Sn–N bond lengths of **1C** are consistent with the values in the range of 2.062-2.072 Å for the same in previously reported related structure²⁵⁰. The Sn–N bond distances of **2D** are 2.070(7) Å (for N(1)–Sn(1)), 2.083(7) Å (for N(2)–Sn(1)), 2.070(7) Å (for N(3)–Sn(1)) and 2.074(7) Å (for N(4)–Sn(1)) respectively. The Sn–C bond length in **1C** has been found to be very close to the observed value of 2.105 Å in a related σ -phenyl tin corrole complex²⁵⁰. The Sn–C bond distances of **1C** and **2D** are 2.111(9) Å and 2.108(9) Å respectively. These Sn–N and Sn–C bond

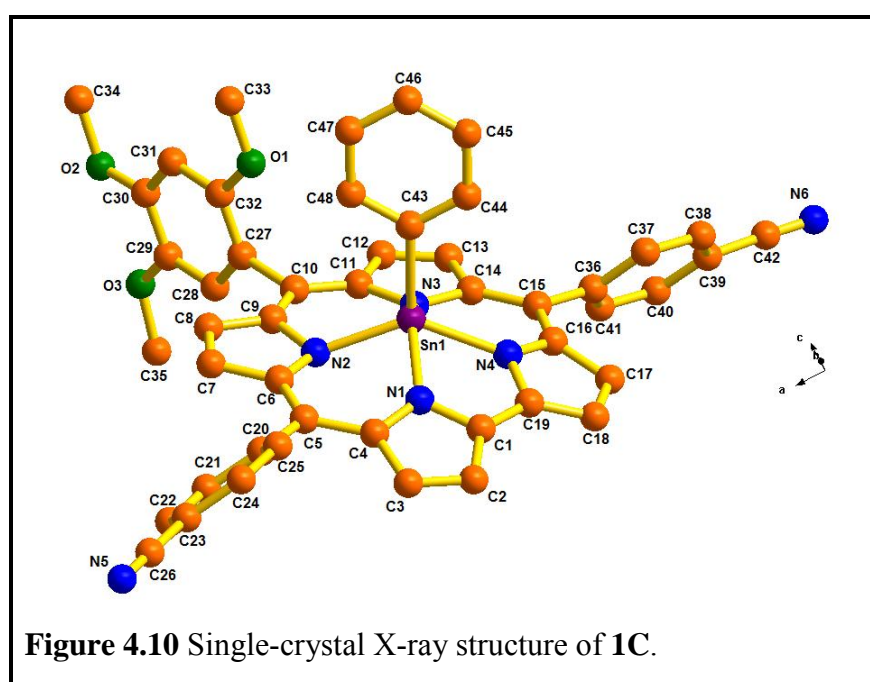
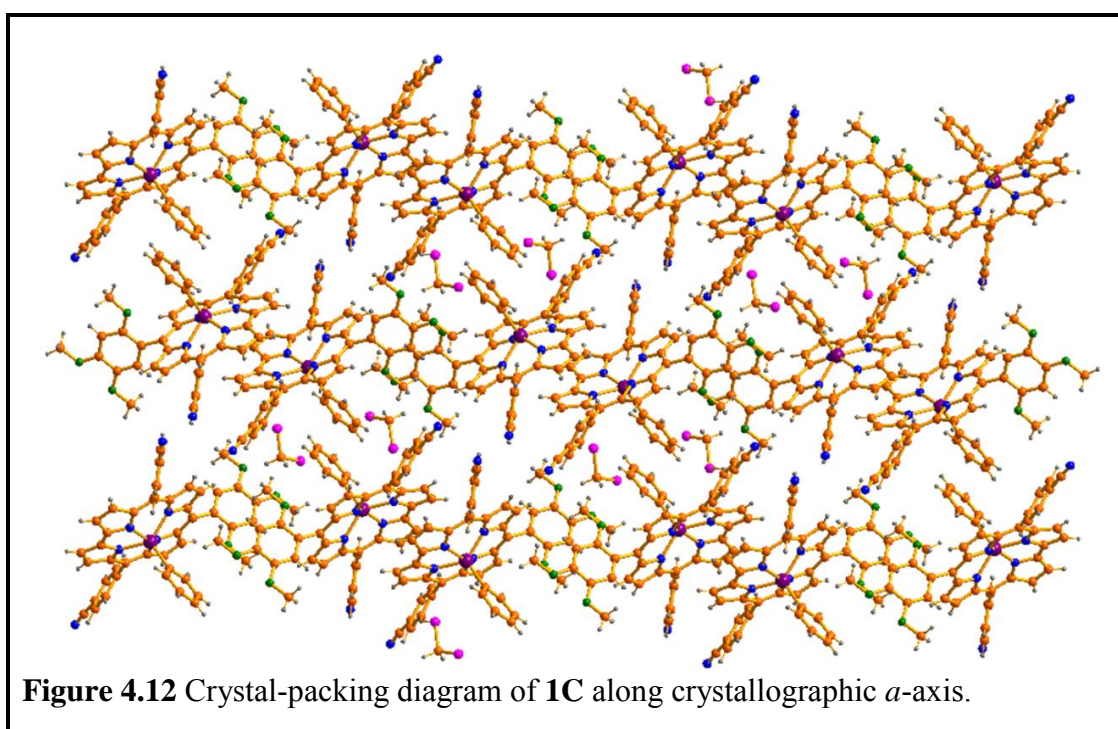
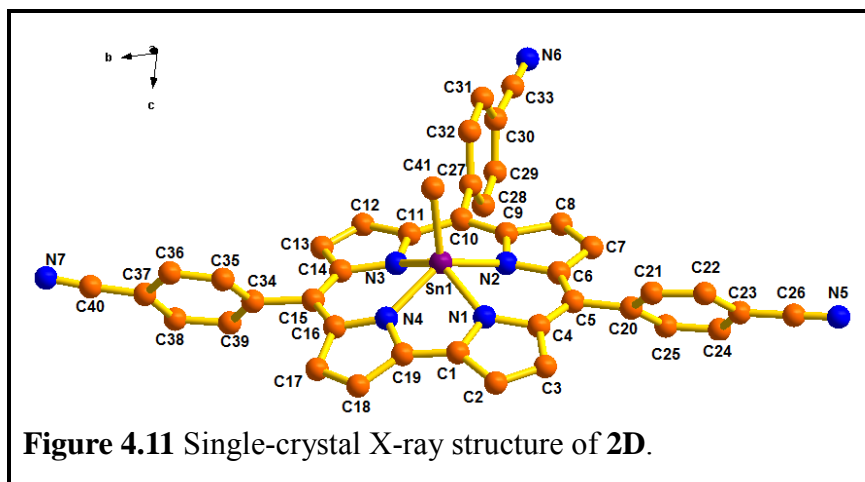


Table 4.4 Crystallographic Data for **1C** and **2D**

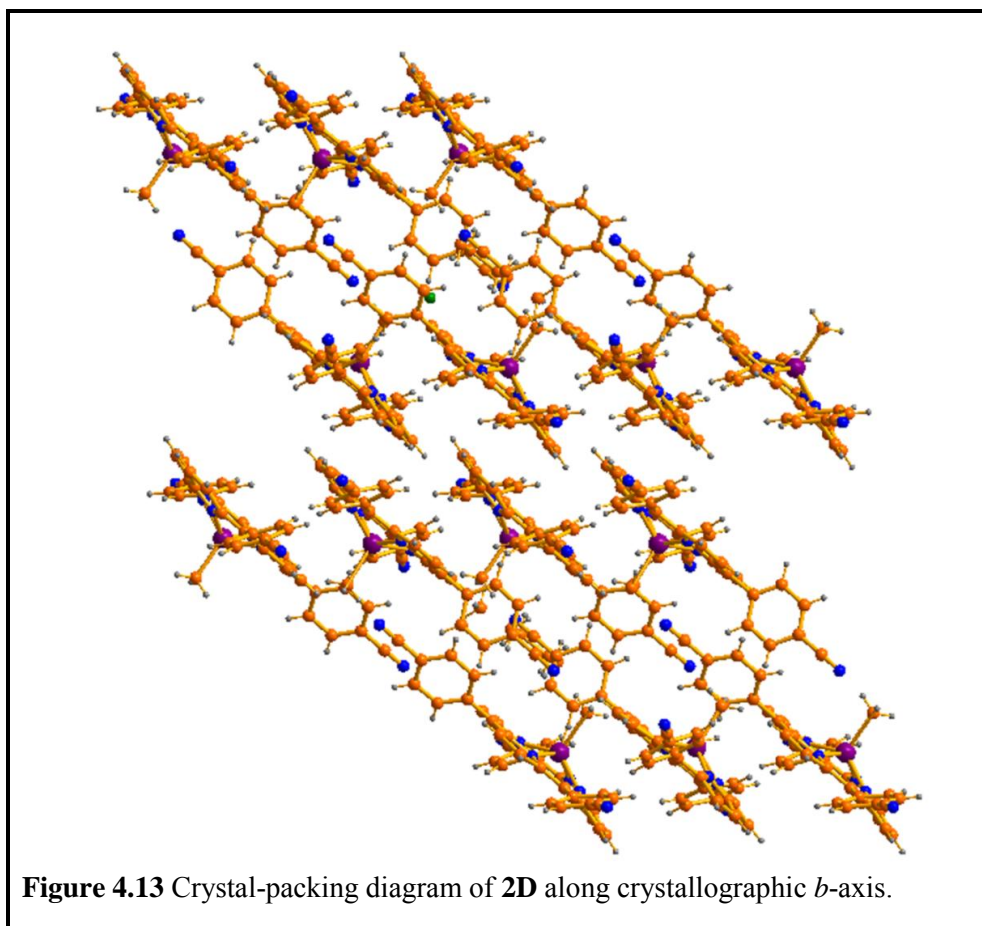
Compound Name	1C	2D
Molecular formula	C ₄₈ H ₃₂ N ₆ O ₃ Sn, CH ₂ Cl ₂	(2×C ₄₁ H ₂₃ N ₇ Sn), O, (0.5×C ₆ H ₁₄)
Formula weight	944.41	1523.79
Radiation	MoK α	MoK α
Crystal symmetry	Triclinic	Triclinic
Space group	P -1	P -1
<i>a</i> (Å)	9.909(17)	12.618(2)
<i>b</i> (Å)	21.806(4)	16.968(3)
<i>c</i> (Å)	37.724(7)	17.561(3)
α (deg)	86.472(5)	76.197(7)
β (deg)	89.862(5)	81.729(8)
γ (deg)	89.919(5)	85.713(7)
<i>V</i> (Å ³)	8135.0(2)	3610.0(10)
<i>Z</i>	8	2
μ (mm ⁻¹)	0.813	0.750
<i>T</i> (K)	100	100
<i>D</i> _{calcd} (g cm ⁻³)	1.542	1.402
2 θ range (deg)	1.88 to 53.66	2.40 to 50.76
<i>e</i> data (<i>R</i> _{int})	33513 (0.0824)	13002 (0.0785)
<i>R</i> 1 (<i>I</i> >2 σ (<i>I</i>))	0.0469	0.0844
<i>wR</i> 2	0.1592	0.2484
GOF	0.952	1.027
Largest diff. peak and hole (e Å ⁻³)	1.043 and -0.790	4.219 and -1.354
CCDC No.	1020850	1020851



distances are shorter than the corresponding tin porphyrins derivatives^{239-241, 243-245, 247, 248}. The crystal packing diagrams of **1C** and **2D** have been represented in Figure 4.12 and Figure 4.13 respectively.

4.3 Conclusions

In summary, we have developed an efficient, mild, and one step methodology for the conversion of tin-corroles to the corresponding free base corroles. Methylmagnesium



chloride has been used as the efficient reagent for the destannation reaction. In addition to that, it has been also shown that the treatment of corrolato-tin(IV)-chlorides with methyl/phenylmagnesium bromide resulted in the formation of the usual σ -methyl/ σ -phenyl tin(IV) corrole derivatives. A mechanism has been proposed for such varied reactivity of similar kinds of Grignard reagents. Structural characterization of representative σ -methyl/ σ -phenyl tin(IV) corrole derivatives are also reported herein. This demetalation scheme will definitely be a landmark in the research of corrole chemistry as there are no reports on the demetalation strategy of tin(IV) corroles and very few in case of other metal corrole complexes till date.

4.4 Experimental Section

4.4.1 Materials

The precursors pyrrole, *p*-chloranil and 2,4,5-trimethoxybenzaldehyde were purchased from Aldrich, USA. 4-cyano benzaldehyde, 4-bromo benzaldehyde, and tin(II) chloride were purchased from Merck, India. Other chemicals were of reagent grade. Hexane and CH₂Cl₂ were distilled from KOH and CaH₂ respectively. For spectroscopy and electrochemical studies HPLC grade solvents were used. The synthetic methodologies and full spectroscopic characterization, including single crystal X-ray structural analysis of **1A**, **2A**, **3A**, **1B**, **2B** and **3B** are provided in Chapter 3³⁰², however; the synthesis of **4A**, **4B**, **1C**, **1D**, **2C**, **2D** and **4D** have been discussed in this chapter.

4.4.2 Physical Measurements

UV–Vis spectral studies were performed on a Perkin–Elmer LAMBDA-750 spectrophotometer. Emission spectral studies were performed on a Perkin Elmer, LS 55 spectrophotometer using optical cell of 1 cm path length. The elemental analyses were carried out with a Perkin–Elmer 240C elemental analyzer. The NMR measurements were carried out using a Bruker AVANCE 400 NMR spectrometer. Chemical shifts are expressed in parts per million (ppm) relative to residual chloroform ($\delta = 7.26$). Electrospray mass spectra were recorded on a Bruker Micro TOF-QII mass spectrometer.

4.4.3 Crystal Structure Determination

Several attempts were made to crystallize the molecules of **1C** and finally single crystals of **1C** were obtained by slow diffusion of a solution of the **1C** in dichloromethane into hexane, followed by slow evaporation under atmospheric conditions. However the crystal quality was not very good. Though a new space group, $P21/n$ was suggested by ADDSYM, yet suitable crystal solution was not possible with that and finally the crystal was solved by $P-1$ space-group. Single crystals for **2D** were grown by slow diffusion of a solution of the **2D** in dichloromethane into benzene, followed by slow evaporation under atmospheric conditions. The crystal data of **1C** and **2D** were collected on a Bruker Kappa APEX II CCD diffractometer at 100 K. Selected data collection parameters and other crystallographic results are summarized in Table 4.4. All data were corrected for Lorentz polarization and absorption effects. The program package SHELXTL¹⁹⁵ was used for structure solution and full matrix least squares refinement on F^2 . Hydrogen atoms were included in the refinement using the riding model. Contributions of H atoms for the water molecules were included but were not fixed. Disordered solvent molecules were taken out using SQUEEZE¹⁹⁶ command in PLATON. CCDC 1020850-1020851 contain the supplementary crystallographic data for **1C** and **2D**.

4.4.4 Synthesis of 5,10,15-Tris(2,4,5-trimethoxyphenyl)corrole, **4A**

4A was prepared according to available procedures of corrole synthesis⁴⁶. A 0.980 g amount of 2,4,5-trimethoxy benzaldehyde (5 mmol) and 697 μ L of pyrrole (10 mmol) were dissolved in 200 mL of methanol and subsequently 200 mL of water was added. Then, 4.25 mL of HCl_{aq} (36%) was added and the reaction was stirred for 3 h. The mixture was extracted with CHCl_3 , and the organic layer was washed twice with

water, dried by anhydrous Na_2SO_4 , filtered and diluted to 300 mL with CHCl_3 . A 1.23 g portion of *p*-chloranil (5 mmol) was added, and the mixture was refluxed for 1 h. The solvent was removed by rotary evaporation and the green coloured crude product was purified by column chromatography through silica gel (100-200 mesh) bed and using 5% MeCN and 95% DCM as eluent. Yield: 19% (252 mg). Anal. Calcd (found) for $\text{C}_{46}\text{H}_{44}\text{N}_4\text{O}_9$ (**4A**): C, 69.33 (69.20); H, 5.57 (5.31); N, 7.03 (6.94). $\lambda_{\text{max}}/\text{nm}$ ($\epsilon/\text{M}^{-1}\text{cm}^{-1}$) in dichloromethane: 420 (85500), 572 (15750), 613 (13375), 646 (10,500). ^1H NMR (400 MHz, CDCl_3) δ 8.86 (d, $^3J(\text{H,H}) = 4.1$ Hz, 2H, β -pyrrole), 8.69 (dd, $^3J(\text{H,H}) = 4.2, 2.6$ Hz, 2H, β -pyrrole), 8.48-8.40 (m, 4H, β -pyrrole), 7.64-7.48 (m, 3H), 6.98 (d, $^5J(\text{H,H}) = 2.6$ Hz, 2H), 6.95 (s, 1H), 4.17 (8H), 3.95 (7H), 3.91 (3H), 3.62 (6H), 3.51 (s, 3H). ^{13}C NMR (101 MHz, CDCl_3) δ 153.80, 153.68, 153.61, 150.16, 149.85, 142.81, 142.47, 142.19, 140.18, 137.15, 137.09, 131.52, 127.39, 125.57, 122.64, 121.30, 120.50, 119.72, 119.42, 115.10, 112.02, 111.93, 105.31, 98.68, 98.52, 57.43, 57.33, 57.26, 56.88, 56.84, 56.49. **4A** displayed strong fluorescence at 662 nm in dichloromethane. The electrospray mass spectrum in methanol showed peaks centered at $m/z = 797.297$ correspond to $[\mathbf{4A+H}]^+$ (796.310 calcd for $\text{C}_{46}\text{H}_{44}\text{N}_4\text{O}_9$).

4.4.5 Synthesis of 5,10,15-Tris(2,4,5-trimethoxyphenyl)corrolato-tin(IV)-chloride, **4B**

4B was prepared according to available procedures of tin(IV) corroles synthesis^{50, 138, 167, 250, 252, 255}. A 100 mg (0.126 mmol) amount of the free base corrole was dissolved in 20 mL of DMF. Then, 238.9 mg (1.26 mmol) of tin(II) chloride was added to the reaction vessel under reflux condition and the stirring was continued till 1 h. Formation of the product was confirmed by TLC examination. The solvent was removed completely by rotary evaporation. The crude product was then purified by

column chromatography using silica gel (100-200 mesh) with 10% MeCN and 80% dichloromethane as eluent. After recrystallization from dichloromethane and hexane, pure compound was collected. Yield: 63% (75 mg). Anal. Calcd (found) for $C_{46}H_{41}ClN_4O_9Sn$: C, 58.28 (58.20); H, 4.36 (4.26); N, 5.91 (5.71). λ_{max}/nm ($\epsilon/M^{-1}cm^{-1}$) in dichloromethane: 424 (104000), 537 (2000), 568 (1000), 605 (8000). 1H NMR (400 MHz, $CDCl_3$) δ 9.17 (d, $^3J(H,H) = 2.7$ Hz, 2H, β -pyrrole), 9.08-8.89 (m, 2H, β -pyrrole), 8.6-8.8 (broad doublet, $^3J(H,H) = 14.9$ Hz, 4H, β -pyrrole), 7.98 (s, 1H), 7.83-7.50 (m, 1H), 7.37-7.03 (m, 2H), 6.98 (m, 2H), 4.22 (9H), 4.08 (3H), 4.00 (2H), 3.97-3.66 (7H), 3.56 (1H), 3.40-3.21 (5H). **4B** displayed strong fluorescence at 619 nm and a broad hump at 669 nm in dichloromethane. The electrospray mass spectrum of **4B** in methanol showed peaks centred at $m/z = 912.003$ corresponding to $[4B-Cl]^+$ (913.189 calcd for $C_{46}H_{41}N_4O_9Sn$).

4.4.6 Synthesis of (Phenyl){10-(2,4,5-trimethoxyphenyl)-5,15-bis(4-cyanophenyl)corrolato}tin(IV), **1C**

1C was prepared by few modifications of the procedure followed by Kadish et. al.²⁵⁰. A 2.3 mmol portion of phenylmagnesium bromide in THF was added in a dropwise manner to a dichloromethane solution of 25 mg (0.03 mmol) of **1B** under nitrogen atmosphere. The reaction was continued under stirring condition for 45 min. Then, after addition of aqueous solution of ammonium chloride and extraction with water, the organic layer was dried with anhydrous Na_2SO_4 and evaporated. The reaction mixture was then subjected to column chromatography through silica gel (100-200 mesh) column using 100% dichloromethane as eluent. After recrystallization with dichloromethane and hexane, pure crystalline compound was obtained. Yield: 72% (19 mg). Anal. Calcd (found) for $C_{48}H_{32}N_6O_3Sn$: C, 67.07 (67.18); H, 3.75 (3.61); N,

9.78 (9.67). λ_{\max}/nm ($\epsilon/\text{M}^{-1}\text{cm}^{-1}$) in dichloromethane: 431 (112000), 527 (13000), 583 (15000), 622 (27000). ^1H NMR (400 MHz, CDCl_3) δ 9.21-9.14 (m, 2H, β -pyrrole), 9.01-8.97 (m, 2H, β -pyrrole), 8.84-8.80 (m, 2H, β -pyrrole), 8.68-8.65 (m, 2H, β -pyrrole), 8.1-8.5 (m, 4H), 8.07 (d, $^3J(\text{H,H}) = 7.8$ Hz, 4H), 7.46 (s, 1H), 6.99 (s, 1H), 6.39 (t, $^3J(\text{H,H}) = 7.5$ Hz, 1H), 6.08 (m, 2H), 4.19 (s, 3H), 3.89 (s, 3H), 3.76 (d, $^3J(\text{H,H}) = 6.8$ Hz, 2H), 3.51 (s, 3H) (Figure 4.4). **1C** displayed strong fluorescence at 640.5 nm with a small hump at around 694.5 nm in dichloromethane. The electrospray mass spectrum of **1C** in methanol showed peaks centred at $m/z = 860.146$ corresponding to $[\mathbf{1C}]^+$ (860.156 calcd for $\text{C}_{48}\text{H}_{32}\text{N}_6\text{O}_3\text{Sn}$).

4.4.7 Synthesis of (Phenyl){5,10,15-tris(4-cyanophenyl)corrolato}tin(IV), **2C**

A 2.475 mmol portion of phenylmagnesium bromide in THF was added to a dichloromethane solution of 25 mg (0.033 mmol) of **2B** under a nitrogen atmosphere. The reaction was continued under stirring condition for 45 min. Then after addition of aqueous solution of ammonium chloride and extraction with water, the organic layer was dried with anhydrous Na_2SO_4 and evaporated. The reaction mixture was then subjected to column chromatography through silica gel (100-200 mesh) column using 100% dichloromethane as eluent. After recrystallization with dichloromethane and hexane, pure compound was obtained in the form of crystals. Yield: 68% (18 mg). Anal. Calcd (found) for $\text{C}_{46}\text{H}_{25}\text{N}_7\text{Sn}$ (**2C**): C, 69.54 (69.38); H, 3.17 (3.26); N, 12.34 (12.20). λ_{\max}/nm ($\epsilon/\text{M}^{-1}\text{cm}^{-1}$) in dichloromethane: 432 (128000), 541 (3000), 580 (4000), 621 (18000). ^1H NMR (400 MHz, CDCl_3) δ 9.27-9.17 (m, 2H, β -pyrrole), 9.13-9.01 (m, 2H, β -pyrrole), 8.83-8.68 (m, 4H, β -pyrrole), 8.2-8.55 (br m, 5H), 8.09 (d, $^3J(\text{H,H}) = 7.8$ Hz, 7H), 6.42 (t, $^3J(\text{H,H}) = 7.5$ Hz, 1H), 6.16-6.02 (m, 2H), 3.62 (m,

2H). **2C** displayed strong fluorescence at 636.5 nm with a small hump at around 692 nm in dichloromethane.

4.4.8 Synthesis of (Methyl){10-(2,4,5-trimethoxyphenyl)-5,15-bis(4-cyanophenyl)corrolato}tin(IV), **1D**

To a solution of 25 mg (0.03 mmol) of **1B** in dichloromethane, 2.3 mmol of methylmagnesium bromide in diethyl ether was added dropwise in an inert atmosphere. The reaction was continued for 45 min in continuous stirring condition. Then after addition of aqueous solution of ammonium chloride and extraction with water, the organic layer was dried with anhydrous Na_2SO_4 and evaporated. The reaction mixture was then subjected to column chromatography through silica gel (100-200 mesh) column using 100% dichloromethane as eluent. After recrystallization with dichloromethane and hexane, pure crystalline compound was obtained. Yield: 78% (19 mg). Anal. Calcd (found) for $\text{C}_{43}\text{H}_{30}\text{N}_6\text{O}_3\text{Sn}$: C, 64.76 (64.67); H, 3.79 (3.62); N, 10.54 (10.39). $\lambda_{\text{max}}/\text{nm}$ ($\epsilon/\text{M}^{-1}\text{cm}^{-1}$) in dichloromethane: 431 (129000), 539 (4000), 581 (7000), 626 (24000). ^1H NMR (400 MHz, CDCl_3) δ 9.11 (t, $^3J(\text{H,H}) = 3.9$ Hz, 2H, β -pyrrole), 8.95 (dd, $^3J(\text{H,H}) = 9.3, 4.6$ Hz, 2H, β -pyrrole), 8.74 (dd, $^3J(\text{H,H}) = 21.3, 4.5$ Hz, 2H, β -pyrrole), 8.62 (d, $^3J(\text{H,H}) = 3.9$ Hz, 2H, β -pyrrole), 8.2 – 8.5 (br m, 3H), 8.08 (d, $^3J(\text{H,H}) = 7.2$ Hz, 4H), 7.76(s, 1H), 7.35 (s, 1H), 7.01 (s, 1H), 4.19 (3H), 4.02 (s, 1H), 3.85 (s, 2H), 3.61 (s, 2H), 3.30 (s, 1H), – 3.39 (s, 3H). **1D** displayed strong fluorescence at 640.5 nm with a small hump at around 703 nm in dichloromethane. The electrospray mass spectrum of **1D** in methanol displays peak distribution around the central peak at $m/z = 798.116$ corresponding to $[\mathbf{1D}]^+$ (798.14 calcd for $\text{C}_{43}\text{H}_{30}\text{N}_6\text{O}_3\text{Sn}$).

4.4.9 Synthesis of (Methyl){5,10,15-tris(4-cyanophenyl)corrolato}tin(IV), 2D.

To a solution of 25 mg (0.033 mmol) of **2B** in dichloromethane, 2.475 mmol of methylmagnesium bromide in diethyl ether was added dropwise in an inert atmosphere. The reaction was continued for 45 min in continuous stirring condition. Then after addition of aqueous solution of ammonium chloride and extraction with water, the organic layer was dried with anhydrous Na₂SO₄ and evaporated. The reaction mixture was then subjected to column chromatography through silica gel (100-200 mesh) column using 100% dichloromethane as eluent. After recrystallization with dichloromethane and hexane, pure compound was obtained in the form of crystals. Yield: 77% (18 mg). Anal. Calcd (found) for C₄₁H₂₃N₇Sn: C, 67.24 (67.38); H, 3.17 (3.28); N, 13.39 (13.50). λ_{\max}/nm ($\epsilon/\text{M}^{-1}\text{cm}^{-1}$) in dichloromethane: 432 (163000), 543 (10000), 581 (12000), 621 (28000). ¹H NMR (400 MHz, CDCl₃) δ 9.16 (d, ³J(H,H) = 4.0 Hz, 2H, β -pyrrole), 9.01 (d, ³J(H,H) = 4.6 Hz, 2H, β -pyrrole), 8.69 (dd, ³J(H,H) = 19.7, 4.3 Hz, 4H, β -pyrrole), 8.2-8.6 (br m, 4H), 8.10 (d, ³J(H,H) = 7.4 Hz, 8H), -3.41 (s, ²J(¹H, ¹¹⁷Sn) = 84 Hz, ²J(¹H, ¹¹⁹Sn) = 92 Hz, ¹J(¹H, ¹³C) = 132 Hz, 3H). **2D** displayed strong fluorescence at 637 nm with a small hump at 691 nm in dichloromethane. The electrospray mass spectrum of **2D** in methanol displays peak distribution around the central peak at $m/z = 733.081$ corresponding to [**2D**]⁺ (733.104 calcd for C₄₁H₂₃N₇Sn).

4.4.10 Synthesis of (Methyl){5,10,15-tris(2,4,5-trimethoxyphenyl)corrolato}tin(IV), 4D

To a solution of 25 mg (0.026 mmol) of **4B** in dichloromethane, 1.95 mmol of methylmagnesium bromide in diethyl ether was added dropwise in an inert atmosphere. The reaction was continued for 45 min in continuous stirring condition.

Then after addition of aqueous solution of ammonium chloride and extraction with water, the organic layer was dried with anhydrous Na_2SO_4 and evaporated. The reaction mixture was then subjected to column chromatography through silica gel (100-200 mesh) column using 100% dichloromethane as eluent. After recrystallization with dichloromethane and hexane, pure compound was obtained. Yield: 81% (20 mg). Anal. Calcd (found) for $\text{C}_{47}\text{H}_{44}\text{N}_4\text{O}_9\text{Sn}$: C, 60.86 (60.69); H, 4.78 (4.67); N, 6.04 (6.17). $\lambda_{\text{max}}/\text{nm}$ ($\epsilon/\text{M}^{-1}\text{cm}^{-1}$) in dichloromethane: 428 (112000), 539 (4000), 579 (7000), 619 (20000). ^1H NMR (400 MHz, CDCl_3) δ 9.02-8.96 (m, 2H, β -pyrrole), 8.82-8.86 (m, 2H, β -pyrrole), 8.63-8.53 (m, 4H, β -pyrrole), 7.97 (d, $^3J(\text{H,H}) = 6.9$ Hz, 1H), 7.82-7.52 (m, 1H), 7.39-7.28 (m, 1H), 7.2-7.0 (m, 2H), 6.88 (d, $^3J(\text{H,H}) = 3.2$ Hz, 1H), 4.34-3.93 (13H), 3.91-3.67 (8H), 3.60 (2H), 3.26 (1H), 3.16-3.07 (3H), -3.28 (s, 3H). **4D** displayed strong fluorescence at 633.5 nm and a small hump at around 692 nm in dichloromethane. The electrospray mass spectrum of **4D** in methanol displays peak distribution around the central peak at $m/z = 928.189$ corresponding to $[\mathbf{4D}]^+$ (928.213 calcd for $\text{C}_{47}\text{H}_{44}\text{N}_4\text{O}_9\text{Sn}$).

4.5 Demetalation

Demetalation was observed in all the synthesized tin(IV)chloride complexes, when they were reacted with methylmagnesium chloride. However the destannation strategy will be discussed on the basis of studies performed on the representative complex, as stated in Table 4.1. 10-(2,4,5-Trimethoxyphenyl)-5,15-bis(4-cyanophenyl)corrolato-tin(IV)-chloride, **1B** (25 mg, 0.030 mmol) was weighed and kept in a two-neck, round-bottom flask under nitrogen atmosphere. Anhydrous dichloromethane (20 mL) was injected into the flask. Then, after dissolution of **1B**, methylmagnesium chloride in THF (2.25 mmol) was added dropwise followed by an almost immediate color

change from deep reddish green to a green colored solution. The solution was stirred for 45 min. Then, after addition of aqueous solution of ammonium chloride and extraction with water, the organic layer was dried with anhydrous Na_2SO_4 and evaporated. The reaction mixture was then subjected to column chromatography through silica gel (100-200 mesh) column using 80% dichloromethane and 20% hexane as eluent. After recrystallization with dichloromethane and hexane, pure demetalated compound, **1A** (18 mg, 0.027 mmol) in 90% yield was obtained. The demetalated compound, i.e, the free base corrole **1A** was characterized by TLC examination, ^1H NMR studies and also by ESI mass spectroscopy and was found to be completely matching with the earlier reported data.

CHAPTER 5

Silver Corrole Complexes: Unusual Oxidation States and NIR Absorbing Dyes

5.1	Introduction	145
5.2	Results and Discussion	148
5.2.1	Synthesis	148
5.2.2	Spectral Characterization	149
5.2.2.1	Mass Spectroscopy	149
5.2.2.2	NMR Spectroscopy	149
5.2.2.3	X-Ray Crystallography	153
5.2.2.4	Electrochemistry	158
5.2.3	EPR Spectroelectrochemistry and Spin Density Calculations	160
5.2.4	UV-Vis-NIR Spectroelectrochemistry and TD-DFT Calculations	163
5.3	Conclusions	169
5.4	Experimental Section	172
5.4.1	Materials	172
5.4.2	Physical Measurements	172
5.4.3	Crystal Structure Determination	173
5.4.4	Computational Details	173
5.4.5	Synthesis of 4-(Di(1H-pyrrol-2-yl)methyl)benzotrile, 1	174
5.4.6	Synthesis of 10-(4,7-Dimethoxynaphthalen-1-yl)-5,15-bis(4-cyanophenyl)corrole, 4A	174
5.4.7	Synthesis of 5,10,15-Tris(4-cyanophenyl)corrolato-silver(III), 1B	175
5.4.8	Synthesis of 10-(4-Bromophenyl)-5,15-bis(4-cyanophenyl)corrolato-silver(III), 2B	176
5.4.9	Synthesis of 10-(2,4,5-Trimethoxyphenyl)-5,15-bis(4-cyanophenyl)corrolato-silver(III), 3B	176
5.4.10	Synthesis of 10-(4,7-Dimethoxynaphthalen-1-yl)-5,15-bis(4-cyanophenyl)corrolato-silver(III), 4B	177

5.1 Introduction

Photosynthesis is an indispensable process in which light energy is harvested and stored as chemical energy with the help of photosynthetic proteins. Photosynthetic proteins consist of the light-harvesting chlorophyll units^{117, 303} and the special-pairs of the photosynthetic reaction center¹³⁴. On excitation of these special-pairs, the electron transfer pathway is created and the oxidation of water to oxygen becomes possible. Photoexcitation of the special pairs leads to the generation of π radical cation porphyrin species. These π -dimer species have been found to exhibit charge-resonance absorption bands in near-IR (NIR) region¹²⁹⁻¹³³.

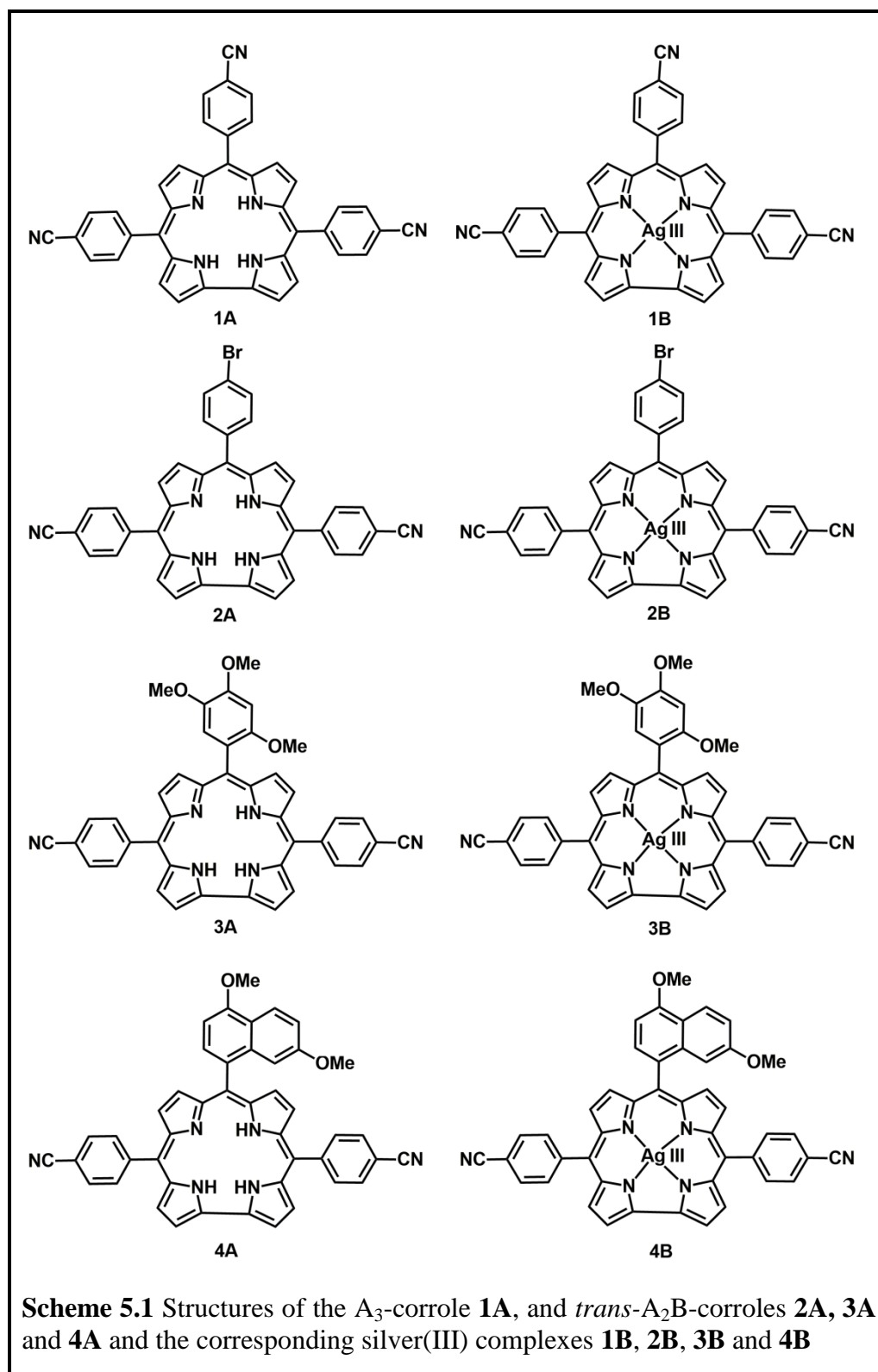
Chemically synthesized porphyrin and corrole^{65, 66, 274-276, 289-298, 304-309} dimers have already been targeted to behave as NIR-absorbing dyes, in order to mimic the naturally occurring photosynthetic proteins. In this context, photo-induced electron- and energy transfer reactions in 1, 8-naphthalimide-corrole dyads have been extensively studied by Tasior et al¹³⁹. Corrole-corrole and corrole-porphyrin dimers are also explored in the context of photoinduced energy- and electron-transfer reactions^{29, 138}. Metallocorroles have been frequently used in various redox-catalytic reactions, as model compounds for artificial photosynthesis, as dyes in solar cells, and in the form of sensors^{135-137, 276}. The emergence of NIR transitions in corrole dimers occurs due to strong electronic interactions²²⁹. However, NIR transitions have never been observed for mononuclear, *meso*-substituted corrole derivatives. This is a particularly important goal considering the simplicity of mononuclear corrole complexes compared to their dimeric counterparts.

Corroles^{65, 66, 274-276, 289-298, 304-309} are known to stabilize unusual metal oxidation states. The most common and stable oxidation state of the coinage metal silver is +1. Reports on Ag^{II} and Ag^{III} complexes remain rare¹⁴⁰. In general, high-

valent silver-containing compounds have been synthesized under harsh conditions. The most famous and earliest known members of this category are the mixed-valent AgO and Ag₃O₄. However, stabilization of the Ag^{III} state has best been demonstrated by the coordination chemistry of silver in +3 state with N-donor ligands, particularly corroles^{58, 126, 284, 310-315}.

In this chapter, the synthesis of another novel *trans*-A₂B-corrole, namely, 10-(4,7-dimethoxynaphthalen-1-yl)-5,15-bis(4-cyanophenyl)corrole, **4A** has been described. In addition, four novel corrolato-Ag^{III} complexes have been also synthesized, namely, 5,10,15-tris(4-cyanophenyl)corrolato-silver(III), **1B**, 10-(4-bromophenyl)-5,15-bis(4-cyanophenyl)corrolato-silver(III), **2B**, 10-(2,4,5-trimethoxyphenyl)-5,15-bis(4-cyanophenyl)corrolato-silver(III), **3B** and 10-(4,7-dimethoxynaphthalen-1-yl)-5,15-bis(4-cyanophenyl)corrolato-silver(III), **4B** (Scheme 5.1). The choices of ligands, **1A-3A**, and the effects of various substituents have been already described in the previous chapters⁵¹. The introduction of a new ligand, **4A**, in this study can be easily understood from the observations of the spectral properties in the present systems. The donor strength of the *meso*-substituents on the corrolato ligands was systematically varied. We present here a combined synthetic, crystallographic, electrochemical, UV-Vis-NIR/EPR spectroelectrochemical and DFT approach to address the following issues:

- 1) Accessibility of Ag^{II}, Ag^{III} and Ag^{IV} in these complexes.
- 2) Detection of NIR absorptions for the mononuclear forms of these complexes.
- 3) Influence of the *meso*-substituents on the corrolato ring on the electronic structures of these complexes, and in turn on their NIR absorption properties.

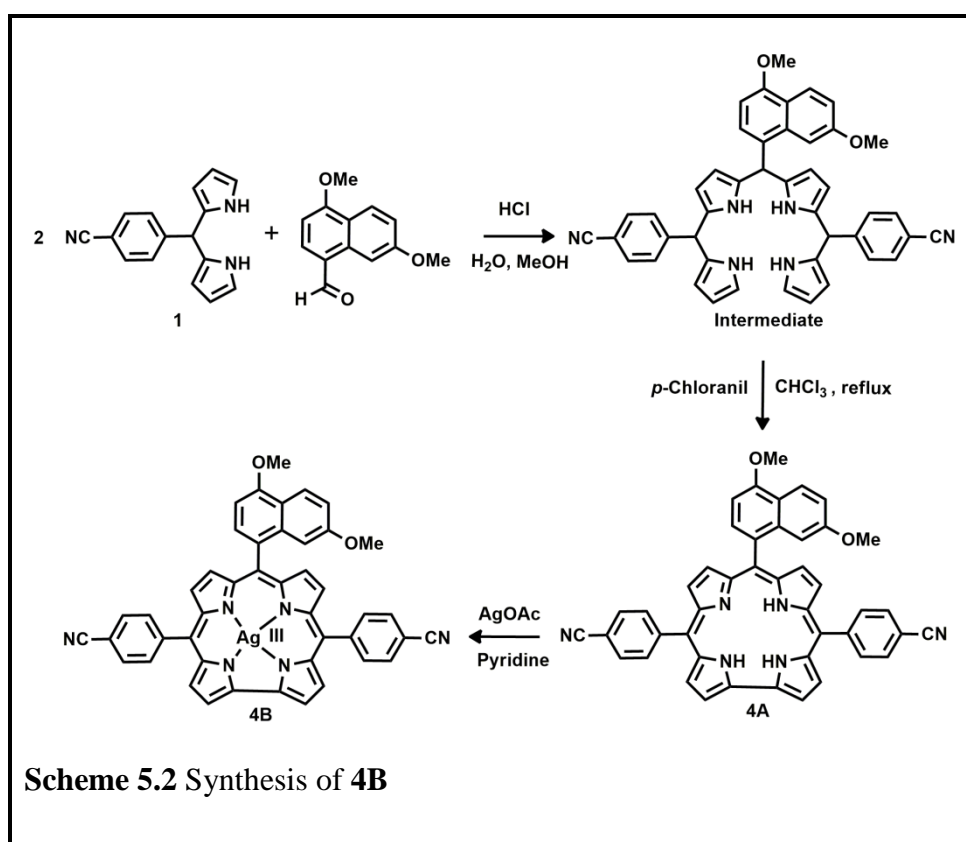


5.2 Results and Discussion

5.2.1 Synthesis

The free-base corroles **1A**, **2A**, **3A** and **4A** were prepared by following a general synthetic procedure for the synthesis of corroles⁴⁶: treatment of aryl-aldehydes and (4-cyanophenyl)dipyrromethane in methanol/water (1:1) with HCl and subsequent oxidation by *p*-chloranil (Scheme 5.2).

The corrolato-silver(III) derivatives were synthesized by slight modifications of a reported procedure^{58, 126, 284, 310-315}. The respective corroles were dissolved in pyridine and stirred with an excess of silver acetate to give rise to the corresponding corrolato-silver(III) derivatives **1B**, **2B**, **3B** and **4B**. The purities and identities of the free-base corroles and corrolato-silver(III) derivatives were demonstrated by satisfactory elemental analyses and electrospray mass spectra.



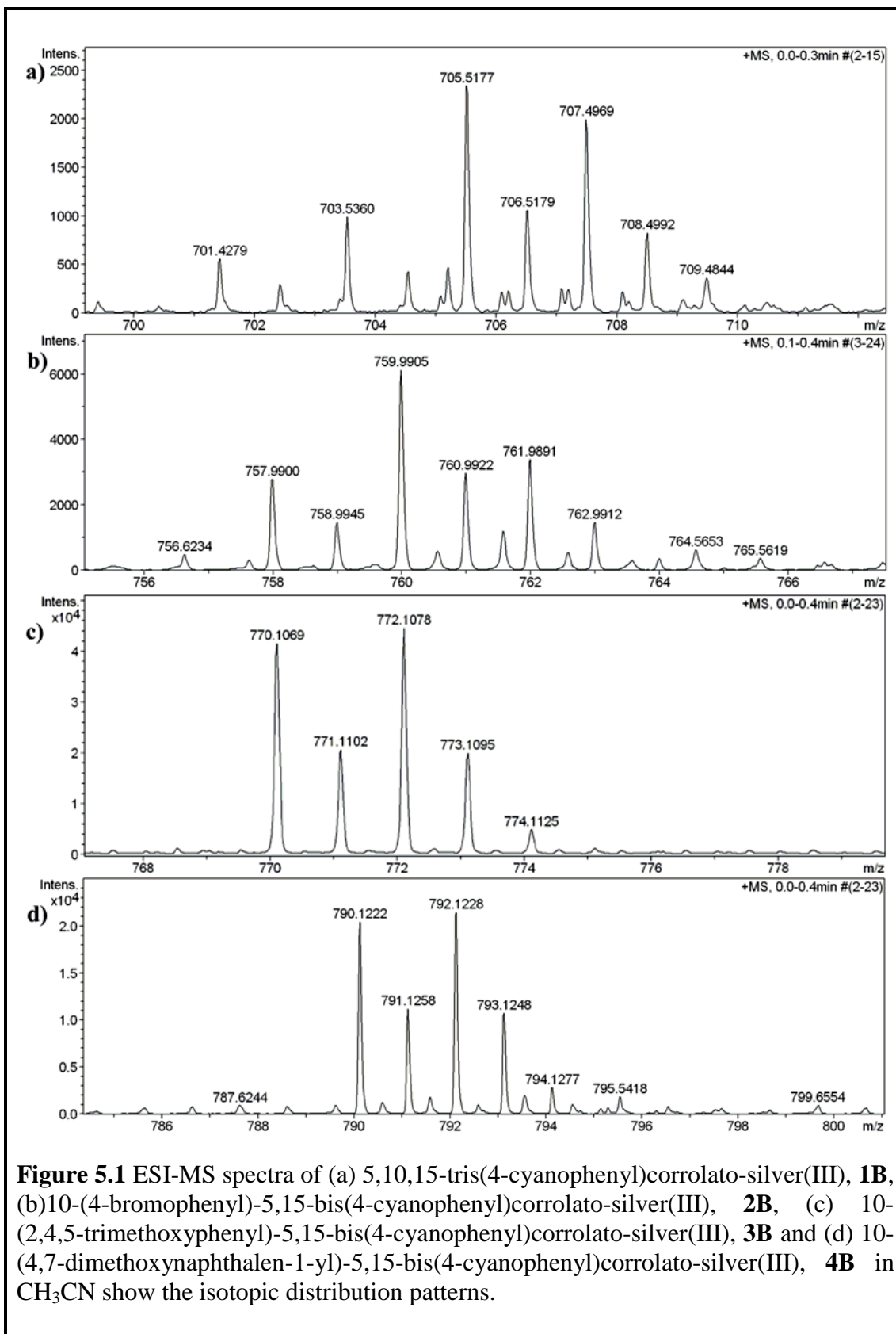
5.2.2 Spectral Characterization

5.2.2.1 Mass Spectroscopy

The electrospray mass spectra of all the corrolato-silver(III) complexes were recorded in acetonitrile solvent (Figure 5.1). The mass spectra of **1B**, **2B**, **3B** and **4B** show peaks centered at $m/z = 705.516$ corresponding to $[\mathbf{1B}]^+$ (calculated molecular mass: 705.0831), $m/z = 759.990$ corresponding to $[\mathbf{2B+H}]^+$ (calculated molecular mass: 757.998), $m/z = 772.1078$ corresponding to $[\mathbf{3B+H}]^+$ (calculated molecular mass: 771.570) and $m/z = 792.123$ corresponding to $[\mathbf{4B+H}]^+$ (calculated molecular mass: 791.603) respectively.

5.2.2.2 NMR Spectroscopy

The ^1H NMR spectra of all four synthesized silver complexes exhibit sharp resonances, revealing their diamagnetic character. The ^1H NMR spectrum of **1B** exhibits sharp peaks corresponding to 20 partially overlapping aromatic protons in the region δ , 9.3-8.1 ppm (Figure 5.2). Out of these signals, four doublets ($\delta = 9.30, 8.97, 8.78, 8.74$ ppm) with characteristic coupling constants $J \approx 4.6$ Hz, can be assigned to β -pyrrolic hydrogen atoms. The signals of the aryl ring protons are observed in the 8.44-8.10 ppm region. The ^1H NMR spectrum of **2B** represents the expected number of 20 distinguishable aromatic protons in the region δ , 9.20-7.93 ppm (Figure 5.3). Out of them, four doublets in the region of $\delta = 9.19$ -8.68 ppm with coupling constants of $J \approx 4.6$ Hz correspond to β -pyrrolic hydrogen atoms while the other doublets in the region of δ , 8.40-7.93 ppm can be assigned to the aryl ring protons. The ^1H NMR spectrum of **3B** shows sharp resonances corresponding to 18 partially overlapping



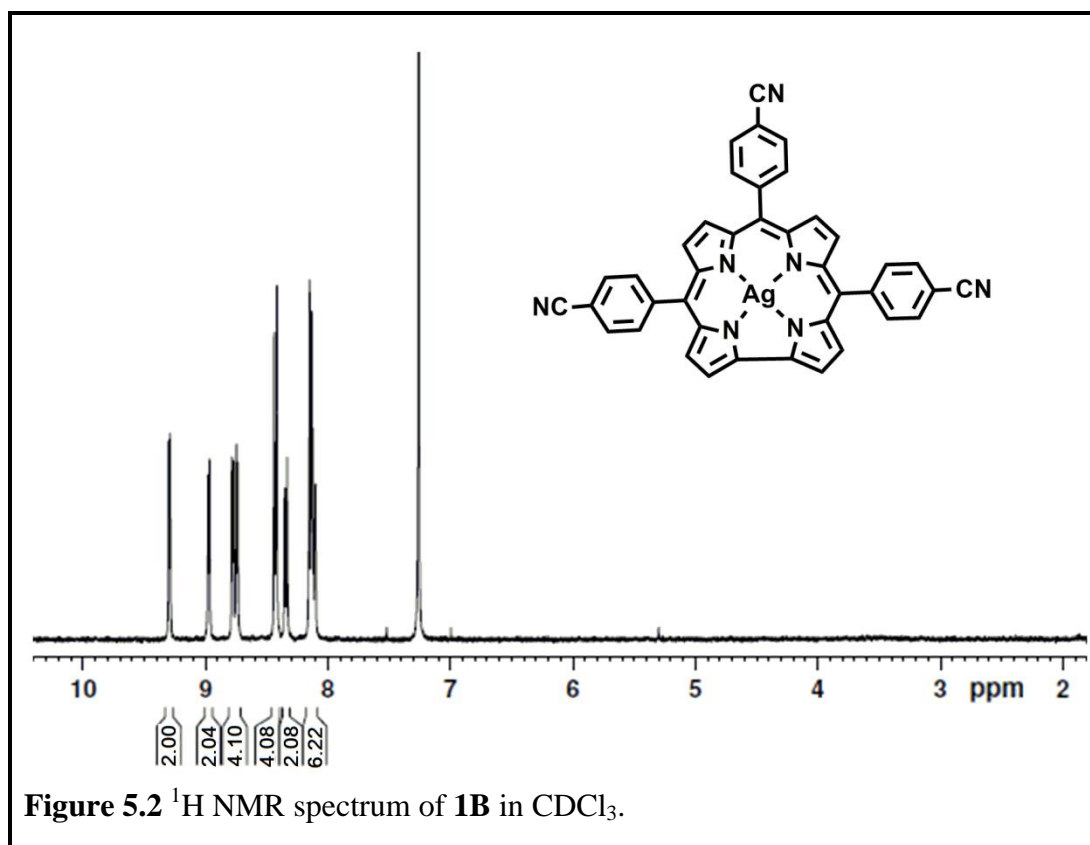


Figure 5.2 ^1H NMR spectrum of **1B** in CDCl_3 .

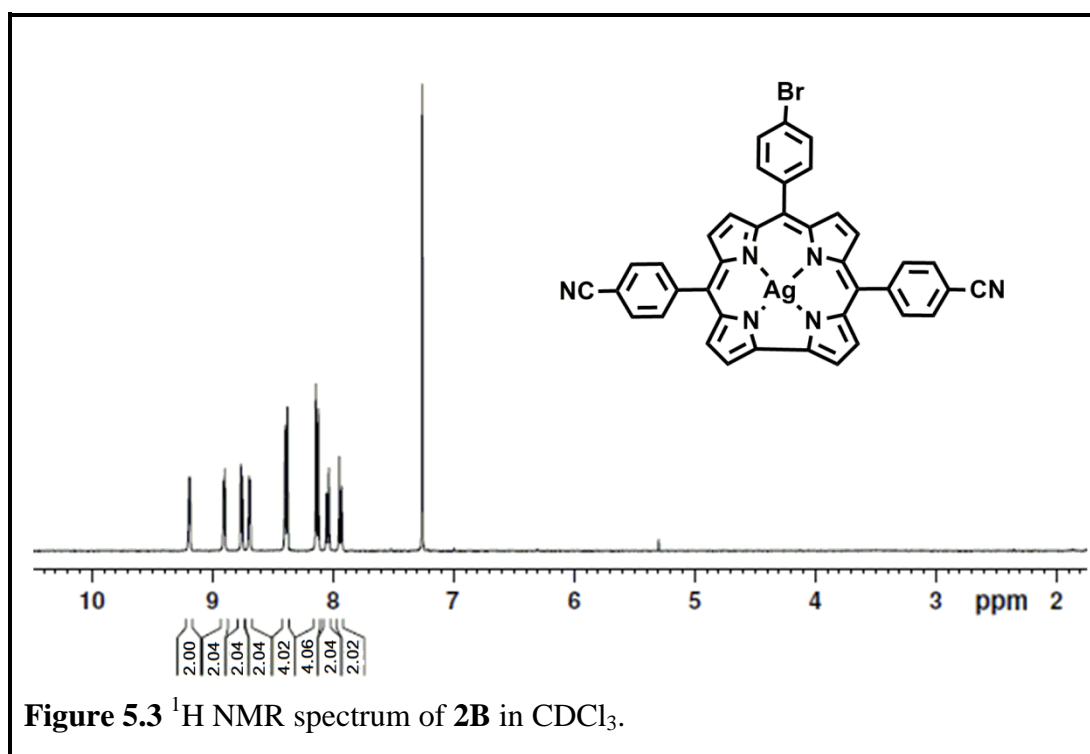
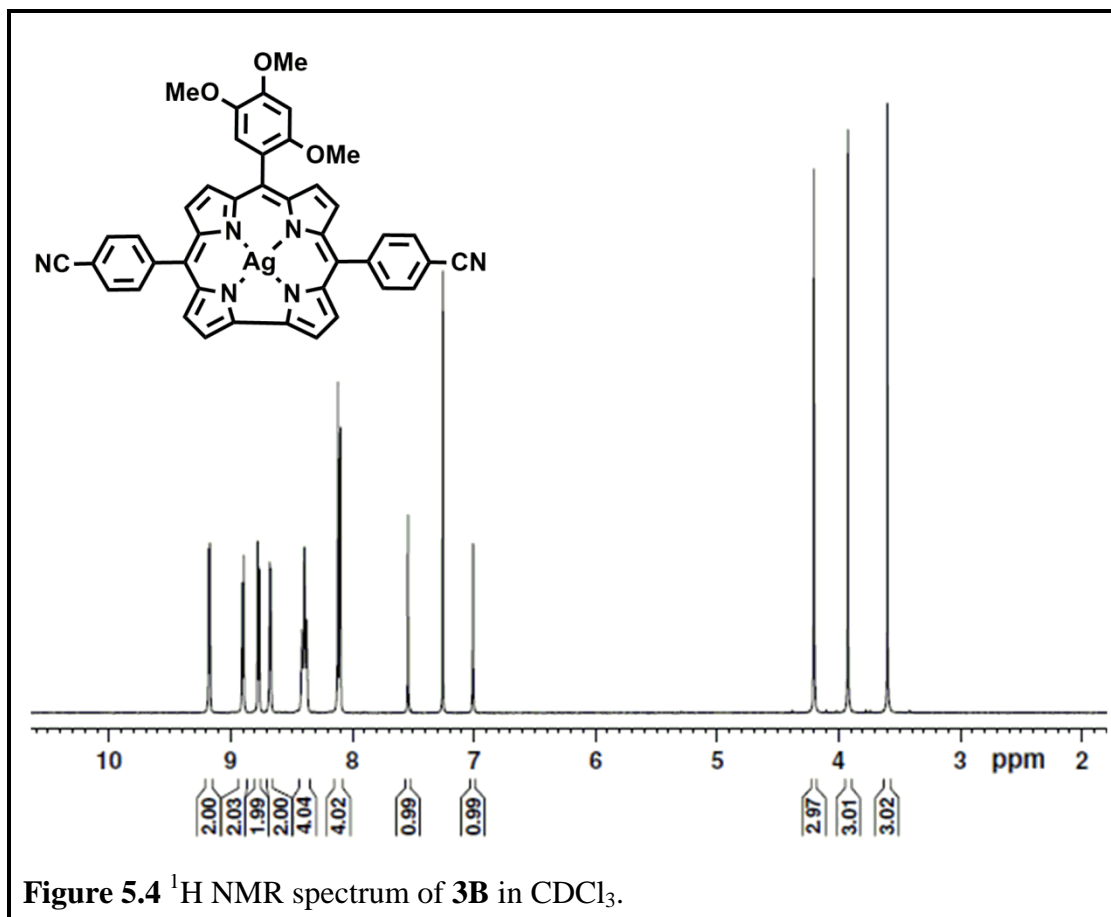
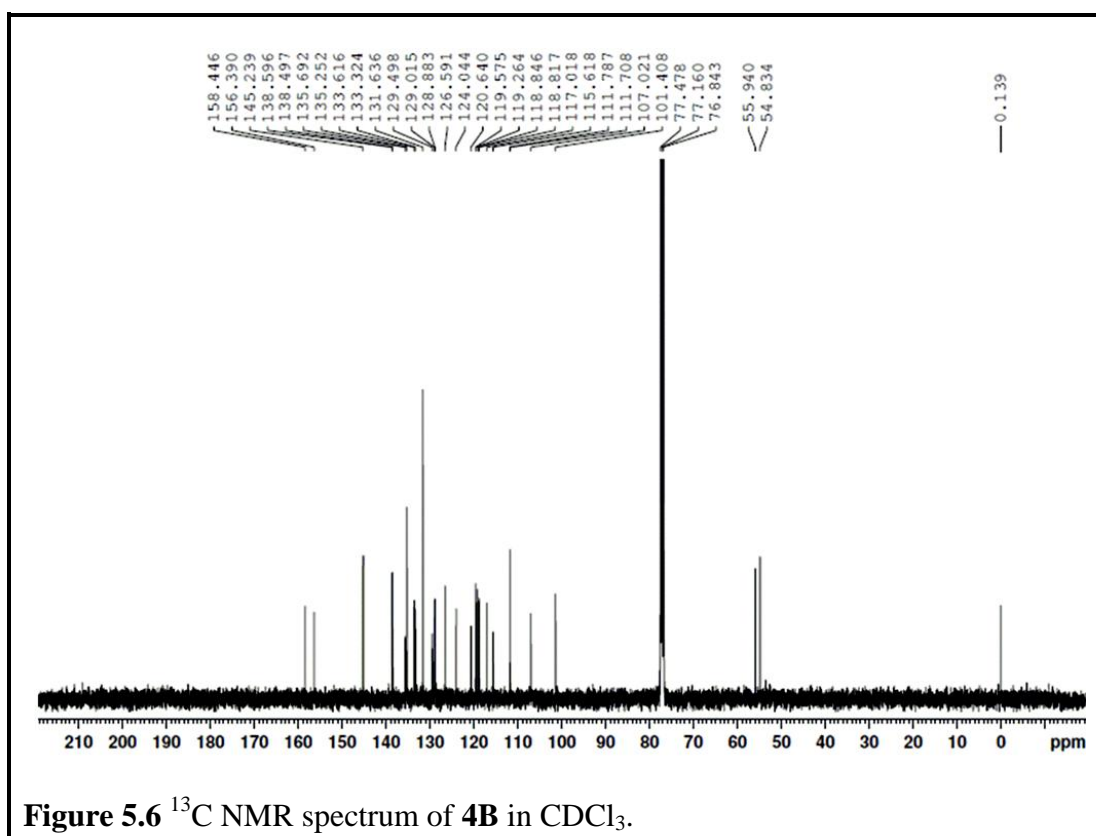
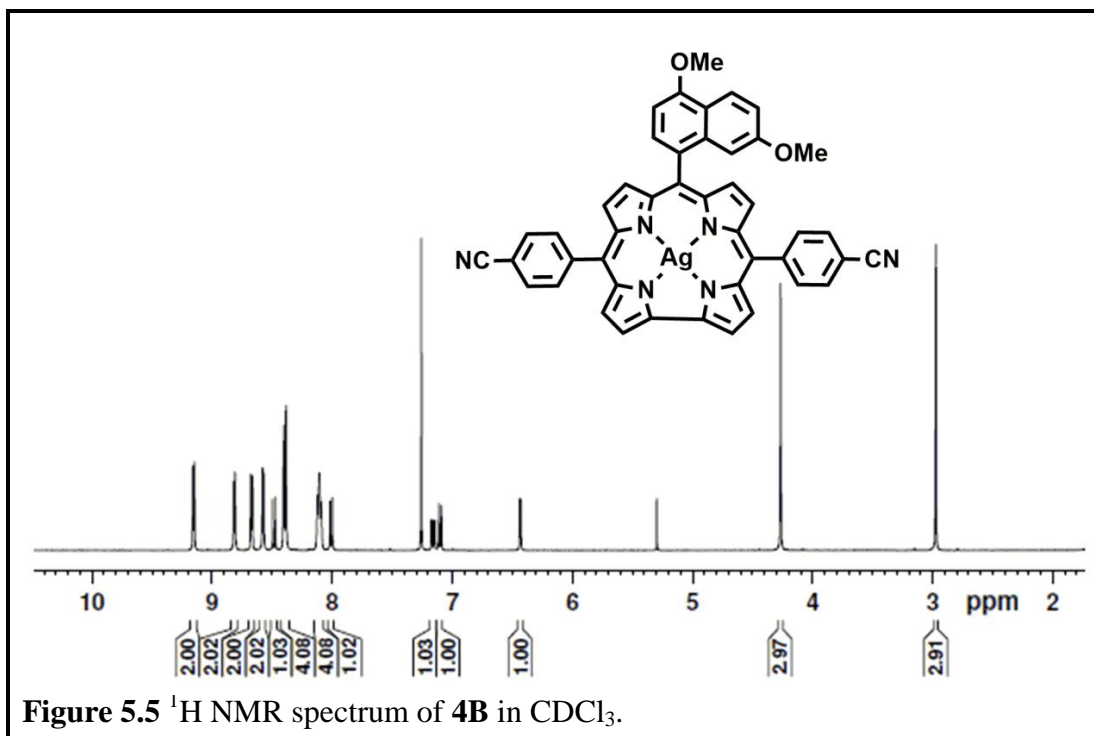


Figure 5.3 ^1H NMR spectrum of **2B** in CDCl_3 .



aromatic protons in the region δ , 9.18-7.01 ppm (Figure 5.4). Nine methoxy protons appear in the region of 4.20-3.60 ppm. Sharp peaks corresponding to twenty-one aromatic protons are observed in the region of δ , 9.16-6.43 ppm in the ^1H NMR spectrum of **4B** (Figure 5.5). Six methoxyl protons appear as distinct singlets at 4.27 and 2.97 ppm respectively. The ^{13}C NMR spectrum of **4B** (Figure 5.6) displays the presence of 26 signals due to the partial asymmetric nature of the molecule. Of these, two methoxyl signals at δ values of 56.01 ppm and 54.91 ppm, can be easily distinguished by their characteristic chemical shifts. From the downfield shift of the β -pyrrolic protons in the ^1H NMR spectra of all the synthesized silver complexes, it can be concluded that these metal complexes achieve more stability and planarity on metalation compared to the free-base corroles.



5.2.2.3 X-Ray Crystallography

The crystal structure of **4B** is shown in Figure 5.7. The compound crystallized in the monoclinic space group C_2/c with eight molecules in each unit cell. Important

crystallographic parameters are reported in Table 5.1. The crystal structure proves the near perfect square-planar geometry of the complex around the central metal ion, in which the Ag^{III} sits almost in the same plane as that of the pyrrole rings (with a minimal deviation of ~0.0194 Å).

However, a slight distortion in the ideal bond-angles for the square-planar geometry is observed due to a smaller bite angle of 81.32° for the N4–Ag1–N1 bond compared to the bite angles in the range of 91.29–96.16° for the other N–Ag1–N bonds. This deviation from ideality can be easily assigned to the presence of direct pyrrole-pyrrole linkage around C1–C19 bond of the corrole ring. The Ag–N bond distances are 1.919 Å (for Ag1–N1), 1.948 Å (for Ag1–N2), 1.945 Å (for Ag1–N3) and 1.927 Å (for Ag1–N4). These distances are slightly shorter than those of the Ag–N bonds in the silver(II) porphyrin complexes³¹⁶⁻³¹⁹. Thus, the strong field corrolato ligand stabilizes the low spin d⁸ Ag^{III} ion in a square planar environment. Compared to the heavier coinage-metal congeners, it has been observed that the Au^{III}–N bond lengths in related β -unsubstituted *meso*-triarylcorroles (1.94–1.95 Å) and pyrrole-brominated corroles (1.93–1.98 Å) are very much similar to that observed in our case^{58, 233}. However the Ag^{III}–N bond length was found to be slightly shorter than the Au^I–N bond length in related metallocorrole derivative²³³.

The pyrrole rings deviate from the mean corrolato plane not exactly in a saddle-type of distortion, but with dihedral angles ranging from as high as 15.23° (for the pyrrole ring containing C17 & C18 atoms) to as low as -8.65° (for the pyrrole ring containing C12 & C13 atoms). The dihedral angles between the *meso*-substituents at 5-, 10- and 15- positions and the corrole ring are 53.04°, 64.18° and 37.36° respectively. The molecules of **4B** are stacked to form grid-like arrays throughout the crystal lattice (along *b*-axis). Along the *a*-direction, a pine-tree-like arrangement is

observed with the naphthyl groups forming the stem and the corrole rings as branches (Figure 5.8). The Ag atoms of neighbouring corrole rings are placed as twins along two parallel lines in a zig-zag (Figure 5.9). The closest Ag...Ag distance between the twinned pair of silver atoms is 3.67 Å while that between two opposite parallelly arranged silver atoms is 4.94 Å. Thus, the ring center-to-ring center distance can be

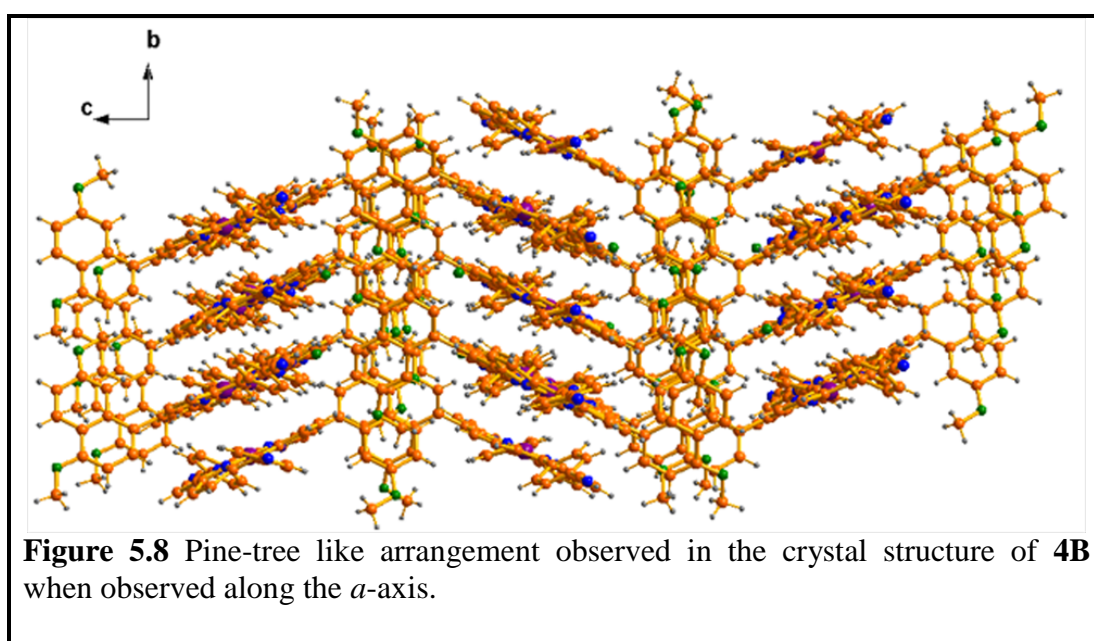
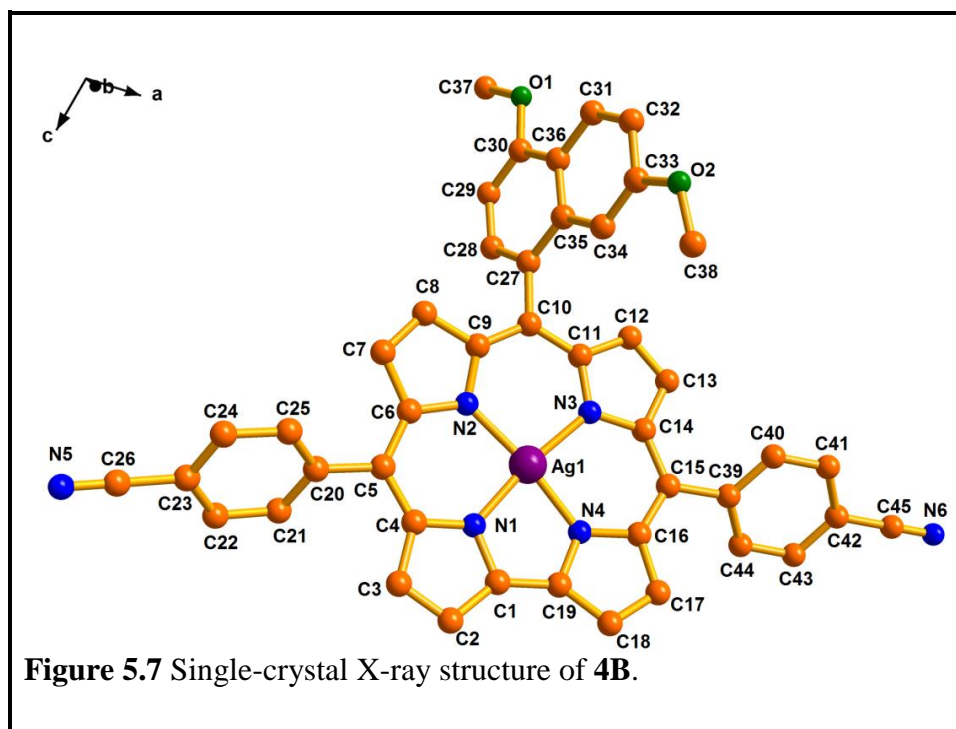


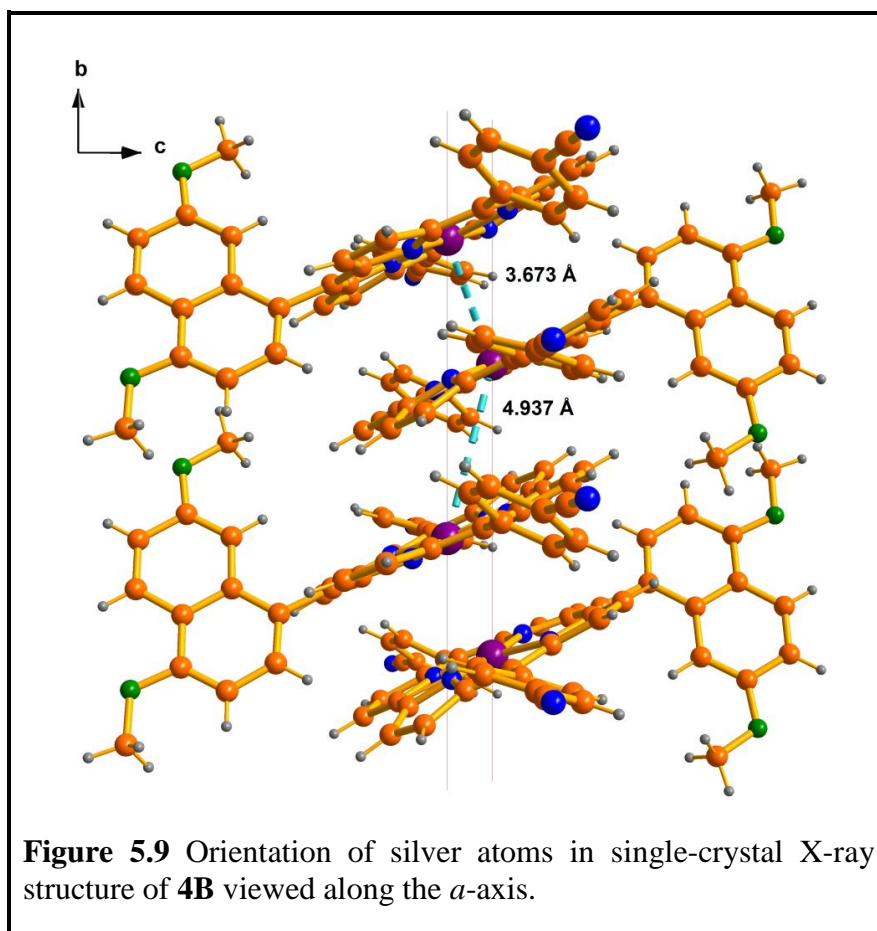
Table 5.1 Crystallographic Data for **4B**

Compound Name	4B
Molecular formula	C ₄₅ H ₂₇ AgN ₆ O ₂ , O
Formula weight	807.62
Radiation	MoK α
Crystal symmetry	Monoclinic
Space group	<i>C</i> ₂ / <i>c</i>
<i>a</i> (Å)	36.604(8)
<i>b</i> (Å)	7.79687(16)
<i>c</i> (Å)	29.343(6)
α (deg)	90
β (deg)	101.533(5)
γ (deg)	90
<i>V</i> (Å ³)	8205(3)
<i>Z</i>	8
μ (mm ⁻¹)	0.537
<i>T</i> (K)	293(2)
<i>D</i> _{calcd} (g cm ⁻³)	1.308
<i>2</i> θ range (deg)	5.58 to 51.10
<i>e</i> data (<i>R</i> _{int})	7493 (0.1027)
<i>R</i> 1 (<i>I</i> > 2 σ (<i>I</i>))	0.0590
<i>wR</i> 2	0.1671
GOF	1.032
Largest diff. peak and hole (e Å ⁻³)	1.162 and -1.347
CCDC No.	1003918

considered to be as ~ 3.67 Å. These distances between two metal centers in the closest neighbors are also very much on par with an earlier reported gold corrole and has been reported to be 3.9296(4) Å and 4.3380(4) Å in the inversion related pairs of a stacked *meso*-triaryl corrole gold(III) derivative⁵⁸. The naphthyl- groups of any two

alternate corrole rings of **4B** are placed in diametrically opposite directions with the corrole rings stabilized by strong π - π stacking interactions. The mean interplane separation of two adjacent corrole rings in parallel arrangement was found to be 3.66 Å. Hence, the lateral shift between two rings was calculated to be as 0.27 Å. Apart from the π - π stacking interactions, C-H $\cdots\pi$ interactions in the range of 3.14 Å-4.06 Å also play an important role in stabilizing the entire crystal lattice.

According to reported high-resolution X-ray crystallographic data, the mean plane distance of the bacteriochlorophylls in special-pairs is around 3.5 Å^{58, 320-325}. Thus, the mean interplane separation in silver corrole, **4B**, stabilized by strong π - π interactions, is similar to that observed in the natural photosynthetic special-pairs. In neutral metalloporphyrin systems with alkyl substituents, sideways displacement varies in the range 1.61-3.48 Å with mean plane separation in the range of 3.42-



3.55 Å. Mean interplane separation and sideways displacement have been reported to follow the order porphyrin radical cation < mixed-valence porphyrin radical cation < neutral porphyrin³²⁶.

5.2.2.4 Electrochemistry

The redox properties of **1B**, **2B**, **3B** and **4B** were investigated in CH₂Cl₂/0.1 M TBAP by using cyclic voltammetric techniques and differential pulse voltammetric techniques (Figure 5.10, Table 5.2). The oxidation and reduction processes at the positive and negative sides of Ag/AgCl reference electrode were recorded by using a platinum working electrode. All four silver complexes **1B**, **2B**, **3B** and **4B** display two successive reversible oxidations and one reversible reduction *versus* ferrocene/

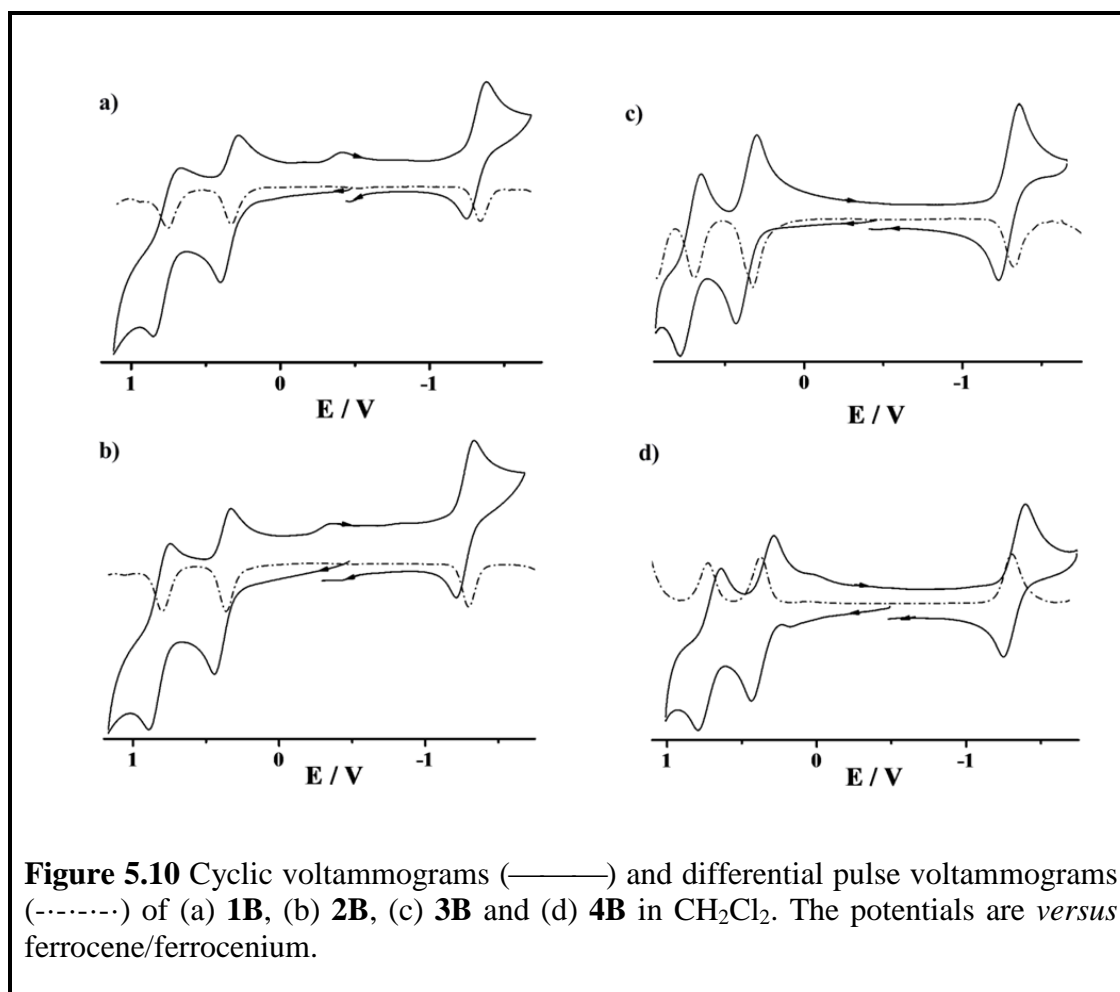


Figure 5.10 Cyclic voltammograms (—) and differential pulse voltammograms (---) of (a) **1B**, (b) **2B**, (c) **3B** and (d) **4B** in CH₂Cl₂. The potentials are *versus* ferrocene/ferrocenium.

ferrocenium each. The first oxidation was observed at E_{298}^0 , V (ΔE_p , mV): 0.34(80), 0.38(80), 0.36(80) and 0.36(90) and the second oxidation process was observed at E_{298}^0 , V (ΔE_p , mV): 0.76(100), 0.82(90), 0.72(80) and 0.78(90) for **1B**, **2B**, **3B** and **4B** respectively *versus* ferrocene/ferrocenium. They also showed one reversible reductive couple E_{298}^0 , V (ΔE_p , mV): -1.31(80) (**1B**), -1.27(80) (**2B**), -1.30(80) (**3B**) and -1.32(90) (**4B**) *versus* ferrocene/ferrocenium. The effect of the substituents on the corrolato ring on the redox potentials of the silver complexes is marginal, as revealed by the similar redox potentials in all of the above-mentioned four cases. To get information on the electronic structures of these complexes in their various redox forms UV-Vis-NIR/EPR spectroelectrochemical measurements were performed and the data obtained were interpreted with the help of DFT and TD-DFT calculations.

Table 5.2 UV-Vis and Electrochemical Data

Compound	UV-Vis Data ^a λ_{\max} / nm (ϵ / M ⁻¹ cm ⁻¹)	Electrochemical Data ^a	
		Oxidation E^0 ,V (ΔE_p , mV)	Reduction E^0 ,V (ΔE_p , mV)
1B	429(103760), 497(4452),	0.34 (80),	-1.31 (80)
	526(6940), 542(8080),	0.76 (100)	
	561(14160), 584(25220)		
2B	427(106000), 497(3612),	0.38 (80),	-1.27 (80)
	525(6000), 541(7400),	0.82 (90)	
	562(15300), 584(27460)		
3B	428(120195), 497(3774)	0.36 (80),	-1.30 (80)
	526(6980), 542(9120)	0.72 (80)	
	565(21371), 584(33772)		
4B	428(133140), 501(4834),	0.36(90),	-1.32 (90)
	525(7780), 538(9860),	0.78(90)	
	566(25240), 584(37280)		

^a In dichloromethane/0.1 M TBAP.

5.2.3 EPR Spectroelectrochemistry and Spin Density Calculations

The unambiguous observation of the diamagnetic character of the silver complexes **1B-4B**, and the reversibility of their one-electron oxidation and reduction process, as observed by cyclic voltammetry, prompted us to investigate the X-band EPR spectroscopic properties of these complexes in their one-electron oxidized as well as reduced states. The oxidized forms of all complexes display spectra that are identical; the same is true for the spectra of the reduced forms of all the complexes. Hence, only one case each will be discussed below. The data for the rest of the complexes have been tabulated in Table 5.3. The *in-situ* generated one-electron oxidized species (**1B**)^{•+} in CH₂Cl₂/0.1 M Bu₄NPF₆ displays an isotropic signal at 295 K which is centered at $g = 2.003$ (Figure 5.11).

This signal, which is observed in fluid solutions, is relatively narrow, with a peak to peak separation of about 10 G (Figure 5.11b). The spectral features mentioned above, clearly point to a predominantly ligand centered spin in (**1B**)^{•+}. However, in the absence of hyperfine coupling, it is difficult to make predictions regarding spin density distribution from experimental data alone. Hence, we turned to DFT calculations for an answer to this problem.

Structure-based DFT calculations were carried out on the complexes **2B** and **4B** and their various redox forms as representative examples in Tables A5.1-A5.12 and Figures A5.1-A5.6 (see Appendix). **4B** was chosen because of the availability of an experimentally determined crystal structure, and **2B** because of the calculations of UV-Vis-NIR absorption properties in the various redox forms (see below). The structures of **2B** and **4B** were optimized using the BP86 functional, and the optimized bond lengths (for **4B**) match reasonably well with the experimental data (Table A5.13, see Appendix). The structural optimization of **2B** was carried out by taking **4B** as a

standard. A look at the spin densities calculated using the Löwdin population analysis for $(2\mathbf{B})^{\bullet+}$ and $(4\mathbf{B})^{\bullet+}$ reveals that less than 1% spin density resides on the silver atom (Figure 5.12 and Table 5.4). The spin density is predominantly located on the meso carbon atoms and the donating nitrogen atoms of the corrolato ring. The calculated g value of 2.004 nicely matches with the experimental value. Spin-density data thus clearly establish the best formulation for the one-electron oxidized complexes as $[(\text{corrolato}^{\bullet-})\text{Ag}^{\text{III}}]^{\bullet+}$ with almost exclusively ligand centered spin. The narrow line width of these signals together with the presence of many nuclear-spin-bearing atoms in the ligand presumably precludes the resolution of the expected hyperfine coupling in the experimental EPR spectra of these complexes.

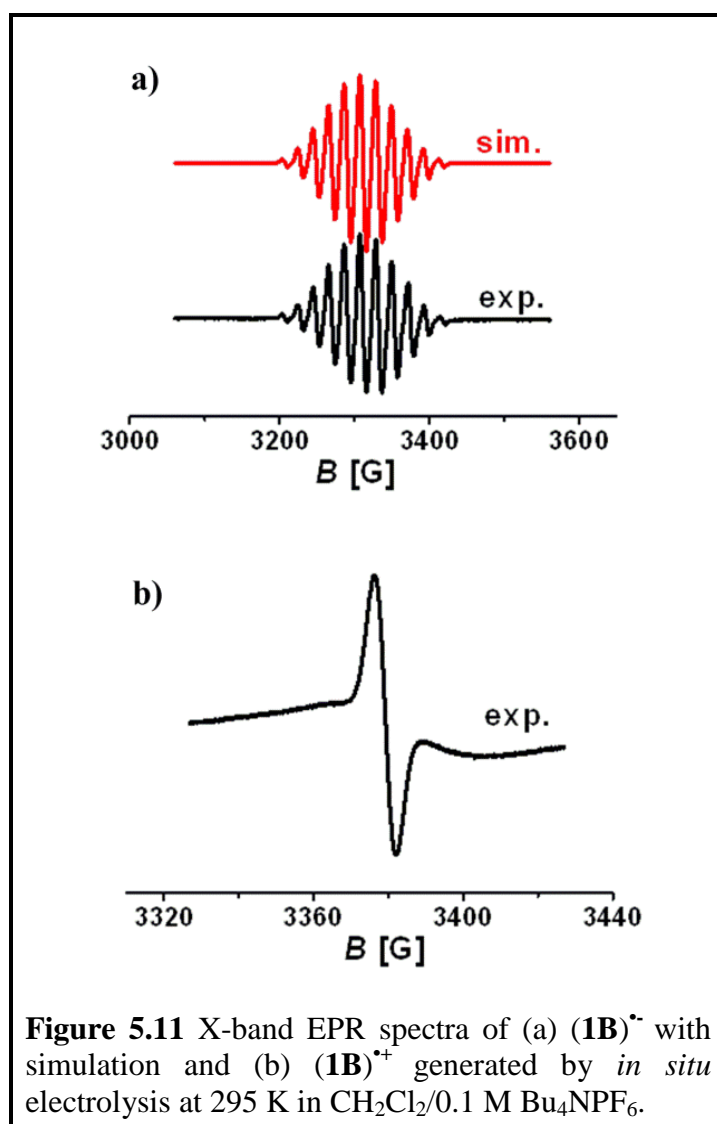


Table 5.3 EPR Data^[a] of Paramagnetic States^[b]

Complex	EPR Data ^[a] (<i>g</i>)
1B⁺	2.003
2B⁺	2.003
3B⁺	2.004
4B⁺	2.003
1B^{•-}	2.003; a (¹⁴ N) = 22.5 G; a (¹⁴ N) = 20.9 G; a = 20.1 G; a (¹⁴ N) = 19.2 G; a(^{107,109} Ag) = 40.8 G
2B^{•-}	2.003; a (¹⁴ N) = 22.3 G; a (¹⁴ N) = 20.7 G; a = 20.0 G; a (¹⁴ N) = 19.4 G; a(^{107,109} Ag) = 40.5 G
3B^{•-}	2.002; a (¹⁴ N) = 22.7 G; a (¹⁴ N) = 20.4 G; a = 20.5 G; a (¹⁴ N) = 19.7 G; a(^{107,109} Ag) = 40.2 G
4B^{•-}	2.004; a (¹⁴ N) = 22.7 G; a (¹⁴ N) = 20.5 G; a = 20.1 G; a (¹⁴ N) = 19.3 G; a(^{107,109} Ag) = 40.7 G

[a] *g* values measured at 295 K. [b] From EPR spectroelectrochemistry in CH₂Cl₂/0.1 M Bu₄NPF₆.

Table 5.4 DFT (B3LYP/TZVPP-ZORA) Calculated Löwdin Spin Densities on Ag

Complex	Ag
4B⁺	< 1%
4B⁻	43%
2B⁺	< 1%
2B⁻	44%

In contrast to the EPR spectra of the one-electron oxidized species, the spectra of the one-electron reduced forms display many additional features (Figure 5.11a). For example, the EPR spectrum of the *in situ* electrochemically generated complex (**1B^{•-}**) displays a line-rich signal at 295 K in CH₂Cl₂/0.1 M Bu₄NPF₆ that is centered at *g* = 2.003. The peak to peak separation of this signal is about 220 G. This spectrum was simulated by considering hyperfine coupling to four different ¹⁴N (*I* = 1) nuclei (Table

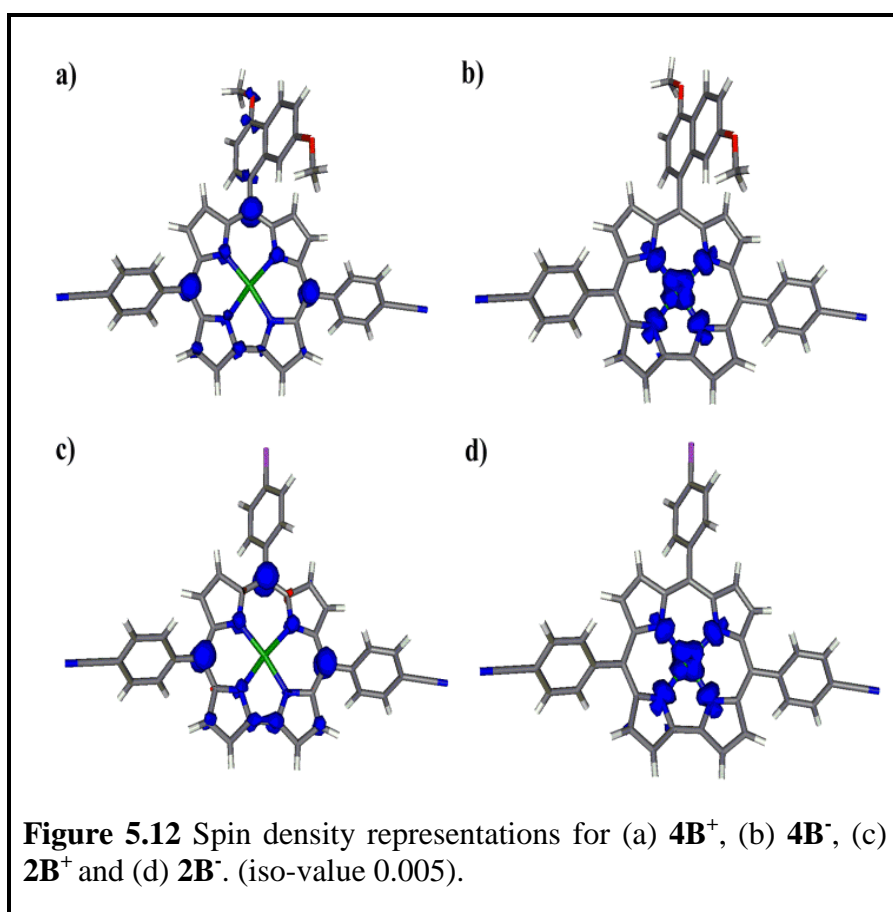
5.3). Additionally, hyperfine coupling to ^{107}Ag and ^{109}Ag ($I = 1/2$, total natural abundance: 100 %) nucleus of about 41 G was also considered for the simulation. This large hyperfine coupling to the silver nucleus points to a substantial spin Löwdin population analysis delivers about 50 % spin density on silver for the one-electron reduced forms of the complexes (Figure 5.12, Table 5.4). The calculated g value of 2.002 matched well with the experimentally determined g value. The experimental EPR data, and the spin density calculations thus point to a large contribution of the $[(\text{corrolato}^{3-})\text{Ag}^{\text{II}}]^-$ form in the one-electron reduced forms of these complexes and stabilization of the unusual Ag^{II} oxidation state.

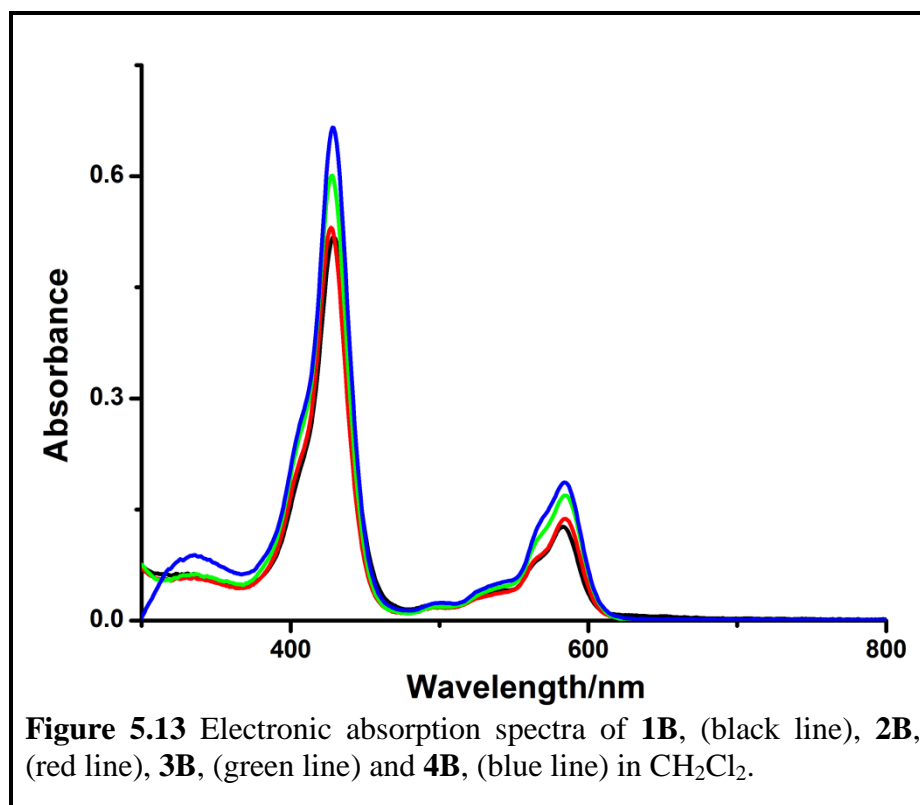
5.2.4 UV-Vis-NIR Spectroelectrochemistry and TD-DFT Calculations

Electronic spectral data of the compounds in CH_2Cl_2 (Figure 5.13) are shown in Table 5.2. All the four silver complexes **1B**, **2B**, **3B** and **4B** exhibit Soret bands in the range of 427-429 nm. Various other weak bands are observed in the region of 497-584 nm (Table 5.4). The obtained values agree well with the related compounds reported in the literature^{58, 126, 284, 310-315}. Although there are striking similarities in the absorption properties among all the synthesized silver corrole complexes in their neutral form, yet the spectroelectrochemical data for the oxidized complexes can be classified into two different groups on the basis of corrole ring substituents-one comprising of **1B** and **2B**, with only electron withdrawing substituents on the phenyl rings at the *meso*-positions and the other comprising of **3B** and **4B**, with electron donating substituents on one of the phenyl rings at the *meso*-position. Hence, in the discussion below we will concentrate on the properties of **2B** and **4B**. TD-DFT calculations were carried out on **2B** and **4B** to shed light on the absorption signatures of these compounds (Figure 5.14). For **2B**, the contributing frontier orbitals to the main transitions are all

ligand based (Table A5.7, see Appendix). The most intense band at 427 nm is a mixture of transitions between HOMO-1 \rightarrow LUMO+2 and HOMO \rightarrow LUMO+4 orbitals (Table A5.10). All these orbitals are based on the corrolato ring. This fact is expected for this intense Soret band.

However, the situation is different for **4B**, which has one donor substituent on the corrolato ring. For **4B**, transitions in the visible region have part of their origin either in intra ligand charge transfer (ILCT) or ligand to metal charge transfer (LMCT) involving the electron rich substituent on the corrolato ring (Tables A5.1 and A5.4, see Appendix). Thus, it can be speculated that donor substituents can modify the electronic structures of such corrolato complexes. The various redox states of these complexes, **1B-4B**, were probed in $\text{CH}_2\text{Cl}_2/0.1 \text{ M Bu}_4\text{NPF}_6$ by using UV-Vis-





NIR spectroelectrochemical measurements using an optically transparent thin-layer electrochemical (OTTLE) cell and the corresponding results have been represented in Table 5.5 and Figures 5.15-5.17. On one-electron reduction of **2B** to (**2B**)⁻, the intense band at 427 nm is shifted to lower energy, the low-energy band at 584 nm loses in intensity, and a new low-energy band appears at 646 nm (Figure 5.15). TD-DFT calculations show this band to be a combination of transitions from HOMO α \rightarrow LUMO+2 α , HOMO-1 α \rightarrow LUMO α and HOMO β \rightarrow LUMO β (Tables A5.9 and 5.12, see Appendix). Thus, this new low-energy band is seen to be an outcome of a mixture of metal to ligand charge transfer (MLCT), ILCT and intra ligand transitions. The MLCT and ILCT transitions have an orbital with large contributions from the acceptor substituents of the corrolato ring as target orbitals. The relatively electron rich formal Ag^{II} centers, generated upon one-electron reduction make these MLCT transitions possible (see EPR results before). The changes in the absorption spectrum on from **4B** to (**4B**)⁻ are similar to the case discussed above (Table 5.5), and TD-DFT

delivers similar origin for the bands in $(\mathbf{4B})^-$ as for $(\mathbf{2B})^-$ (Tables A5.3 and A5.6). On one-electron oxidation of $\mathbf{2B}$ to $(\mathbf{2B})^{+\cdot}$, all existing bands in the visible region get diminished in intensity, and new, broad absorptions appear between 600 and 800 nm (Figure 5.16). Whereas most bands in the visible region have a mixed origin according to TD-DFT calculations, the lowest energy was calculated for an ILCT transition from the substituent in the *meso*-position to the central corrolato ring (Tables A5.8 and A5.11). The generation of a hole at corrolato ring on one-electron oxidation makes this transition facile (see EPR section before). For $(\mathbf{4B})^{+\cdot}$, the bands in the visible region are all of mixed origin as has been discussed for $(\mathbf{2B})^{+\cdot}$. However, for $(\mathbf{4B})^{+\cdot}$ the lowest energy band now is further shifted into the NIR region and appears at about 1200 nm. TD-DFT reveals the origin of this band as transitions from HOMO-1 β \rightarrow LUMO β and HOMO β \rightarrow LUMO β (Table A5.5, see Appendix). These bands are thus of ILCT and intra ligand transitions in nature (Table A5.2). On further oxidation of these complexes to $(\mathbf{2B})^{2+}$ or $(\mathbf{4B})^{2+}$, the NIR bands persist and slightly gain in intensity (Figure 5.17). These results are consistent with the generation of further holes on the corrolato core, and hence the ILCT transition becoming more facile. Thus, it can be concluded that the introduction of electron donating substituents at the *meso*-positions of the corrolato ring shifts the energy of the long-wavelength band further into the NIR region. This observation can be explained by a destabilization of the origin orbitals which are localized on those substituents. Such a destabilization would result in a smaller energy gap between the relevant orbitals and hence shift these ILCT bands to even lower energy. Similar observations have also been made for the oxidized forms of $\mathbf{1B}$ and $\mathbf{3B}$ (Figures 5.16 and 5.17). On returning back to the starting potential, the initial spectrum of all the corrolato-silver(III) derivatives were restored to 100% in position and intensity, and thus the formation of

dimers of the oxidized species is ruled out. Hence, these transitions originate from the mononuclear complexes. TD-DFT gives a good qualitative explanation for these transitions, even though the quantitative fit is not always excellent.

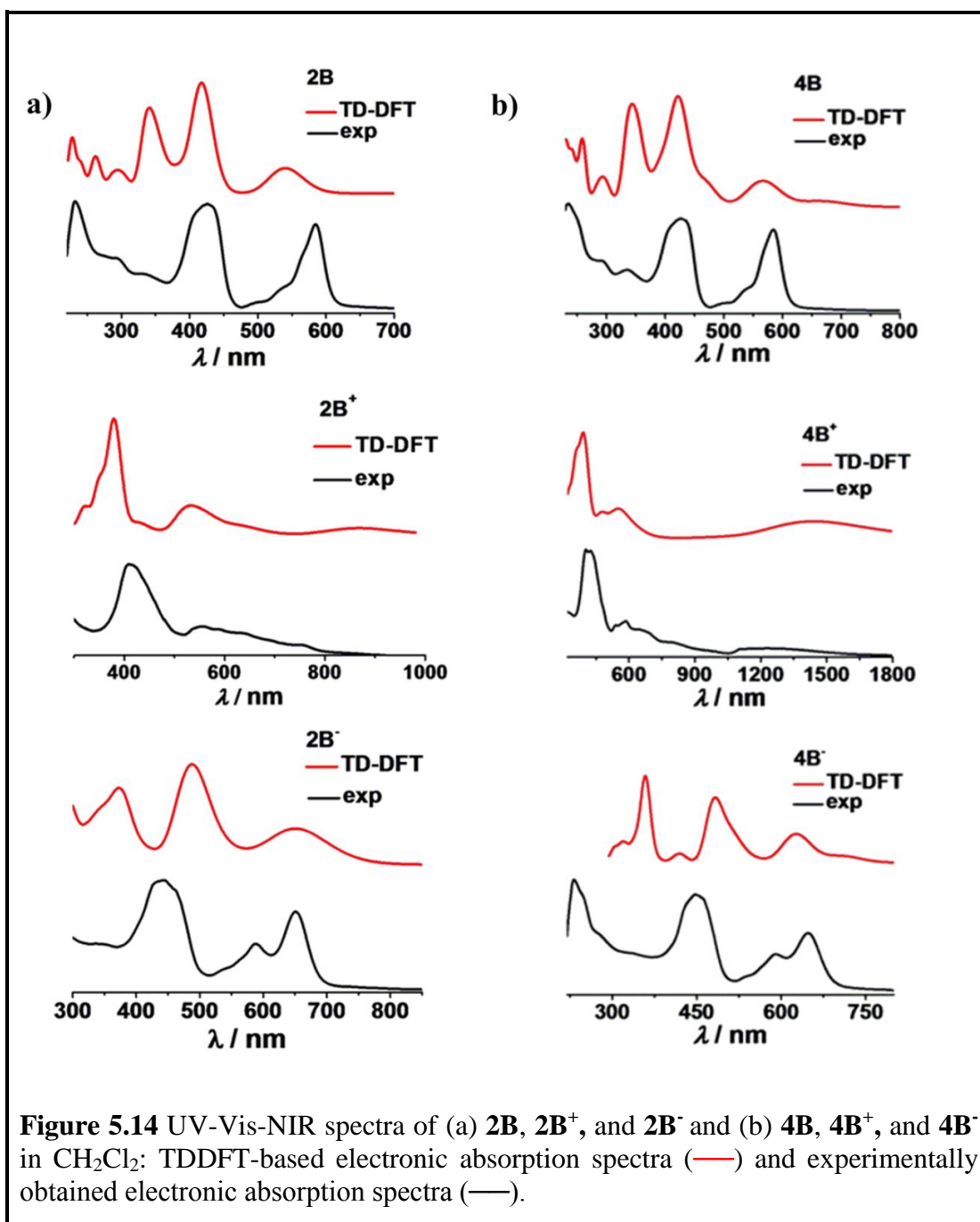
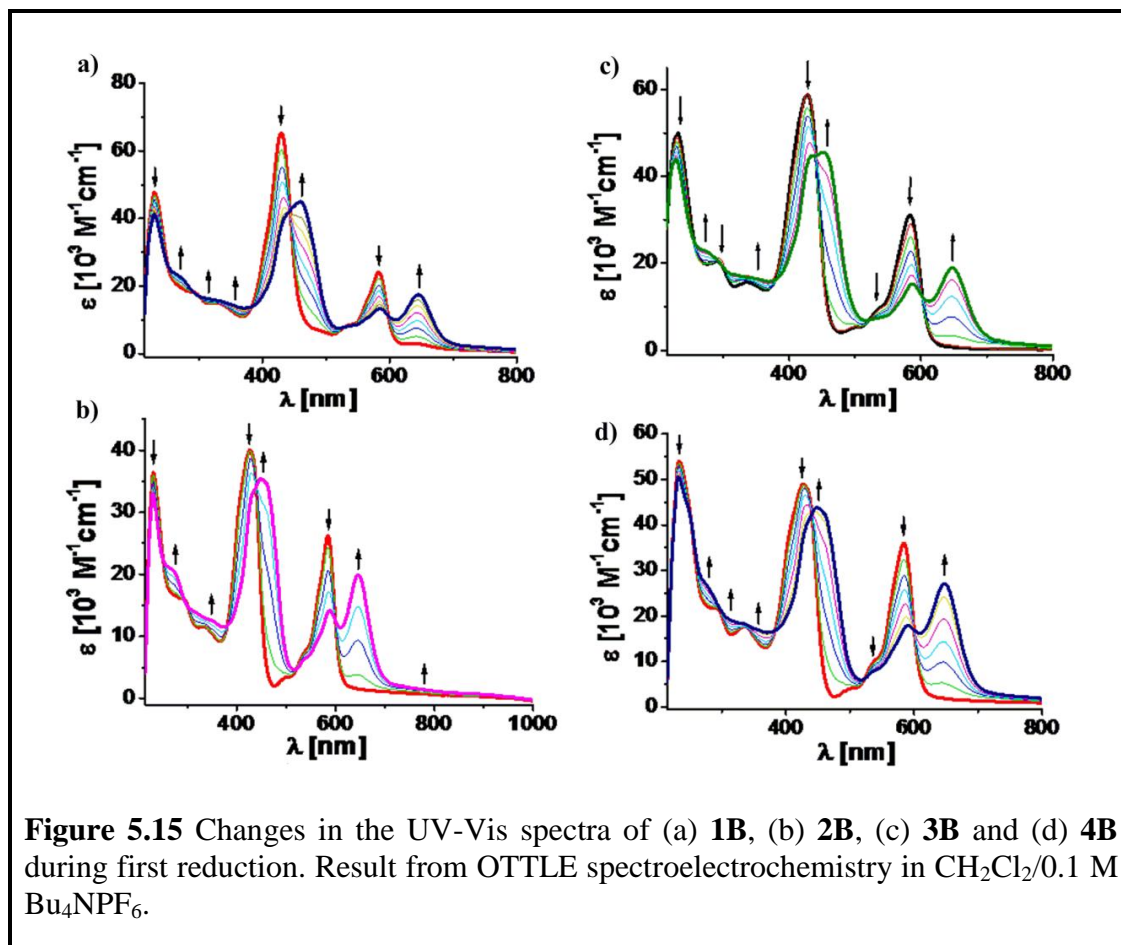


Figure 5.14 UV-Vis-NIR spectra of (a) **2B**, **2B⁺**, and **2B⁻** and (b) **4B**, **4B⁺**, and **4B⁻** in CH₂Cl₂: TDDFT-based electronic absorption spectra (—) and experimentally obtained electronic absorption spectra (—).

Table 5.5 UV-Vis-NIR Data of **1Bⁿ**, **2Bⁿ**, **3Bⁿ**, and **4Bⁿ**, [*n* = -1, +1, +2, 0] from Spectroelectrochemistry^[a]

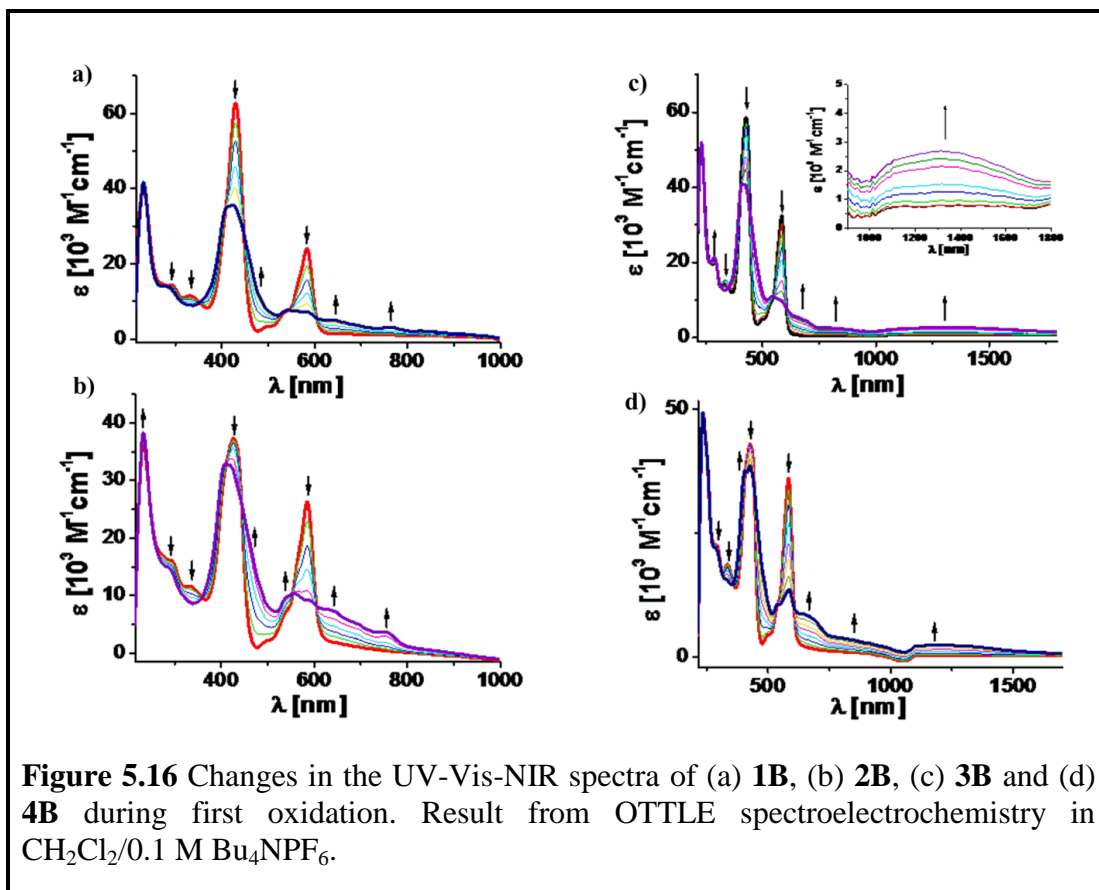
Complex	λ_{\max} [nm] (ϵ [$10^3 \text{ M}^{-1} \text{ cm}^{-1}$])
1B⁰	230 (40.8); 291 (14.3); 331 (11.4); 429 (62.7); 500 (3.4); 536 sh; 564 sh; 584 (24.2)
1B⁻	230 (41.3); 268 sh; 327 sh; 438 sh; 461 (45.1); 543 sh; 585 (13.5); 646 (17.5)
1B⁺	231 (41.6); 277 (14.1); 420 (35.5); 542 (7.6); 579 (7.1); 638 (5.6); 760 (3.6)
1B²⁺	232 (33.1); 283 sh; 364 sh; 412 (23.7); 597 (7.8); 641 (8.4); 762 (4.2)
2B⁰	232 (36.6); 289 (16.2); 330 (11.6); 427 (37.3); 501 sh; 538 sh; 584 (26.6)
2B⁻	231 (33.1); 270 sh; 314 sh; 352 sh; 449 (35.5); 539 sh; 589 (14.2); 646 (20.0)
2B⁺	232 (38.4); 285 (15.0); 409 (33.1); 419 (32.7); 557 (10.4); 588 (9.3); 636 (7.6); 694 (5.4); 752 (3.9)
2B²⁺	233 (37.4); 287 sh; 412 (31.0); 561 (10.1); 594 (10.2); 638 (9.3); 751 (4.0); 846 sh
3B⁰	231 (50.5); 293 (20.0); 335 (14.1); 428 (58.6); 503 (5.0); 537 sh; 566 sh; 584 (32.4)
3B⁻	229 (44.1); 276 (22.8); 345 sh; 434 (44.7); 452 (45.7); 536 sh; 587 (15.3); 648 (19.0)
3B⁺	231 (51.5); 288 (21.2); 407 (40.8); 426 (44.9); 544 sh; 584 (12.3); 690 sh; 831 (2.1); 1319 (2.4)
3B²⁺	232 (54.7); 284 (21.0); 418 (41.8); 527 sh; 691 (6.5); 1237 (6.3)
4B⁰	234 (49.2); 290 (22.7); 336 (18.8); 426 (42.9); 506 (4.7); 538 sh; 584 (36.2)
4B⁻	232 (50.6); 249 sh; 276 sh; 334 (18.3); 447 (44.0); 537 sh; 591 (18.0); 648 (27.2)
4B⁺	234 (49.3); 251 sh; 286 (22.1); 332 (15.6); 407 (37.5); 427 (38.7); 541 (10.7); 586 (13.7); 647 (8.5); 844 (3.9); 1203 (2.7)
4B²⁺	234 (49.0); 250 sh; 288 (21.6); 328 (15.9); 405 (36.1); 426 (36.3); 539 (10.7); 587 (12.4); 647 (9.5); 827 sh; 1212 (2.6)

[a] Measurements in CH₂Cl₂/0.1 M Bu₄NPF₆ (OTTLE spectroelectrochemistry).

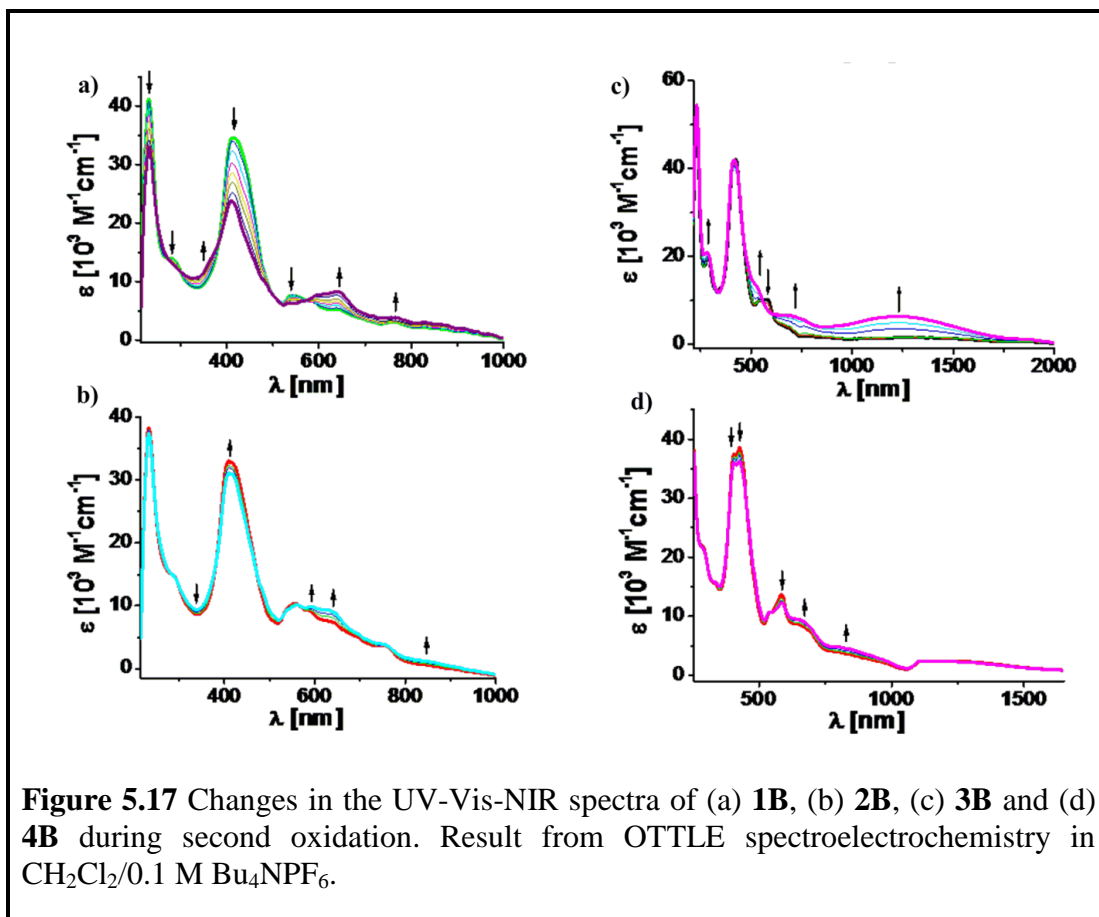


5.3 Conclusions

A series of corrolato-silver(III) complexes was prepared in which the donor properties of the *meso*-substituents on the corrolato rings were systematically varied. ^1H NMR spectra of the corrolato-silver(III) complexes show sharp resonances indicating their diamagnetic nature. The Ag atom sits almost in the same plane as the pyrrole rings (with a minimal deviation of $\sim 0.0194 \text{ \AA}$) as observed in the case of **4B**. In the packing diagram of **4B**, if viewed along the x direction, a pine-tree-like arrangement is observed with the naphthyl-groups forming the stem and the corrole rings as branches. The low-spin d^8 configuration is thus stabilized in these Ag^{III} complexes. All four corrolato-silver(III) complexes exhibited two reversible oxidative couples and one reversible reductive couple. EPR spectroscopy and spin-density calculations clearly



deliver evidence for the stabilization of the unusual Ag^{II} oxidation state in the one-electron reduced state of these complexes. Both the one- and two-electron oxidized forms of two of the complexes display absorptions in the NIR region. The position of the NIR band can be tuned by the use of suitable substituents on the corrolato ring, with electron-donating substituents shifting the bands to lower energy. Thus, even though the substituents at the corrolato ring do not have any significant influence on the redox properties of the neutral complexes, they do show a strong influence on the position of the long-wavelength bands of the oxidized complexes. EPR spectroscopy and spin-density calculations confirm the one-electron oxidized form contains corrolato-based radicals (as opposed to Ag^{IV}), and TD-DFT calculations confirm that the origin of the NIR bands is of ILCT/intraligand nature. In contrast to most literature reports, in which such NIR absorptions have been assigned to transitions



involving π - π stacked dimers, our results here clearly prove that these transitions originate from mononuclear complexes.

We have thus presented systems that can stabilize various unusual oxidation states at the metal center. Furthermore, we have described new design strategies for generating tunable NIR-absorbing dyes. These studies also show the importance of varying the *meso*-substituents on the corrolato rings for perturbing the electronic structures of such complexes and generating systems with tailor-made properties. Thus, suitable design of such systems may lead to the discovery of new varieties of chlorophyll-like light-harvesting units that may not solely depend on the photosynthetic special-pairs for light harvesting purposes.

5.4 Experimental Section

5.4.1 Materials

The precursors pyrrole, *p*-chloranil, 4-cyano benzaldehyde, 2,4,5-trimethoxy benzaldehyde, 4-bromo benzaldehyde, 4,7-dimethoxy naphthaldehyde and TBAP (Tetrabutyl ammonium perchlorate) were purchased from Aldrich, USA. Ag(OAc) was purchased from Merck, India. Other chemicals were of reagent grade. Hexane and CH₂Cl₂ were distilled from KOH and CaH₂ respectively. For spectroscopy and electrochemical studies HPLC grade solvents were used.

5.4.2 Physical Measurements

UV–Vis spectral studies were performed on a Perkin–Elmer LAMBDA-750 spectrophotometer. The elemental analyses were carried out with a Perkin–Elmer 240C elemental analyzer. The NMR measurements were carried out using a Bruker AVANCE 400 NMR spectrometer. Tetramethylsilane (TMS) was the internal standard. Electrospray mass spectra were recorded on a Bruker Micro TOF-QII mass spectrometer. Cyclic voltammetry measurements were carried out using a CH Instruments model CHI1120A electrochemistry system. A glassy–carbon working electrode, a platinum wire as an auxiliary electrode and a saturated calomel reference electrode (SCE) were used in a three–electrode configuration. Tetrabutyl ammonium perchlorate (TBAP) was the supporting electrolyte (0.1M) and the concentration of the solution was 10⁻³M with respect to the complex. The half wave potential E_{298}^0 was set equal to $0.5(E_{pa} + E_{pc})$, where E_{pa} and E_{pc} are anodic and cathodic cyclic voltammetric peak potentials, respectively. The scan rate used was 100 mV s⁻¹. EPR spectra in the X band were recorded with a Bruker System EMX. Simulations of EPR

spectra were done using the Simfonia program. UV-Vis-NIR absorption spectra were recorded on an Avantes spectrometer system: Ava Light-DH-BAL (light source), AvaSpec-ULS2048 (UV-Vis-detector) and AvaSpec-NIR256-2.5TEC (NIR-detector). Spectroelectrochemical measurements were carried out using an optically transparent thin layer electrochemical (OTTLE) cell ¹⁹³.

5.4.3 Crystal Structure Determination

Single crystals of **4B** were grown by slow diffusion of a solution of **4B** in dichloromethane into methanol, followed by slow evaporation under atmospheric conditions. The crystal data of **4B** were collected on a Bruker Kappa APEX II CCD diffractometer at 293 K. Selected data collection parameters and other crystallographic results are summarized in Table 5.1. All data were corrected for Lorentz polarization and absorption effects. The program package SHELXTL ¹⁹⁵ was used for structure solution and full matrix least squares refinement on F^2 . Hydrogen atoms were included in the refinement using the riding model. Contributions of H atoms for the water molecules were included but were not fixed. Disordered solvent molecules were taken out using SQUEEZE ¹⁹⁶ command in PLATON. CCDC 1003918 contains the supplementary crystallographic data for **4B**.

5.4.4 Computational Details

DFT calculations were done with the ORCA 3.0.0 program ³²⁷ package using the BP86 and B3LYP functional for the geometry optimization and single-point calculations respectively ^{197, 328, 329}. The restricted and unrestricted DFT method was employed for closed and open shell molecules respectively. All calculations were run with empirical Van der Waals correction (D3) ³³⁰. Convergence criteria were set to default for the geometry-optimizations (OPT) and tight for SCF calculations

(TIGHTSCF). Relativistic effects were included with the zeroth-order relativistic approximation (ZORA)³³¹. Triple- ζ -valence basis sets (TZVPP- ZORA)³³² were employed for all atoms. Calculations were performed using the resolution of the identity approximation³³³⁻³³⁶ with matching auxiliary basis sets. Low-lying excitation energies were calculated with time-dependent DFT (TD-DFT). Solvent effects were taken into account with the conductor-like screening model (COSMO)^{337, 338} for all calculations. Spin densities were calculated according to the Löwdin population analysis³³⁹. The contribution of molecular fragments to molecular orbitals was analyzed with the MOAnalyzer tool³⁴⁰. Molecular orbitals and spin densities were visualized with the Molekel 5.4.0.8 program³⁴¹.

5.4.5 Synthesis of 4-(Di(1H-pyrrol-2-yl)methyl)benzotrile, 1

Compound, **1** was characterized by various spectral techniques. These analyses matched well with the earlier reported values³⁴².

5.4.6 Synthesis of 10-(4,7-Dimethoxynaphthalen-1-yl)-5,15-bis(4-cyanophenyl)corrole, 4A

4A was prepared by following a general procedure of corrole synthesis. 5-(4-Cyanophenyl)dipyrromethane (247 mg, 1 mmol) and 4,7-dimethoxy naphthaldehyde (108 mg, 0.5 mmol) were dissolved in MeOH (50 mL). The reaction was kept for stirring for 1 h. the mixture was extracted with CHCl₃, the organic layer was washed twice with H₂O, dried by anhydrous Na₂SO₄, filtered, and diluted to 250 mL with CHCl₃. Then *p*-chloranil (369 mg, 1.5 mmol) was added, and the mixture was refluxed for 1 h. The solvent was removed by rotary evaporation and the green colored crude product was purified by column chromatography through silica gel (100-200 mesh) column and using 80% DCM and 20% hexane as eluent. Yield: 50%

(172 mg). ^1H NMR (400 MHz, CDCl_3) δ 9.03 (s, 2H), 8.74 (s, 2H), 8.50 (t, $J = 30.4$ Hz, 9H), 8.06 (t, $J = 23.2$ Hz, 5H), 7.19 – 7.02 (m, 2H), 6.48 (s, 1H), 4.26 (s, 3H), 2.99 (s, 3H); UV/Vis (dichloromethane): λ_{max} (ϵ) = 429 (126000), 576 (25000), 629 (18600), 648 nm ($18000 \text{ M}^{-1}\text{cm}^{-1}$); MS (ESI $^+$): m/z : calcd for $\text{C}_{45}\text{H}_{30}\text{N}_6\text{O}_3$: 686.24; found: 687.24 $[\text{M}+\text{H}]^+$; elemental analysis calcd (%) for $\text{C}_{45}\text{H}_{30}\text{N}_6\text{O}_3$ (**4A**): C 78.78, H 4.46, N 12.30; found: C 78.66, H 4.33, N 12.19; **4A** displayed strong fluorescence at 676 nm.

5.4.7 Synthesis of 5,10,15-Tris(4-cyanophenyl)corrolato-silver(III), **1B**

5,10,15-tris(4-cyanophenyl) corrole (25 mg, 0.041 mmol) was dissolved in pyridine (6 mL) and silver acetate (68 mg, 0.41 mmol) was added to it. The reaction mixture was kept at stirring for 40 min at room temperature during which, the colour of the reaction mixture changed from green to dark reddish-brown. The solvent was then removed by rotary evaporation and the dark red-brown crude product was purified by column chromatography through silica gel (100-200 mesh) column using 100% DCM as eluent. Subsequent recrystallization ($\text{CH}_2\text{Cl}_2/\text{hexane}$) gave the pure crystalline 5,10,15-tris(4-cyanophenyl)corrolato-silver(III), **1B**. Yield: 58% (17 mg). ^1H NMR (400 MHz, CDCl_3) δ 9.29 (d, $J = 4.5$ Hz, 2H), 8.97 (d, $J = 4.6$ Hz, 2H), 8.76 (dd, $J = 14.2, 4.6$ Hz, 4H), 8.43 (d, $J = 8.1$ Hz, 4H), 8.34 (d, $J = 8.0$ Hz, 2H), 8.13 (dd, $J = 12.0, 8.1$ Hz, 6H) (Figure 1); UV/Vis (dichloromethane): λ_{max} (ϵ) = 429 (103800), 497 (4400), 526 (6900), 542 (8000), 561 (14200), 584 nm ($25200 \text{ M}^{-1}\text{cm}^{-1}$); MS (ESI $^+$): m/z : calcd for $\text{C}_{40}\text{H}_{20}\text{N}_7\text{Ag}_1$: 705.0831; found: 705.516 $[\text{M}+\text{H}]^+$; elemental analysis calcd (%) for $\text{C}_{40}\text{H}_{20}\text{N}_7\text{Ag}_1$ (**1B**): C, 68.20; H, 2.97; N, 14.00; found: C 68.00, H 2.85, N 13.88.

5.4.8 Synthesis of 10-(4-Bromophenyl)-5,15-bis(4-cyanophenyl)corrolato-silver(III), **2B**

10-(4-bromophenyl)-5,15-bis(4-cyanophenyl) corrole (0.025 mg, 0.038 mmol) was dissolved in pyridine (6 mL) and silver acetate (63 mg, 0.38 mmol) was added to it. The reaction mixture was kept at stirring for 40 min at room temperature during which, the colour of the reaction mixture changed from green to dark reddish-brown. The solvent was then removed by rotary evaporation and the dark red-brown crude product was purified by column chromatography through silica gel (100-200 mesh) column using 80% DCM and 20% hexane as eluent. Subsequent recrystallization (CH₂Cl₂/hexane) gave the pure crystalline 10-(4-bromophenyl)-5,15-bis(4-cyanophenyl)corrolato-silver(III), **2B**. Yield: 70%(20mg). ¹H NMR (400 MHz, CDCl₃) δ 9.19 (d, *J* = 4.4 Hz, 2H), 8.90 (d, *J* = 4.8 Hz, 2H), 8.76 (d, *J* = 4.8 Hz, 2H), 8.69 (d, *J* = 4.5 Hz, 2H), 8.39 (d, *J* = 7.9 Hz, 4H), 8.14 (d, *J* = 8.0 Hz, 4H), 8.05 (d, *J* = 8.1 Hz, 2H), 7.94 (d, *J* = 8.2 Hz, 2H); UV/Vis (dichloromethane): λ_{max} (ε) = 427 (106000); 497 (3600); 525 (6000); 541 (7400); 562 (15300); 584 nm (27500 M⁻¹cm⁻¹); MS (ESI⁺): *m/z*: calcd for C₃₉H₂₀Ag₁Br₁N₆: 757.998; found: 759.990 [M+H]⁺; elemental analysis calcd (%) for C₃₉H₂₀Ag₁Br₁N₆ (**2B**): C, 61.81; H, 2.84; N, 11.27; found: C 61.60, H 2.65, N 11.05.

5.4.9 Synthesis of 10-(2,4,5-Trimethoxyphenyl)-5,15-bis(4-cyanophenyl)corrolato-silver(III), **3B**

10-(2,4,5-Trimethoxyphenyl)-5,15-bis(4-cyanophenyl) corrole (25 mg, 0.037 mmol) was dissolved in pyridine (6 mL) and silver acetate (62 mg, 0.37 mmol) was added to it. The reaction mixture was kept at stirring for 40 min at room temperature during which, the colour of the reaction mixture changed from green to dark reddish-brown.

The solvent was then removed by rotary evaporation and the dark red-brown crude product was purified by column chromatography through silica gel (100-200 mesh) column using 100% DCM as eluent. Subsequent recrystallization (CH₂Cl₂/hexane) gave the pure crystalline 10-(2,4,5-Trimethoxyphenyl)-5,15-bis(4-cyanophenyl)corrolato-silver(III), **3B**. Yield: 75% (21mg). ¹H NMR (400 MHz, CDCl₃) δ 9.18 (d, *J* = 4.4 Hz, 2H), 8.90 (d, *J* = 4.8 Hz, 2H), 8.77 (d, *J* = 4.8 Hz, 2H), 8.67 (d, *J* = 4.4 Hz, 2H), 8.39 (t, *J* = 7.7 Hz, 4H), 8.11 (d, *J* = 8.5 Hz, 4H), 7.54 (s, 1H), 7.01 (s, 1H), 4.20 (s, 3H), 3.92 (s, 3H), 3.60 (s, 3H); ¹³C NMR (101 MHz, CDCl₃) δ 153.86, 150.36, 154.33, 142.60, 138.07, 135.68, 135.65, 135.24, 133.26, 131.60, 129.41, 129.40, 128.95, 128.93, 126.26, 120.91, 119.51, 119.31, 119.29, 118.77, 115.55, 115.53, 111.68, 109.64, 98.10, 57.19, 56.86, 56.55; UV/Vis (dichloromethane): λ_{max} (ε) = 428 (120200), 497 (3800), 526 (7000), 542 (9100), 565 (21400), 584 nm (33800 M⁻¹cm⁻¹); MS (ESI⁺): *m/z*: calcd for C₄₂H₂₇Ag₁N₆O₃: 771.570; found: 772.1078 [M+H]⁺; elemental analysis calcd (%) for C₄₂H₂₇Ag₁N₆O₃ (**3B**): C, 65.53, H 3.76, N 10.94; found: C 65.38, H 3.53; N 10.89.

5.4.10 Synthesis of 10-(4,7-Dimethoxynaphthalen-1-yl)-5,15-bis(4-cyanophenyl)corrolato-silver(III), **4B**

10-(4,7-dimethoxynaphthalen-1-yl)-5,15-bis(4-cyanophenyl) corrole (25 mg, 0.036 mmol) was dissolved in pyridine (6 mL) and silver acetate (60 mg, 0.36 mmol) was added to it. The reaction mixture was kept at stirring for 40 min at room temperature during which, the color of the reaction mixture changed from green to dark reddish-brown. The solvent was then removed by rotary evaporation and the dark red-brown crude product was purified by column chromatography through silica gel (100-200 mesh) column using 100% DCM as eluent. Subsequent recrystallization (CH₂Cl₂/hexane) gave the pure crystalline 10-(4,7-dimethoxynaphthalen-1-yl)-5,15-

bis(4-cyanophenyl)corrolato-silver(III), **4B**. Yield: 72% (20mg). ^1H NMR (400 MHz, CDCl_3) δ 9.15 (d, $J = 4.4$ Hz, 2H), 8.81 (dd, $J = 4.8, 0.8$ Hz, 2H), 8.67 (d, $J = 4.5$ Hz, 2H), 8.58 (d, $J = 4.8$ Hz, 2H), 8.48 (d, $J = 9.3$ Hz, 1H), 8.39 (d, $J = 8.5$ Hz, 4H), 8.15 – 8.07 (m, 4H), 8.01 (d, $J = 7.8$ Hz, 1H), 7.20 – 7.07 (m, 2H), 6.43 (d, $J = 2.5$ Hz, 1H), 4.27 (s, 3H), 2.97 (s, 3H); ^{13}C NMR (101 MHz, CDCl_3) δ 158.52, 156.26, 145.31, 138.67, 138.57, 135.76, 135.32, 133.69, 133.39, 131.71, 129.59, 129.09, 128.96, 126.66, 124.11, 120.71, 119.65, 119.34, 118.89, 117.09, 115.69, 111.78, 107.09, 101.48, 56.01, 54.91. UV/Vis (dichloromethane): λ_{max} (ϵ) = 428 (133100), 501 (4800), 525 (7800), 538 (9900), 566 (25200), 584 nm (37300 $\text{M}^{-1}\text{cm}^{-1}$). MS (ESI $^+$): m/z : calcd for $\text{C}_{45}\text{H}_{27}\text{Ag}_1\text{N}_6\text{O}_2$: 791.603; found: 792.123 $[\text{M}+\text{H}]^+$; elemental analysis calcd (%) for $\text{C}_{45}\text{H}_{27}\text{Ag}_1\text{N}_6\text{O}_2$ (**4B**): C 68.42; H 3.61; N 10.87; found: C 68.28, H 3.44; N 10.62.

CHAPTER 6

Experimental and Theoretical Investigations of the Existence of Cu^{II}, Cu^{III} and Cu^{IV} in Copper Corrolato Complexes

6.1	Introduction	181
6.2	Results and Discussion	183
6.2.1	Synthesis	183
6.2.2	Spectral Characterization	184
6.2.2.1	Mass Spectroscopy	184
6.2.2.2	NMR Spectroscopy	185
6.2.2.3	X-Ray Crystallography	187
6.2.2.4	XANES Measurements	190
6.2.2.5	Electrochemistry	191
6.2.3	EPR Spectroelectrochemistry and Spin Density Calculations	193
6.2.4	UV-Vis-NIR Spectroelectrochemistry and TD-DFT Calculations	198
6.3	Conclusions	204
6.4	Experimental Section	204
6.4.1	Materials	204
6.4.2	Physical Measurements	205
6.4.3	Crystal Structure Determination	206
6.4.4	Computational Details	206
6.4.5	X-Ray Absorption Measurements	207
6.4.6	Synthesis of 5,10,15-tris(4-cyanophenyl)corrolato-copper(III), 1	207
6.4.7	Synthesis of 10-(2,4,5-Trimethoxyphenyl)-5,15-bis(4-cyanophenyl)corrolato-copper(III), 2	208
6.4.8	Synthesis of 10-(4,7-dimethoxynaphthalen-1-yl)-5,15-bis(4-cyanophenyl)corrolato-copper(III), 3	209

6.1 Introduction

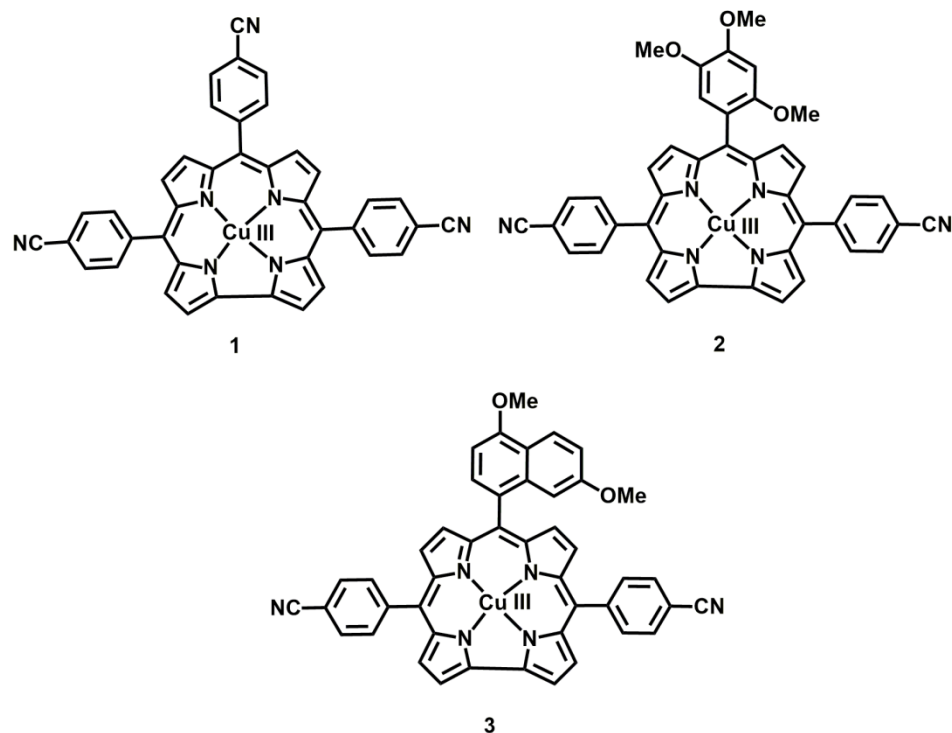
The concept of formal oxidation state, even though sometimes criticized, forms an excellent basis for electron bookkeeping and often for the explanation of trends in chemical reactivity^{141, 343}. With regard to the latter, the pursuit of discovering the highest possible oxidation states for a particular element is a topic of high interest¹⁴². One reason for this quest is the involvement of metal centers in high oxidation states in various catalytic processes^{141, 142}, with the water oxidation reaction being a prominent current example³⁴⁴. The most frequently encountered oxidation states of copper are 0 (usually in the metallic form), and +I and +II in metal complexes and salts³⁴⁵. Furthermore, Cu^{III} species have often been proposed as catalytic intermediates, and there are also few examples of well characterized Cu^{III} compounds¹⁴⁵. Higher oxidation states of copper, like Cu^{III}, are of great importance in copper-based high-temperature superconductors¹⁴³. High-valent copper species, like, organometallic Cu^{III} species have been explored in carbon–carbon coupling reactions¹⁴⁸. Theoretical calculations have suggested the involvement of Cu^{III} species in catalytic dioxygenation reactions with various monooxygenase enzymes¹⁴⁶.

Cs₂[CuF₆] is the oldest example of copper in the +IV oxidation state¹⁴⁷. However, there are several limitations related to dealing with this compound, including its synthesis under harsh reaction conditions (at very high temperature and pressure) inside an autoclave and its tendency to react vigorously with water and thereby decompose¹⁴⁷. If we ignore these rare examples of Cu^{IV} species in the solid, such as the fluoride cuprates, then, to the best of our knowledge, no examples of copper in the +IV oxidation state have been described. Recent reports on the use of copper complexes for the water oxidation reaction have invoked the role of a ‘formal’ copper(IV) oxidation state during the explanation of the proposed catalytic cycle¹⁴⁴.

However, no experimental evidence has yet been collected on the existence of such species. It is indeed true that the observation of oxidation state, +IV, is very rare in copper chemistry. The rich and extensive application of higher oxidation states of copper certainly points that a new addition of a high-valent copper species, i.e. copper(IV) might even be relevant in nature. The discovery of a new higher oxidation state of an abundant (in the earth's crust) non precious metal, like copper, can open up entirely new avenues for chemical reactivity.

Corroles in their deprotonated forms are known to stabilize transition metals in high oxidation states¹⁷⁰. In many cases, unusually high oxidation states that are unlikely to be stabilized in other ligand environments are found to be stable inside the corrolato cavity (see Chapter 1). The trianionic nature of the corrolato ligand is certainly helpful for this purpose. Some of the higher oxidation states of metals that have been stabilized in corrolato environments include Cu^{III}, Ag^{III}, Fe^{IV}, Co^{IV}, Co^V, Cr^V, Cr^{VI}, etc⁴⁹.

We have recently presented unambiguous experimental and theoretical evidence for the existence of silver(II) and silver(III) within the same corrolato framework²⁷². In the following chapter, the syntheses of three new copper complexes 5,10,15-tris(4-cyanophenyl)corrolato-copper(III), **1**, 10-(2,4,5-trimethoxyphenyl)-5,15-bis(4-cyanophenyl)corrolato-copper(III), **2**, and 10-(4,7-dimethoxynaphthalen-1-yl)-5,15-bis(4-cyanophenyl)corrolato-copper(III), **3** with corrolato ligands that are symmetrically as well as non-symmetrically substituted have been presented (Scheme 6.1).



Scheme 6.1 Structures of three novel corrolato-copper(III) complexes **1**, **2** and **3**

An approach combining synthetic, electrochemical, UV-Vis-NIR/EPR spectroelectrochemical, crystallographic, and DFT studies has been adapted to establish the origin of Cu^{II} , Cu^{III} and Cu^{IV} within the three-step redox series of these complexes.

6.2 Results and Discussion

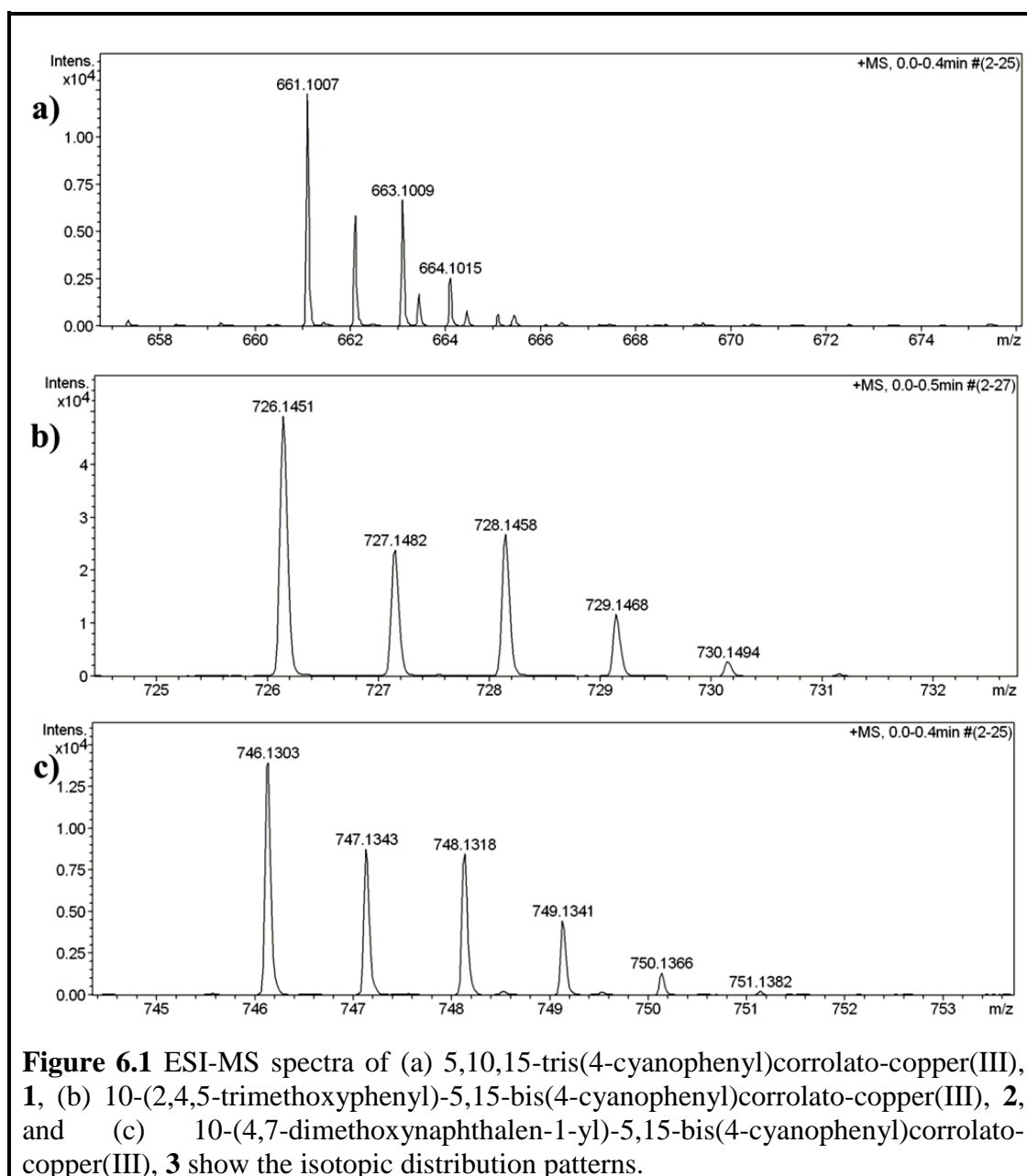
6.2.1 Synthesis

The corrolato-copper(III) derivatives were synthesized by slight modifications of a reported procedure³⁰⁶. The respective corroles were dissolved in pyridine and stirred with excess copper(II) acetate hydrate to yield the corresponding corrolato-copper(III) derivatives **1**, **2** and **3**. The purity and identity of the corrolato-copper(III) derivatives are demonstrated by their satisfactory elemental analyses and NMR and electrospray mass spectra.

6.2.2 Spectral Characterization

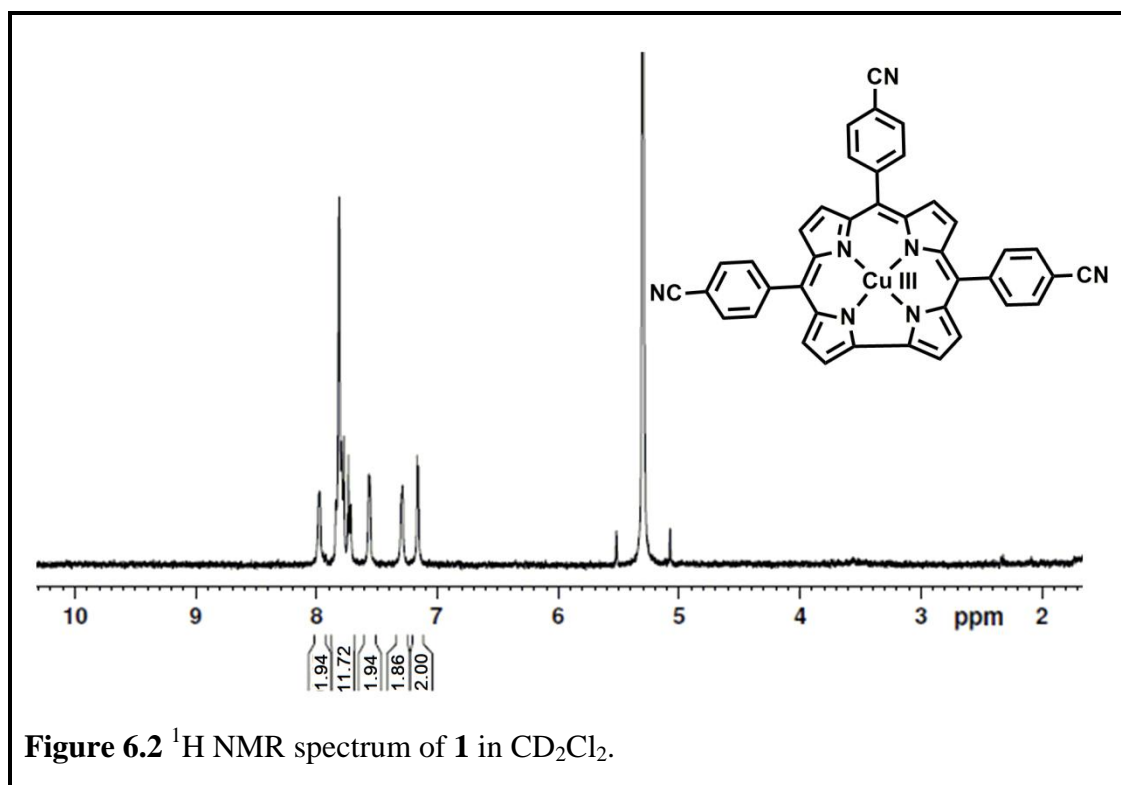
6.2.2.1 Mass Spectroscopy

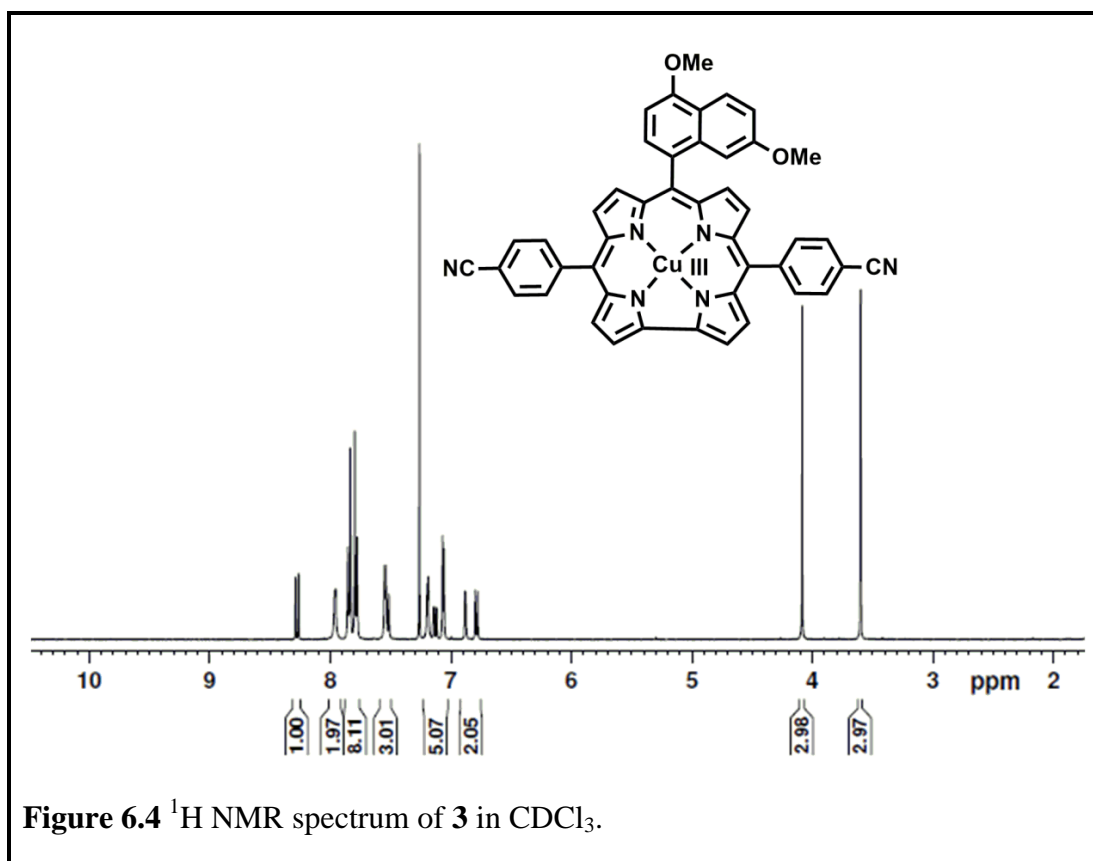
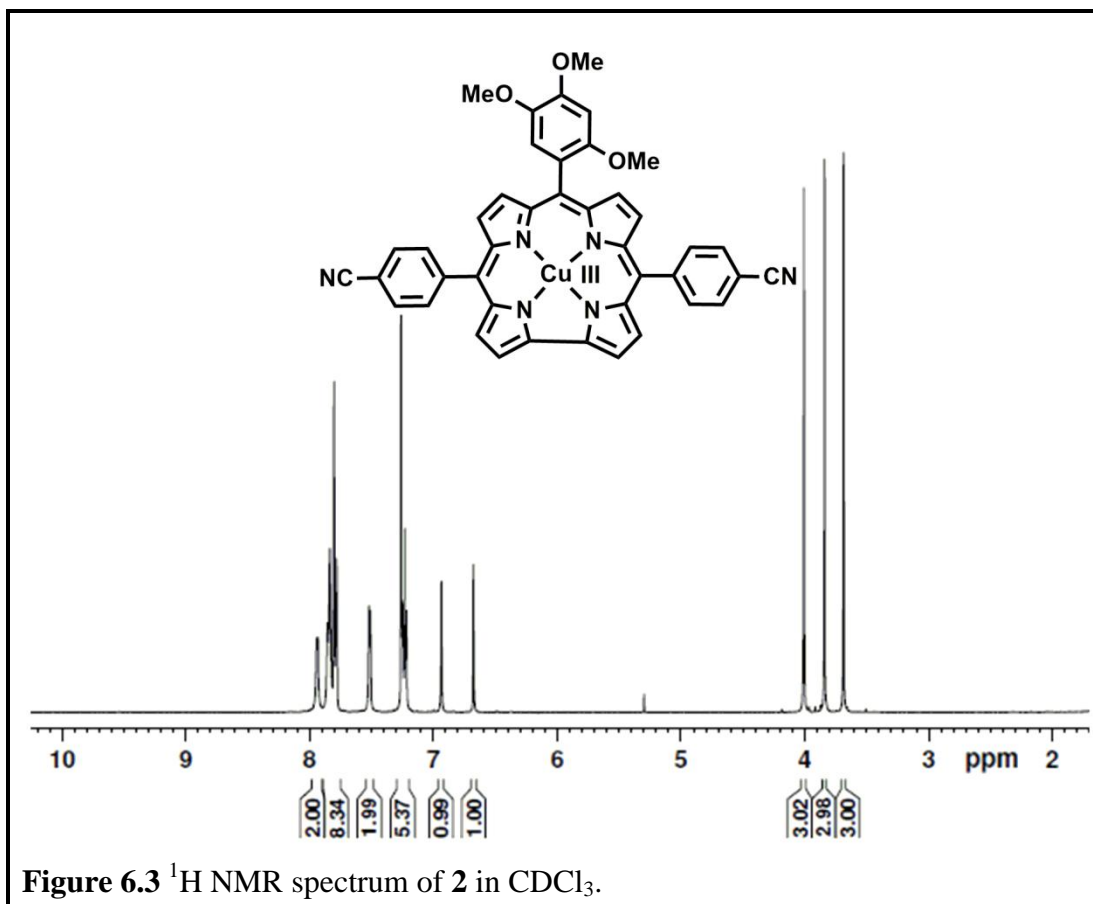
The electrospray mass spectra of the corrolato-copper(III) complexes **1**, **2** and **3** in acetonitrile reveal peaks centered at $m/z = 661.1007$ corresponding to $[1]^+$ (calculated molecular mass: 661.1076), $m/z = 726.1451$ corresponding to $[2]^+$ (calculated molecular mass: 726.1440) and $m/z = 746.1303$ corresponding to $[3]^+$ (calculated molecular mass: 746.1491) respectively (Figure 6.1).



6.2.2.2 NMR Spectroscopy

All the complexes, **1-3** exhibit diamagnetic ^1H NMR spectra. In case of **1**, the ^1H NMR spectrum in CD_2Cl_2 supports the formation of the complex having peaks corresponding to twenty partially overlapping aromatic protons in the region of 7.97-7.16 ppm (Figure 6.2). The ^1H NMR spectrum of **2** in CDCl_3 corresponds to eighteen partially overlapping aromatic protons in the range of 7.94 to 6.67 ppm (Figure 6.3). Three signals corresponding to the nine methoxy protons are also clearly visible in the region 4.01-3.67 ppm in the upfield region. Partially overlapping peaks corresponding to eight β -pyrrolic hydrogen atoms and thirteen aryl ring protons are observed in the region of 8.29-6.78 ppm in case of CDCl_3 solution of **3** (Figure 6.4). Two types of methoxy protons are also confirmed by the peaks at 4.08 ppm and 3.60 ppm.





6.2.2.3 X-Ray Crystallography

Structural confirmation of the corrolato-copper(III) complex, **3** has been supported by single crystal X-ray crystallographic studies (Figure 6.5). Important crystallographic parameters for **3** are presented in Table 6.1. All the bond distances and angles are comparable with previously reported corrolato-copper(III) molecules⁵⁹. The central copper atom fits well in the cavity of the corrolato ring in a slightly distorted square planar geometry with a minimal deviation of 0.0301 Å from the N4 plane. The distortion is due to slight deviations in the N–Cu–N bite angles in the range of 82.2–96.6° from the ideal ones. As a consequence the pyrrole ring nitrogen atoms are tilted

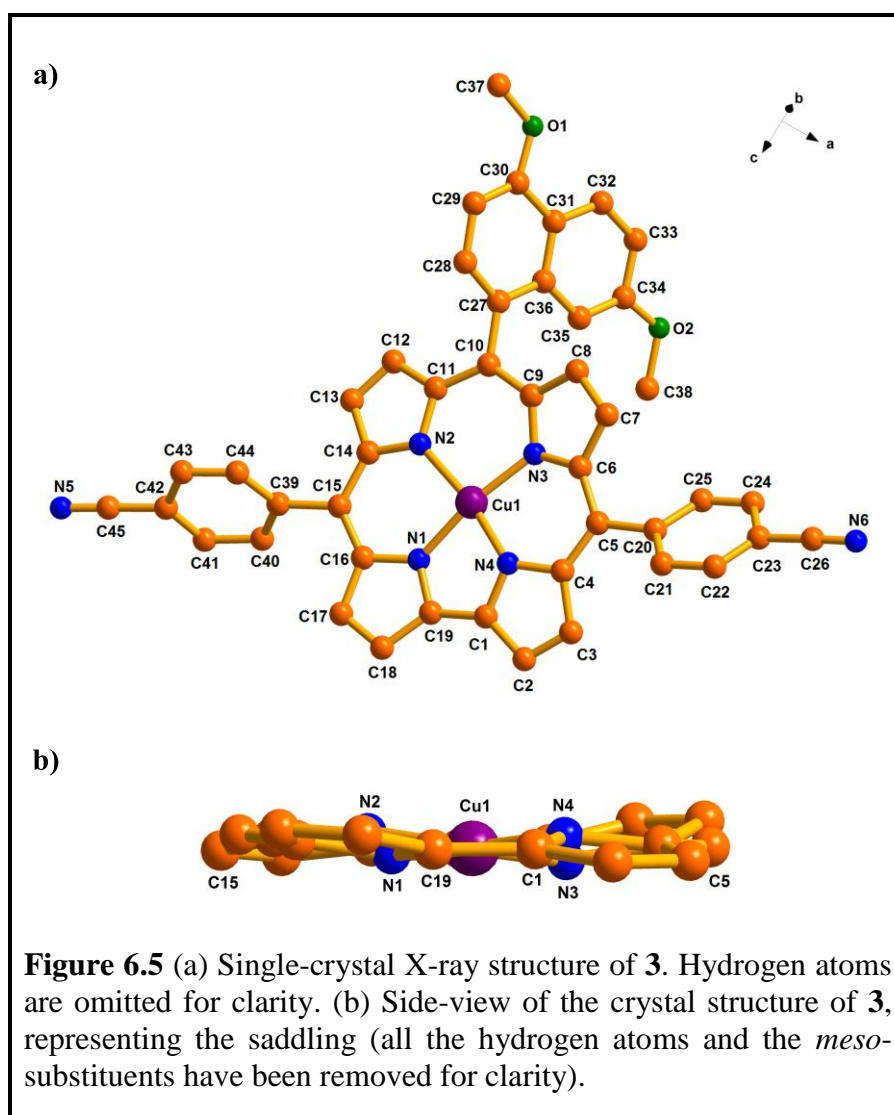


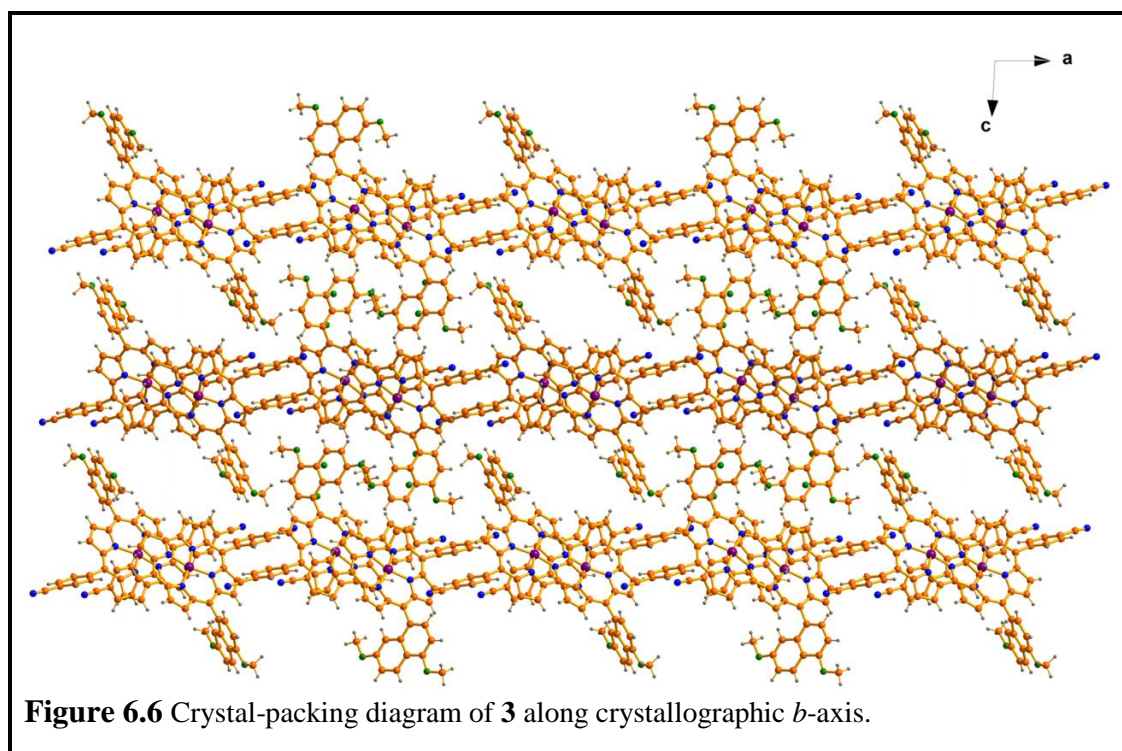
Table 6.1 Crystallographic Data for **3**

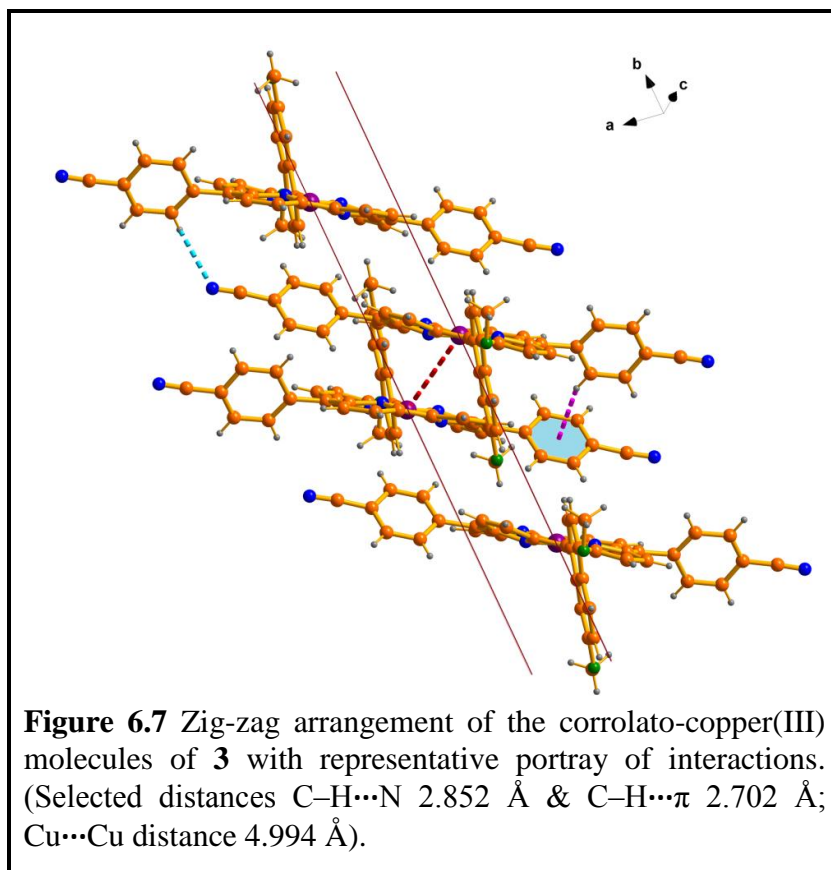
Compound Name	3
Molecular formula	C ₄₅ H ₂₇ CuN ₆ O ₃
Formula weight	763.30
Radiation	MoK α
Crystal symmetry	Monoclinic
Space group	<i>C</i> ₂ / <i>c</i>
<i>a</i> (Å)	61.151(7)
<i>b</i> (Å)	9.904(11)
<i>c</i> (Å)	26.478(3)
α (deg)	90.00
β (deg)	93.146(12)
γ (deg)	90.00
<i>V</i> (Å ³)	16012(3)
<i>Z</i>	16
μ (mm ⁻¹)	0.592
<i>T</i> (K)	100
<i>D</i> _{calcd} (g cm ⁻³)	1.267
<i>2</i> θ range (deg)	1.34 to 51.04
<i>e</i> data (<i>R</i> _{int})	14847 (0.1085)
<i>R</i> 1 (<i>I</i> > 2 σ (<i>I</i>))	0.0911
<i>wR</i> 2	0.2676
GOF	1.003
Largest diff. peak and hole (e Å ⁻³)	1.304 and -0.713
CCDC No.	994306

from (-0.133) Å to (+0.252) Å alternately. The net effect is the saddling of the metallocorrolato ring in which the pyrrole rings alternately move down and up to accommodate the central metal atom, copper and hence stabilize the structure (see discussion below and Table A6.7a, see Appendix). The Cu–N distances in **3** lie between 1.873 Å and 1.907 Å and are at par with the earlier reported characteristic

Cu^{III}-N bonds⁵⁹. The *meso*-substituted phenyl rings at -5 and -15 positions and the naphthyl group at -10 position have been found to make dihedral angles of 42.5°, 58.5° and 62.5° with the mean corrolato plane.

In the packing diagram the copper(III) corrole molecules are arranged in pairs along two parallel lines in a zig-zag pattern (Figure 6.6 and Figure 6.7). In a pair, each of the two molecules of **3** is placed in opposite parallelly-placed lines. The closest distance between any two neighbouring Cu centres in a pair is 4.994 Å and that between two pairs is 8.192 Å. The naphthyl groups of **3** in any two neighbours are present diametrically opposite to each other. The entire crystal-framework has been stabilized by several interactions involving the π - π stacking, C-H \cdots π as well as the C-H \cdots N interactions as shown in the Figure 6.7. The separation between the mean planes of any two closely placed corrolato-Cu^{III} molecules is 3.533 Å. Off-centre parallel π - π stacking is observed between any two molecules of **3** in a pair. The shortest distance between two carbon atoms, C3-C'16 of the interacting corrole planes

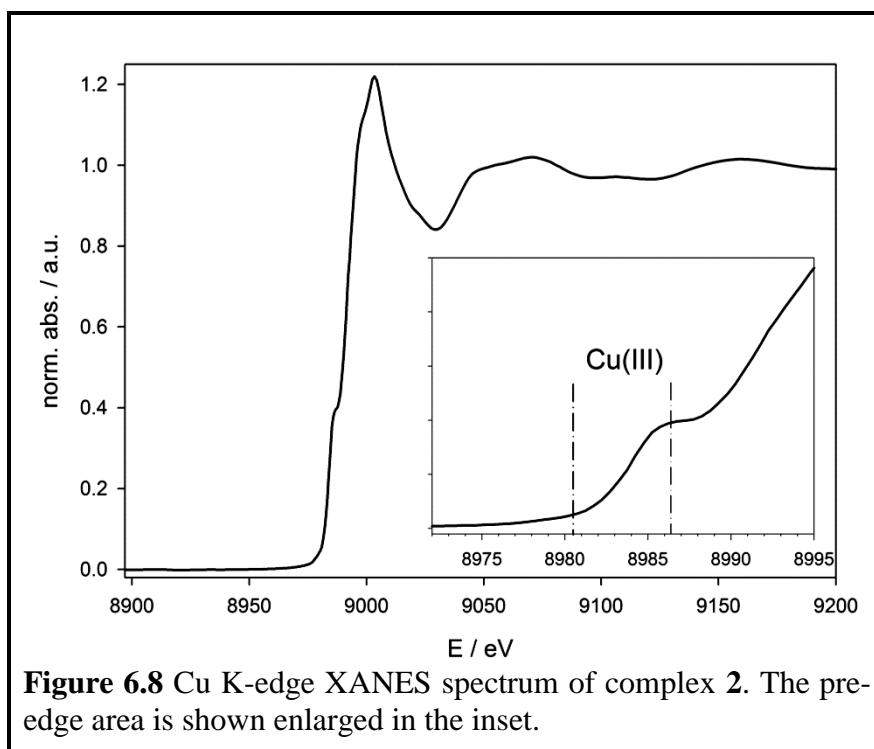




of adjacent molecules was observed to be 3.650 Å in an offset pair of π - π stacked corrole rings.

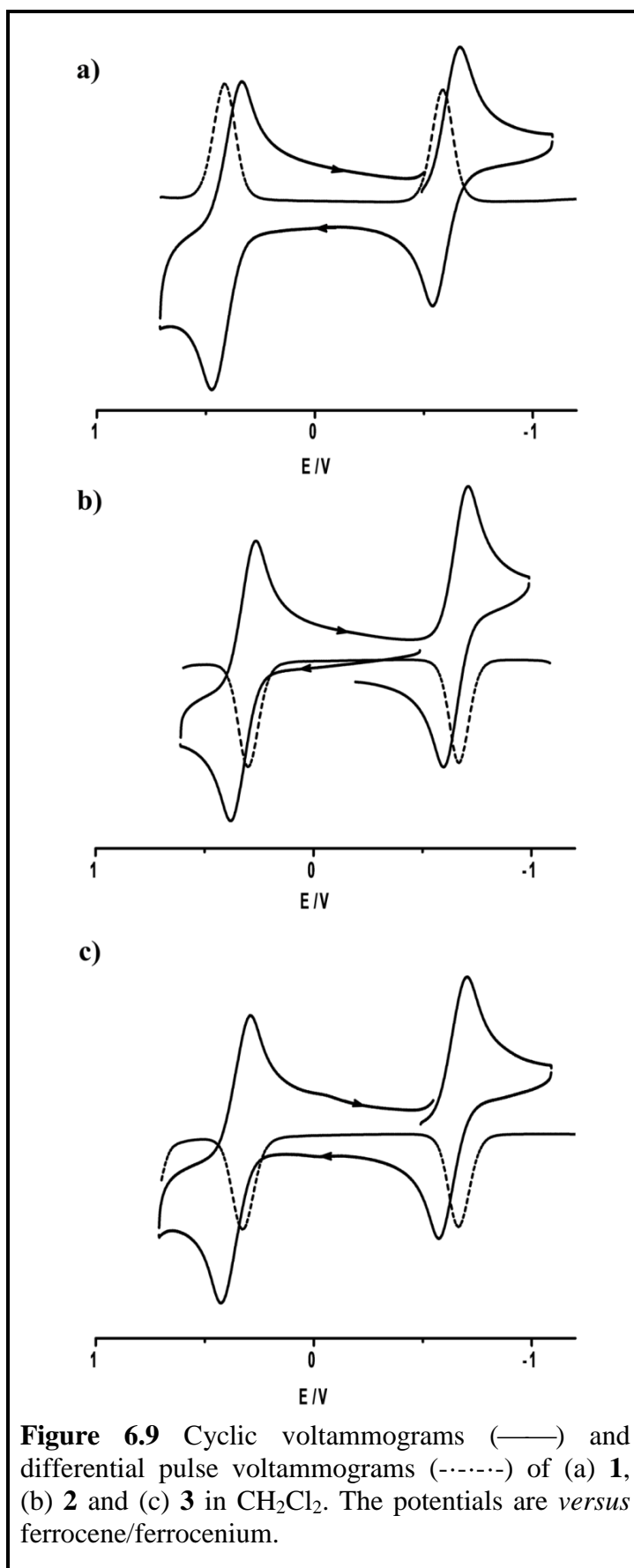
6.2.2.4 XANES Measurements

XANES measurements³⁴⁶ at the copper K-edge of complex **2** confirm the oxidation state of Cu^{III}. As can be seen in Figure 6.8, two characteristic features lead to this conclusion. A very weak pre-edge peak is detected at 8980.5 eV, while a more intense feature is observed in the edge at 8986.5 eV. While the position of the first 1s \rightarrow 3d transition is an unambiguous diagnostic of Cu^{III}, the more intense 1s \rightarrow 4p + LMCT shakedown transition is more ligand dependent and can only support the conclusion drawn from the weak quadrupole transition³⁴⁷.



6.2.2.5 Electrochemistry

The cyclic voltammograms and the differential pulse voltammograms of the complexes **1**, **2**, and **3** were measured in $\text{CH}_2\text{Cl}_2/0.1 \text{ M TBAP}$ (see Figure 6.9 and Table 6.2). Each of the three copper complexes **1**, **2**, and **3** displayed one reversible oxidation and one reversible reduction step. The oxidation couple was observed at $E_{298}^0, \text{ V}$ ($\Delta E_p, \text{ mV}$): 0.41(80), 0.35(80), and 0.36(80) for **1**, **2**, and **3** respectively *versus* ferrocene/ferrocenium. These complexes also exhibited one reversible reductive couple $E_{298}^0, \text{ V}$ ($\Delta E_p, \text{ mV}$): -0.61(80) (**1**), -0.63(80) (**2**) and -0.64(90) (**3**) *versus* ferrocene/ferrocenium. Along the series, **1** \rightarrow **2** \rightarrow **3**, the electronic effects of various substituents on the aryl rings on their redox potential visibly appeared to be insignificant. The oxidation potentials of the copper complexes are similar to those of their silver analogues²⁷², whereas the reduction potentials are shifted in the positive direction.



To gain a more detailed knowledge about the electronic structures of these complexes and to ascertain the electronic structures in their various redox states, UV-Vis-NIR and EPR spectroelectrochemical measurements, combined with DFT and TD-DFT calculations were performed.

Table 6.2 UV-Vis and Electrochemical Data

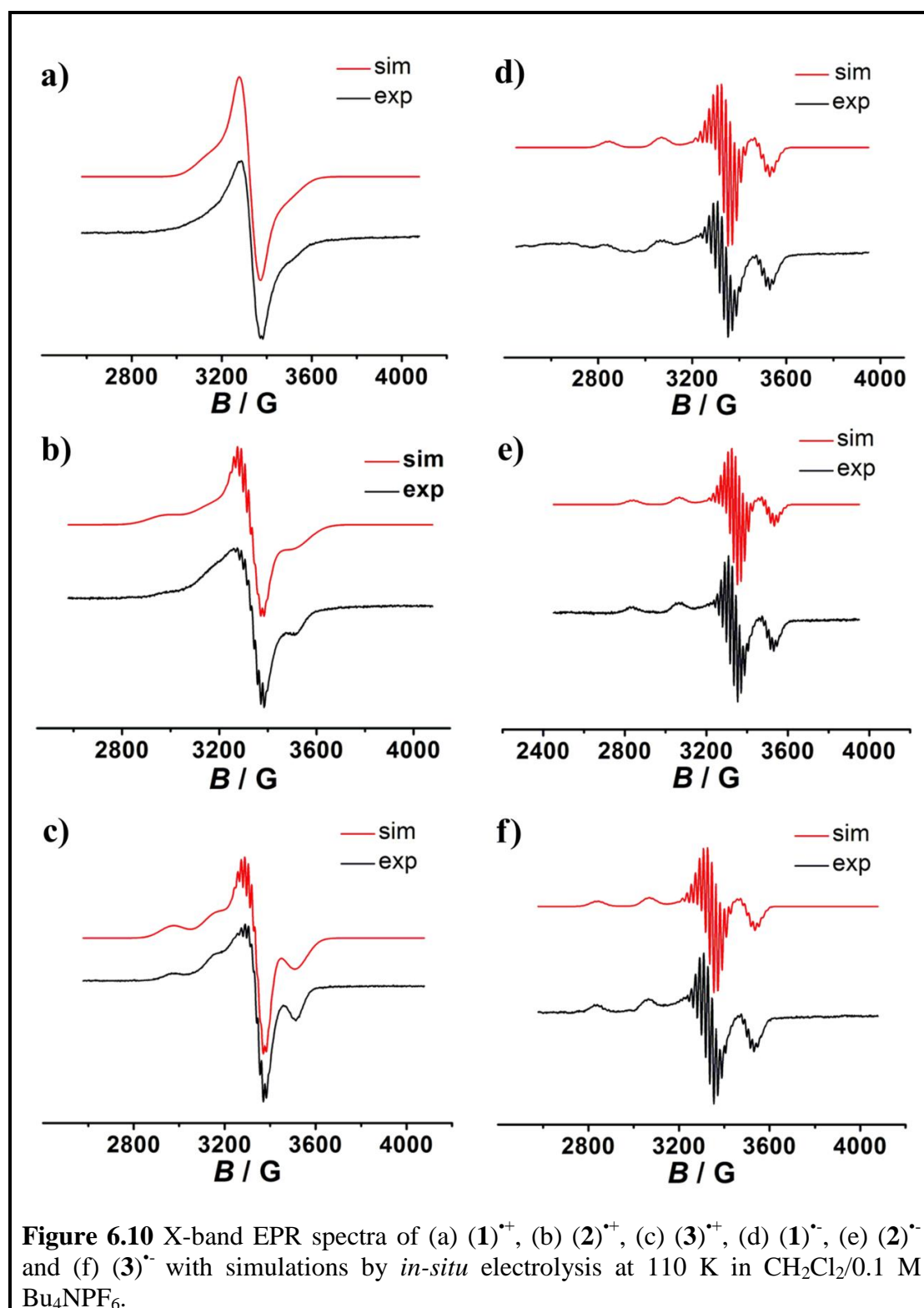
Compound	UV-Vis Data ^a $\lambda_{\max} / \text{nm} (\epsilon / \text{M}^{-1}\text{cm}^{-1})$	Electrochemical Data ^{a,b}	
		Oxidation $E^0, \text{V} (\Delta E_p, \text{mV})$	Reduction $E^0, \text{V} (\Delta E_p, \text{mV})$
1	414 (77226), 539 (6036), 617(4244)	0.41(80)	-0.61(80)
2	411(89266), 554(8960), 633(5960)	0.35 (80)	-0.63 (80)
3	411 (77626), 554 (8162), 623(5551)	0.36 (80)	-0.64 (90)

^a In dichloromethane/0.1 M TBAP. ^b The potentials are versus. ferrocene/ ferrocenium.

6.2.3 EPR Spectroelectrochemistry and Spin Density Calculations

As expected, no characteristic EPR signals were obtained from the diamagnetic native states of the three complexes (**1-3**). Since EPR spectrum of the one electron oxidized species of all the three complexes have similar pattern and the same holds true for the one electron reduced species as well, one in each case has been discussed in detail (Figure 6.10). The EPR data of all the complexes are presented in Table 6.3. The *in-situ* generated one-electron reduced species (**3**)^{•-} in CH₂Cl₂/0.1 M Bu₄NPF₆ displays a typical Cu^{II}-type EPR spectrum (Figure 6.10f). The experimental data were simulated with the Easyspin³⁴⁸ software by considering an axial *g*-tensor with $g_{\parallel} = 2.127$ and $g_{\perp} = 2.034$. Furthermore, hyperfine and super hyperfine interactions were observed with

the copper ($^{63,65}\text{Cu}$, $I = 3/2$) and nitrogen (^{14}N , $I = 1$) nuclei respectively. Simulation of the spectrum delivered an axial hyperfine coupling tensor for both Cu and N.



The values obtained for Cu are $A_{//} = 665$ and $A_{\perp} = 80$ MHz. The absolute values as well as their trends fit well with known Cu^{II} EPR parameters. As expected, the hyperfine coupling constants to the ^{14}N atoms are much smaller compared to those to Cu^{II} (Table 6.3).

Structure-based calculations of the EPR spectra at the B3LYP/aug-cc-pVTZ-J level of theory reproduced the experimental results with reasonable accuracy with the calculated g -tensors for $(\mathbf{3})^{\bullet-}$ being $g_{//} = 2.104$ and $g_{\perp} = 2.034$. DFT delivers a slight rhombicity to the A -tensor (albeit with two A values very close to each other, see Table 6.3). The trends in the A values are reproduced well by the calculations with the absolute values being a bit exaggerated, as is typical for this level of theory. The spin densities calculated from the Löwdin population analysis indicated that about 64 % spin density resides on copper center for the one-electron reduced forms of the complexes (Figure 6.11 and Table 6.4). Such a spin density distribution is very similar to what has been reported recently by us for the Ag analogues of these copper complexes. The experimental EPR data, together with the DFT calculations thus point to a major contribution of the $[(\text{corrolato}^3)\text{Cu}^{\text{II}}]^{\bullet-}$ form to the one-electron reduced forms of these complexes, stabilizing the usual formal Cu^{II} oxidation state.

The resolution of the spectrum for $(\mathbf{1})^{\bullet+}$ is rather poor and hence the data presented for that complex should be seen as approximate limits. However, for $(\mathbf{2})^{\bullet+}$ and $(\mathbf{3})^{\bullet+}$ the resolution of the spectra are good enough to allow the extraction of g and A tensors with reasonable accuracy. The *in-situ* generated one-electron oxidized species $(\mathbf{3})^{\bullet+}$ in $\text{CH}_2\text{Cl}_2/0.1 \text{ M Bu}_4\text{NPF}_6$ displays a pattern that also points to a predominantly copper-centered spin⁵⁹. Simulation of the spectrum of $(\mathbf{3})^{\bullet+}$ delivered an axial g -tensor with values of $g_{//} = 2.089$ and $g_{\perp} = 2.035$. Furthermore, the simulations delivered $A_{//} = 520$ and $A_{\perp} = 50$ MHz. Furthermore, superhyperfine

Table 6.3 EPR Data^[a] of Paramagnetic States^[b]

Complex	EPR Data ^a (g)
1^{•+} ^[b]	$g_1 = 2.0344, g_2 = 2.0344, g_3 = 2.039$; A(MHz) Cu $a_1 = 40 a_2 = 40 a_3 = 350$; N $a_1 = 38 a_2 = 49 a_3 = 30$; N $a_1 = 45 a_2 = 38 a_3 = 54$; N $a_1 = 47 a_2 = 36 a_3 = 38$; N $a_1 = 42 a_2 = 34 a_3 = 28$; N $a_1 = 48 a_2 = 38 a_3 = 24$
1^{•+} ^[c]	$g_1 = 2.023, g_2 = 2.027, g_3 = 2.066$; A(MHz) Cu $a_1 = 18 a_2 = 9 a_3 = -449$; N $a_1 = 45 a_2 = 38 a_3 = 54$; N $a_1 = 47 a_2 = 36 a_3 = 38$; N $a_1 = 42 a_2 = 34 a_3 = 28$; N $a_1 = 48 a_2 = 38 a_3 = 24$
2^{•+} ^[b]	$g_1 = 2.035, g_2 = 2.035, g_3 = 2.089$; A(MHz) Cu $a_1 = 50 a_2 = 52 a_3 = 520$; N $a_1 = 38 a_2 = 49 a_3 = 30$; N $a_1 = 45 a_2 = 36 a_3 = 31$; N $a_1 = 47 a_2 = 36 a_3 = 35$; N $a_1 = 40 a_2 = 39 a_3 = 50$
3^{•+} ^[b]	$g_1 = 2.035, g_2 = 2.035, g_3 = 2.089$; A(MHz) Cu $a_1 = 50 a_2 = 52 a_3 = 520$; N $a_1 = 38 a_2 = 49 a_3 = 30$; N $a_1 = 45 a_2 = 36 a_3 = 31$; N $a_1 = 47 a_2 = 36 a_3 = 35$; N $a_1 = 40 a_2 = 39 a_3 = 50$
3^{•+} ^[c]	$g_1 = 2.023, g_2 = 2.026, g_3 = 2.066$; A(MHz) Cu $a_1 = 19 a_2 = 17 a_3 = -445$; N $a_1 = 38 a_2 = 49 a_3 = 30$; N $a_1 = 45 a_2 = 36 a_3 = 31$; N $a_1 = 47 a_2 = 36 a_3 = 35$; N $a_1 = 40 a_2 = 39 a_3 = 50$
1^{•-} ^[b]	$g_1 = 2.034, g_2 = 2.034, g_3 = 2.1275$; A(MHz) Cu $a_1 = 80; a_2 = 80 a_3 = 665$; N $a_1 = 64 a_2 = 49 a_3 = 50$; N $a_1 = 46 a_2 = 44 a_3 = 57$; $a_1 = 46 a_2 = 58 a_1 = 44$; N $a_1 = 64 a_2 = 49 a_3 = 50$
1^{•-} ^[c]	$g_1 = 2.034, g_2 = 2.034, g_3 = 2.104$; A(MHz) = Cu $a_1 = -9 a_2 = -7 a_3 = -643$; N $a_1 = 65 a_2 = 50 a_3 = 51$; N $a_1 = 47 a_2 = 46 a_3 = 59$; N $a_1 = 47 a_2 = 58 a_3 = 46$; N $a_1 = 49 a_2 = 65 a_3 = 50$
2^{•-} ^[b]	$g_1 = 2.0345, g_2 = 2.0345, g_3 = 2.128$; A(MHz) Cu $a_1 = 80; a_2 = 80 a_3 = 665$; N $a_1 = 64 a_2 = 49 a_3 = 50$; N $a_1 = 46 a_2 = 44 a_3 = 57$; $a_1 = 46 a_2 = 58 a_1 = 44$; N $a_1 = 64 a_2 = 49 a_3 = 50$
3^{•-} ^[b]	$g_1 = 2.034, g_2 = 2.034, g_3 = 2.1275$; A(MHz) Cu $a_1 = 80; a_2 = 80 a_3 = 665$; N $a_1 = 64 a_2 = 49 a_3 = 50$; N $a_1 = 46 a_2 = 44 a_3 = 57$; $a_1 = 46 a_2 = 58 a_1 = 44$; N $a_1 = 64 a_2 = 49 a_3 = 50$
3^{•-} ^[c]	$g_1 = 2.034, g_2 = 2.034, g_3 = 2.104$; A(MHz) Cu $a_1 = -6; a_2 = -8 a_3 = -638$; N $a_1 = 64 a_2 = 49 a_3 = 50$; N $a_1 = 46 a_2 = 44 a_3 = 57$; $a_1 = 46 a_2 = 58 a_1 = 44$; N $a_1 = 64 a_2 = 49 a_3 = 50$

[a] From EPR spectroelectrochemistry in CH₂Cl₂/0.1 M Bu₄NPF₆ at 110 K. [b] g values (from simulated data). [c] g values (from DFT (B3LYP/aug-cc-pVTZ-J(Cu,N)) calculations).

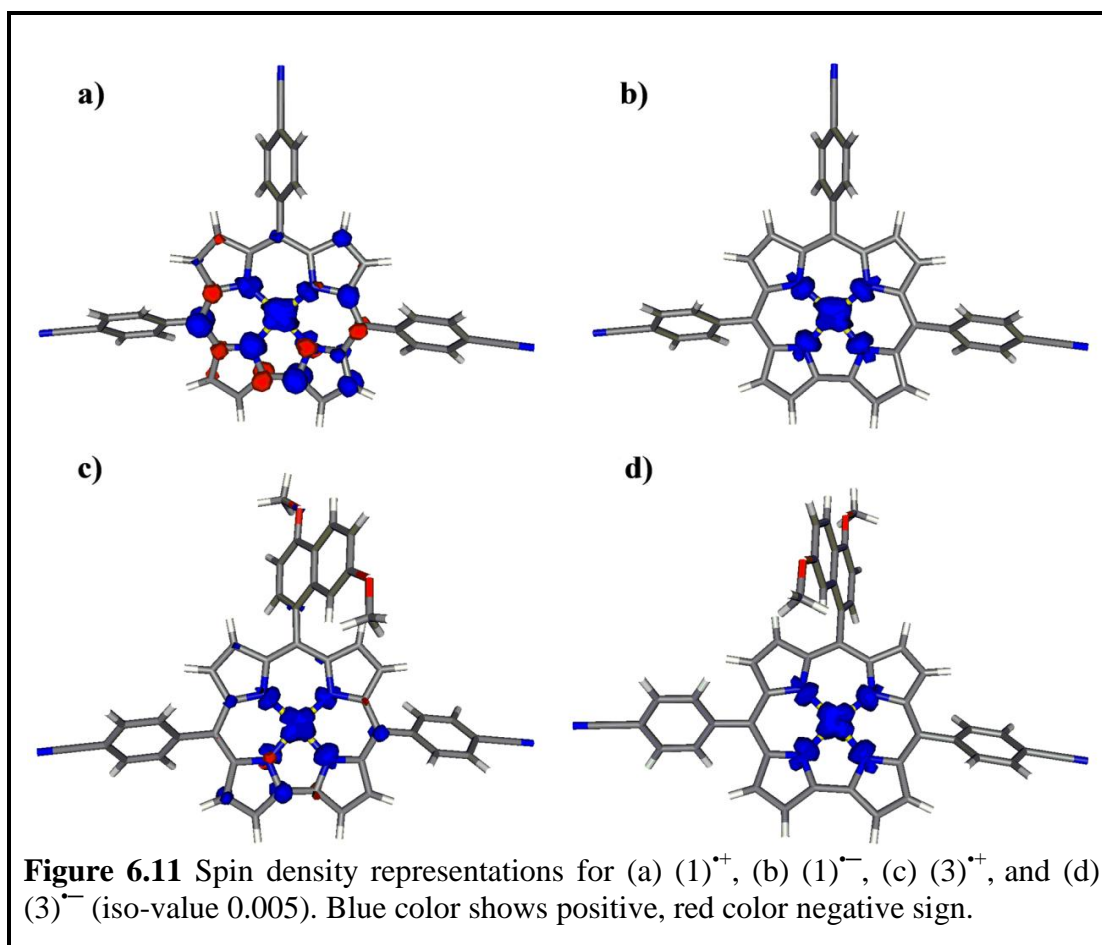


Table 6.4 DFT (B3LYP/TZVPP-ZORA) Calculated Löwdin Spin Densities on Cu

Complex	Cu
1^+	43%
1^-	64%
3^+	44%
3^-	64%

coupling to the ^{14}N atoms were also considered for the simulations (Table 6.3). The absolute values of the hyperfine coupling constants for copper are slightly larger for the reduced forms than for the oxidized ones, whereas the trend is opposite for the ^{14}N superhyperfine coupling. Nevertheless, the values obtained for $(3)^+$ clearly point to a predominantly metal centered spin. DFT calculations delivered a slightly rhombic g -tensor for $(3)^+$ with g -values of 2.066, 2.026 and 2.023. However, the absolute values

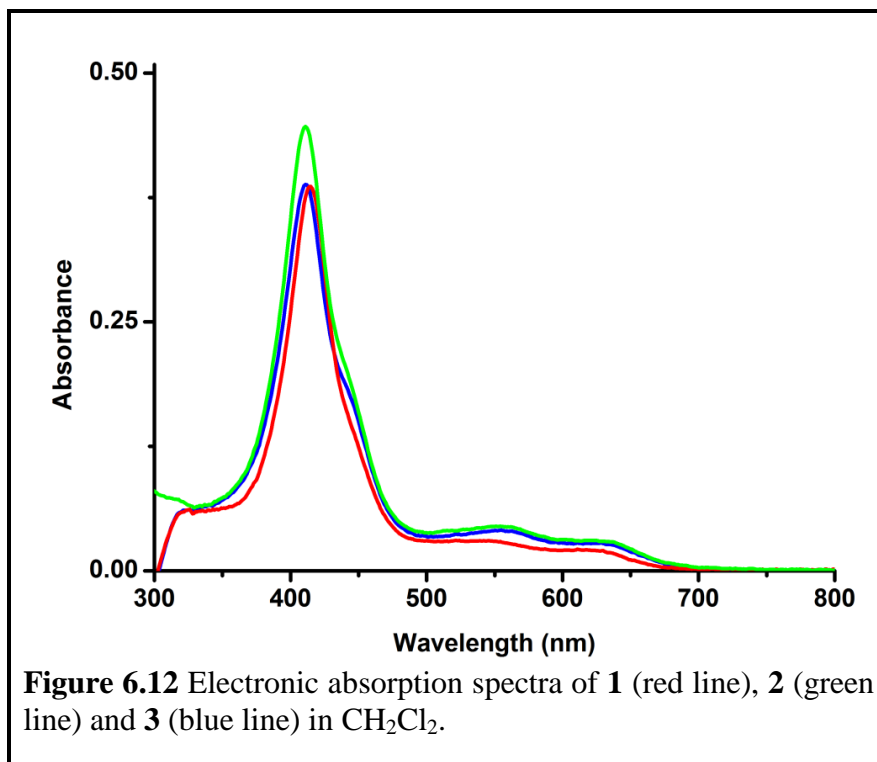
match reasonably well with the experimental values. The trends in the calculated A tensors for copper and nitrogen match reasonably well with the experiments, and the calculations also deliver smaller values for the hyperfine coupling constant to copper in comparison to the reduced species (Table 6.3). A look at the spin densities calculated using the Löwdin population analysis for $(\mathbf{3})^{+\bullet}$ delivered 44 % spin density on the corresponding copper atom (Figure 6.11 and Table 6.4). For the corresponding silver complexes less than 1% spin density was located at the metal center for the oxidized forms ²⁷² leading to their description as [(corrolato^{•2-})Ag^{III}]^{•+} (Chapter 5). For the present case, both the experimental EPR spectra as well as spin density data thus clearly establish that formulations with spin on the copper center are essentially to correctly describe the oxidized species (see below).

6.2.4 UV-Vis-NIR spectroelectrochemistry and TD-DFT calculations

As the spectra of $\mathbf{2}$ and $\mathbf{3}$ in all redox states are virtually identical, only the cases $\mathbf{1}$ and $\mathbf{3}$ will be discussed in detail below. The native states of the complexes display typical spectra expected for a neutral Cu-corrolato species (Table 6.2 and Figure 6.12) ³⁴⁹. The Soret bands were observed for all cases and the position of these bands are hardly influenced by the substituents on the corrolato rings. Details of the interpretation obtained through TD-DFT calculations are given in Tables A6.1-A6.6 and Figures A6.1-A6.6 (see Appendix).

Upon one-electron reduction of $\mathbf{1}$ to $(\mathbf{1})^{•-}$, all the bands in the visible region are shifted to lower energy (Table 6.5). Similarly on one-electron reduction of $\mathbf{3}$ to $(\mathbf{3})^{•-}$ the Soret band decreases in intensity and finally disappears giving rise to a new band of higher intensity at 446 nm at a longer wavelength. The other low-energy bands in the visible region also decrease in intensity along with the development of a new

intense band at 620 nm. Such a spectral change matches well with the metal-centered reduction processes reported earlier in related corrolato-copper(III) complexes (Figure 6.13)²⁷⁷. Contributions from the HOMO-2 α →LUMO α , HOMO α →LUMO α , and



HOMO β →LUMO β were calculated for this transition (Figure A6.6 and Table A6.6, see Appendix). The origin of the band at 620 nm is thus calculated by TD-DFT to be a mixture of ILCT and MLCT transitions. Similar bands are also observed for (1)^{•-}.

Upon one-electron reduction the generated formal Cu^{II} centers (see EPR section above) are relatively electron rich and thus the probability of metal to ligand charge transfer (MLCT) transitions becomes highly feasible here. The most prominent changes in the UV-Vis-NIR spectra of these complexes on one-electron oxidation is the appearance of long wavelength bands, particularly for (2)^{•+} and (3)^{•+} in the NIR region (Figure 6.13). These bands appear at 947 nm and 921 nm respectively for the two aforementioned species. On one electron-oxidation of copper(III) corroles, such bands in the NIR region have never been reported before. Origin of this new low energy band can be explained with the help of TD-DFT calculations and has

contributions from HOMO-2 α →LUMO α and HOMO-1 β →LUMO β orbitals. This low energy band is a manifestation of mixed intra ligand charge transfer (ILCT) and ligand to metal charge transfer (LMCT) transitions (Table A6.4 and Figure A6.4, see Appendix). For (1)⁺⁺ no such bands in the NIR region were experimentally detected, and TD-DFT calculations also do not predict any NIR bands for this case. Such an observation would fit with the proposed LMCT character of the band, with the substituents on the backbone of the corrolato ligands in (2)⁺⁺ and (3)⁺⁺ being

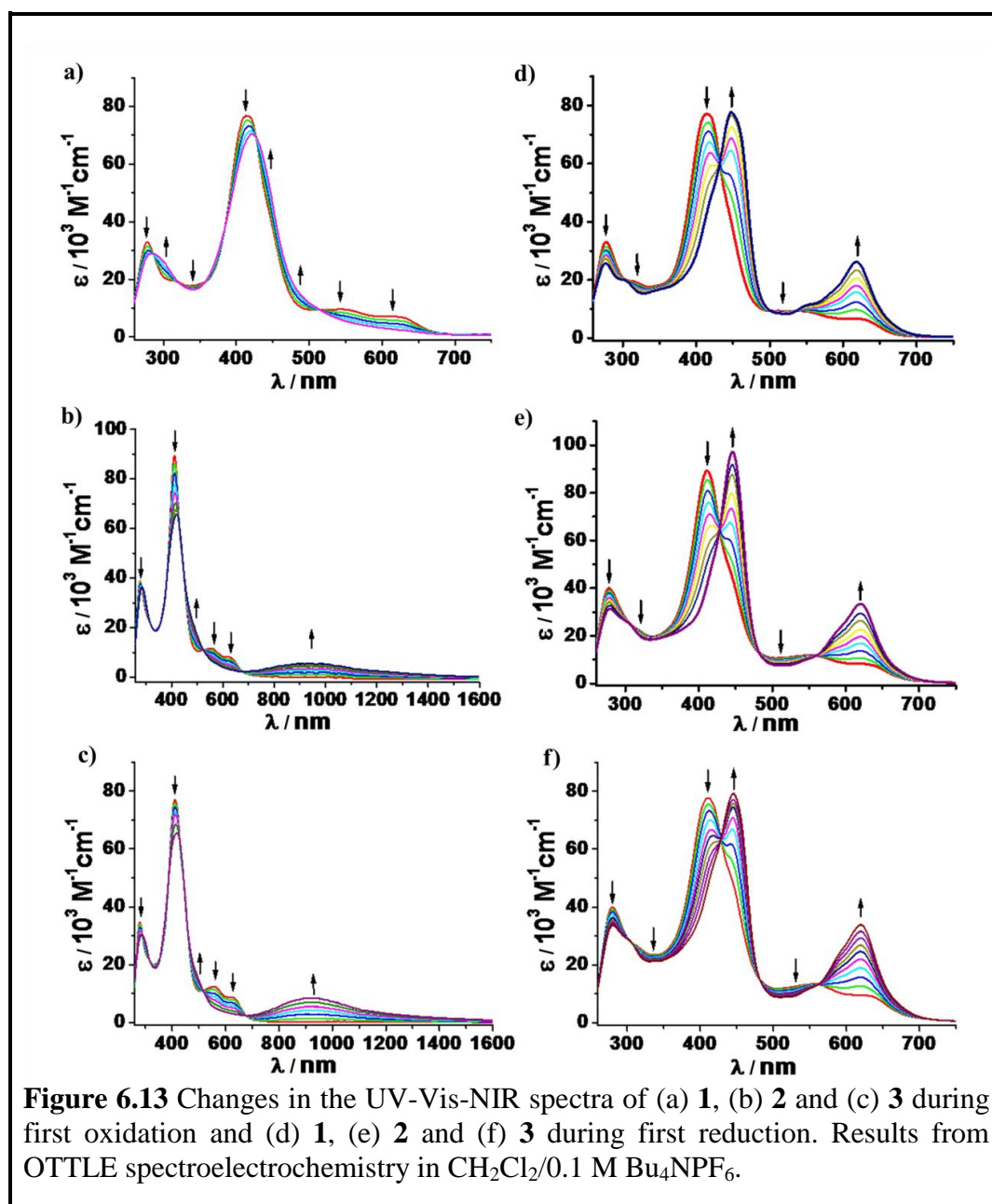


Table 6.5 UV-Vis-NIR Data of $\mathbf{1}^n$, $\mathbf{2}^n$ and $\mathbf{3}^n$ [$n = -1, +1, 0$] from Spectroelectrochemistry^[a]

Complex	λ_{\max} [nm] (ϵ [$10^3 \text{ M}^{-1} \text{ cm}^{-1}$])
$\mathbf{1}^0$	277 (32.9); 313 sh; 414 (76.9); 542 (9.8); 614 (7.1)
$\mathbf{1}^-$	278 (25.8); 301 (20.0); 349 sh; 419 sh; 448 (77.9); 549 (11.3); 587 sh; 618 (26.3)
$\mathbf{1}^+$	284 (29.0); 422 (70.6); 550 sh
$\mathbf{2}^0$	278 (39.0); 315 sh; 411 (89.4); 443 sh; 556 (11.9); 623 (8.1)
$\mathbf{2}^-$	279 (31.2); 303 sh; 413 sh; 446 (97.3); 546 sh; 587 sh; 620 (33.4)
$\mathbf{2}^+$	286 (36.4); 420 (65.8); 487 sh; 947 (5.6)
$\mathbf{3}^0$	279 (34.8); 317 sh; 411 (76.9); 444 sh; 557 (12.5); 621 (8.7)
$\mathbf{3}^-$	280 (33.6); 303 sh; 420 sh; 446 (79.3); 547 (11.4); 593 sh; 620 (33.9)
$\mathbf{3}^+$	286 (30.3); 419 (65.6); 495 sh; 921 (8.4)

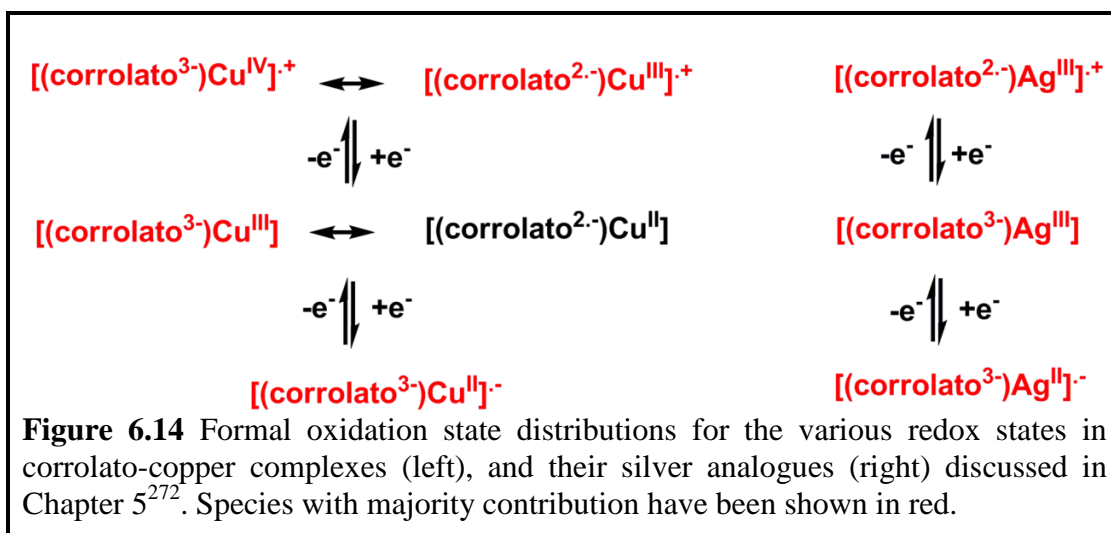
[a] Measurements in $\text{CH}_2\text{Cl}_2/0.1 \text{ M Bu}_4\text{NPF}_6$ (OTTLE spectroelectrochemistry).

responsible for a smaller energy gap between the relevant orbitals, an effect that is missing for $(\mathbf{1})^{*+}$. We note that the changes in the Soret bands on one-electron oxidation of these species are minimal (Figure 6.13).

As has been discussed above, saddling of the corrolato ring is a common feature in corrolato-copper(III) complexes and has been observed previously^{285, 349-351}. DFT geometry optimizations were performed to get insights into this phenomenon. Three different cases, namely, a singlet, a triplet and a broken symmetry case were calculated using the BP 86 functional. The calculated saddling values for the singlet and the broken symmetry cases match reasonably well with the experimental values (Table A6.7, see Appendix). Calculations for the triplet state delivered an almost non-saddled structure, confirming that the ground state of the corrolato-copper(III) complexes is indeed the singlet state (as has been experimental observed). To exclude functional dependent errors as source of the saddling we also used higher generation (OLYP) and hybrid (B3LYP) functionals to look into the

saddling effect for the singlet case, and all functionals, with or without empirical van der Waals corrections, delivered a saddled structure (Table A6.7, see Appendix). This saddling which has been invoked to account for electron flow from the corrolato unit to the $d_{x^2-y^2}$ orbital of the copper center has important consequences for the formal oxidation state distribution in these complexes (non-innocent character of the corrolato unit)^{285, 349-351}. The $d_{x^2-y^2}$ orbitals of copper are closer in energy to the corrolato based orbitals in comparison to the cases of their higher homologues silver and gold. This fact leads to a situation where extensive overlap between the copper $d_{x^2-y^2}$ and corrolato orbitals occur (higher covalency!), a fact that is missing for its higher homologues. As a result, usually no saddling of the corrolato structure is observed in complexes of the higher homologues of the coinage metal copper. The saddling introduces a certain Cu^{II} character into the otherwise formally corrolato-Cu^{III} complexes^{285, 349-351}. Interestingly, a certain amount of saddling was also calculated for the oxidized and reduced forms of the complexes, and the saddling effect for those redox forms also turned out to be independent of the functional used (Table A6.7, see Appendix). For the native state of the complexes, the formally cor³⁻ ligand has two electrons (for donating) and the formally Cu^{III} center has two holes (empty $d_{x^2-y^2}$ orbital), this makes electron flow from cor³⁻ to Cu^{III} possible and saddling unavoidable. As saddling is also observed for the oxidized and reduced forms, electrons on the corrolato ligand and holes on the copper center should be present to make such saddling happen. Thus, we feel that forms such as (cor)⁻ and Cu^I are less likely to contribute to the various redox forms of these copper complexes. As has been discussed above, the reduced forms of the copper complexes described here as well as the silver analogues reported by us previously display a predominantly metal centered spin, with a Cu^{II} or Ag^{II} formulation being appropriate for them. For the

oxidized forms however, both experiment and theory deliver large spin densities on the copper center whereas for the silver analogues no spin density was detected at the metal center (see discussion above). This difference has interesting consequences for formal oxidation state distributions in these complexes as is shown below (Figure 6.14):



Thus, it is seen that for the oxidized species, formulations with spin on the copper center are necessary (Figure 6.14) to correctly depict the electronic structure, a phenomenon that is not relevant for the oxidized silver complexes. Such a situation thus leads to a form with Cu^{IV} which seems to be relevant for the present case. An alternative with Cu^{II} will contain a doubly oxidized mono-negative corrolato ligand. We feel that such a form will make no significant contribution to the electronic structure (see discussion above).

It needs to be mentioned here that redox induced electron transfer has been invoked earlier for metal complexes of non-innocent ligands. Surprisingly, the copper complexes display a more mixed orbital situation compared to the silver cases. For most metal complexes, higher covalency is usually observed for the higher homologues. This fact is likely related to the structural saddling as has been discussed

above. The copper complexes thus provide an ideal platform for investigating reactivity studies with metal-ligand cooperativity³⁵²⁻³⁵⁶.

6.3 Conclusions

In conclusion, we have discussed here the various redox states of corrolato-copper complexes in comparison with their silver analogues. This is the first spectroscopic and structural characterization of the oxidized forms of corrolato-copper complexes. We have used a combination of structural, electrochemical, spectroelectrochemical and theoretical methods to show that the native states of these complexes can be best described as a mixture of Cu^{II} and Cu^{III}, a fact that was recognized earlier in the literature and is different from their silver analogues. The reduced forms of both species can be best described as divalent metal centers. Finally, the oxidized forms show interesting differences. Whereas, the oxidized silver complex can be exclusively formulated as a Ag^{III} species bound to a dianionic corrolato radical, the copper analogues present a more complicated and intriguing feature. Cu^{IV} should indeed be invoked to correctly describe the electronic structure of that redox state. Surprising, a more mixed orbital situation is observed for the copper complexes than their silver analogues. This fact is contrary to what is usually observed for metal complexes of non-innocent ligands³⁵⁷⁻³⁶². The more mixed situation observed for the copper complexes should thus lead to interesting reactivity patterns, where metal-ligand cooperativity³⁵²⁻³⁵⁶ can be used for bond activation reactions and catalysis.

6.4 Experimental Section

6.4.1 Materials

The precursors pyrrole, *p*-chloranil, 4-Cyano benzaldehyde, 2,4,5-Trimethoxy

benzaldehyde, 4,7-Dimethoxy naphthaldehyde and TBAP (Tetrabutyl ammonium perchlorate) were purchased from Aldrich, USA. $\text{Cu}(\text{OAc})_2 \cdot \text{H}_2\text{O}$ was purchased from Merck, India. Other chemicals were of reagent grade. Hexane and CH_2Cl_2 were distilled from KOH and CaH_2 respectively. For spectroscopy and electrochemical studies HPLC grade solvents were used.

6.4.2 Physical Measurements

UV–Vis spectral studies were performed on a Perkin–Elmer LAMBDA-750 spectrophotometer. The elemental analyses were carried out with a Perkin–Elmer 240C elemental analyzer. The NMR measurements were carried out using a Bruker AVANCE 400 NMR spectrometer. Chemical shifts are expressed in parts per million (ppm) relative to residual chloroform ($\delta = 7.26$). Electrospray mass spectra were recorded on a Bruker Micro TOF–QII mass spectrometer. Cyclic voltammetry measurements were carried out using a CH Instruments model CHI1120A electrochemistry system. A glassy–carbon working electrode, a platinum wire as an auxiliary electrode and a saturated calomel reference electrode (SCE) were used in a three–electrode configuration. Tetrabutyl ammonium perchlorate (TBAP) was the supporting electrolyte (0.1M) and the concentration of the solution was 10^{-3}M with respect to the complex. The half wave potential E_{298}^0 was set equal to $0.5(E_{\text{pa}} + E_{\text{pc}})$, where E_{pa} and E_{pc} are anodic and cathodic cyclic voltammetric peak potentials, respectively. The scan rate used was 100 mV s^{-1} . EPR spectra in the X band were recorded with a Bruker System EMX. Simulations of EPR spectra were done using the Simfonia program. UV-Vis-NIR absorption spectra were recorded on an Avantes spectrometer system: Ava Light-DH-BAL (light source), AvaSpec-ULS2048 (UV-Vis-detector) and AvaSpec-NIR256-2.5TEC (NIR-detector). Spectroelectrochemical

measurements were carried out using an optically transparent thin layer electrochemical (OTTLE) cell ¹⁹³.

6.4.3 Crystal Structure Determination

Single crystals of **3** were grown by slow diffusion of a solution of the **3** in dichloromethane into hexane, followed by slow evaporation under atmospheric conditions. The crystal data of **3** were collected on a Bruker Kappa APEX II CCD diffractometer at 100 K. Selected data collection parameters and other crystallographic results are summarized in Table 6.1. All data were corrected for Lorentz polarization and absorption effects. The program package SHELXTL ¹⁹⁵ was used for structure solution and full matrix least squares refinement on F^2 . Hydrogen atoms were included in the refinement using the riding model. Contributions of H atoms for the water molecules were included but were not fixed. Disordered solvent molecules were taken out using SQUEEZE command in PLATON ¹⁹⁶.

6.4.4 Computational Details

DFT calculations were done with the ORCA 3.0.0 program package ³²⁷. Geometry optimizations with the BP86 ^{328, 363} and B3LYP functional were run with empirical Van der Waals correction (D3) ³³⁰ unless otherwise stated. The geometry optimization with the OLYP functional ³⁶⁴ was done without D3, as this functional is not parameterized for D3. Single point calculations were run with the B3LYP functional with D3, starting from BP86-D3 optimized geometries. The restricted and unrestricted DFT methods were employed for closed and open shell molecules respectively unless otherwise stated. Convergence criteria were set to default for the geometry-optimizations (OPT) and tight for SCF calculations (TIGHTSCF). Relativistic effects were included with the zeroth-order relativistic approximation (ZORA) ³³¹. Triple- ζ -

valence basis sets (TZVPP-ZORA)³³² were employed for all atoms. Calculations were performed using the resolution of the identity approximation³³³⁻³³⁶ with matching auxiliary basis sets. Low-lying excitation energies were calculated with time-dependent DFT (TD-DFT). Solvent effects were taken into account with the conductor-like screening model (COSMO)^{337, 338} for all calculations. Spin densities were calculated according to the Löwdin population analysis³³⁹. Molecular orbitals and spin densities were visualized with the Molekel 5.4.0.8 program³⁴¹. Calculations of EPR parameters were performed with the B3LYP functional on DFT optimized structures using COSMO. Here the aug-cc-pVTZ-J^[19] basis set was used for all copper and nitrogen atoms and the def2-TZVP³⁶⁵ basis set for all other atoms. To improve the description of the core density the integration grid at copper and nitrogen atoms was kept very large (AngularGrid 7, IntAcc 7). To avoid inaccuracy the RIJCOSX approximation was not employed in the calculation of the epr parameters.

6.4.5 X-ray Absorption Measurements

Measurements were performed at XAS beamline of the ANKA synchrotron (Karlsruhe, Germany) under ambient conditions at 293 K. A Si(111) double crystal monochromator was used for measurements at the Cu K-edge (8.979 keV). The second monochromator crystal was tilt for optimal harmonic rejection. The spectra were recorded in transmission mode with ionisation chambers filled with nitrogen. The individual pressures were adjusted to optimize the signal to noise ratio. Energy calibration was performed with a copper metal foil. The solid samples were embedded in an oxygen free boron nitride matrix and pressed into pellets.

6.4.6 Synthesis of 5,10,15-tris(4-cyanophenyl)corrolato-copper(III), 1

0.025 g of 5,10,15-tris(4-cyanophenyl) corrole⁴⁶ (0.041 mmol) was dissolved in 6 mL

of pyridine and 0.082 g of copper acetate hydrate (0.41 mmol) was added to it. The reaction mixture was kept at stirring for 40 min at room temperature during which, the colour of the reaction mixture changed from green to brown. The solvent was then removed by rotary evaporation and the brown crude product was purified by column chromatography through silica gel (100-200 mesh) column using 100% DCM as eluent. Subsequent recrystallization (CH₂Cl₂/hexane) gave the pure crystalline **1**. Yield: 66% (18 mg, 0.027mmol). Anal. Calcd (found) for C₄₀H₂₀N₇Cu (**1**): C, 72.55 (72.75); H, 3.04 (3.16); N, 14.81 (14.97). λ_{\max}/nm ($\epsilon/M^{-1}\text{cm}^{-1}$) in dichloromethane: 414 (77000), 539 (6000), 617 (4200). ¹H NMR (400 MHz, CD₂Cl₂) δ 7.97 (s, 2H), 7.87 – 7.70 (m, 12H), 7.56 (d, $J = 3.8$ Hz, 2H), 7.29 (s, 2H), 7.16 (d, $J = 4.3$ Hz, 2H). The electrospray mass spectrum of **1** in acetonitrile shows peaks centered at $m/z = 661.1007$ corresponding to [**1**]⁺ (661.1076 calcd for C₄₀H₂₀N₇Cu).

6.4.7 Synthesis of 10-(2,4,5-Trimethoxyphenyl)-5,15-bis(4-cyanophenyl)corrolato-copper(III), 2

0.025 g of 10-(2,4,5-Trimethoxyphenyl)-5,15-bis(4-cyanophenyl) corrole ⁵¹ (0.037 mmol) was dissolved in 6 mL of pyridine and 0.074 g of copper acetate hydrate (0.37 mmol) was added to it. The reaction mixture was kept at stirring for 40 min at room temperature during which, the colour of the reaction mixture changed from green to brown. The solvent was then removed by rotary evaporation and the brown crude product was purified by column chromatography through silica gel (100-200 mesh) column using 100% DCM as eluent. Subsequent recrystallization (CH₂Cl₂/hexane) gave the pure crystalline **2**. Yield: 73% (20 mg, 0.027mmol). Anal. Calcd (found) for C₄₂H₂₇CuN₆O₃ (**2**): C, 69.36 (69.52); H, 3.74 (3.86); N, 11.56 (11.69). λ_{\max}/nm ($\epsilon/M^{-1}\text{cm}^{-1}$) in dichloromethane: 411 (89300), 554 (9000), 633 (6000). ¹H NMR (400

MHz, CDCl₃) δ 7.94 (d, J = 3.2 Hz, 2H), 7.82 (dd, J = 21.8, 8.0 Hz, 8H), 7.51 (d, J = 4.2 Hz, 2H), 7.23 (m, J = 6.4 Hz, 4H), 6.93 (s, 1H), 6.67 (s, 1H), 4.01 (s, 3H), 3.84 (s, 3H), 3.69 (s, 3H). The electrospray mass spectrum of **2** in acetonitrile shows peaks centered at m/z = 726.1451 corresponding to [**2**]⁺ (726.1440 calcd for C₄₂H₂₇CuN₆O₃).

6.4.8 Synthesis of 10-(4,7-dimethoxynaphthalen-1-yl)-5,15-bis(4-cyanophenyl)corrolato-copper(III), **3**

0.025 g of 10-(4,7-dimethoxynaphthalen-1-yl)-5,15-bis(4-cyanophenyl)corrole²⁷² (0.036 mmol) was dissolved in 6 mL of pyridine and 0.072 g of copper acetate hydrate (0.36 mmol) was added to it. The reaction mixture was kept at stirring for 40 min at room temperature during which, the color of the reaction mixture changed from green to brown. The solvent was then removed by rotary evaporation and the brown crude product was purified by column chromatography through silica gel (100-200 mesh) column using a solution of 80% DCM and 20% hexane as eluent. Subsequent recrystallization (CH₂Cl₂/hexane) gave the pure crystalline **3**. Yield: 70% (19 mg, 0.025mmol). Anal. Calcd (found) for C₄₅H₂₇CuN₆O₂ (**3**): C, 72.33 (72.51); H, 3.64 (3.77); N, 11.25 (11.44). λ_{\max}/nm ($\epsilon/\text{M}^{-1}\text{cm}^{-1}$) in dichloromethane: 411 (77600), 554 (8200), 623 (5500). ¹H NMR (400 MHz, CDCl₃) δ 8.28 (d, J = 9.2 Hz, 1H), 7.96 (d, J = 3.4 Hz, 2H), 7.82 (dd, J = 22.8, 8.2 Hz, 8H), 7.54 (dd, J = 9.1, 6.1 Hz, 3H), 7.20 (d, J = 4.3 Hz, 2H), 7.13 (dd, J = 9.2, 2.2 Hz, 1H), 7.07 (d, J = 4.6 Hz, 2H), 6.88 (d, J = 2.3 Hz, 1H), 6.79 (d, J = 7.9 Hz, 1H), 4.09 (s, 3H), 3.60 (s, 3H). The electrospray mass spectrum of **3** in acetonitrile shows peaks centered at m/z = 746.1303 corresponding to [**3**]⁺ (746.1491 calcd for C₄₅H₂₇CuN₆O₂).

Summary and Future Prospect

Corroles are tetrapyrrolic aromatic macrocycles resembling the naturally occurring biological pigments, porphyrins and corrins. Corroles have recently gained a lot of research interest for its interesting structural and spectroscopic properties. In this thesis, various scaffolds of corrole frameworks and their corresponding metalated derivatives have been explored on the basis of either biological or physical significances. Efforts are laid to comprehend the mechanistic aspects of their reactivity and also electronic, structural and spectroscopic changes on electron transfer in individual cases.

In separate studies, oxidation state distributions in corrolato iron nitrosyl complexes, semi-insulating device fabrication with nanoaggregates of tin(IV) corroles, efficient and mild demetalation strategy of tin(IV) corroles have been investigated. Oxidation state distributions in corrolato iron nitrosyl complexes, studied here will be useful to comprehend their role in redox catalytic reactions. While the semi-insulating property of the tin(IV) corroles can be directly implemented for the construction of high-electron-mobility transistors (HEMT) in modern communication devices after adequate precise optimizations, the acid-free efficient demetalation strategy will be definitely useful in performing various organic transformations.

Furthermore, oxidized forms of monomeric silver(III) and copper(III) complexes of corroles have been found to behave as near-IR absorbing dyes. Thus suitable design of such systems may lead to the discovery of newer varieties of chlorophyll-like light-harvesting units that may not solely depend on the photosynthetic special-pairs for light harvesting purposes. With the simultaneous stabilization of unusual oxidation states of metals, e.g. Ag^{II} forms and Cu^{IV} forms on one-electron reduction of silver(III) corroles and one-electron oxidation of copper(III)

corroles respectively can lead to interesting reactivity patterns, where metal-ligand cooperativity may be used for bond activation reactions and catalysis.

References

1. Battersby, A. R.; Fookes, C.; Matcham, G.; McDonald, E., *Nature* **1980**, 285, 17-21.
2. Kadish, K. M.; Smith, K. M.; Guillard, R.; Editors, *The Porphyrin Handbook; Volume 2, Heteroporphyrins, Expanded Porphyrins and Related Macrocycles*. Academic Press: 2000.
3. Berg, J. M.; Lippard, S., *Principles of bioinorganic chemistry*. Mill Valley, 411 s. ed.; University Science Books: 1994.
4. Weiss, C., *J. Mol. Spectrosc.* **1972**, 44, 37-80.
5. Soret, J.-L., *Compt. Rend.* **1883**, 97, 1269-1273.
6. Senge, M. O.; Smith, K. M., *Photochem. Photobiol.* **1991**, 54, 841-846.
7. Smith, K. M.; Goff, D. A.; Abraham, R. J., *Org. Magn. Resonance* **1984**, 22, 779-783.
8. Sessler, J. L.; Weghorn, S. J., *Expanded, contracted & isomeric porphyrins*. Elsevier: 1997; Vol. 15.
9. Franck, B.; Nonn, A., *Angew. Chem. Int. Ed. Engl.* **1995**, 34, 1795-1811.
10. Kadish, K. M.; Smith, K. M.; Guillard, R.; Editors, *The Porphyrin Handbook; Volume 1, Synthesis and Organic Chemistry*. Academic Press: 2000.
11. Hodgkin, D. C.; Kamper, J.; Lindsey, J.; MacKay, M.; Pickworth, J.; Robertson, J.; Shoemaker, C. B.; White, J.; Prosen, R.; Trueblood, K., *Proc. R. Soc. Lond. A* **1957**, 242, 228-263.
12. Johnson, A.; Todd, A., *Vitam. Horm.* **1957**, 15, 1.
13. Bonnett, R., *Chem. Rev.* **1963**, 63, 573-605.
14. Battersby, A. R., *J. Nat. Prod.* **1988**, 51, 629-642.
15. Johnson, A.; Price, R., *J. Chem. Soc.* **1960**, 1649-1653.
16. Johnson, A.; Kay, I., *J. Chem. Soc.* **1965**, 1620-1629.

-
17. Claessens, C. G.; González-Rodríguez, D.; del Rey, B.; Torres, T.; Mark, G.; Schuchmann, H. P.; von Sonntag, C.; MacDonald, J. G.; Nohr, R. S., *Eur. J. Org. Chem.* **2003**, *2003*, 2547-2551.
 18. Claessens, C. G.; Gonzalez-Rodriguez, D.; Rodríguez-Morgade, M. S.; Medina, A.; Torres, T., *Chem. Rev.* **2013**, *114*, 2192-2277.
 19. Vogel, E.; Binsack, B.; Hellwig, Y.; Erben, C.; Heger, A.; Lex, J.; Wu, Y. D., *Angew. Chem. Int. Ed. Engl.* **1997**, *36*, 2612-2615.
 20. Inokuma, Y.; Osuka, A., *Dalton Trans.* **2008**, 2517.
 21. Myśliborski, R.; Latos-Grażyński, L.; Szterenber, L.; Lis, T., *Angew. Chem. Int. Ed.* **2006**, *45*, 3670-3674.
 22. Ito, T.; Hayashi, Y.; Shimizu, S.; Shin, J. Y.; Kobayashi, N.; Shinokubo, H., *Angew. Chem. Int. Ed. Engl.* **2012**, *51*, 8542-5.
 23. Broring, M.; Kohler, S.; Kleeberg, C., *Angew. Chem. Int. Ed. Engl.* **2008**, *47*, 5658-60.
 24. Meller, A.; Ossko, A., *Monatsh. Chem.* **1972**, *103*, 150-155.
 25. Will, S.; Rahbar, A.; Schmickler, H.; Lex, J.; Vogel, E., *Angew. Chem. Int. Ed. Engl.* **1990**, *29*, 1390-1393.
 26. Inokuma, Y.; Kwon, J. H.; Ahn, T. K.; Yoo, M. C.; Kim, D.; Osuka, A., *Angew. Chem. Int. Ed.* **2006**, *45*, 961-964.
 27. Dyke, J.; Hush, N.; Williams, M.; Woolsey, I., *Mol. Phys.* **1971**, *20*, 1149-1152.
 28. Ghosh, A.; Jynge, K., *Chem. Eur. J.* **1997**, *3*, 823-833.
 29. Paolesse, R.; Sagone, F.; Macagnano, A.; Boschi, T.; Prodi, L.; Montalti, M.; Zaccheroni, N.; Bolletta, F.; Smith, K. M., *J. Porphyrins Phthalocyanines* **1999**, *3*, 364-370.
-

-
30. Broadhurst, M. J.; Grigg, R.; Shelton, G.; Johnson, A. W., *J. Chem. Soc., Perkin Trans. 1* **1972**, 143-151.
 31. Balazs, Y. S.; Saltsman, I.; Mahammed, A.; Tkachenko, E.; Golubkov, G.; Levine, J.; Gross, Z., *Magn. Reson. Chem.* **2004**, *42*, 624-635.
 32. Harrison, H. R.; Hodder, O. J. R.; Hodgkin, D. C., *J. Chem. Soc. B* **1971**, 640.
 33. Gross, Z.; Galili, N.; Simkhovich, L.; Saltsman, I.; Botoshansky, M.; Blaeser, D.; Boese, R.; Goldberg, I., *Org. Lett.* **1999**, *1*, 599-602.
 34. Paolesse, R.; Pandey, R. K.; Forsyth, T. P.; Jaquinod, L.; Gerzevske, K. R.; Nurco, D. J.; Senge, M. O.; Licoccia, S.; Boschi, T.; Smith, K. M., *J. Am. Chem. Soc.* **1996**, *118*, 3869-3882.
 35. Broadhurst, M.; Grigg, R.; Johnson, A., *J. Chem. Soc., Perkin Trans. 1* **1972**, 1124-1135.
 36. Tse, M.; Chan, K., *Chem. Commun.* **1998**, 1199-1200.
 37. Conlon, M.; Johnson, A. W.; Overend, W. R.; Rajapaksa, D.; Elson, C. M., *J. Chem. Soc., Perkin Trans. 1* **1973**, 2281-2288.
 38. Paolesse, R.; Licoccia, S.; Bandoli, G.; Dolmella, A.; Boschi, T., *Inorg. Chem.* **1994**, *33*, 1171-1176.
 39. Licoccia, S.; Tassoni, E.; Paolesse, R.; Boschi, T., *Inorg. Chim. Acta* **1995**, *235*, 15-20.
 40. Paolesse, R.; Tassoni, E.; Licoccia, S.; Paci, M.; Boschi, T., *Inorg. Chim. Acta* **1996**, *241*, 55-60.
 41. Sheldon, R. A., *Metalloporphyrins in catalytic oxidations*. CRC Press: 1994.
 42. Chmielewski, P. J.; Latos-Grażyński, L.; Rachlewicz, K., *Chem. Eur. J.* **1995**, *1*, 68-73.
-

-
43. Rose, E.; Kossanyi, A.; Quelquejeu, M.; Soleilhavoup, M.; Duwavran, F.; Bernard, N.; Lecas, A., *J. Am. Chem. Soc.* **1996**, *118*, 1567-1568.
 44. Gross, Z.; Galili, N.; Saltsman, I., *Angew. Chem. Int. Ed.* **1999**, *38*, 1427-1429.
 45. Paolesse, R.; Mini, S.; Sagone, F.; Boschi, T.; Jaquinod, L.; J. Nurco, D.; M. Smith, K., *Chem. Commun.* **1999**, 1307-1308.
 46. Koszarna, B.; Gryko, D. T., *J. Org. Chem.* **2006**, *71*, 3707-17.
 47. Král, V.; Vašek, P.; Dolensky, B., *Collect. Czech. Chem. Commun.* **2004**, *69*, 1126-1136.
 48. Aviv-Harel, I.; Gross, Z., *Chem. Eur. J.* **2009**, *15*, 8382-94.
 49. Gross, Z., *J. Biol. Inorg. Chem.* **2001**, *6*, 733-738.
 50. Simkhovich, L.; Mahammed, A.; Goldberg, I.; Gross, Z., *Chem. Eur. J.* **2001**, *7*, 1041-55.
 51. Sinha, W.; Deibel, N.; Agarwala, H.; Garai, A.; Schweinfurth, D.; Purohit, C. S.; Lahiri, G. K.; Sarkar, B.; Kar, S., *Inorg. Chem.* **2014**, *53*, 1417-1429.
 52. Palmer, J. H.; Day, M. W.; Wilson, A. D.; Henling, L. M.; Gross, Z.; Gray, H. B., *J. Am. Chem. Soc.* **2008**, *130*, 7786-7787.
 53. Mahammed, A.; Giladi, I.; Goldberg, I.; Gross, Z., *Chem. Eur. J.* **2001**, *7*, 4259-65.
 54. Bendix, J.; Dmochowski, I. J.; Gray, H. B.; Mahammed, A.; Simkhovich, L.; Gross, Z., *Angew. Chem. Int. Ed.* **2000**, *39*, 4048-4051.
 55. Mahammed, A.; Gross, Z., *J. Inorg. Biochem.* **2002**, *88*, 305-309.
 56. Will, S.; Lex, J.; Vogel, E.; Schmickler, H.; Gisselbrecht, J.-P.; Hauptmann, C.; Bernard, M.; Gorss, M., *Angew. Chem. Int. Ed. Engl.* **1997**, *36*, 357-361.
-

-
57. Kadish, K. M.; Erben, C.; Ou, Z.; Adamian, V. A.; Will, S.; Vogel, E., *Inorg. Chem.* **2000**, *39*, 3312-3319.
58. Thomas, K. E.; Alemayehu, A. B.; Conradie, J.; Beavers, C.; Ghosh, A., *Inorg. Chem.* **2011**, *50*, 12844-12851.
59. Brückner, C.; Barta, C. A.; Brinas, R. P.; Krause Bauer, J. A., *Inorg. Chem.* **2003**, *42*, 1673-1680.
60. Ou, Z.; Erben, C.; Autret, M.; Will, S.; Rosen, D.; Lex, J.; Vogel, E.; Kadish, K. M., *J. Porphyrins Phthalocyanines* **2005**, *09*, 398-412.
61. Jérôme, F.; Billier, B.; Barbe, J. M.; Espinosa, E.; Dahaoui, S.; Lecomte, C.; Guillard, R., *Angew. Chem. Int. Ed.* **2000**, *39*, 4051-4053.
62. Licoccia, S.; Paolesse, R.; Tassoni, E.; Polizio, F.; Boschi, T., *J. Chem. Soc., Dalton Trans.* **1995**, 3617-21.
63. Buckley, H. L.; Arnold, J., *Dalton Trans.* **2015**, *44*, 30-6.
64. Aviv-Harel, I.; Gross, Z., *Coord. Chem. Rev.* **2011**, *255*, 717-736.
65. Buckley, H. L.; Chomitz, W. A.; Koszarna, B.; Tasiar, M.; Gryko, D. T.; Brothers, P. J.; Arnold, J., *Chem. Commun.* **2012**, *48*, 10766-10768.
66. Ward, A. L.; Buckley, H. L.; Lukens, W. W.; Arnold, J., *J. Am. Chem. Soc.* **2013**, *135*, 13965-13971.
67. Kadish, K. M.; Smith, K. M.; Guillard, R.; Editors, *The Porphyrin Handbook: Volume 8, Electron Transfer*. Academic Press: 2000.
68. Aviv, I.; Gross, Z., *Chem. Commun.* **2007**, 1987.
69. Gross, Z.; Simkhovich, L.; Galili, N., *Chem. Commun.* **1999**, 599-600.
70. Golubkov, G.; Bendix, J.; Gray, H. B.; Mahammed, A.; Goldberg, I.; DiBilio, A. J.; Gross, Z., *Angew. Chem. Int. Ed. Engl.* **2001**, *40*, 2132-2134.
71. Liu, H. Y.; Lai, T. S.; Yeung, L. L.; Chang, C. K., *Org. Lett.* **2003**, *5*, 617-20.
-

-
72. Luobeznova, I.; Raizman, M.; Goldberg, I.; Gross, Z., *Inorg. Chem.* **2006**, *45*, 386-94.
 73. Mahammed, A.; Gross, Z., *J. Am. Chem. Soc.* **2005**, *127*, 2883-7.
 74. Mahammed, A.; Gross, Z., *Angew. Chem. Int. Ed. Engl.* **2006**, *45*, 6544-7.
 75. Barnham, K. J.; Masters, C. L.; Bush, A. I., *Nat. Rev. Drug Discov.* **2004**, *3*, 205-214.
 76. Beckman, J. S., *Chem. Res. Toxicol.* **1996**, *9*, 836-44.
 77. Merenyi, G.; Lind, J.; Goldstein, S.; Czapski, G., *Chem. Res. Toxicol.* **1998**, *11*, 712-3.
 78. Bryk, R.; Griffin, P.; Nathan, C., *Nature* **2000**, *407*, 211-215.
 79. Szabo, C., *Toxicol Lett.* **2003**, *140-141*, 105-12.
 80. Gershman, Z.; Goldberg, I.; Gross, Z., *Angew. Chem. Int. Ed. Engl.* **2007**, *46*, 4320-4.
 81. Meier-Callahan, A. E.; Di Bilio, A. J.; Simkhovich, L.; Mahammed, A.; Goldberg, I.; Gray, H. B.; Gross, Z., *Inorg. Chem.* **2001**, *40*, 6788-93.
 82. Mahammed, A.; Gray, H. B.; Meier-Callahan, A. E.; Gross, Z., *J. Am. Chem. Soc.* **2003**, *125*, 1162-3.
 83. Simkhovich, L.; Goldberg, I.; Gross, Z., *J. Porphyrins Phthalocyanines* **2002**, *6*, 439-444.
 84. Saltsman, I.; Simkhovich, L.; Balazs, Y.; Goldberg, I.; Gross, Z., *Inorg. Chim. Acta* **2004**, *357*, 3038-3046.
 85. Guillard, R.; Gros, C. P.; Bolze, F.; Jerome, F.; Ou, Z.; Shao, J.; Fischer, J.; Weiss, R.; Kadish, K. M., *Inorg. Chem.* **2001**, *40*, 4845-55.
 86. Kadish, K. M.; Ou, Z.; Shao, J.; Gros, C. P.; Barbe, J. M.; Jerome, F.; Bolze, F.; Burdet, F.; Guillard, R., *Inorg. Chem.* **2002**, *41*, 3990-4005.
-

-
87. Barbe, J. M.; Canard, G.; Brandes, S.; Jerome, F.; Dubois, G.; Guillard, R., *Dalton Trans.* **2004**, 1208-14.
88. Campbell, W. M.; Burrell, A. K.; Officer, D. L.; Jolley, K. W., *Coord. Chem. Rev.* **2004**, *248*, 1363-1379.
89. Wang, Q.; Campbell, W. M.; Bonfantani, E. E.; Jolley, K. W.; Officer, D. L.; Walsh, P. J.; Gordon, K.; Humphry-Baker, R.; Nazeeruddin, M. K.; Gratzel, M., *J. Phys. Chem. B* **2005**, *109*, 15397-409.
90. Urbani, M.; Gratzel, M.; Nazeeruddin, M. K.; Torres, T., *Chem. Rev.* **2014**, *114*, 12330-96.
91. Walker, D.; Chappel, S.; Mahammed, A.; Brunshwig, B. S.; Winkler, J. R.; Gray, H. B.; Zaban, A.; Gross, Z., *J. Porphyrins Phthalocyanines* **2006**, *10*, 1259-1262.
92. Haber, A.; Mahammed, A.; Fuhrman, B.; Volkova, N.; Coleman, R.; Hayek, T.; Aviram, M.; Gross, Z., *Angew. Chem. Int. Ed. Engl.* **2008**, *47*, 7896-900.
93. Agadjanian, H.; Weaver, J. J.; Mahammed, A.; Rentsendorj, A.; Bass, S.; Kim, J.; Dmochowski, I. J.; Margalit, R.; Gray, H. B.; Gross, Z.; Medina-Kauwe, L. K., *Pharm. Res.* **2006**, *23*, 367-77.
94. Agadjanian, H.; Ma, J.; Rentsendorj, A.; Valluripalli, V.; Hwang, J. Y.; Mahammed, A.; Farkas, D. L.; Gray, H. B.; Gross, Z.; Medina-Kauwe, L. K., *Proc. Natl. Acad. Sci. U. S. A.* **2009**, *106*, 6105-10.
95. Arnold, W. P.; Mittal, C. K.; Katsuki, S.; Murad, F., *Proc. Natl. Acad. Sci. U. S. A.* **1977**, *74*, 3203-7.
96. Wolin, M. S.; Wood, K. S.; Ignarro, L. J., *J. Biol. Chem.* **1982**, *257*, 13312-20.
97. Sundaresan, M.; Yu, Z. X.; Ferrans, V. J.; Irani, K.; Finkel, T., *Science* **1995**, *270*, 296-9.
-

-
98. Henry, Y. A.; Guissani, A.; Ducastel, B., *Nitric oxide research from chemistry to biology: EPR spectroscopy of nitrosylated compounds*. Springer Science & Business Media: 2012.
 99. Olson, L. W.; Schaeper, D.; Lancon, D.; Kadish, K. M., *J. Am. Chem. Soc.* **1982**, *104*, 2042-4.
 100. Lancon, D.; Kadish, K. M., *J. Am. Chem. Soc.* **1983**, *105*, 5610-5617.
 101. Mu, X. H.; Kadish, K. M., *Inorg. Chem.* **1988**, *27*, 4720-5.
 102. Choi, I. K.; Liu, Y.; Feng, D.; Paeng, K. J.; Ryan, M. D., *Inorg. Chem.* **1991**, *30*, 1832-1839.
 103. Ozawa, S.; Fujii, H.; Morishima, I., *J. Am. Chem. Soc.* **1992**, *114*, 1548-54.
 104. Autret, M.; Will, S.; Caemelbecke, E. V.; Lex, J.; Gisselbrecht, J.-P.; Gross, M.; Vogel, E.; Kadish, K. M., *J. Am. Chem. Soc.* **1994**, *116*, 9141-9.
 105. Simkhovich, L.; Goldberg, I.; Gross, Z., *Inorg. Chem.* **2002**, *41*, 5433-5439.
 106. Joseph, C. A.; Ford, P. C., *J. Am. Chem. Soc.* **2005**, *127*, 6737-6743.
 107. Joseph, C. A.; Lee, M. S.; Ireetskii, A. V.; Wu, G.; Ford, P. C., *Inorg. Chem.* **2006**, *45*, 2075-2082.
 108. Broering, M.; Milsmann, C.; Ruck, S.; Koehler, S., *J. Organomet. Chem.* **2009**, *694*, 1011-1015.
 109. Singh, P.; Saltsman, I.; Mahammed, A.; Goldberg, I.; Tumanskii, B.; Gross, Z., *J. Porphyrins Phthalocyanines* **2012**, *16*, 663-673.
 110. Kim, D.; Osuka, A., *Acc. Chem. Res.* **2004**, *37*, 735-745.
 111. Balaban, T. S.; Bhise, A. D.; Fischer, M.; Linke-Schaetzl, M.; Roussel, C.; Vanthuyne, N., *Angew. Chem. Int. Ed.* **2003**, *42*, 2140-2144.
 112. Burrell, A. K.; Officer, D. L.; Plieger, P. G.; Reid, D. C., *Chem. Rev.* **2001**, *101*, 2751-96.
-

-
113. Balaban, T. S.; Linke-Schaetzel, M.; Bhise, A. D.; Vanthuyne, N.; Roussel, C.; Anson, C. E.; Buth, G.; Eichhoefer, A.; Foster, K.; Garab, G.; Gliemann, H.; Goddard, R.; Javorfi, T.; Powell, A. K.; Roesner, H.; Schimmel, T., *Chem. Eur. J.* **2005**, *11*, 2267-2275.
114. Otsuki, J.; Iwasaki, K.; Nakano, Y.; Itou, M.; Araki, Y.; Ito, O., *Chem. Eur. J.* **2004**, *10*, 3461-3466.
115. Takahashi, R.; Kobuke, Y., *J. Am. Chem. Soc.* **2003**, *125*, 2372-2373.
116. Wang, Z.; Medforth, C. J.; Shelnut, J. A., *J. Am. Chem. Soc.* **2004**, *126*, 15954-15955.
117. McDermott, G.; Prince, S. M.; Freer, A. A.; Hawthornthwaite-Lawless, A. M.; Papiz, M. Z.; Cogdell, R. J.; Isaacs, N. W., *Nature (London)* **1995**, *374*, 517-21.
118. Bahatyrova, S.; Frese, R. N.; Siebert, C. A.; Olsen, J. D.; van der Werf, K. O.; van Grondelle, R.; Niederman, R. A.; Bullough, P. A.; Otto, C.; Hunter, C. N., *Nature (London, U. K.)* **2004**, *430*, 1058-1062.
119. Ribo, J. M.; Crusats, J.; Sagues, F.; Claret, J.; Rubires, R., *Science* **2001**, *292*, 2063-6.
120. Linke-Schaetzel, M.; Bhise, A. D.; Gliemann, H.; Koch, T.; Schimmel, T.; Balaban, T. S., *Thin Solid Films* **2004**, *451-452*, 16-21.
121. Kwag, G.; Park, E.; Kim, S., *Bull. Korean Chem. Soc.* **2004**, *25*, 298-300.
122. Dini, F.; Martinelli, E.; Pomarico, G.; Paolesse, R.; Monti, D.; Filippini, D.; D'Amico, A.; Lundstrom, I.; Di Natale, C., *Nanotechnology* **2009**, *20*, 055502.
123. Roales, J.; Pedrosa, J. M.; Castellero, P.; Cano, M.; Richardson, T. H.; Barranco, A.; Gonzalez-Elipe, A. R., *ACS Appl. Mater. Interfaces* **2012**, *4*, 5147-5154.
-

-
124. Patra, R.; Titi, H. M.; Goldberg, I., *Cryst. Growth Des.* **2013**, *13*, 1342-1349.
 125. Broering, M.; Hell, C., *Chem. Commun.* **2001**, 2336-2337.
 126. Brueckner, C.; Barta, C. A.; Brinas, R. P.; Bauer, J. A. K., *Inorg. Chem.* **2003**, *42*, 1673-1680.
 127. Liu, H. Y.; Chen, L.; Yam, F.; Zhan, H. Y.; Ying, X.; Wang, X. L.; Jiang, H. F.; Chang, C. K., *Chin. Chem. Lett.* **2008**, *19*, 1000-1003.
 128. Ngo, T. H.; Van Rossom, W.; Dehaen, W.; Maes, W., *Org. Biomol. Chem.* **2009**, *7*, 439-443.
 129. Lewis, I. C.; Singer, L. S., *J. Chem. Phys.* **1965**, *43*, 2712-27.
 130. Bally, T.; Roth, K.; Straub, R., *J. Am. Chem. Soc.* **1988**, *110*, 1639-41.
 131. Kochi, J. K.; Rathore, R.; Le Magueres, P., *J. Org. Chem.* **2000**, *65*, 6826-6836.
 132. Ganesan, V.; Rosokha, S. V.; Kochi, J. K., *J. Am. Chem. Soc.* **2003**, *125*, 2559-2571.
 133. Lü, J.-M.; Rosokha, S. V.; Kochi, J. K., *J. Am. Chem. Soc.* **2003**, *125*, 12161-12171.
 134. Deisenhofer, J.; Norris, J. R., *Photosynthetic Reaction Center*. Academic Press: 2013; Vol. 2.
 135. Zhu, C.; Liang, J.; Cao, Z., *J. Phys. Chem. C* **2013**, *117*, 13388-13395.
 136. Tasior, M.; Gryko, D. T.; Shen, J.; Kadish, K. M.; Becherer, T.; Langhals, H.; Ventura, B.; Flamigni, L., *J. Phys. Chem. C* **2008**, *112*, 19699-19709.
 137. Okun, Z.; Gross, Z., *Inorg. Chem.* **2012**, *51*, 8083-8090.
 138. Poulin, J.; Stern, C.; Guillard, R.; Harvey, P. D., *Photochem. Photobiol.* **2006**, *82*, 171-176.
-

-
139. Tasiar, M.; Gryko, D. T.; Cembor, M.; Jaworski, J. S.; Ventura, B.; Flamigni, L., *New J. Chem.* **2007**, *31*, 247-259.
140. Cotton, A. F.; Wilkinson, G.; Bochmann, M.; Murillo, C. A., *Advanced inorganic chemistry*. Wiley: 1999.
141. Sheldon, R., *Metal-catalyzed oxidations of organic compounds: mechanistic principles and synthetic methodology including biochemical processes*. Elsevier: 2012.
142. Wang, G.; Zhou, M.; Goettel, J. T.; Schrobilgen, G. J.; Su, J.; Li, J.; Schlöder, T.; Riedel, S., *Nature* **2014**, *514*, 475-477.
143. Chen, G.; Langlois, J.-M.; Guo, Y.; Goddard, W. A., *Proc. Natl. Acad. Sci. U. S. A.* **1989**, *86*, 3447-3451.
144. Zhang, M.-T.; Chen, Z.; Kang, P.; Meyer, T. J., *J. Am. Chem. Soc.* **2013**, *135*, 2048-2051.
145. Maeda, H.; Osuka, A.; Furuta, H., *J. Am. Chem. Soc.* **2003**, *125*, 15690-15691.
146. Aboeella, N. W.; Kryatov, S. V.; Gherman, B. F.; Brennessel, W. W.; Young, V. G.; Sarangi, R.; Rybak-Akimova, E. V.; Hodgson, K. O.; Hedman, B.; Solomon, E. I., *J. Am. Chem. Soc.* **2004**, *126*, 16896-16911.
147. Harnischmacher, W.; Hoppe, R., *Angew. Chem. Int. Ed. Engl.* **1973**, *12*, 582-583.
148. Hickman, A. J.; Sanford, M. S., *Nature* **2012**, *484*, 177-185.
149. Hoshino, M.; Ozawa, K.; Seki, H.; Ford, P. C., *J. Am. Chem. Soc.* **1993**, *115*, 9568-75.
150. Laverman, L. E.; Hoshino, M.; Ford, P. C., *J. Am. Chem. Soc.* **1997**, *119*, 12663-12664.
151. Lorkovic, I. M.; Ford, P. C., *Inorg. Chem.* **1999**, *38*, 1467-1473.
-

-
152. Lorkovic, I.; Ford, P. C., *J. Am. Chem. Soc.* **2000**, *122*, 6516-6517.
153. Cai, S.; Licoccia, S.; Walker, F. A., *Inorg. Chem.* **2001**, *40*, 5795-8.
154. Laverman, L. E.; Ford, P. C., *J. Am. Chem. Soc.* **2001**, *123*, 11614-11622.
155. Simkhovich, L.; Gross, Z., *Tetrahedron Lett.* **2001**, *42*, 8089-8092.
156. Steene, E.; Wondimagegn, T.; Ghosh, A., *J. Phys. Chem. B* **2001**, *105*, 11406-11413.
157. Kurtikyan, T. S.; Martirosyan, G. G.; Lorkovic, I. M.; Ford, P. C., *J. Am. Chem. Soc.* **2002**, *124*, 10124-10129.
158. Ramdhanie, B.; Zakharov, L. N.; Rheingold, A. L.; Goldberg, D. P., *Inorg. Chem.* **2002**, *41*, 4105-4107.
159. Fernandez, B. O.; Ford, P. C., *J. Am. Chem. Soc.* **2003**, *125*, 10510-10511.
160. Patterson, J. C.; Lorkovic, I. M.; Ford, P. C., *Inorg. Chem.* **2003**, *42*, 4902-4908.
161. Fernandez, B. O.; Lorkovic, I. M.; Ford, P. C., *Inorg. Chem.* **2004**, *43*, 5393-5402.
162. Gryko, D. T.; Fox, J. P.; Goldberg, D. P., *J. Porphyrins Phthalocyanines* **2004**, *8*, 1091-1105.
163. Collman, J. P.; Decreau, R. A., *Org. Lett.* **2005**, *7*, 975-978.
164. Edwards, N. Y.; Eikley, R. A.; Loring, M. I.; Abu-Omar, M. M., *Inorg. Chem.* **2005**, *44*, 3700-3708.
165. Harischandra, D. N.; Zhang, R.; Newcomb, M., *J. Am. Chem. Soc.* **2005**, *127*, 13776-13777.
166. Kadish, K. M.; Fremond, L.; Ou, Z.; Shao, J.; Shi, C.; Anson, F. C.; Burdet, F.; Gros, C. P.; Barbe, J.-M.; Guillard, R., *J. Am. Chem. Soc.* **2005**, *127*, 5625-5631.
-

-
167. Pomarico, G.; Fronczek, F. R.; Nardis, S.; Smith, K. M.; Paolesse, R., *J. Porphyrins Phthalocyanines* **2011**, *15*, 1085-1092.
168. Stefanelli, M.; Nardis, S.; Tortora, L.; Fronczek, F. R.; Smith, K. M.; Licoccia, S.; Paolesse, R., *Chem. Commun.* **2011**, *47*, 4255-4257.
169. Nardis, S.; Stefanelli, M.; Mohite, P.; Pomarico, G.; Tortora, L.; Manowong, M.; Chen, P.; Kadish, K. M.; Fronczek, F. R.; McCandless, G. T.; Smith, K. M.; Paolesse, R., *Inorg. Chem.* **2012**, *51*, 3910-3920.
170. Vogel, E.; Will, S.; Tilling, A. S.; Neumann, L.; Lex, J.; Bill, E.; Trautwein, A. X.; Wiegardt, K., *Angew. Chem. Int. Ed. Engl.* **1994**, *33*, 731-735.
171. Caemelbecke, E. V.; Will, S.; Autret, M.; Adamian, V. A.; Lex, J.; Gisselbrecht, J. P.; Gross, M.; Vogel, E.; Kadish, K. M., *Inorg. Chem.* **1996**, *35*, 184-192.
172. Simkhovich, L.; Galili, N.; Saltsman, I.; Goldberg, I.; Gross, Z., *Inorg. Chem.* **2000**, *39*, 2704-5.
173. Zakhariyeva, O.; Schuenemann, V.; Gerdan, M.; Licoccia, S.; Cai, S.; Walker, F. A.; Trautwein, A. X., *J. Am. Chem. Soc.* **2002**, *124*, 6636-6648.
174. Steene, E.; Dey, A.; Ghosh, A., *J. Am. Chem. Soc.* **2003**, *125*, 16300-16309.
175. Mahammed, A.; Gray, H. B.; Weaver, J. J.; Sorasaene, K.; Gross, Z., *Bioconjugate Chem.* **2004**, *15*, 738-746.
176. Simkhovich, L.; Gross, Z., *Inorg. Chem.* **2004**, *43*, 6136-6138.
177. Nardis, S.; Paolesse, R.; Licoccia, S.; Fronczek, F. R.; Vicente, M. G. H.; Shokhireva, T. K.; Cai, S.; Walker, F. A., *Inorg. Chem.* **2005**, *44*, 7030-7046.
178. Ye, S.; Tuttle, T.; Bill, E.; Simkhovich, L.; Gross, Z.; Thiel, W.; Neese, F., *Chem. Eur. J.* **2008**, *14*, 10839-10851.
-

-
179. Pan, Z.; Harischandra, D. N.; Newcomb, M., *J. Inorg. Biochem.* **2009**, *103*, 174-181.
180. Biswas, A. N.; Das, P.; Agarwala, A.; Bandyopadhyay, D.; Bandyopadhyay, P., *J. Mol. Catal. A: Chem.* **2010**, *326*, 94-98.
181. Schwalbe, M.; Dogutan, D. K.; Stoian, S. A.; Teets, T. S.; Nocera, D. G., *Inorg. Chem.* **2011**, *50*, 1368-1377.
182. Graham, D. J.; Dogutan, D. K.; Schwalbe, M.; Nocera, D. G., *Chem. Commun.* **2012**, *48*, 4175-4177.
183. Zyska, B.; Schwalbe, M., *Chem. Commun.* **2013**, *49*, 3799-3801.
184. Cai, S.; Licoccia, S.; D'Ottavi, C.; Paolesse, R.; Nardis, S.; Bulach, V.; Zimmer, B.; Shokhireva, T. K.; Ann Walker, F., *Inorg. Chim. Acta* **2002**, *339*, 171-178.
185. Enemark, J. H.; Feltham, R. D., *Coord. Chem. Rev.* **1974**, *13*, 339-406.
186. Paolesse, R.; Nardis, S.; Sagone, F.; Khoury, R. G., *J. Org. Chem.* **2001**, *66*, 550-6.
187. Byrn, M. P.; Curtis, C. J.; Khan, S. I.; Sawin, P. A.; Tsurumi, R.; Strouse, C. E., *J. Am. Chem. Soc.* **1990**, *112*, 1865-74.
188. Dastidar, P.; Goldberg, I., *Acta Crystallogr., Sect. C: Cryst. Struct. Commun.* **1996**, *C52*, 1976-1980.
189. Desiraju, G. R., *Acc. Chem. Res.* **1996**, *29*, 441-449.
190. Musah, R. A.; Jensen, G. M.; Rosenfeld, R. J.; McRee, D. E.; Goodin, D. B.; Bunte, S. W., *J. Am. Chem. Soc.* **1997**, *119*, 9083-9084.
191. Sugiura, K.-i.; Ushiroda, K.; Tanaka, T.; Sawada, M.; Sakata, Y., *Chem. Lett.* **1997**, 927-928.
192. Mingos, D. M. P.; Sherman, D. J., *Adv. Inorg. Chem.* **1989**, *34*, 293-377.
-

-
193. Krejčík, M.; Danek, M.; Hartl, F., *J. Electroanal. Chem. Interfacial Electrochem.* **1991**, *317*, 179-87.
194. Singh, P.; Das, A. K.; Sarkar, B.; Niemeyer, M.; Roncaroli, F.; Olabe, J. A.; Fiedler, J.; Zalis, S.; Kaim, W., *Inorg. Chem.* **2008**, *47*, 7106-7113.
195. Sheldrick, G. M., *Acta Crystallogr., Sect. A: Found. Crystallogr.* **2008**, *64*, 112-122.
196. Van der Sluis, P.; Spek, A., *Acta Crystallogr., Sect. A: Found. Crystallogr.* **1990**, *46*, 194-201.
197. Lee, C.; Yang, W.; Parr, R. G., *Phys. Rev. B: Condens. Matter* **1988**, *37*, 785-9.
198. Fuentealba, P.; Preuss, H.; Stoll, H.; Von Szentpály, L., *Chem. Phys. Lett.* **1982**, *89*, 418-22.
199. Andrae, D.; Haeussermann, U.; Dolg, M.; Stoll, H.; Preuss, H., *Theor. Chim. Acta* **1990**, *77*, 123-41.
200. Frisch, M.; Trucks, G.; Schlegel, H.; Scuseria, G.; Robb, M.; Cheeseman, J.; Zakrzewski, V.; Montgomery Jr, J.; Stratmann, R.; Burant, J., Gaussian 09, Gaussian, Inc., Pittsburgh, PA, 2009;(b) Dalton 2.0 Program Package. In.
201. Bauernschmitt, R.; Ahlrichs, R., *Chem. Phys. Lett.* **1996**, *256*, 454-464.
202. Casida, M. E.; Jamorski, C.; Casida, K. C.; Salahub, D. R., *J. Chem. Phys.* **1998**, *108*, 4439-4449.
203. Stratmann, R. E.; Scuseria, G. E.; Frisch, M. J., *J. Chem. Phys.* **1998**, *109*, 8218-8224.
204. Barone, V.; Cossi, M., *J. Phys. Chem. A* **1998**, *102*, 1995-2001.
205. Cossi, M.; Barone, V., *J. Chem. Phys.* **2001**, *115*, 4708-4717.
-

-
206. Cossi, M.; Rega, N.; Scalmani, G.; Barone, V., *J. Comput. Chem.* **2003**, *24*, 669-681.
207. Leonid, S., Chemissian 1.7; 2005– 2010. In.
208. Zhurko, G.; Zhurko, D., ChemCraft, version 1.6. In Build: 2009.
209. Lee, C.-H.; Lindsey, J. S., *Tetrahedron* **1994**, *50*, 11427-40.
210. Schouten, P. G.; Warman, J. M.; De Haas, M. P.; Fox, M. A.; Pan, H. L., *Nature (London)* **1991**, *353*, 736-7.
211. Schenning, A. P. H. J.; Meijer, E. W., *Chem. Commun.* **2005**, 3245-3258.
212. Patwardhan, S.; Sengupta, S.; Siebbeles, L. D. A.; Wuerthner, F.; Grozema, F. C., *J. Am. Chem. Soc.* **2012**, *134*, 16147-16150.
213. Sengupta, S.; Wuerthner, F., *Acc. Chem. Res.* **2013**, *46*, 2498-2512.
214. Hoshino, M.; Maeda, M.; Konishi, R.; Seki, H.; Ford, P. C., *J. Am. Chem. Soc.* **1996**, *118*, 5702-5707.
215. Gros, C. P.; Barbe, J.-M.; Espinosa, E.; Guillard, R., *Angew. Chem. Int. Ed.* **2006**, *45*, 5642-5645.
216. Gros, C. P.; Brisach, F.; Meristoudi, A.; Espinosa, E.; Guillard, R.; Harvey, P. D., *Inorg. Chem.* **2007**, *46*, 125-135.
217. Kadish, K. M.; Shen, J.; Fremont, L.; Chen, P.; El Ojaimi, M.; Chkounda, M.; Gros, C. P.; Barbe, J.-M.; Ohkubo, K.; Fukuzumi, S.; Guillard, R., *Inorg. Chem.* **2008**, *47*, 6726-6737.
218. Brizet, B.; Desbois, N.; Bonnot, A.; Langlois, A.; Dubois, A.; Barbe, J.-M.; Gros, C. P.; Goze, C.; Denat, F.; Harvey, P. D., *Inorg. Chem.* **2014**, *53*, 3392-3403.
219. Liang, X.; Mack, J.; Zheng, L.-M.; Shen, Z.; Kobayashi, N., *Inorg. Chem.* **2014**, *53*, 2797-2802.
-

-
220. Padilla, R.; Buckley, H. L.; Ward, A. L.; Arnold, J., *Chem. Commun.* **2014**, *50*, 2922-2924.
221. Kadish, K. M.; Ou, Z.; Adamian, V. A.; Guillard, R.; Gros, C. P.; Erben, C.; Will, S.; Vogel, E., *Inorg. Chem.* **2000**, *39*, 5675-5682.
222. Stavitski, E.; Berg, A.; Ganguly, T.; Mahammed, A.; Gross, Z.; Levanon, H., *J. Am. Chem. Soc.* **2004**, *126*, 6886-6890.
223. Ding, T.; Aleman, E. A.; Modarelli, D. A.; Ziegler, C. J., *J. Phys. Chem. A* **2005**, *109*, 7411-7417.
224. Ventura, B.; Degli Esposti, A.; Koszarna, B.; Gryko, D. T.; Flamigni, L., *New J. Chem.* **2005**, *29*, 1559-1566.
225. Gao, Y.; Liu, J.; Jiang, W.; Xia, M.; Zhang, W.; Li, M.; Akermark, B.; Sun, L., *J. Porphyrins Phthalocyanines* **2007**, *11*, 463-469.
226. Koszarna, B.; Gryko, D. T., *Chem. Commun.* **2007**, 2994-2996.
227. Nardis, S.; Mandoj, F.; Paolesse, R.; Fronczek, F. R.; Smith, K. M.; Prodi, L.; Montalti, M.; Battistini, G., *Eur. J. Inorg. Chem.* **2007**, 2345-2352.
228. D'Souza, F.; Chitta, R.; Ohkubo, K.; Tasior, M.; Subbaiyan, N. K.; Zandler, M. E.; Rogacki, M. K.; Gryko, D. T.; Fukuzumi, S., *J. Am. Chem. Soc.* **2008**, *130*, 14263-14272.
229. Cho, S.; Lim, J. M.; Hiroto, S.; Kim, P.; Shinokubo, H.; Osuka, A.; Kim, D., *J. Am. Chem. Soc.* **2009**, *131*, 6412-6420.
230. Flamigni, L.; Gryko, D. T., *Chem. Soc. Rev.* **2009**, *38*, 1635-1646.
231. Maeda, D.; Shimakoshi, H.; Abe, M.; Hisaeda, Y., *Inorg. Chem.* **2009**, *48*, 9853-9860.
-

-
232. Palmer, J. H.; Brock-Nannestad, T.; Mahammed, A.; Durrell, A. C.; Vander Velde, D.; Virgil, S.; Gross, Z.; Gray, H. B., *Angew. Chem. Int. Ed.* **2011**, *50*, 9433-9436, S9433/1-S9433/11.
233. Rabinovich, E.; Goldberg, I.; Gross, Z., *Chem. Eur. J.* **2011**, *17*, 12294-12301, S12294/1-S12294/8.
234. Ngo, T. H.; Nastasi, F.; Puntoriero, F.; Campagna, S.; Dehaen, W.; Maes, W., *Eur. J. Inorg. Chem.* **2012**, *2012*, 5605-5617, S5605/1-S5605/11.
235. Santos, C. I. M.; Oliveira, E.; Barata, J. F. B.; Faustino, M. A. F.; Cavaleiro, J. A. S.; Neves, M. G. P. M. S.; Lodeiro, C., *J. Mater. Chem.* **2012**, *22*, 13811-13819.
236. Peuntinger, K.; Lazarides, T.; Dafnomili, D.; Charalambidis, G.; Landrou, G.; Kahnt, A.; Sabatini, R. P.; McCamant, D. W.; Gryko, D. T.; Coutsolelos, A. G.; Guldi, D. M., *J. Phys. Chem. C* **2013**, *117*, 1647-1655.
237. Pomarico, G.; Nardis, S.; Stefanelli, M.; Cicero, D. O.; Vicente, M. G. H.; Fang, Y.; Chen, P.; Kadish, K. M.; Paolesse, R., *Inorg. Chem.* **2013**, *52*, 8834-8844.
238. Wagnert, L.; Rubin, R.; Berg, A.; Mahammed, A.; Gross, Z.; Levanon, H., *J. Phys. Chem. B* **2010**, *114*, 14303-14308.
239. Collins, D. M.; Scheidt, W. R.; Hoard, J. L., *J. Am. Chem. Soc.* **1972**, *94*, 6689-96.
240. Chandrasekaran, K.; Whitten, D. G., *J. Am. Chem. Soc.* **1980**, *102*, 5119-20.
241. Rodriguez, J.; Kirmaier, C.; Holten, D., *J. Am. Chem. Soc.* **1989**, *111*, 6500-6.
242. Wang, Z.; Li, Z.; Medforth, C. J.; Shelnutt, J. A., *J. Am. Chem. Soc.* **2007**, *129*, 2440-2441.
-

-
243. Lang, T.; Guenet, A.; Graf, E.; Kyritsakas, N.; Hosseini, M. W., *Chem. Commun.* **2010**, *46*, 3508-3510.
244. Martin, K. E.; Wang, Z.; Busani, T.; Garcia, R. M.; Chen, Z.; Jiang, Y.; Song, Y.; Jacobsen, J. L.; Vu, T. T.; Schore, N. E.; Swartzentruber, B. S.; Medforth, C. J.; Shelnut, J. A., *J. Am. Chem. Soc.* **2010**, *132*, 8194-8201.
245. Shultz, A. M.; Farha, O. K.; Adhikari, D.; Sarjeant, A. A.; Hupp, J. T.; Nguyen, S. T., *Inorg. Chem.* **2011**, *50*, 3174-3176.
246. Tian, Y.; Martin, K. E.; Shelnut, J. Y. T.; Evans, L.; Busani, T.; Miller, J. E.; Medforth, C. J.; Shelnut, J. A., *Chem. Commun.* **2011**, *47*, 6069-6071.
247. Lazarides, T.; Kuhri, S.; Charalambidis, G.; Panda, M. K.; Guldi, D. M.; Coutsolelos, A. G., *Inorg. Chem.* **2012**, *51*, 4193-4204.
248. Oppelt, K. T.; Woess, E.; Stifinger, M.; Schoefberger, W.; Buchberger, W.; Knoer, G., *Inorg. Chem.* **2013**, *52*, 11910-11922.
249. Guenet, A.; Graf, E.; Kyritsakas, N.; Hosseini, M. W., *Inorg. Chem.* **2010**, *49*, 1872-1883.
250. Kadish, K. M.; Will, S.; Adamian, V. A.; Walther, B.; Erben, C.; Ou, Z.; Guo, N.; Vogel, E., *Inorg. Chem.* **1998**, *37*, 4573-4577.
251. Saltsman, I.; Mahammed, A.; Goldberg, I.; Tkachenko, E.; Botoshansky, M.; Gross, Z., *J. Am. Chem. Soc.* **2002**, *124*, 7411-7420.
252. Wagnert, L.; Berg, A.; Stavitski, E.; Berthold, T.; Kothe, G.; Goldberg, I.; Mahammed, A.; Simkhovich, L.; Gross, Z.; Levanon, H., *Appl. Magn. Reson.* **2006**, *30*, 591-604.
253. Rozenshtein, V.; Wagnert, L.; Berg, A.; Stavitski, E.; Berthold, T.; Kothe, G.; Saltsman, I.; Gross, Z.; Levanon, H., *J. Phys. Chem. A* **2008**, *112*, 5338-5343.
-

-
254. Pomarico, G.; Nardis, S.; Paolesse, R.; Ongayi, O. C.; Courtney, B. H.; Fronczek, F. R.; Vicente, M. G. H., *J. Org. Chem.* **2011**, *76*, 3765-3773.
255. Tsay, O. G.; Kim, B.-K.; Luu, T. L.; Kwak, J.; Churchill, D. G., *Inorg. Chem.* **2013**, *52*, 1991-1999.
256. Bale, D. S.; Szeles, C., *Phys. Rev. B* **2008**, *77*, 035205.
257. Yu, X.; Li, C.; Low, Z. N.; Lin, J.; Anderson, T. J.; Wang, H. T.; Ren, F.; Wang, Y. L.; Chang, C. Y.; Pearton, S. J.; Hsu, C. H.; Osinsky, A.; Dabiran, A.; Chow, P.; Balaban, C.; Painter, J., *Sens. Actuators, B* **2008**, *135*, 188-194.
258. Ohgo, Y.; Neya, S.; Ikeue, T.; Takahashi, M.; Takeda, M.; Funasaki, N.; Nakamura, M., *Inorg. Chem.* **2002**, *41*, 4627-4629.
259. Aakeroy, C. B.; Evans, T. A.; Seddon, K. R.; Palinko, I., *New J. Chem.* **1999**, *23*, 145-152.
260. Nangia, A., *CrystEngComm* **2002**, *4*, 93-101.
261. Balamurugan, V.; Jacob, W.; Mukherjee, J.; Mukherjee, R., *CrystEngComm* **2004**, *6*, 396-400.
262. Balamurugan, V.; Hundal, M. S.; Mukherjee, R., *Chem. Eur. J.* **2004**, *10*, 1683-1690.
263. Srinivasarao, M.; Collings, D.; Philips, A.; Patel, S., *Science* **2001**, *292*, 79-83.
264. Gao, Y.; Zhang, X.; Ma, C.; Li, X.; Jiang, J., *J. Am. Chem. Soc.* **2008**, *130*, 17044-17052.
265. Lee, S. J.; Hupp, J. T.; Nguyen, S. T., *J. Am. Chem. Soc.* **2008**, *130*, 9632-9633.
266. Sinha, W.; Deibel, N.; Garai, A.; Schweinfurth, D.; Anwar, S.; Purohit, C. S.; Sarkar, B.; Kar, S., *Dyes Pigm.* **2014**, *107*, 29-37.
-

-
267. Schwab, A. D.; Smith, D. E.; Bond-Watts, B.; Johnston, D. E.; Hone, J.; Johnson, A. T.; De Paula, J. C.; Smith, W. F., *Nano Lett.* **2004**, *4*, 1261-1265.
268. Hsu, F.-C.; Prigodin, V. N.; Epstein, A. J., *Phys. Rev. B* **2006**, *74*, 235219.
269. Friesen, B. A.; Wiggins, B.; McHale, J. L.; Mazur, U.; Hipps, K. W., *J. Am. Chem. Soc.* **2010**, *132*, 8554-8556.
270. Spek, A., *J. Appl. Crystallogr.* **2003**, *36*, 7-13.
271. Sinha, W.; Deibel, N.; Agarwala, H.; Garai, A.; Schweinfurth, D.; Purohit, C. S.; Lahiri, G. K.; Sarkar, B.; Kar, S., *Inorg. Chem.* **2014**, *53*, 1417-1429.
272. Sinha, W.; Sommer, M. G.; Deibel, N.; Ehret, F.; Sarkar, B.; Kar, S., *Chem. Eur. J.* **2014**, *20*, 15920-15932.
273. Kadish, K. M.; Burdet, F.; Jerome, F.; Barbe, J.-M.; Ou, Z.; Shao, J.; Guillard, R., *J. Organomet. Chem.* **2002**, *652*, 69-76.
274. Abu-Omar, M. M., *Dalton Trans.* **2011**, *40*, 3435-3444.
275. Nardis, S.; Cicero, D. O.; Licoccia, S.; Pomarico, G.; Berionni Berna, B.; Sette, M.; Ricciardi, G.; Rosa, A.; Fronczek, F. R.; Smith, K. M.; Paollesse, R., *Inorg. Chem.* **2014**, *53*, 4215-4227.
276. Kadish, K. M.; Fremond, L.; Shen, J.; Chen, P.; Ohkubo, K.; Fukuzumi, S.; El Ojaimi, M.; Gros, C. P.; Barbe, J.-M.; Guillard, R., *Inorg. Chem.* **2009**, *48*, 2571-2582.
277. Ou, Z.; Shao, J.; Zhao, H.; Ohkubo, K.; Wasbotten, I. H.; Fukuzumi, S.; Ghosh, A.; Kadish, K. M., *J. Porphyrins Phthalocyanines* **2004**, *8*, 1236-1247.
278. Chen, P.; El Ojaimi, M.; Gros, C. P.; Barbe, J.-M.; Guillard, R.; Shen, J.; Kadish, K. M., *J. Porphyrins Phthalocyanines* **2011**, *15*, 188-196.
279. Guillard, R.; Burdet, F.; Barbe, J.-M.; Gros, C. P.; Espinosa, E.; Shao, J.; Ou, Z.; Zhan, R.; Kadish, K. M., *Inorg. Chem.* **2005**, *44*, 3972-3983.
-

-
280. Ciuciu, A. I.; Flamigni, L.; Voloshchuk, R.; Gryko, D. T., *Chem. Asian J.* **2013**, *8*, 1004-1014.
281. Flamigni, L.; Ciuciu, A. I.; Langhals, H.; Boeck, B.; Gryko, D. T., *Chem. Asian J.* **2012**, *7*, 582-592.
282. Gisk, B.; Bregier, F.; Krueger, R. A.; Broering, M.; Frankenberg-Dinkel, N., *Biochemistry* **2010**, *49*, 10042-10044.
283. Kuck, S.; Hoffmann, G.; Broering, M.; Fichtel, M.; Funk, M.; Wiesendanger, R., *J. Am. Chem. Soc.* **2008**, *130*, 14072-14073.
284. Alemayehu, A.; Conradie, J.; Ghosh, A., *Eur. J. Inorg. Chem.* **2011**, 1857-1864.
285. Thomas, K. E.; Alemayehu, A. B.; Conradie, J.; Beavers, C. M.; Ghosh, A., *Acc. Chem. Res.* **2012**, *45*, 1203-1214.
286. Zhao, H.; Pierloot, K.; Langner, E. H. G.; Swarts, J. C.; Conradie, J.; Ghosh, A., *Inorg. Chem.* **2012**, *51*, 4002-4006.
287. Liu, H.-Y.; Fei, Y.; Xie, Y.-T.; Li, X.-Y.; Chang, C. K., *J. Am. Chem. Soc.* **2009**, *131*, 12890-12891.
288. Paolesse, R.; Nardis, S.; Venanzi, M.; Mastroianni, M.; Russo, M.; Fronczek, F. R.; Vicente, M. G. H., *Chem. Eur. J.* **2003**, *9*, 1192-1197.
289. Santos, C. I. M.; Oliveira, E.; Fernandez-Lodeiro, J.; Barata, J. F. B.; Santos, S. M.; Faustino, M. A. F.; Cavaleiro, J. A. S.; Neves, M. G. P. M. S.; Lodeiro, C., *Inorg. Chem.* **2013**, *52*, 8564-8572.
290. Blumenfeld, C. M.; Grubbs, R. H.; Moats, R. A.; Gray, H. B.; Sorasaene, K., *Inorg. Chem.* **2013**, *52*, 4774-4776.
291. Palmer, J. H.; Durrell, A. C.; Gross, Z.; Winkler, J. R.; Gray, H. B., *J. Am. Chem. Soc.* **2010**, *132*, 9230-9231.
-

-
292. Paolesse, R., *Synlett* **2008**, 2215-2230.
293. El Ojaimi, M.; Gros, C. P.; Barbe, J.-M., *Eur. J. Inorg. Chem.* **2008**, 1181-1186.
294. Mahammed, A.; Botoshansky, M.; Gross, Z., *Dalton Trans.* **2012**, *41*, 10938-10940.
295. Mahammed, A.; Mondal, B.; Rana, A.; Dey, A.; Gross, Z., *Chem. Commun.* **2014**, *50*, 2725-2727.
296. Nigel-Etinger, I.; Goldberg, I.; Gross, Z., *Inorg. Chem.* **2012**, *51*, 1983-1985.
297. Leeladee, P.; Jameson, G. N. L.; Siegler, M. A.; Kumar, D.; de Visser, S. P.; Goldberg, D. P., *Inorg. Chem.* **2013**, *52*, 4668-4682.
298. McGown, A. J.; Kerber, W. D.; Fujii, H.; Goldberg, D. P., *J. Am. Chem. Soc.* **2009**, *131*, 8040-8048.
299. Mandoj, F.; Nardis, S.; Pomarico, G.; Paolesse, R., *J. Porphyrins Phthalocyanines* **2008**, *12*, 19-26.
300. Murakami, K.; Yamamoto, Y.; Yorimitsu, H.; Osuka, A., *Chem. Eur. J.* **2013**, *19*, 9123-9126.
301. Yun, L.; Vazquez-Lima, H.; Fang, H.; Yao, Z.; Geisberger, G.; Dietl, C.; Ghosh, A.; Brothers, P. J.; Fu, X., *Inorg. Chem.* **2014**, *53*, 7047-7054.
302. Sinha, W.; Kumar, M.; Garai, A.; Purohit, C. S.; Som, T.; Kar, S., *Dalton Trans.* **2014**, *43*, 12564-12573.
303. Kuhlbrandt, W.; Wang, D. N.; Fujiyoshi, Y., *Nature* **1994**, *367*, 614-21.
304. Czernuszewicz, R. S.; Mody, V.; Czader, A.; Galezowski, M.; Gryko, D. T., *J. Am. Chem. Soc.* **2009**, *131*, 14214-14215.
305. Mahammed, A.; Tumanskii, B.; Gross, Z., *J. Porphyrins Phthalocyanines* **2011**, *15*, 1275-1286.
-

-
306. Kadish, K. M.; Adamian, V. A.; Van Caemelbecke, E.; Gueletii, E.; Will, S.; Erben, C.; Vogel, E., *J. Am. Chem. Soc.* **1998**, *120*, 11986-11993.
307. Zdilla, M. J.; Abu-Omar, M. M., *Inorg. Chem.* **2008**, *47*, 10718-10722.
308. Paolesse, R.; Nardis, S.; Stefanelli, M.; Fronczek, F. R.; Vicente, M. G. H., *Angew. Chem. Int. Ed.* **2005**, *44*, 3047-3050.
309. Stefanelli, M.; Pomarico, G.; Tortora, L.; Nardis, S.; Fronczek, F. R.; McCandless, G. T.; Smith, K. M.; Manowong, M.; Chen, P.; Kadish, K. M.; Rosa, A.; Ricciardi, G.; Paolesse, R., *Inorg. Chem.* **2012**, *51*, 6928-6942.
310. Bruckner, C., *J. Chem. Educ.* **2004**, *81*, 1665-1669.
311. Pacholska, E.; Espinosa, E.; Guillard, R., *Dalton Trans.* **2004**, 3181-3183.
312. Stefanelli, M.; Mastroianni, M.; Nardis, S.; Licoccia, S.; Fronczek, F. R.; Smith, K. M.; Zhu, W.; Ou, Z.; Kadish, K. M.; Paolesse, R., *Inorg. Chem.* **2007**, *46*, 10791-10799.
313. Stefanelli, M.; Shen, J.; Zhu, W.; Mastroianni, M.; Mandoj, F.; Nardis, S.; Ou, Z.; Kadish, K. M.; Fronczek, F. R.; Smith, K. M.; Paolesse, R., *Inorg. Chem.* **2009**, *48*, 6879-6887.
314. Ngo, T. H.; Puntoriero, F.; Nastasi, F.; Robeyns, K.; Van Meervelt, L.; Campagna, S.; Dehaen, W.; Maes, W., *Chem. Eur. J.* **2010**, *16*, 5691-5705, S5691/1-S5691/27.
315. Johansen, I.; Norheim, H.-K.; Larsen, S.; Alemayehu, A. B.; Conradie, J.; Ghosh, A., *J. Porphyrins Phthalocyanines* **2011**, *15*, 1335-1344.
316. Brown, T. G.; Petersen, J. L.; Lozos, G. P.; Anderson, J. R.; Hoffman, B. M., *Inorg. Chem.* **1977**, *16*, 1563-5.
317. Scheidt, W. R.; Mondal, J. U.; Eigenbrot, C. W.; Adler, A.; Radonovich, L. J.; Hoard, J. L., *Inorg. Chem.* **1986**, *25*, 795-9.
-

-
318. Xu, Y.-J.; Yang, X.-X.; Cao, H.; Zhao, H.-B., *Acta Crystallogr., Sect. E: Struct. Rep. Online* **2007**, *63*, m1437-m1437.
319. So, M.-H.; Roy, V. A. L.; Xu, Z.-X.; Chui, S. S.-Y.; Yuen, M.-Y.; Ho, C.-M.; Che, C.-M., *Chem. Asian J.* **2008**, *3*, 1968-1978.
320. Jordan, P.; Fromme, P.; Witt, H. T.; Klukas, O.; Saenger, W.; Krauss, N., *Nature* **2001**, *411*, 909-17.
321. Ferreira, K. N.; Iverson, T. M.; Maghlaoui, K.; Barber, J.; Iwata, S., *Science (Washington, DC, U. S.)* **2004**, *303*, 1831-1838.
322. Liu, Z.; Yan, H.; Wang, K.; Kuang, T.; Zhang, J.; Gui, L.; An, X.; Chang, W., *Nature (London, U. K.)* **2004**, *428*, 287-292.
323. Loll, B.; Kern, J.; Saenger, W.; Zouni, A.; Biesiadka, J., *Nature (London, U. K.)* **2005**, *438*, 1040-1044.
324. Pascal, A. A.; Liu, Z.; Broess, K.; van Oort, B.; van Amerongen, H.; Wang, C.; Horton, P.; Robert, B.; Chang, W.; Ruban, A., *Nature (London, U. K.)* **2005**, *436*, 134-137.
325. Amunts, A.; Drory, O.; Nelson, N., *Nature (London, U. K.)* **2007**, *447*, 58-63.
326. Scheidt, W. R.; Brancato-Buentello, K. E.; Song, H.; Reddy, K. V.; Cheng, B., *Inorg. Chem.* **1996**, *35*, 7500-7507.
327. Neese, F., *Wiley Interdiscip. Rev.: Comput. Mol. Sci.* **2012**, *2*, 73-78.
328. Becke, A. D., *Phys. Rev. A: Gen. Phys.* **1988**, *38*, 3098-100.
329. Becke, A. D., *J. Chem. Phys.* **1993**, *98*, 5648-52.
330. Grimme, S.; Antony, J.; Ehrlich, S.; Krieg, H., *J. Chem. Phys.* **2010**, *132*, 154104.
331. van Wullen, C., *J. Chem. Phys.* **1998**, *109*, 392-399.
-

-
332. Pantazis, D. A.; Chen, X.-Y.; Landis, C. R.; Neese, F., *J. Chem. Theory Comput.* **2008**, *4*, 908-919.
333. Whitten, J. L., *J. Chem. Phys.* **1973**, *58*, 4496-501.
334. Vahtras, O.; Almlöf, J.; Feyereisen, M. W., *Chem. Phys. Lett.* **1993**, *213*, 514-18.
335. Neese, F., *J. Comput. Chem.* **2003**, *24*, 1740-1747.
336. Neese, F.; Wennmohs, F.; Hansen, A.; Becker, U., *Chem. Phys.* **2009**, *356*, 98-109.
337. Klamt, A.; Schueuermann, G., *J. Chem. Soc., Perkin Trans. 2* **1993**, 799-805.
338. Sinnecker, S.; Rajendran, A.; Klamt, A.; Diedenhofen, M.; Neese, F., *J. Phys. Chem. A* **2006**, *110*, 2235-2245.
339. Lowdin, P. O., *J. Chem. Phys.* **1950**, *18*, 365-75.
340. Delgado-Jaime, M. U.; DeBeer, S., *J. Comput. Chem.* **2012**, *33*, 2180-2185.
341. Portmann, S., *CSCS/UNI Geneva: Geneva, Switzerland* **2009**.
342. Vigmond, S. J.; Chang, M. C.; Kallury, K. M. R.; Thompson, M., *Tetrahedron Lett.* **1994**, *35*, 2455-8.
343. Jørgensen, C. K.; Jørgensen, C. K., *Oxidation numbers and oxidation states*. Springer Berlin-Heidelberg-New York: 1969.
344. Barnett, S. M.; Goldberg, K. I.; Mayer, J. M., *Nat. Chem.* **2012**, *4*, 498-502.
345. Ribas, X.; Casitas, A.; Pignataro, B., *Ideas in Chemistry and Molecular Sciences: Where Chemistry Meets Life*. Wiley-VCH Weinheim, Germany: 2010.
346. Ene, A. B.; Bauer, M.; Archipov, T.; Roduner, E., *Phys. Chem. Chem. Phys.* **2010**, *12*, 6531.
-

-
347. DuBois, J. L.; Mukherjee, P.; Collier, A. M.; Mayer, J. M.; Solomon, E. I.; Hedman, B.; Stack, T.; Hodgson, K. O., *J. Am. Chem. Soc.* **1997**, *119*, 8578-8579.
348. Stoll, S.; Schweiger, A., *J. Magn. Reson.* **2006**, *178*, 42-55.
349. Wasbotten, I. H.; Wondimagegn, T.; Ghosh, A., *J. Am. Chem. Soc.* **2002**, *124*, 8104-8116.
350. Alemayehu, A. B.; Gonzalez, E.; Hansen, L. K.; Ghosh, A., *Inorg. Chem.* **2009**, *48*, 7794-7799.
351. Bröring, M.; Bregier, F.; Cónsul Tejero, E.; Hell, C.; Holthausen, M. C., *Angew. Chem. Int. Ed.* **2007**, *46*, 445-448.
352. Lyaskovskyy, V.; de Bruin, B., *ACS Catal.* **2012**, *2*, 270-279.
353. Kundu, S.; Miceli, E.; Farquhar, E.; Pfaff, F. F.; Kuhlmann, U.; Hildebrandt, P.; Braun, B.; Greco, C.; Ray, K., *J. Am. Chem. Soc.* **2012**, *134*, 14710-14713.
354. Comba, P.; Knoppe, S.; Martin, B.; Rajaraman, G.; Rolli, C.; Shapiro, B.; Stork, T., *Chem. Eur. J.* **2008**, *14*, 344-357.
355. Alesi, S.; Brancolini, G.; Melucci, M.; Capobianco, M. L.; Venturini, A.; Camaioni, N.; Barbarella, G., *Chem. Eur. J.* **2008**, *14*, 513-521.
356. Reinaud, O.; Capdevielle, P.; Maumy, M., *J. Chem. Soc., Chem. Commun.* **1990**, 566-568.
357. Caulton, K. G., *Eur. J. Inorg. Chem.* **2012**, *2012*, 435-443.
358. Kaim, W., *Inorg. Chem.* **2011**, *50*, 9752-9765.
359. Eisenberg, R.; Gray, H. B., *Inorg. Chem.* **2011**, *50*, 9741-9751.
360. Chirik, P. J., *Inorg. Chem.* **2011**, *50*, 9737-9740.
361. Grützmacher, H., *Angew. Chem. Int. Ed.* **2008**, *47*, 1814-1818.
362. Gunanathan, C.; Milstein, D., *Acc. Chem. Res.* **2011**, *44*, 588-602.
-

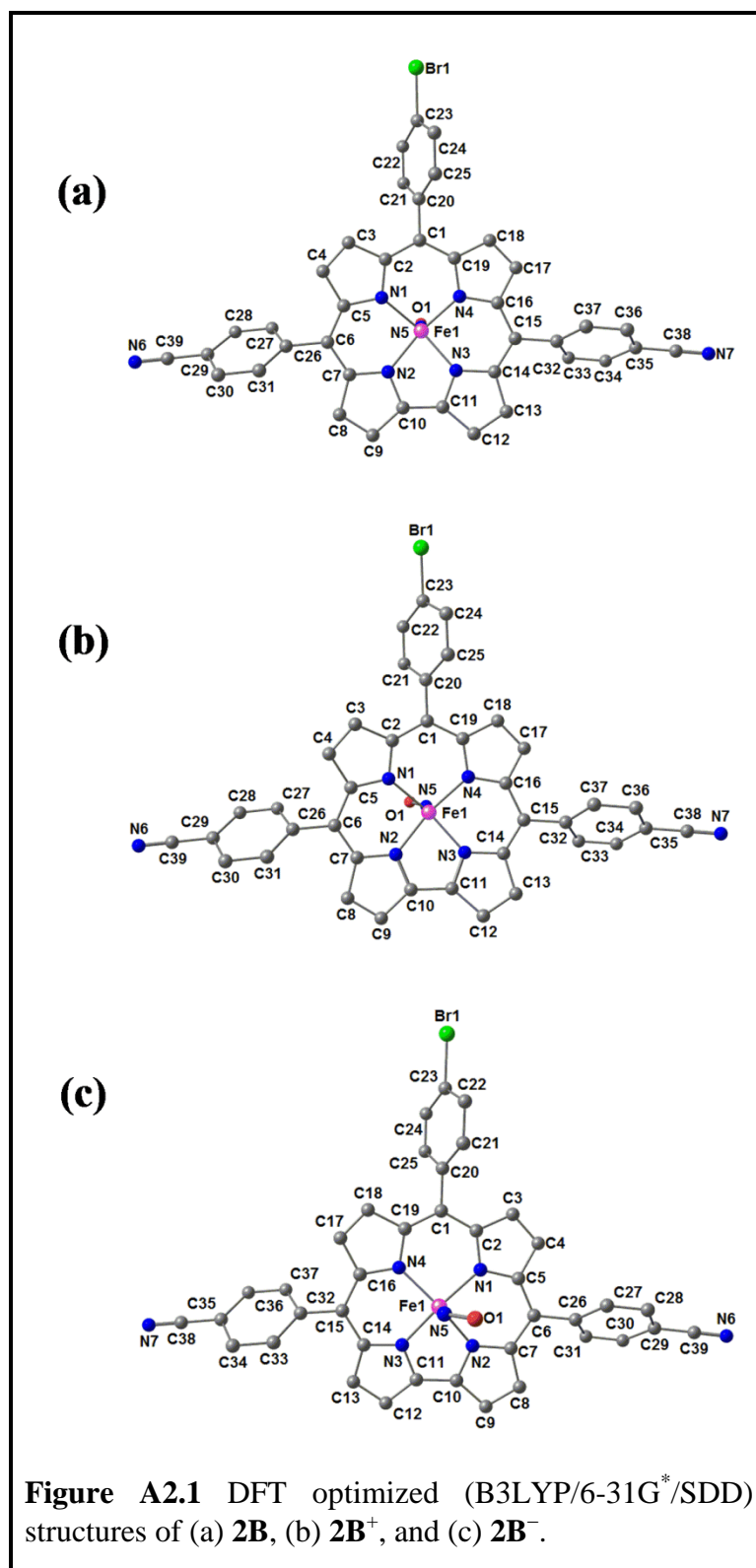
363. Perdew, J. P., *Phys. Rev. B: Condens. Matter* **1986**, 33, 8822-8824.
364. Handy, N. C.; Cohen, A. J., *Mol. Phys.* **2001**, 99, 403-412.
365. Weigend, F.; Ahlrichs, R., *Phys. Chem. Chem. Phys.* **2005**, 7, 3297-3305.

Appendix

Table A2.1 Selected X-ray and DFT Calculated (B3LYP/6-31G*/SDD) Bond Distances (Å) and Angles (deg) for **2Bⁿ** ($n = 1+, 0, 1-$)

	2B (X-ray)	2B (DFT) ($S=0$)	2B⁺ (DFT) ($S=1/2$)	2B⁻ (DFT) ($S=1/2$)
Fe(1)-N(1)	1.919(3)	1.927	1.931	1.934
Fe(1)-N(2)	1.895(2)	1.902	1.918	1.911
Fe(1)-N(3)	1.889(3)	1.901	1.918	1.923
Fe(1)-N(4)	1.939(3)	1.932	1.970	1.962
Fe(1)-N(5)	1.650(3)	1.597	1.764	1.837
N(5)-O(1)	1.162(3)	1.162	1.174	1.196
N(1)-C(2)	1.389(4)	1.387	1.380	1.377
N(1)-C(5)	1.385(4)	1.387	1.371	1.386
N(2)-C(7)	1.386(4)	1.380	1.381	1.364
N(2)-C(10)	1.357(5)	1.366	1.344	1.372
N(3)-C(11)	1.357(4)	1.364	1.340	1.369
N(3)-C(14)	1.386(4)	1.377	1.380	1.361
N(4)-C(16)	1.383(4)	1.390	1.369	1.386
N(4)-C(19)	1.379(5)	1.390	1.380	1.376
C(1)-C(2)	1.404(4)	1.407	1.424	1.414
C(2)-C(3)	1.428(5)	1.434	1.430	1.440
C(3)-C(4)	1.354(5)	1.367	1.377	1.369
C(4)-C(5)	1.431(5)	1.436	1.428	1.441
C(5)-C(6)	1.423(5)	1.419	1.457	1.419
C(6)-C(7)	1.383(5)	1.397	1.390	1.418
C(7)-C(8)	1.437(5)	1.438	1.449	1.439
C(8)-C(9)	1.367(5)	1.381	1.378	1.388
C(9)-C(10)	1.428(5)	1.427	1.432	1.422
C(10)-C(11)	1.421(5)	1.415	1.456	1.420
C(11)-C(12)	1.428(5)	1.427	1.433	1.425
C(12)-C(13)	1.372(5)	1.381	1.377	1.386
C(13)-C(14)	1.433(5)	1.438	1.447	1.441
C(14)-C(15)	1.389(5)	1.398	1.393	1.418

C(15)-C(16)	1.414(5)	1.418	1.454	1.419
C(16)-C(17)	1.431(5)	1.436	1.431	1.441
C(17)-C(18)	1.352(6)	1.367	1.376	1.369
C(18)-C(19)	1.433(4)	1.434	1.431	1.440
C(19)-C(1)	1.398(5)	1.405	1.423	1.415
O(1)-N(5)-Fe(1)	171.70(3)	179.94	147.89	135.56
N(1)-Fe(1)-N(2)	87.91(11)	87.72	88.99	89.12
N(1)-Fe(1)-N(3)	152.50(12)	153.99	158.20	159.22
N(1)-Fe(1)-N(4)	92.32(11)	93.10	93.73	93.92
N(1)-Fe(1)-N(5)	105.45(13)	101.80	96.81	95.89
N(2)-Fe(1)-N(3)	79.06(12)	79.45	79.61	80.29
N(2)-Fe(1)-N(4)	150.94(11)	150.93	151.96	154.21
N(2)-Fe(1)-N(5)	101.25(13)	105.20	103.38	101.01
N(3)-Fe(1)-N(4)	87.82(12)	87.59	88.04	88.25
N(3)-Fe(1)-N(5)	100.81(14)	103.36	103.84	103.62
N(4)-Fe(1)-N(5)	106.66(12)	103.07	103.99	104.12



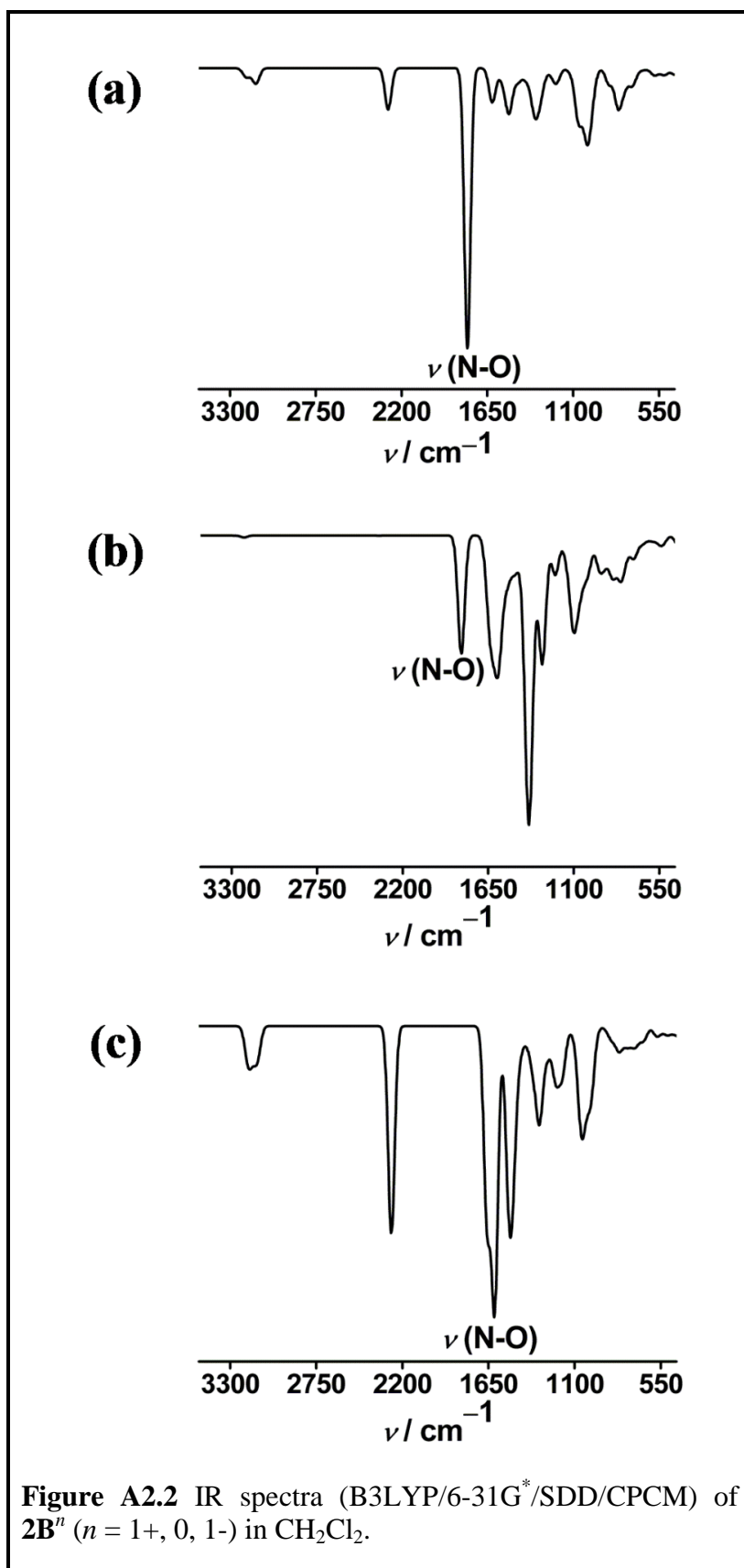


Table A2.2 Composition and Energies of Selected Molecular Orbitals of **2B** ($S=0$)

MO	energy (eV)	composition		
		Fe	NO	cor
HOMO-14	-7.939	0.02	0.01	0.97
HOMO-13	-7.814	0.66	0.02	0.33
HOMO-12	-7.775	0.22	0.04	0.74
HOMO-11	-7.743	0.11	0.02	0.87
HOMO-10	-7.710	0.01	0.00	0.99
HOMO-9	-7.591	0.02	0.01	0.97
HOMO-8	-7.526	0.00	0.00	0.99
HOMO-7	-7.389	0.01	0.00	0.98
HOMO-6	-7.267	0.01	0.01	0.98
HOMO-5	-6.987	0.01	0.01	0.98
HOMO-4	-6.834	0.01	0.00	0.99
HOMO-3	-6.652	0.17	0.13	0.70
HOMO-2	-6.579	0.17	0.12	0.72
HOMO-1	-5.462	0.23	0.04	0.72
HOMO	-5.351	0.01	0.01	0.99
LUMO	-3.277	0.40	0.23	0.38
LUMO+1	-2.691	0.26	0.61	0.13
LUMO+2	-2.500	0.33	0.50	0.17
LUMO+3	-2.354	0.03	0.02	0.95
LUMO+4	-1.932	0.02	0.00	0.98
LUMO+5	-1.381	0.01	0.00	0.99
LUMO+6	-1.37	0.01	0.00	0.99
LUMO+7	-0.884	0.03	0.00	0.97
LUMO+8	-0.863	0.15	0.00	0.85
LUMO+9	-0.855	0.34	0.00	0.66
LUMO+10	-0.697	0.00	0.00	1.00

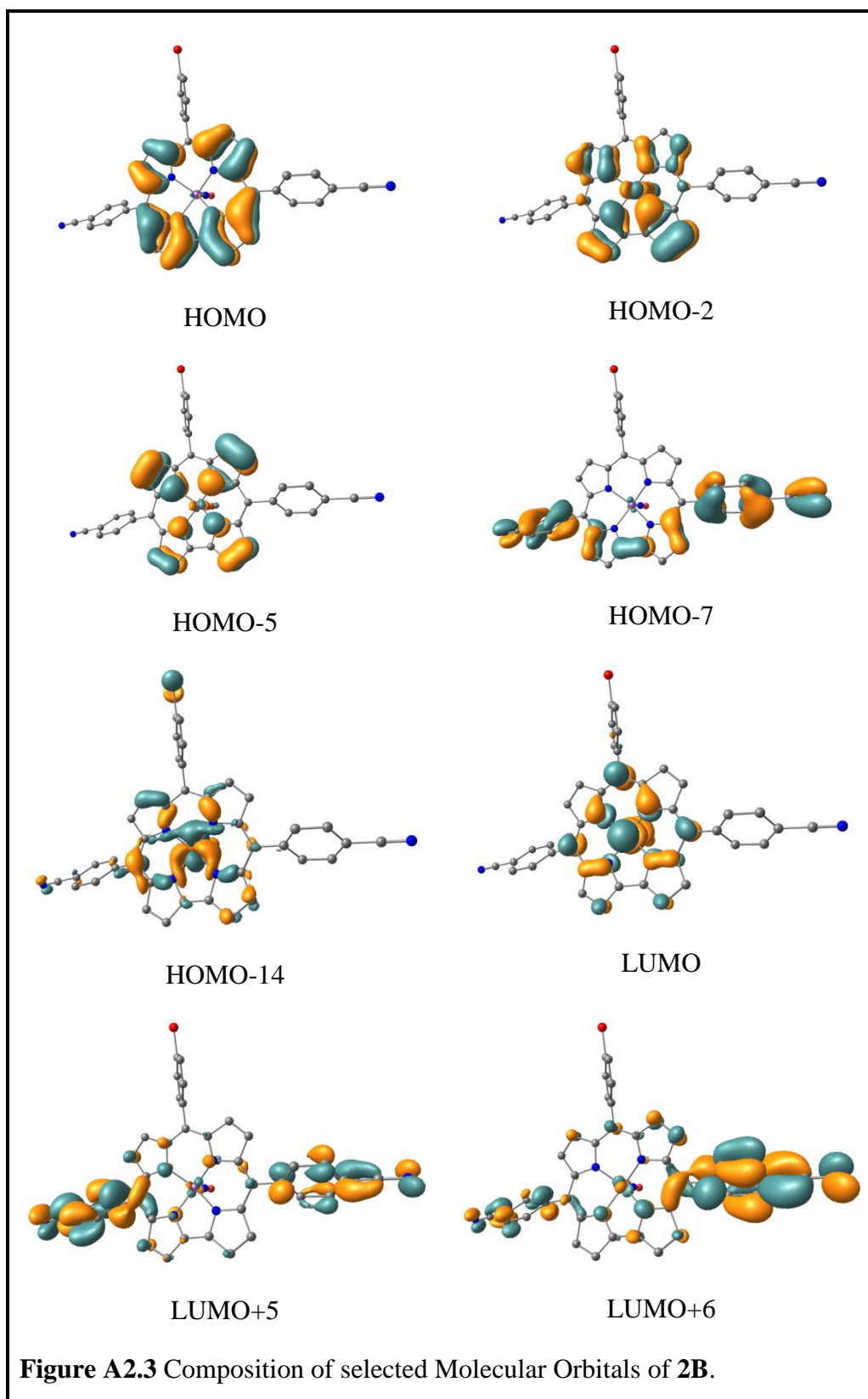


Table A2.3 Composition and Energies of Selected Molecular Orbitals of **2B⁺**
($S=1/2$)

MO	Energy (eV)	Composition		
		Fe	NO	cor
α -spin				
HOMO-12	-10.742	0.02	0.00	0.98
HOMO-11	-10.152	0.01	0.00	0.99
HOMO-10	-10.097	0.01	0.00	0.99
HOMO-9	-10.062	0.00	0.00	1.00
HOMO-8	-10.055	0.01	0.00	0.99
HOMO-7	-9.948	0.12	0.02	0.86
HOMO-6	-9.900	0.05	0.01	0.94
HOMO-5	-9.876	0.12	0.02	0.86
HOMO-4	-9.780	0.03	0.01	0.96
HOMO-3	-9.618	0.01	0.00	0.98
HOMO-2	-9.241	0.11	0.03	0.86
HOMO-1	-9.051	0.24	0.07	0.69
SOMO	-8.599	0.04	0.01	0.95
LUMO	-6.914	0.22	0.07	0.71
LUMO+1	-5.558	0.01	0.00	0.99
LUMO+2	-5.132	0.10	0.28	0.62
LUMO+3	-5.121	0.10	0.53	0.37
LUMO+4	-5.084	0.16	0.70	0.15
LUMO+5	-4.518	0.47	0.00	0.53
LUMO+6	-3.938	0.01	0.00	0.99
LUMO+7	-3.919	0.00	0.00	1.00
LUMO+8	-3.298	0.03	0.00	0.97
LUMO+9	-3.276	0.04	0.00	0.96
LUMO+10	-3.237	0.01	0.00	0.99
β -spin				
HOMO-10	-10.143	0.01	0.01	0.99
HOMO-9	-10.089	0.00	0.01	0.99

HOMO-8	-10.060	0.00	0.00	1.00
HOMO-7	-10.046	0.01	0.01	0.98
HOMO-6	-9.905	0.00	0.01	0.99
HOMO-5	-9.762	0.02	0.02	0.96
HOMO-4	-9.689	0.12	0.21	0.67
HOMO-3	-9.634	0.13	0.21	0.67
HOMO-2	-9.544	0.08	0.14	0.78
HOMO-1	-9.159	0.00	0.00	1.00
HOMO	-8.523	0.01	0.01	0.98
LUMO	-7.536	0.04	0.01	0.96
LUMO+1	-5.486	0.03	0.06	0.91
LUMO+2	-5.283	0.2	0.25	0.55
LUMO+3	-4.973	0.4	0.4	0.2
LUMO+4	-4.905	0.42	0.33	0.26
LUMO+5	-4.775	0.4	0.08	0.52
LUMO+6	-3.913	0.01	0	0.99
LUMO+7	-3.883	0.04	0.01	0.95
LUMO+8	-3.549	0.46	0	0.54
LUMO+9	-3.287	0.03	0	0.97
LUMO+10	-3.277	0.04	0	0.96

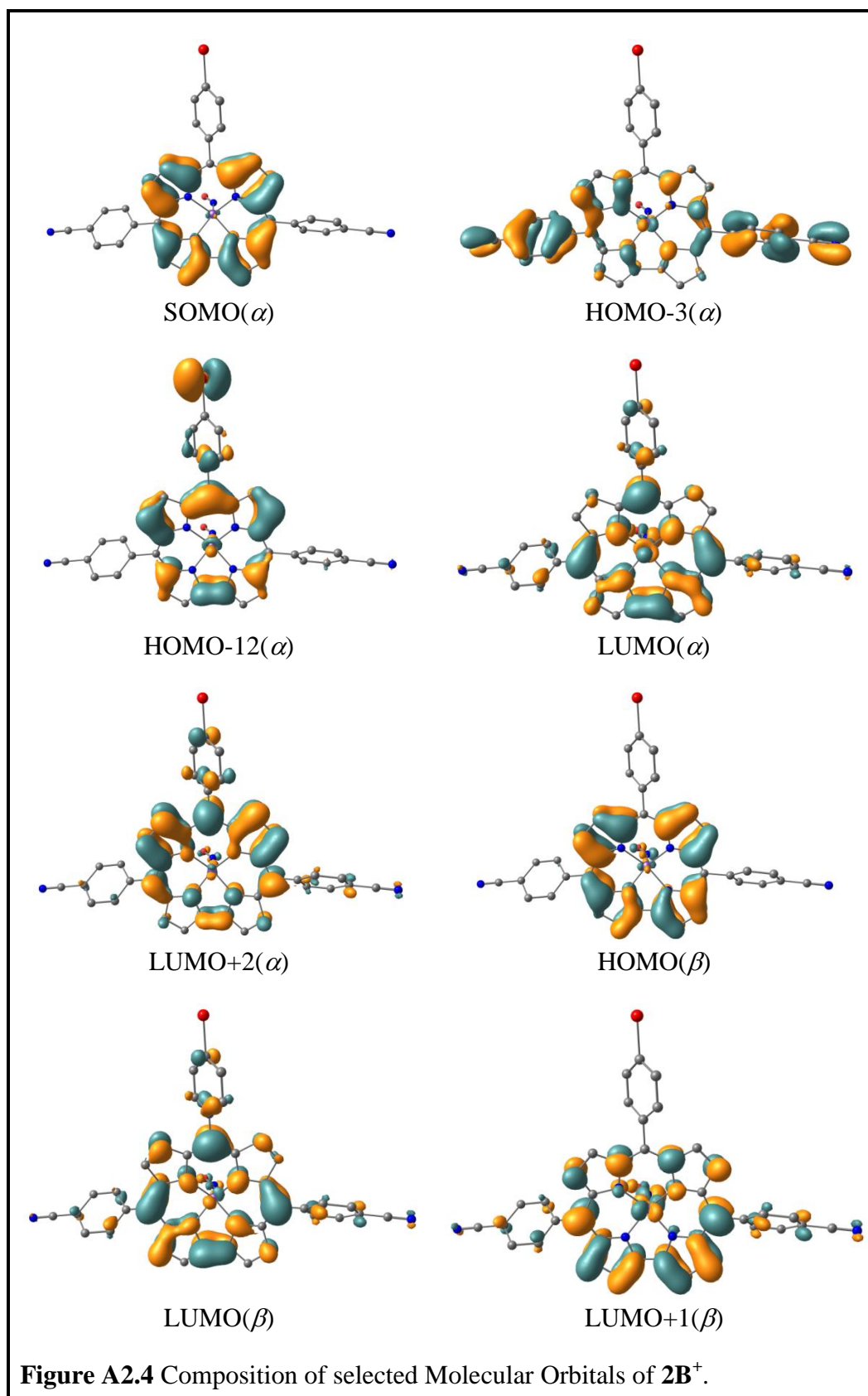


Table A2.4 Composition and Energies of Selected Molecular Orbitals of $2B^-$
($S=1/2$)

MO	Energy (eV)	Composition		
		Fe	NO	cor
α -spin				
HOMO-10	-4.853	0.30	0.05	0.65
HOMO-9	-4.73	0.03	0.01	0.96
HOMO-8	-4.617	0.68	0.03	0.29
HOMO-7	-4.481	0.03	0.01	0.97
HOMO-6	-4.345	0.05	0.01	0.93
HOMO-5	-3.867	0.03	0.01	0.96
HOMO-4	-3.54	0.25	0.05	0.70
HOMO-3	-3.478	0.21	0.04	0.74
HOMO-2	-3.002	0.41	0.13	0.45
HOMO-1	-2.275	0.01	0.00	0.99
SOMO	-1.588	0.18	0.06	0.76
LUMO	0.283	0.00	0.00	1.00
LUMO+1	0.572	0.00	0.00	1.00
LUMO+2	1.018	0.01	0.00	0.99
LUMO+3	1.128	0.01	0.00	0.99
LUMO+4	1.468	0.09	0.00	0.91
LUMO+5	1.484	0.03	0.00	0.97
LUMO+6	1.62	0.08	0.00	0.92
LUMO+7	1.707	0.00	0.01	0.99
LUMO+8	1.798	0.17	0.71	0.12
LUMO+9	1.83	0.17	0.71	0.12
LUMO+10	1.914	0.44	0.01	0.56
β -spin				
HOMO-10	-4.603	0.12	0.12	0.76
HOMO-9	-4.574	0.08	0.10	0.83
HOMO-8	-4.481	0.07	0.02	0.92
HOMO-7	-4.366	0.09	0.13	0.78

HOMO-6	-4.238	0.07	0.08	0.84
HOMO-5	-3.804	0.01	0.01	0.98
HOMO-4	-3.571	0.89	0.01	0.1
HOMO-3	-3.034	0.22	0.43	0.35
HOMO-2	-3.01	0.20	0.40	0.40
HOMO-1	-2.255	0.01	0.04	0.95
HOMO	-2.097	0.04	0.00	0.96
LUMO	0.302	0.00	0.01	0.99
LUMO+1	0.586	0.00	0.01	0.99
LUMO+2	1.01	0.01	0.02	0.97
LUMO+3	1.032	0.03	0.03	0.94
LUMO+4	1.466	0.10	0.00	0.90
LUMO+5	1.486	0.03	0.00	0.97
LUMO+6	1.62	0.09	0.00	0.91
LUMO+7	1.69	0.02	0.03	0.95
LUMO+8	1.902	0.52	0.01	0.47
LUMO+9	2.045	0.43	0.08	0.49
LUMO+10	2.096	0.58	0.10	0.32
LUMO+11	2.177	0.53	0.28	0.19
LUMO+12	2.261	0.64	0.13	0.23
LUMO+13	2.865	0.00	0.00	1.00

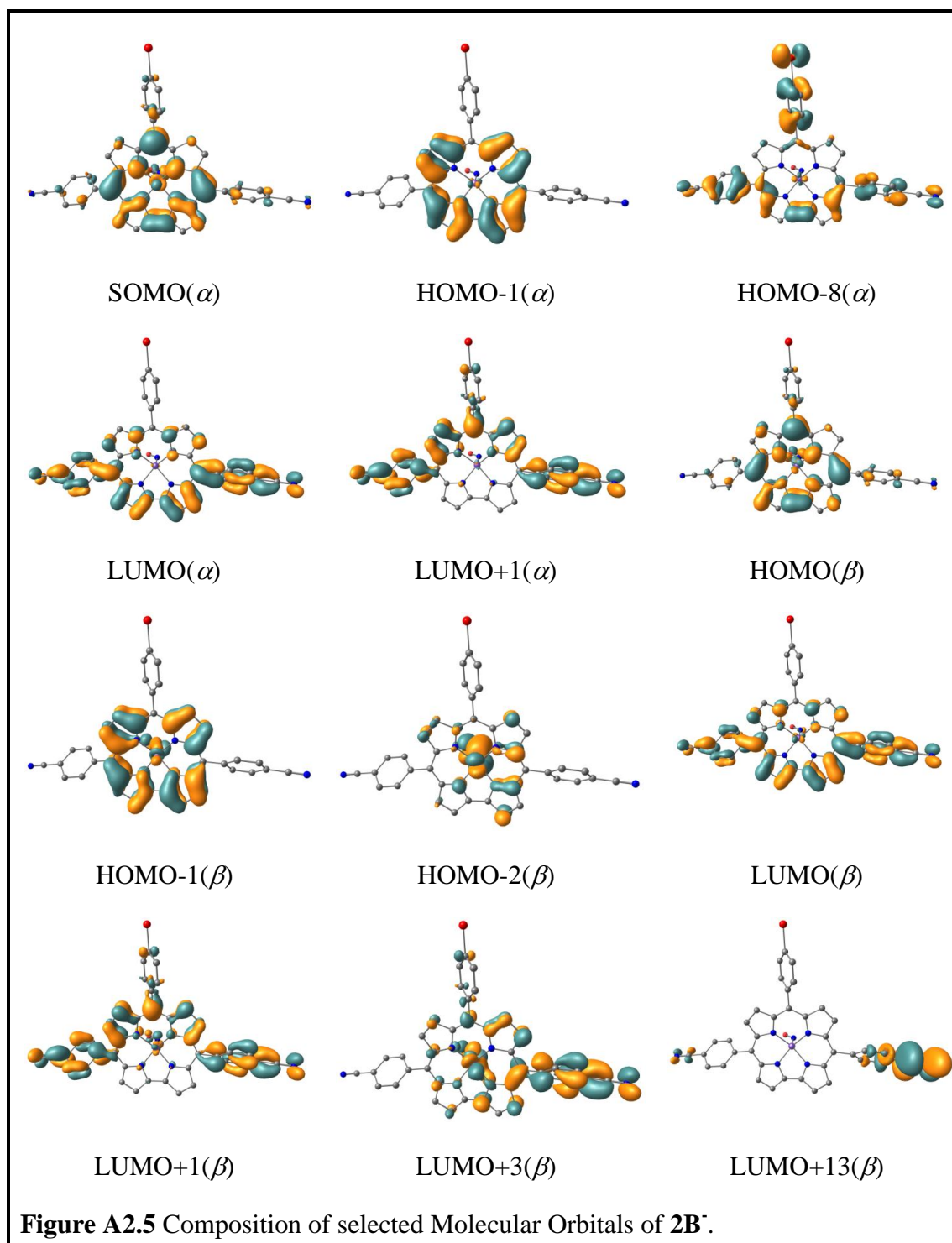


Table A5.1 Composition and Energies of Selected Molecular Orbitals of **4B**

Orbital	Energy (Eh)	Cor	Sub	Ag
HOMO-5	-0,25733	79,5	0,7	5,3
HOMO-4	-0,25289	79	0	3,8
HOMO-3	-0,23426	0,1	81	0
HOMO-2	-0,2114	12,6	67	0,1
HOMO-1	-0,20115	73,3	3,2	0,3
HOMO	-0,1911	65,1	8,1	1,6
LUMO	-0,10893	47,9	0	37,3
LUMO+1	-0,09974	70,3	0,1	2,5
LUMO+2	-0,08247	69,7	1,2	0,4
LUMO+3	-0,05938	69,5	0	0,4
LUMO+4	-0,0577	69,3	0,1	0,2

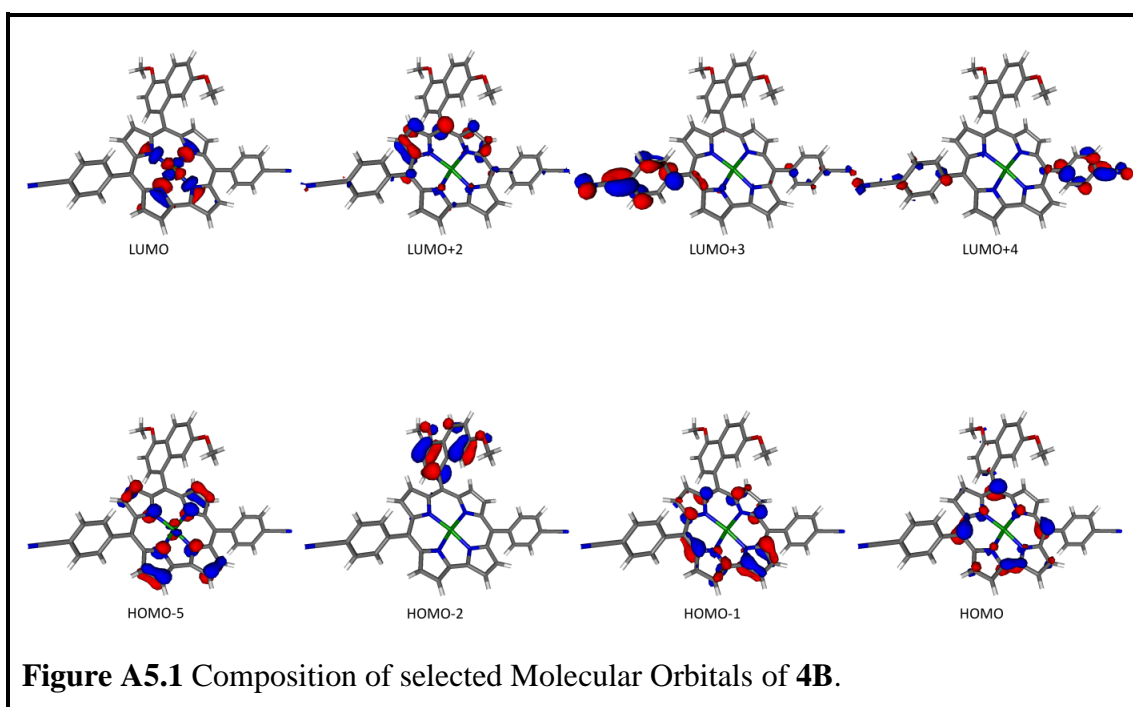


Table A5.2 Composition and Energies of Selected Molecular Orbitals of **4B⁺**

Orbital	Energy (Eh)	Cor	Sub	Ag
HOMO-5 a	-0,28691	67,5	12,6	3,1
HOMO-4 a	-0,28098	78,5	0,6	1,3
HOMO-3 a	-0,25702	1,4	79,2	0
HOMO-2 a	-0,24053	30,6	46,8	0,2
HOMO-1 a	-0,23082	75,8	1,4	0,3
HOMO a	-0,22097	45	29,8	1
LUMO a	-0,14383	48	0	37,9
LUMO+1 a	-0,13006	70,9	0,1	2,1
LUMO+2 a	-0,11641	68,1	3,2	0,7
LUMO+3 a	-0,07844	68,3	0	0,5
LUMO+4 a	-0,07663	68,7	0,3	0,1
LUMO+5 a	-0,07192	1,8	68,9	0
Orbital	Energy (Eh)	Cor	Sub	Ag
HOMO-5 b	-0,28399	78	2,5	3,8
HOMO-4 b	-0,28368	65,2	15,7	3,3
HOMO-3 b	-0,27784	78	1	1,6
HOMO-2 b	-0,25506	0,6	80,3	0
HOMO-1 b	-0,23351	62,6	14,3	0,4
HOMO b	-0,2293	33,3	43,5	0,2
LUMO b	-0,18328	56,2	17,1	1,5
LUMO+1 b	-0,14228	47,8	0	38,6
LUMO+2 b	-0,11982	71	0	0,9
LUMO+3 b	-0,10603	66,5	4,6	0,7
LUMO+4 b	-0,07717	68,4	0,2	0,6
LUMO+5 b	-0,07492	68,7	0	0,1

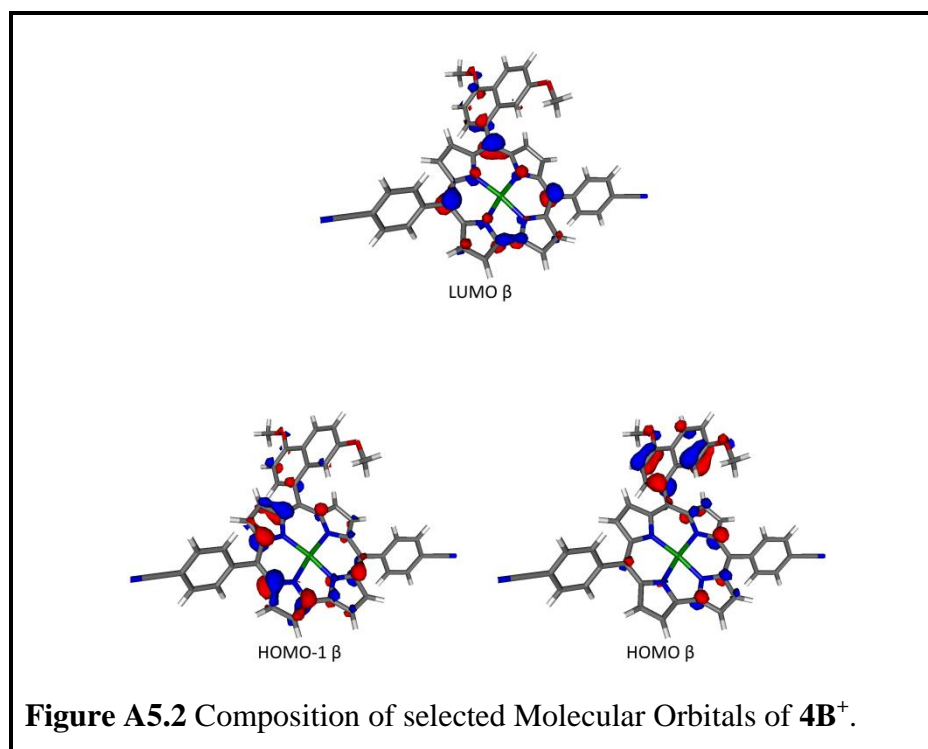


Table A5.3 Composition and Energies of Selected Molecular Orbitals of **4B⁻**

Orbital	Energy (Eh)	Cor	Sub	Ag
HOMO-5 a	-0,21947	71,2	5,3	8,2
HOMO-4 a	-0,21598	76	0	7,8
HOMO-3 a	-0,19441	6,4	72,8	0
HOMO-2 a	-0,16879	75,6	0,6	1,1
HOMO-1 a	-0,15569	69,6	3,1	1,3
HOMO a	-0,1298	50,8	0	34,9
LUMO a	-0,076	70,8	0,1	1,8
LUMO+1 a	-0,0589	69,7	1,3	0,2
LUMO+2 a	-0,03377	69	0,3	0,6
LUMO+3 a	-0,03277	66,5	2,9	0,6
LUMO+4 a	-0,03032	2,5	68,5	0
LUMO+5 a	-0,01403	70,3	0	0
Orbital	Energy (Eh)	Cor	Sub	Ag
HOMO-5 b	-0,22052	1,8	79,5	0
HOMO-4 b	-0,2163	73,9	1	9,5
HOMO-3 b	-0,21158	75,9	0	8,2
HOMO-2 b	-0,19433	6,5	72,8	0
HOMO-1 b	-0,16685	75,9	0,6	0,8
HOMO b	-0,15409	69,7	2,8	1,3
LUMO b	-0,07665	71,8	0	0,7
LUMO+1 b	-0,05884	68,8	1,2	0,4
LUMO+2 b	-0,04063	54	0,2	24,1
LUMO+3 b	-0,03311	68,3	1,2	0,6
LUMO+4 b	-0,03032	1,5	69,8	0,1
LUMO+5 b	-0,02688	55,1	0,6	20,3

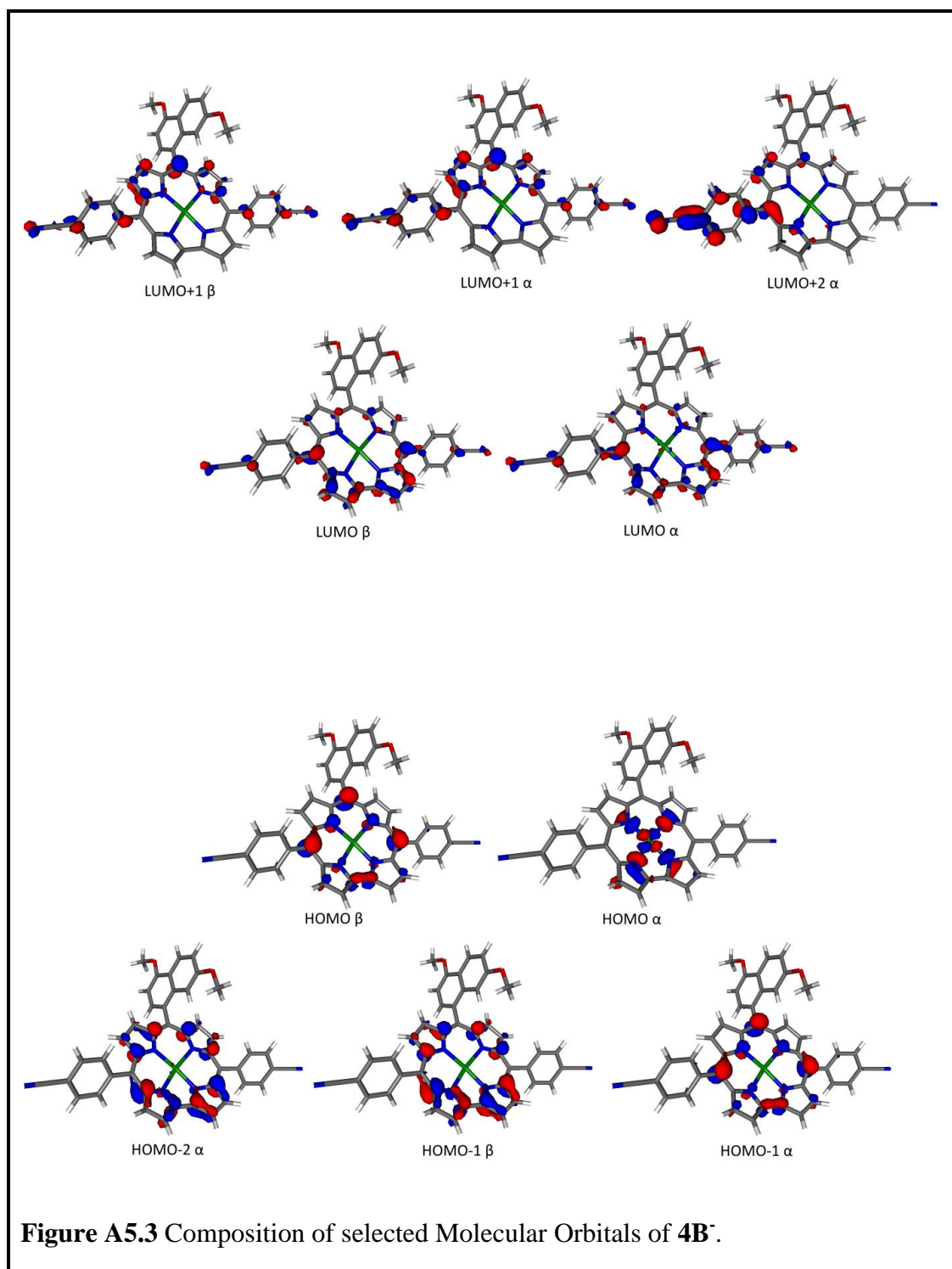


Table A5.4 TD-DFT Calculated Electronic Transitions for **4B**

Comp.	Main Contributing Excitation (%)	Transition Wavelength (nm)	Oscillator Strength	Exp. Transition Wavelength (nm)	Molar Absorption Coefficient, $M^{-1}cm^{-1}$
4B	HOMO \rightarrow LUMO(58 %)	568	0.211	566/584	25,240/37,280
	HOMO-2 \rightarrow LUMO(19 %)				
	HOMO-2 \rightarrow LUMO+2(48 %)	467	0.205	428	133,140
	HOMO \rightarrow LUMO+2(21 %)				
	HOMO \rightarrow LUMO+3(31 %)	424	0.266		
	HOMO-5 \rightarrow LUMO(18 %)				
	HOMO-2 \rightarrow LUMO+2(20 %)	424	0.586		
	HOMO-1 \rightarrow LUMO+2(17 %)				
	HOMO \rightarrow LUMO+4(43 %)				

Table A5.5 TD-DFT Calculated Electronic Transitions for **4B⁺**

Comp.	Main Contributing Excitation (%)	Transition Wavelength (nm)	Oscillator Strength	Exp. Transition Wavelength (nm)	Molar Absorption Coefficient, $M^{-1}cm^{-1}$
4B⁺	HOMO-1 β \rightarrow LUMO β (35 %)	1445	0.172	1203	2,700
	HOMO β \rightarrow LUMO β (59 %)				
	Many excitations between 400 and 650 nm of similar fosc				

Table A5.6 TD-DFT Calculated Electronic Transitions for **4B⁻**

Comp.	Main Contributing Excitation (%)	Transition Wavelength (nm)	Oscillator Strength	Exp. Transition Wavelength (nm)	Molar Absorption Coefficient, M ⁻¹ cm ⁻¹
4B⁻	HOMO-1 α \rightarrow LUMO α (32 %)	627	0.374	648	27,000
	HOMO α \rightarrow LUMO+2 α (18 %)				
	HOMO β \rightarrow LUMO β (28 %)				
	HOMO-2 α \rightarrow LUMO +1 α (29 %)	481	0.714	447	44,000
	HOMO-1 β \rightarrow LUMO+1 β (27 %)				
	mixed	359	0.382	334	18,300
	mixed	361	0.255		
mixed	359	0.240			

Table A5.7 Composition and Energies of Selected Molecular Orbitals of **2B**

Orbital	Energy (Eh)	Cor	Sub	Ag
HOMO-5	-0,26306	74,9	9,2	1,1
HOMO-4	-0,25912	76,1	3,6	5,2
HOMO-3	-0,25422	79,7	0	3,8
HOMO-2	-0,25004	13,7	71,3	0,2
HOMO-1	-0,20333	76,6	0,2	0,5
HOMO	-0,19328	69,7	3,7	1,8
LUMO	-0,11058	48,1	0	37,4
LUMO+1	-0,10089	70,2	0,2	2,4
LUMO+2	-0,08478	68,1	3	0,5
LUMO+3	-0,06025	68,8	0,2	0,4
LUMO+4	-0,05833	69	0,2	0,3
LUMO+5	-0,03323	65,9	3,9	0,1

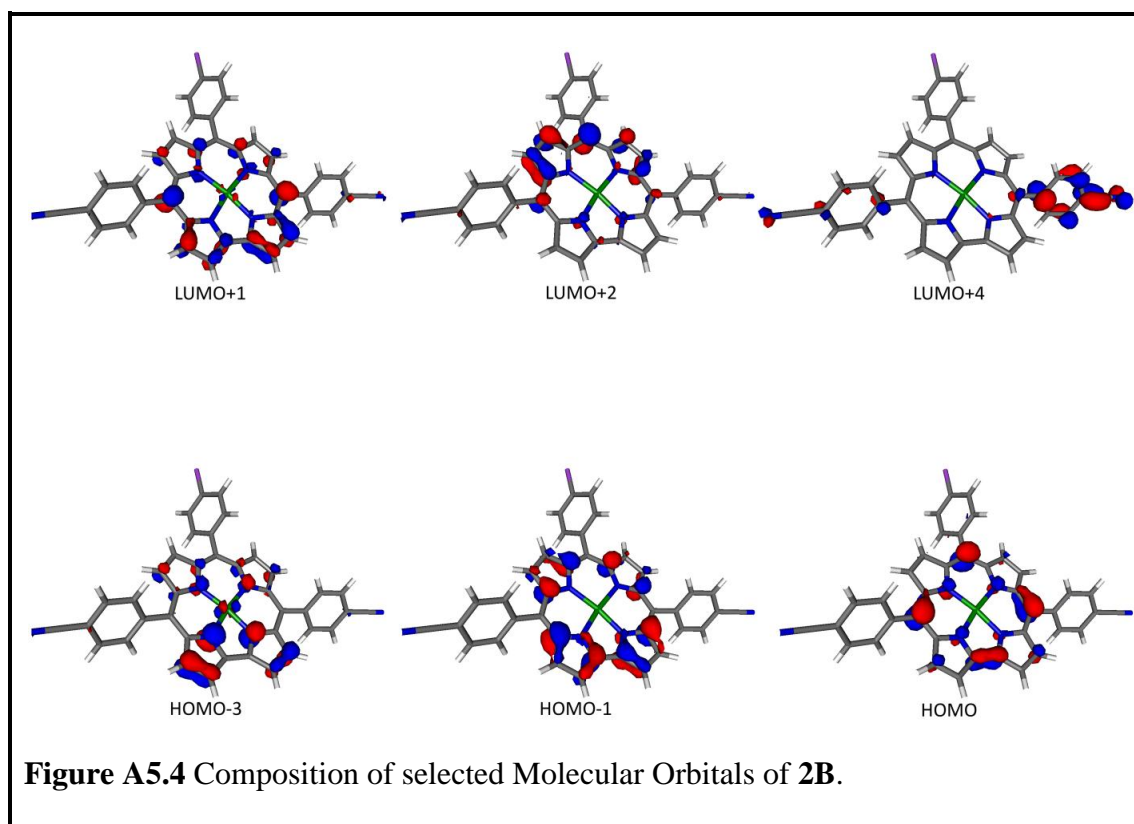


Table A5.8 Composition and Energies of Selected Molecular Orbitals of **2B⁺**

Orbital	Energy (Eh)	Cor	Sub	Ag
HOMO-6 α	-0,29351	64,3	18,5	2
HOMO-5 α	-0,29184	79,5	0,7	4,1
HOMO-4 α	-0,29038	38,9	44,2	1,9
HOMO-3 α	-0,28432	78,4	0,8	0,8
HOMO-2 α	-0,27052	12,6	72,7	0
HOMO-1 α	-0,23669	76,7	0,2	0,3
HOMO α	-0,23112	66,3	7,5	1
LUMO α	-0,14938	48	0	38
LUMO+1 α	-0,13519	70,9	0	2,2
LUMO+2 α	-0,12253	68,6	3,5	0,8
LUMO+3 α	-0,08093	68,1	0	0,5
LUMO+4 α	-0,07892	69,2	0	0,1
LUMO+5 α	-0,05336	47	22,3	0,1
LUMO+6 α	-0,05245	68,9	0,3	0
Orbital	Energy (Eh)	Cor	Sub	Ag
HOMO-6 β	-0,2912	69,5	12,6	0,7
HOMO-5 β	-0,29099	74,9	5,2	0,4
HOMO-4 β	-0,28825	78,5	1,6	4,4
HOMO-3 β	-0,28758	60,8	21,2	2,6
HOMO-2 β	-0,28078	78,9	0,8	1
HOMO-1 β	-0,26795	11,1	73,6	0
HOMO β	-0,23827	76,8	0,2	0,5
LUMO β	-0,18814	68,5	4,4	1,5
LUMO+1 β	-0,14791	47,8	0	38,9
LUMO+2 β	-0,12322	71,1	0	0,9
LUMO+3 β	-0,10945	66,3	4,6	0,6
LUMO+4 β	-0,07939	68,8	0,3	0,6
LUMO+5 β	-0,07689	69	0,1	0,1
LUMO+6 β	-0,05241	54,7	14,5	0,1

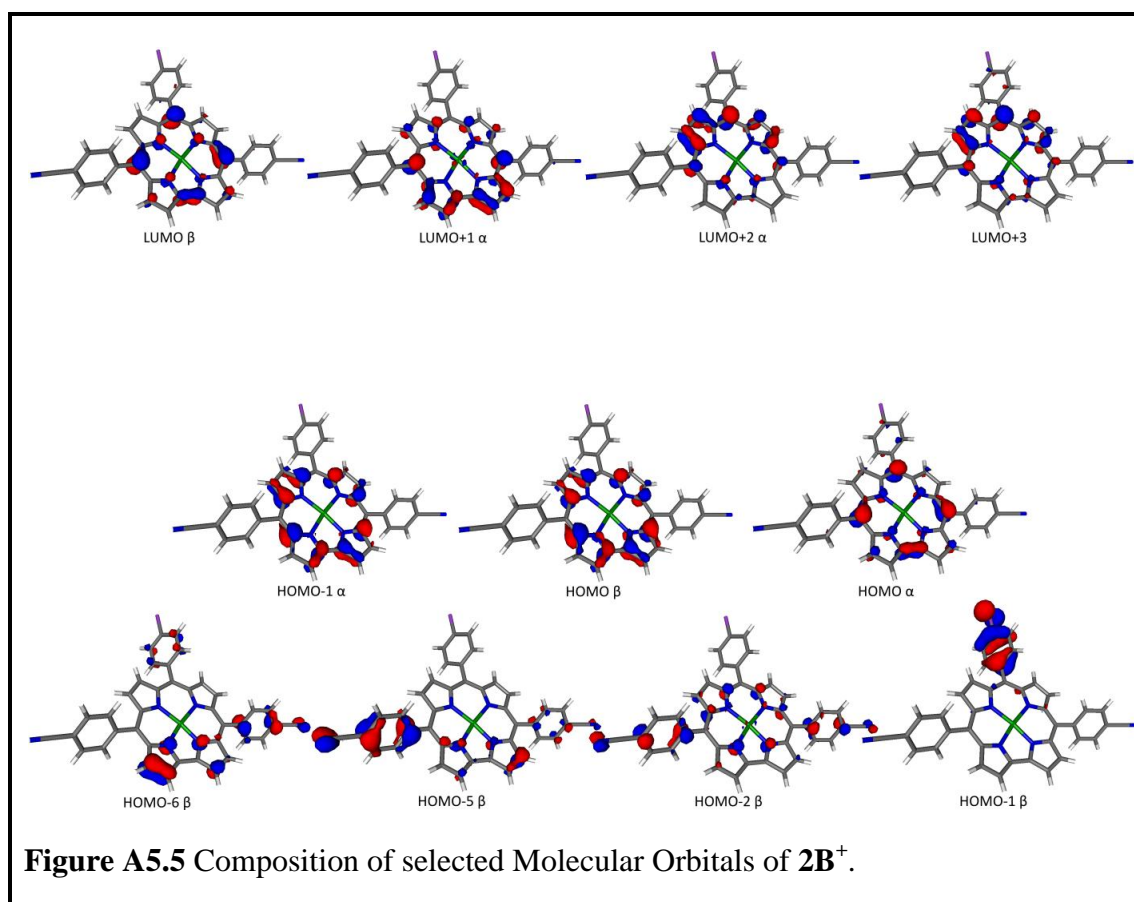


Table A5.9 Composition and Energies of Selected Molecular Orbitals of **2B⁺**

Orbital	Energy (Eh)	Cor	Sub	Ag
HOMO-6 α	-0,23166	28,7	54,4	1,1
HOMO-5 α	-0,22878	83,6	0,5	0,7
HOMO-4 α	-0,22077	74,3	2,8	7,9
HOMO-3 α	-0,21777	76,2	0	7,6
HOMO-2 α	-0,17071	76	0	1,4
HOMO -1 α	-0,15752	70,2	2,8	1,5
HOMO α	-0,13241	51,2	0	34,7
LUMO α	-0,07697	71,1	0,1	1,7
LUMO+1 α	-0,06129	67,6	3,5	0,3
LUMO+2 α	-0,03564	67,9	2,2	0,7
LUMO+3 α	-0,03383	67,7	1,4	0,6
LUMO+4 α	-0,01493	64,1	5	0,1
LUMO+5 α	-0,0146	68,5	0,8	0
Orbital	Energy (Eh)	Cor	Sub	Ag
HOMO-6 β	-0,23509	78,6	1,1	0,6
HOMO-5 β	-0,23085	32,9	50,1	1,1
HOMO-4 β	-0,22627	84	0,5	0,8
HOMO-3 β	-0,21768	74,4	1,1	9
HOMO-2 β	-0,21344	76	0	8,1
HOMO-1 β	-0,16875	76,4	0	0,8
HOMO β	-0,15592	70,1	2,9	1,2
LUMO β	-0,07759	71,2	0	0,7
LUMO+1 β	-0,06132	67,2	3,2	0,4
LUMO+2 β	-0,04255	52,2	0,1	26,4
LUMO+3 β	-0,03496	67,5	2,7	0,7
LUMO+4 β	-0,02877	55,7	2	17,5
LUMO+5 β	-0,01494	64,5	5,1	0,1

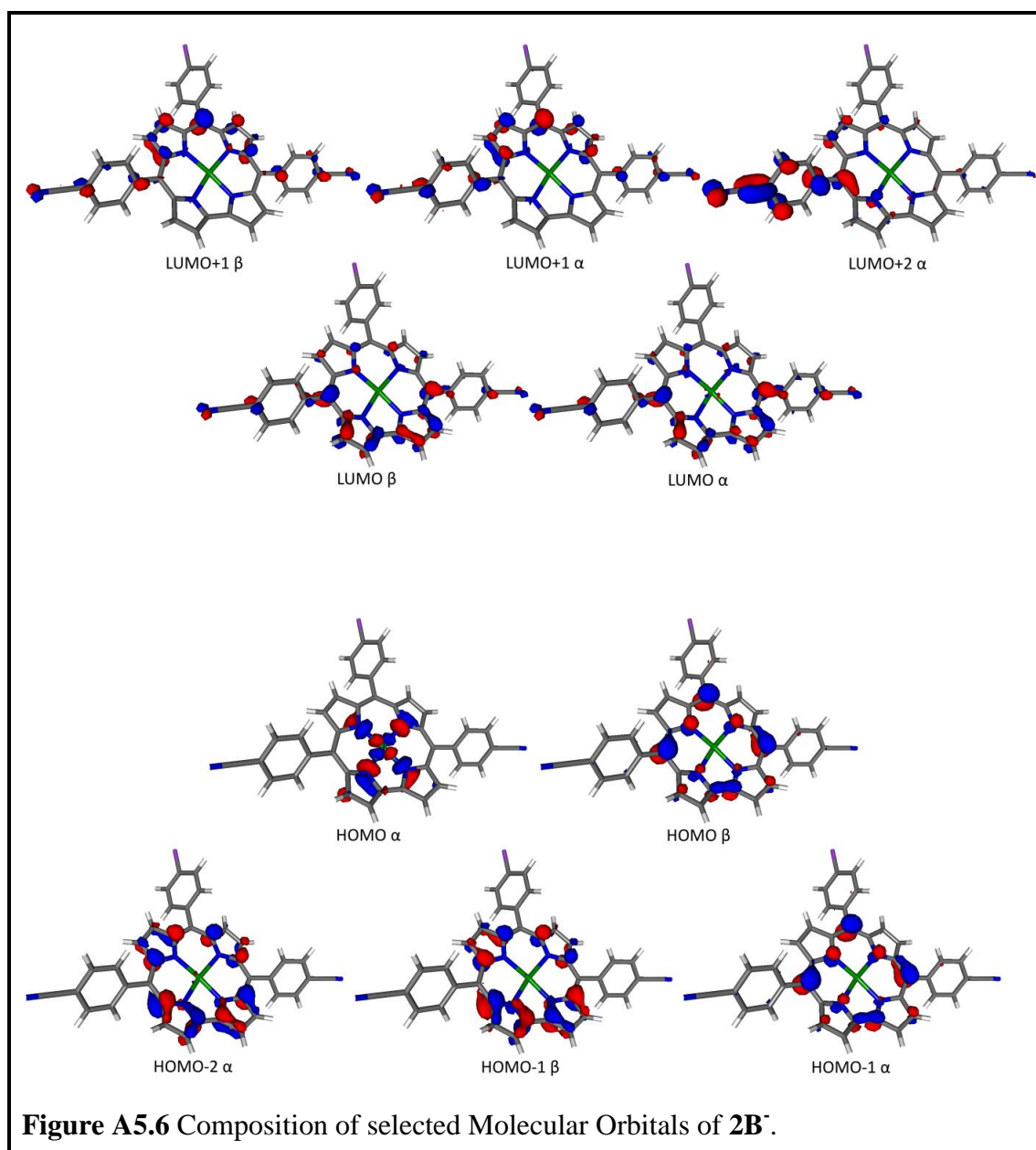


Table A5.10 TD-DFT Calculated Electronic Transitions for **2B**

Comp.	Main Contributing Excitation (%)	Transition Wavelength (nm)	Oscillator Strength	Exp. Transition Wavelength (nm)	Molar Absorption Coefficient, $M^{-1}cm^{-1}$
2B	HOMO \rightarrow LUMO+1(70 %)	541	0.288	584	32,000
	HOMO-1 \rightarrow LUMO+2(24 %)				
	HOMO-1 \rightarrow LUMO+2(39 %)	419	0.903	427	37,300
	HOMO \rightarrow LUMO+4(39 %)				
	HOMO-3 \rightarrow LUMO+1(41 %)	338	0.535	330	11,600

Table A5.11 TD-DFT Calculated Electronic Transitions for **2B⁺**

Comp.	Main Contributing Excitation (%)	Transition Wavelength (nm)	Oscillator Strength	Exp. Transition Wavelength (nm)	Molar Absorption Coefficient, $M^{-1}cm^{-1}$
2B⁺	HOMO-1 $\beta \rightarrow$ LUMO β (87 %)	869	0.075	752	3,900
	HOMO-1 $\alpha \rightarrow$ LUMO+2 α (22 %)	569	0.132	557-694	
	HOMO-6 $\beta \rightarrow$ LUMO β (34 %)				
	HOMO $\alpha \rightarrow$ LUMO+1 α (13%)				
	HOMO-5 $\beta \rightarrow$ LUMO β (15 %)				
	HOMO-1 $\alpha \rightarrow$ LUMO+2 α (28 %)	522	0.267		
	HOMO-2 $\beta \rightarrow$ LUMO β (16 %)				
	HOMO $\beta \rightarrow$ LUMO+3 β (26 %)				
	mixed	385	0.209	419/409	32,700/ 33,100
	mixed	383	0.274		
mixed	376	0.570			
mixed	351	0.342			

Table A5.12 TD-DFT Calculated Electronic Transitions for $2B^-$

Comp.	Main Contributing Excitation (%)	Transition Wavelength (nm)	Oscillator Strength	Exp. Transition Wavelength (nm)	Molar Absorption Coefficient, $M^{-1}cm^{-1}$
$2B^-$	HOMO α \rightarrow HOMO+2 α (45 %)	660	0.202	646	20,000
	HOMO-1 α \rightarrow LUMO α (20 %)				
	HOMO β \rightarrow LUMO β (15 %)				
	HOMO-1 α \rightarrow LUMO α (19 %)	646	0.199	589	14,200
	HOMO α \rightarrow LUMO+2 α (47 %)				
	HOMO β \rightarrow LUMO β (17 %)				
	HOMO-2 α \rightarrow LUMO+1 α (28 %)	486	0.869	449	35,500
	HOMO-1 β \rightarrow LUMO+1 β (25 %)				
	mixed	378	0.467		

Table A5.13 Selected X-ray and DFT Calculated (BP86/def2-TZVP-ZORA) Bond Distances (Å) and Angles (deg) for **4B**

	4B (X-ray)	4B (DFT)
Ag(1)-N(1)	1.919(4)	1.952
Ag(1)-N(4)	1.928(4)	1.955
Ag(1)-N(3)	1.945(4)	1.968
Ag(1)-N(2)	1.949(4)	1.970
N(1)-C(1)	1.367(7)	1.381
N(1)-C(4)	1.373(6)	1.363
N(2)-C(6)	1.393(6)	1.386
N(2)-C(9)	1.360(6)	1.379
N(3)-C(11)	1.362(6)	1.379
N(3)-C(14)	1.392(6)	1.387
N(4)-C(16)	1.366(6)	1.367
N(4)-C(19)	1.391(7)	1.384
C(1)-C(2)	1.410(7)	1.426
C(2)-C(3)	1.428(5)	1.395
C(3)-C(4)	1.429(7)	1.441
C(4)-C(5)	1.396(7)	1.421
C(5)-C(6)	1.409(7)	1.420
C(6)-C(7)	1.426(7)	1.444
C(7)-C(8)	1.353(7)	1.378
C(8)-C(9)	1.437(6)	1.440
C(9)-C(10)	1.395(6)	1.414
C(10)-C(11)	1.401(7)	1.415
C(11)-C(12)	1.439(7)	1.439
C(12)-C(13)	1.347(7)	1.378
C(13)-C(14)	1.432(7)	1.443
C(14)-C(15)	1.410(7)	1.420
C(15)-C(16)	1.410(7)	1.421
C(16)-C(17)	1.422(7)	1.440
C(17)-C(18)	1.368(7)	1.396

C(18)-C(19)	1.410(7)	1.425
C(19)-C(1)	1.419(7)	1.426
N(1)-Ag(1)-N(4)	81.32(17)	80.62
N(1)-Ag(1)-N(3)	171.70(18)	172.20
N(4)-Ag(1)-N(3)	91.32(16)	92.01
N(1)-Ag(1)-N(2)	91.30(17)	91.70
N(4)-Ag(1)-N(2)	172.43(16)	172.20
N(3)-Ag(1)-N(2)	96.15(16)	95.72
C(1)-N(1)-Ag(1)	116.7(3)	116.03
C(4)-N(1)-Ag(1)	131.2(4)	130.22
C(9)-N(2)-Ag(1)	123.1(3)	123.60
C(6)-N(2)-Ag(1)	125.5(3)	125.02
C(11)-N(3)-Ag(1)	123.0(3)	123.15
C(14)-N(3)-Ag(1)	125.2(3)	124.73
C(16)-N(4)-Ag(1)	130.2(3)	129.44
C(19)-N(4)-Ag(1)	114.5(3)	115.59

Table A6.1 TD-DFT Calculated Electronic Transitions for **1**

Compound	Main Contributing Excitation (%)	Transition Wavelength (nm)	Oscillator Strength	Exp. Transition Wavelength (nm)	Molar Absorption Coefficient, $M^{-1}cm^{-1}$
1	HOMO-1→LUMO+2 (27)	516	0.122	619/548	7 065/9 539
	HOMO→LUMO+1 (51)				
	HOMO-6→LUMO(46)	429	0.138	414	76 698
	HOMO-1→LUMO+1 (15)				
	HOMO→LUMO+2 (20)				
	HOMO-5→LUMO (47)	426	0.142		
	HOMO-1→LUMO+2 (29)				
	HOMO-5→LUMO (35)	403	0.576		
	HOMO-1→LUMO+2 (20)				
	HOMO-6→LUMO (29)	401	0.409		
HOMO→LUMO+2 (15)					

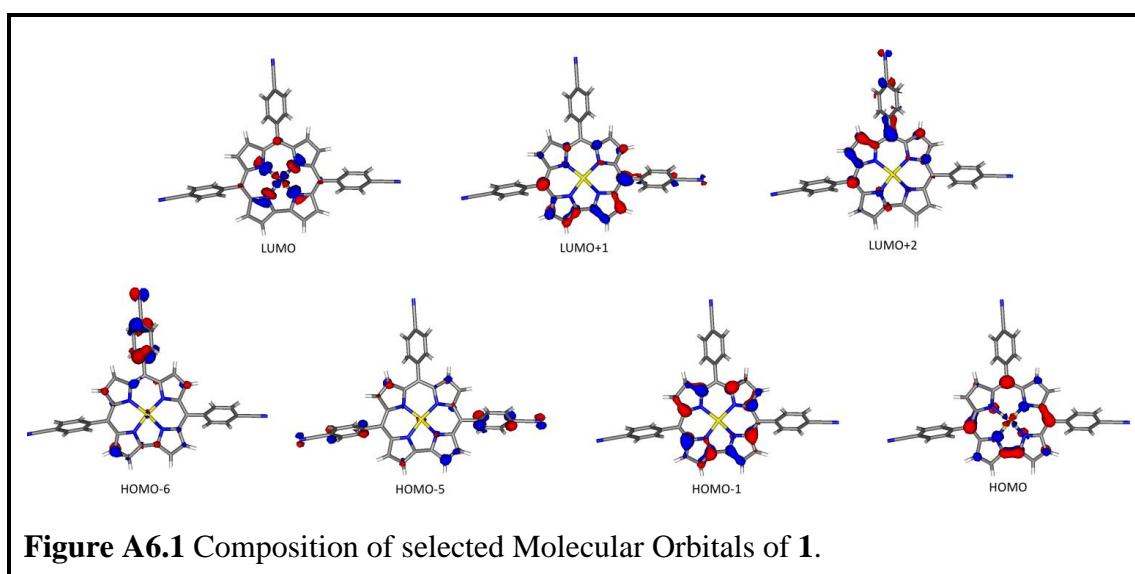


Table A6.2 TD-DFT Calculated Electronic Transitions for **3**

Compound	Main Contributing Excitation (%)	Transition Wavelength (nm)	Oscillator Strength	Exp. Transition Wavelength (nm)	Molar Absorption Coefficient, $M^{-1}cm^{-1}$
3	HOMO→LUMO+1 (67)	552	0.133	557/621	12500/8700
	HOMO-4→LUMO (19)				
	HOMO→LUMO+2 (39)	450	0.332	443	sh
	HOMO-1→LUMO+1 (21)				
	HOMO-8→LUMO+3 (18)	421	0.233	411	76900
	HOMO-7→LUMO (38)				
	HOMO-1→LUMO+2 (33)	394	0.751		
	HOMO-7→LUMO(38)				
	HOMO-2→LUMO+3 (30)	352	0.311		
	HOMO-1→LUMO+4 (19)				
	HOMO-1→LUMO+4 (19)	353	0.326		
HOMO→LUMO+5 (27)					

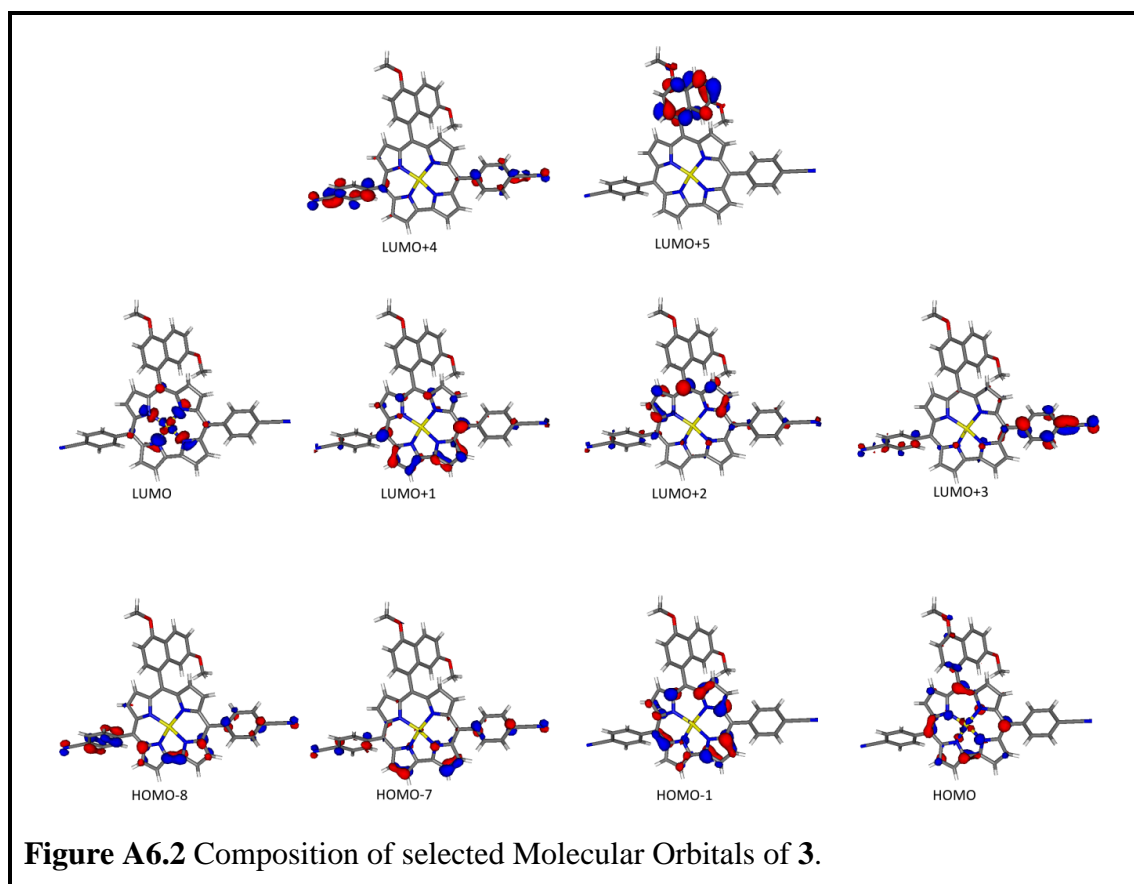


Table A6.3 TD-DFT Calculated Electronic Transitions for 1^+

Compound	Main Contributing Excitation (%)	Transition Wavelength (nm)	Oscillator Strength	Exp. Transition Wavelength (nm)	Molar Absorption Coefficient, $M^{-1}cm^{-1}$
1^+	HOMO-7 α →LUMO α (13)	604	0.095	550	sh
	HOMO-5 α →LUMO α (27)				
	HOMO-3 α →LUMO α (26)				
	HOMO-6 α →LUMO α (31)				
	HOMO-2 α →LUMO α (17)				
	HOMO-6 β →LUMO β (15)	536	0.123		
	HOMO-11 α →LUMO α (11)				
	HOMO-1 α →LUMO+1 α (18)				
	HOMO α →LUMO+2 α (14)				
	HOMO-10 β →LUMO β (24)				

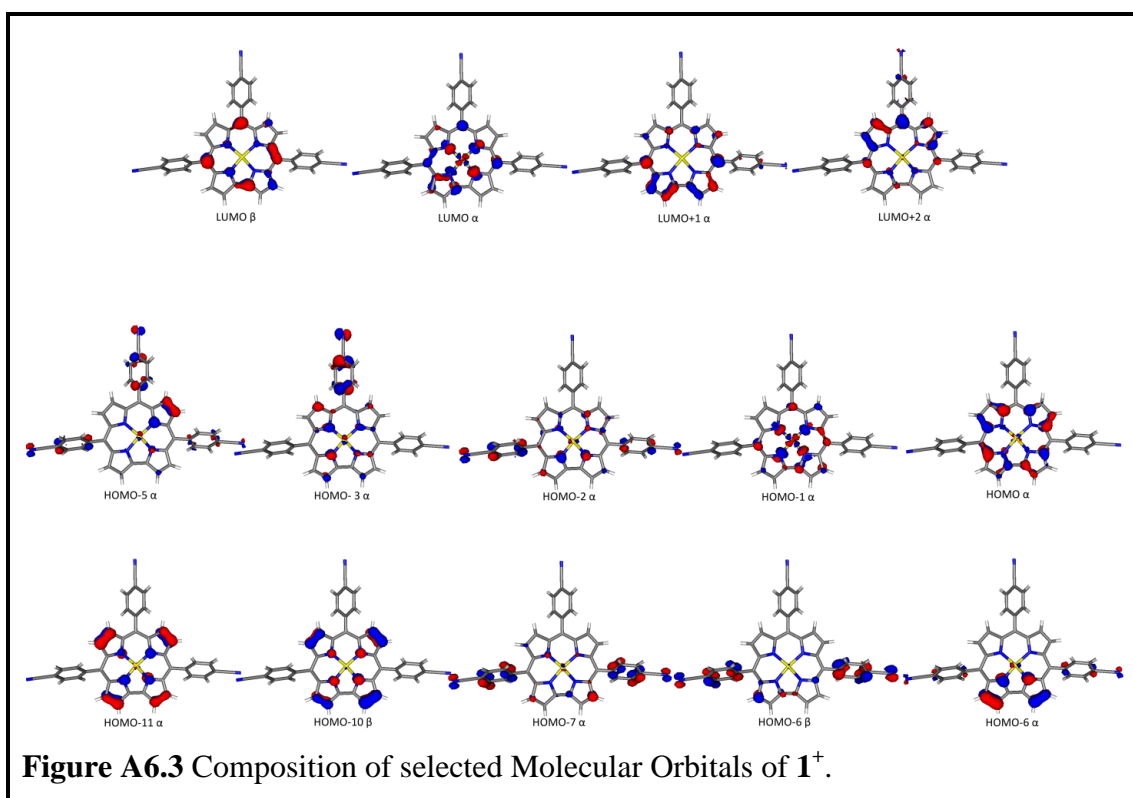


Table A6.4 TD-DFT Calculated Electronic Transitions for **3⁺**

Compound	Main Contributing Excitation (%)	Transition Wavelength (nm)	Oscillator Strength	Exp. Transition Wavelength (nm)	Molar Absorption Coefficient, M ⁻¹ cm ⁻¹
3⁺	HOMO-2 α →LUMO α (59)	1670	0.023	921	8400
	HOMO-1 β →LUMO β (22)				
	HOMO-2 α →LUMO α (32)	1419	0.148		
	HOMO-1 β →LUMO β (27)				
	HOMO-2 β →LUMO β (15)				
	HOMO-2 β →LUMO β (78)	1310	0.055		
	HOMO-3 α →LUMO α (90)	1188	0.028		
	HOMO-7 α →LUMO α (40)	553	0.231	495	sh
	HOMO-6 β →LUMO β (15)				
	HOMO-14 α →LUMO α (46)	406	0.370	419	65600
	mixed	366	0.231		
	mixed	360	0.184		
	mixed	358	0.196		
	HOMO-1 α →LUMO+4 α (26)	337	0.181		
	HOMO β →LUMO+5 β (16)				
mixed	313	0.166			

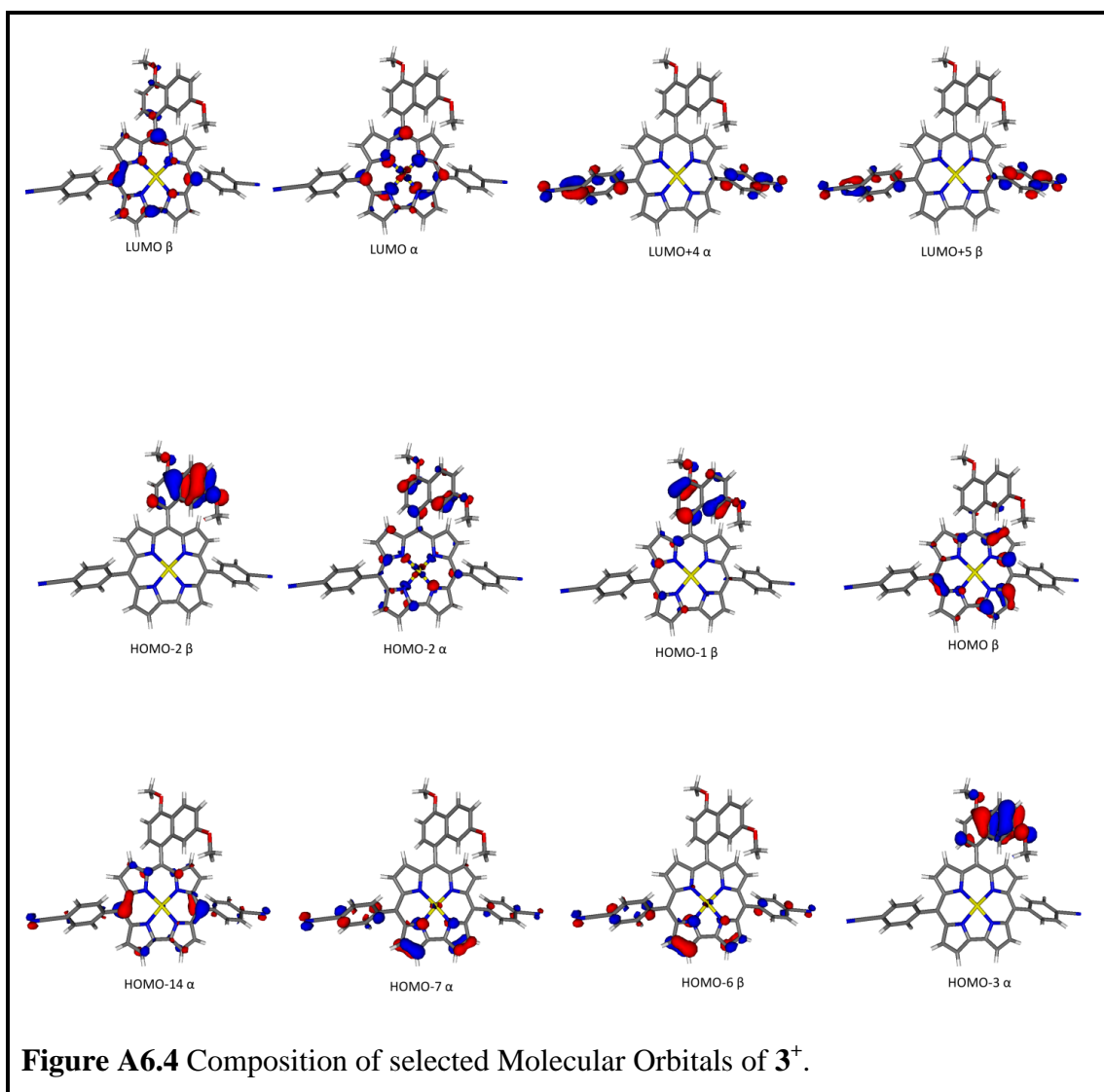


Table A6.5 TD-DFT Calculated Electronic Transitions for 1^-

Compound	Main Contributing Excitation (%)	Transition Wavelength (nm)	Oscillator Strength	Exp. Transition Wavelength (nm)	Molar Absorption Coefficient, $M^{-1}cm^{-1}$
1^-	HOMO α →LUMO α (29)	591	0.257	618/587/ 549	26300/sh/ 11300
	HOMO-1 β →LUMO+1 β (20)				
	HOMO β →LUMO β (28)				
	HOMO-1 α →LUMO α (15)	523	0.342		
	HOMO α →LUMO α (16)				
	HOMO-1 β →LUMO β (16)				
	HOMO β →LUMO+1 β (17)				
	HOMO β →LUMO+4 β (13)				
	HOMO-1 α →LUMO+1 α (24)				
	HOMO α →LUMO+3 α (13)	511	0.699		
	HOMO-1 β →LUMO+1 β (27)				
	HOMO-3 α →LUMO+1 α (14)				
	HOMO-1 α →LUMO+4 α (16)	362	0.601	448/419	77900/sh
	HOMO-1 β →LUMO+4 β (18)				
	HOMO-1 α →LUMO+6 α (15)				
	HOMO-1 α →LUMO+5 α (11)	359	0.313		
	Mixed				
	HOMO-3 α →LUMO+4 α (38)				
HOMO-2 β →LUMO+1 β (21)	342	0.333			

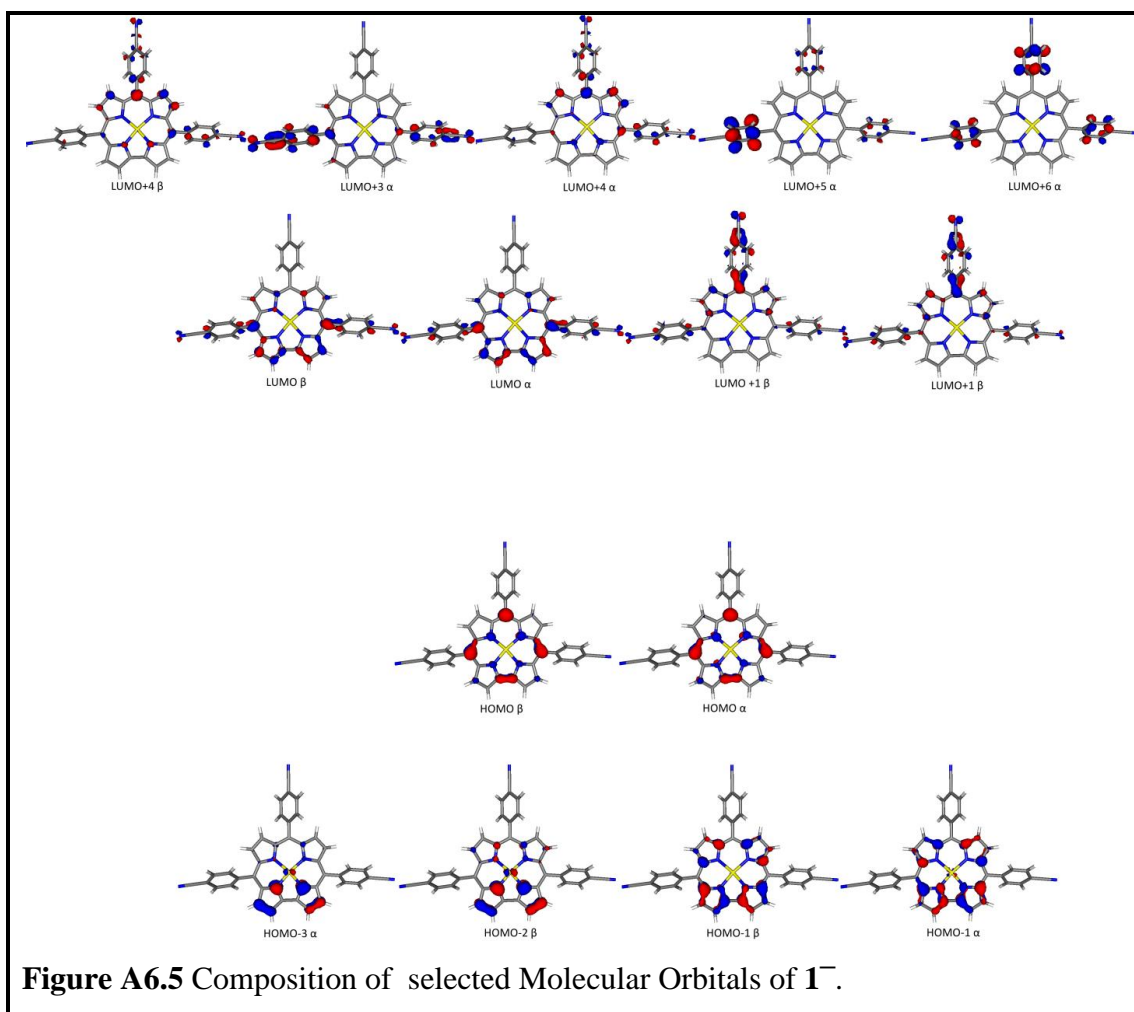


Table A6.6 TD-DFT Calculated Electronic Transitions for 3^-

Compound	Main Contributing Excitation (%)	Transition Wavelength (nm)	Oscillator Strength	Exp. Transition Wavelength (nm)	Molar Absorption Coefficient, $M^{-1}cm^{-1}$
3^-	HOMO-2 α →LUMO α (54)	680	0.125	620	33900
	HOMO α →LUMO α (20)				
	HOMO β →LUMO β (20)				
	HOMO-2 α →LUMO α (29)	584	0.236	593	sh
	HOMO-1 α →LUMO+1 α (28)				
	HOMO β →LUMO β (19)	503	0.567	547	11400
	HOMO-1 α →LUMO+1 α (25)				
	HOMO-1 β →LUMO+1 β (30)				
	HOMO β →LUMO+2 β (16)	363	0.668	446/420	79300/sh
	mixed				
HOMO β →LUMO+8 β (31)	358	0.445			
mixed					
		347	0.563		

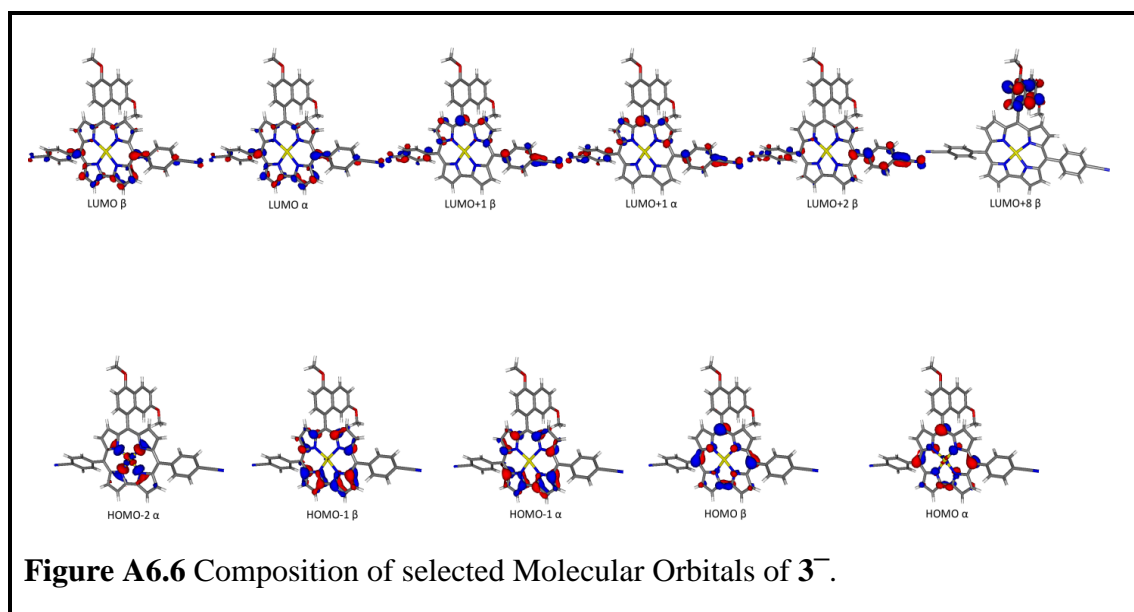


Table A6.7(a) DFT Calculated Saddling Values for **3**, **3⁺**, and **3⁻** and Experimental Values for **3**

3	BP86 Singlet	BP86 BS	BP86 Triplet	Olyp (RKS/UKS)	B3lyp	BP86 no D3	Exp
Planes 1-3	20.1°	20.1°	3.1°	18.7°/18.8°	19.3°	18.2°	24°/24°
Planes 2-4	19.5°	19.5°	3.0°	19.2°/19.1°	18.3°	18.8°	15°/18°

3⁻	BP86 Doublet	BP86 BS	BP86 Quartet	Olyp	B3lyp
Planes 1-3	10.4°	10.4°	8.9°	6.2°	8.2°
Planes 2-4	8.5°	8.5°	8.0°	6.5°	6.8°

3⁺	BP86 Doublet	BP86 BS	BP86 Quartet	Olyp	B3lyp
Planes 1-3	9.8°	10.8°	1.5°	12.3°	18.7°
Planes 2-4	10.8°	7.0°	2.1°	12.4°	11.1°

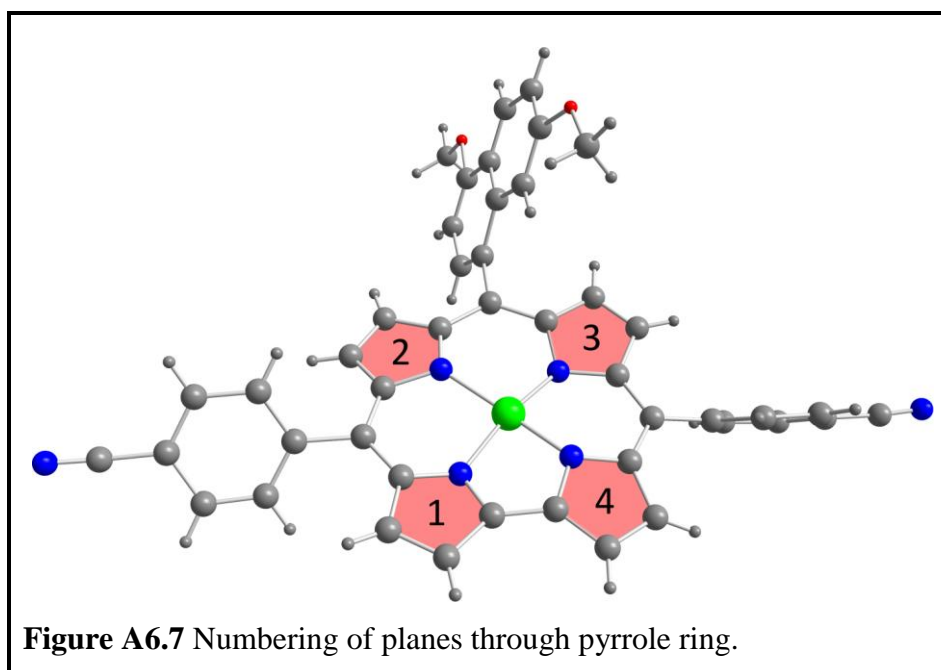


Table A6.7(b) Total Energies of Geometry Optimized Structures of **3**

Method	Final Single Point Energy (Eh)
BP86 (singlet)	-3875.99
BP86 (BS)	-3875.99
BP86(triplet)	-3875.98
BP86 (singlet no D3)	-3875.77
OLYP(UKS)	-3875.09
OLYP(RKS)	-3875.09
B3LYP(singlet)	-3874.28

Table A6.7(c) Total Energies of Geometry Optimized Structures of **3⁺**

Method	Final Single Point Energy (Eh)
BP86 (doublet)	-3875.80
BP86 (BS)	-3875.80
BP86(quartet)	-3875.78
OLYP	-3874.90
B3LYP(doublet)	-3874.08

Table A6.7(d) Total Energies of Geometry Optimized Structures of **3⁻**

Method	Final Single Point Energy (Eh)
BP86 (doublet)	-3876.14
BP86 (BS)	-3876.14
BP86(quartet)	-3876.09
OLYP	-3875.22
B3LYP(doublet)	-3874.42